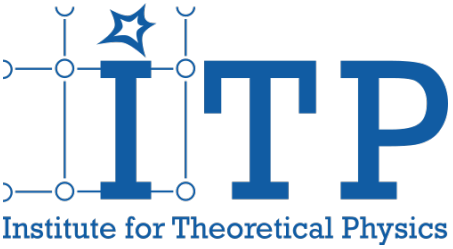

Dissipative and shearing dynamics in astrophysical compact objects

Dissertation
zur Erlangung des Doktorgrades
der Naturwissenschaften

vorgelegt beim Fachbereich Physik
der Johann Wolfgang Goethe-Universität
in Frankfurt am Main

von
Michail Chabanov
aus Moskau, Russland

Frankfurt am Main (2023)
(D30)

vom Fachbereich Physik der
Johann Wolfgang Goethe-Universität als Dissertation angenommen.

Dekan: Prof. Dr. Roger Erb

Gutachter: Prof. Dr. Luciano Rezzolla (Goethe-Universität, Frankfurt am Main)
Prof. Dr. Dirk H. Rischke (Goethe-Universität, Frankfurt am Main)

Datum der Disputation:

Eigenständigkeitserklärung

Ich erkläre hiermit, dass ich die vorgelegte Dissertation über "Dissipative and shearing dynamics in astrophysical compact objects" selbstständig angefertigt und mich anderer Hilfsmittel als der in ihr angegebenen nicht bedient habe, insbesondere, dass alle Entlehnungen aus anderen Schriften mit Angabe der betreffenden Schrift gekennzeichnet sind.

Ich versichere, die Grundsätze der guten wissenschaftlichen Praxis beachtet, und nicht die Hilfe einer kommerziellen Promotionsvermittlung in Anspruch genommen zu haben.

_____

Michail Chabanov

Abstract

Binary neutron star mergers represent unique observational phenomena because all four fundamental interactions play an important role at various stages of their evolution by leaving imprints in astronomical observables. This makes their accurate numerical modeling a challenging multiphysics problem that promises to increase our understanding of the high-energy astrophysics at play, thereby providing constraints for the underlying fundamental theories such as the gravitational interaction or the strong interaction of dense matter. For example, the first and so far only multi-messenger observation of the binary neutron star merger GW170817 resulted in numerous bounds on the parameters of isolated non-rotating neutron stars, e.g., their maximum mass or their distribution in radii, which can be directly used to constrain the equation of state of cold nuclear matter. While many of these results stem from the observation of the inspiral gravitational-wave signal, the postmerger phase of binary neutron star mergers encodes even more details about the extreme physics of hot and dense neutron star matter. In this Thesis we focus on the exploration of dissipative and shearing effects in binary neutron star mergers in order to identify novel approaches to constrain hot and dense neutron star matter.

The first effect is the well-motivated dissipation of energy due to the bulk viscosity which arises from violations of weak chemical equilibrium. We start by exploring the impact of bulk viscosity on black-hole accretion. This simplified problem gives us the opportunity to develop a test case for future codes taking into account the effects of dissipation in a fully general-relativistic setup and build intuition in the physics of relativistic dissipation. Next, we move on to isolated neutron stars and binary neutron star mergers by developing a robust implementation of bulk-viscous dissipation for numerical relativity simulations. We test our implementation by calculating the damping of eigenmodes of isolated neutron stars and the violent migration scenario. Finally, we present the first results on the impact of bulk viscosity on binary neutron star mergers. We identify a number of ways how bulk viscosity impacts the postmerger phase, out of which the suppression of gravitational-wave emission and dynamical mass ejection are the most notable ones.

In the last part of this Thesis we investigate how the shearing dynamics at the beginning of the merger affects the amplification of different initial magnetic-field topologies. We explore the hypothesis that magnetic fields which are located only in a small region near the stellar surface prior to merger lead to a weaker magnetic-field amplification. We show first evidence which confirms this hypothesis and discuss possible implications for constraining the physics of superconduction in cold neutron stars.

Acknowledgements

I would like to express my sincere gratitude to those people without whom the completion of this Thesis would not have been possible.

First, I would like to thank Luciano Rezzolla, my adviser, for his invaluable support, guidance and, of course, helpful criticism during the preparation of this Thesis. I am deeply indebted to him for the numerous lessons that I have learned during my time as a PhD student in his group. Most notably, I want to thank him for the seemingly infinite amount of ideas and suggestions I encountered almost on a weekly basis during our meetings. That helped me not only to appreciate the multitude of exciting questions which can be asked about every subject but also to challenge myself by going beyond my current understanding and constantly improving.

Next, I would like to thank Dirk Rischke, my second adviser, for refereeing this Thesis, his advices during my PhD committee meetings and his guidance on dissipative hydrodynamics.

I am grateful for having met a lot of great people during my doctoral studies in Frankfurt all of whom had valuable input into the preparation of my Thesis. In particular, I want to thank Masoud Shokri for his thoughts and our discussions about the viscous black-hole accretion problem and dissipative hydrodynamics in general. A special thanks deserves also Vasilis Mpisketzis for his valuable insights on magnetohydrodynamics during my work on crustal magnetic fields and the countless discussions we had about a wide range of topics in high-energy astrophysics.

I also want to thank all current and former members of the RelAstro group I had the pleasure to meet during my time in Frankfurt. Numerous discussions over lunch, coffee, dinner or otherwise have provided if not direct input, then definitely motivation due to the open and exciting atmosphere in our conversations. Without any particular order I would like to thank Antonios Nathanail, Christian Ecker, Raphaël Duque, Matthias Hanauske, Jin-Liang Jiang, Kotaro Moriyama, Alejandro Cruz-Osorio, Samuel Tootle, Marie Cassing, Natey Kübler, Yixuan Ma, Markus Mayer, Carlo Musolino, Harry Ho-Yin Ng, Khalil Pierre, Alina Stehr, Konrad Topolski, David Leemüller, Lukas Weih, Zhenyu Zhu, Frederike Kubandt, Jan Roeder, Ludwig Jens Papenfort, Elias Most and Héctor Olivares.

A special thanks goes to Paramvir Singh for the delicious apples and inviting me to Europe's oldest jazz club, the "Jazzkeller". Additionally, I would like to thank Prashant "Steve" Kocherlakota for countless discussions about a variety of political topics and social issues, sometimes over one or two glasses of fine whisky.

Furthermore, I thank Max Hansen for the conversations over our weekly lunches and his patient endurance of my complaints about the amount of work on this Thesis which seemed to be forbidden to decrease as a result of the fifth force of nature.

I am thankful to Nawid Albinger who supported me during the last stages of this Thesis by his invaluable opinion on the delicate issue of the right amount of garlic in a variety of dishes. This helped me to focus deeply on my Thesis by reducing external disturbances the most persistent of which are human interactions.

Of course, I am deeply grateful for my close circle of friends, the “Alles und Nichts” – family, without whom this Thesis would not have been possible: Rahul Gulati, David Hilger geb. Koch, Yaya Jaiteh, Nikolas Kockelmann, Harsh Manocha, David Morgese, Luka Nićin, Nikola Nićin and Giulio Politano. Thank you for continuous support in various forms out of which regular group trips and other joint activities helped me to maintain a private live during my PhD studies.

Most importantly, I am deeply indebted to my family for their unconditional love and support. I express my deepest gratitude to my mother, Irina, my father, Serguei, my grandmother, Galina, my grandfather, Mark, and my sister, Anastasia, who are always there for me. I want to thank you for always caring about me and providing support in every possible way.

Zusammenfassung

Die Multimessenger-Ära [188] in der Astrophysik von Neutronensternen begann im Jahr 2017 durch das bis dato einmalige Ereignis der Kollision eines binären Neutronensternsystems (BNS), was zu zahlreichen Beobachtungen und Erkenntnissen geführt hat. Zum Beispiel wurde dieses Ereignis, auch genannt GW170817, durch die fundamentale Wechselwirkung der Gravitation, d.h. durch Gravitationswellen, und durch Licht beobachtet [1, 101, 81]. Besonders interessant ist dabei, dass ein sogenannter kurzer Gammablitz, GRB 170817A, sowie eine Kilonova, AT2017gfo, beobachtet wurden.

Damit wurde starke empirische Evidenz für die langstehende Hypothese gefunden, dass Kollisionen von BNS zu der Produktion eines solchen energiereichen Gammablitzes, GRB 170817A war ca. 10^{47} erg s^{-1} hell, d.h. ca. 10^{13} Mal heller als die Sonne, führen können. Damit gehört GRB 170817A tatsächlich noch zu den "dunklen" kurzen Gammablitzen und es gibt viele Modelle, die darauf hindeuten, dass GRB 170817A nicht direkt sondern mit einem geometrischen Beobachtungswinkel beobachtet wurde. Neue Berechnungen zeigen, dass ein Beobachtungswinkel von ca. 35° [208] realistisch sein kann.

Eine Kilonova ist ein kurzzeitiges, helles, thermisches Lichtsignal, welches in den Wellenlängen der UV-Strahlung über das sichtbare Lichtspektrum bis hin zu den Wellenlängen der Infrarotstrahlung sichtbar ist [187]. Die Energie des Signals stammt aus dem radioaktiven Zerfall schwerer Elemente, welche aus dem ursprünglichen, sehr neutronenreichen Neutronensternmaterial synthetisiert werden. Die Beobachtung der Kilonova AT2017gfo konnte viele dieser Annahmen bestätigen, wobei sogar das schwere Element Strontium nachgewiesen wurde [312].

Zweifellos bieten Kollisionen von BNS ein ideales kosmisches Labor, um die extremalsten Bereiche unseres Verständnisses der fundamentalen Physik zu testen. Diese reichen von Fragen über die Synthese schwerer Elemente in unserem Universum [225] bis hin zum Verständnis der Quantenchromodynamik, die fundamentale Kraft, welche die Eigenschaften von Protonen und Neutronen bestimmt. Vorallem bieten Beobachtungen von Kollisionen von BNS einen komplementären Zugang zu Experimenten auf der Erde, welche die gleichen Fragestellungen in Angriff nehmen.

Diese Dissertation widmet sich der Fragestellung, welche neuen "Kanäle" oder physikalischen Mechanismen in Kollisionen von BNS existieren, die neue Erkenntnisse über den Zustand der Materie von Neutronensternen liefern können. Dabei liegt der Fokus insbesondere auf dissipativen Dynamiken, d.h. Prozessen, welche in der Regel kinetische Energie in Wärme umwandeln und dabei die Entropie des Systems erhöhen, und scherenden Dynamiken, d.h. Prozessen, die auf transversalen Gradienten im Geschwindigkeitsprofil basieren. Die konkreten Prozesse, welche hier untersucht werden, sind zum einen der Einfluss der Volumenviskosität auf eine Kollision von einem BNS und zum anderen der Einfluss der Scherung in der Dynamik von Kollisionen von BNS auf die Verstärkung von Magnetfeldern.

Kapitel 1 dieser Dissertation führt einige grundlegende Informationen zu Neutro-

nensternen sowie BNS ein und Kapitel 2 ist eine Einführung in die theoretischen, mathematischen und numerischen Grundlagen. Damit wird ein konsistenter Rahmen geschaffen, um die Methoden zu verstehen, welche die Grundlage der Resultate dieser Dissertation sind. Die Kapitel 3, 4 und 5 präsentieren die Ergebnisse, welche während der Arbeit an dieser Dissertation erarbeitet wurden. Zuletzt bietet Kapitel 6 den Schluss dieser Dissertationen, wo wir die Resultate zu einem übergreifenden Rahmen in Bezug setzen und einen möglichen Ausblick formulieren. Die folgenden drei Unterkapitel fassen die Resultate der Kapitel 3, 4 und 5 zusammen.

Viskose Akkretion von Schwarzen Löchern

In Kapitel 3 wird der Einfluss einer Volumenviskosität auf den Akkretionsfluss eines Schwarzen Loches untersucht, welches durch die Schwarzschild Metrik beschrieben wird. Der sphärisch symmetrische Akkretionsfluss auf ein Schwarzes Loch wurde bereits in den Arbeiten von Bondi [51] und Michel [190] für ein "perfektes" Fluid untersucht, die oft auch als Testszenarien für numerische Codes verwendet werden, welche die Gleichungen der allgemein relativistischen Hydrodynamik und Magnetohydrodynamik lösen. Der Einbau einer relativistischen Viskosität hat später auch stattgefunden [307]. Der grundlegende Unterschied zu der Untersuchung in dieser Dissertation ist dadurch gekennzeichnet, dass hier eine Viskositätsbeschreibung verwendet wird, welche konsistent mit dem physikalischen Prinzip der Kausalität formuliert ist. Bei den Berechnungen von [307] ist dieses Prinzip verletzt, führt jedoch zu keinen Instabilitäten, was ein bekannter Nebeneffekt von akausalen Beschreibungen einer relativistischen Viskosität ist [149, 126]. Die Beschreibung der Volumenviskosität (hier wird die Scherungsviskosität sowie die Wärmeleitung vernachlässigt) erfolgt durch die sogannte Müller-Israel-Stewart (MIS) [204, 157, 158] Theorie, welche Korrekturen der zweiten Ordnung in Nichtgleichgewichtsbeiträgen berücksichtigt. Die entscheidende Gleichung hat folgende Form:

$$\tau_{\Pi}\dot{\Pi} = -\zeta\Theta - \Pi, \tag{1}$$

wobei τ_{Π} die Relaxationszeit, $\dot{\Pi}$ die mitbewegte Zeitableitung der isotropen, viskosen Druckkorrektur Π, ζ die Volumenviskosität und Θ die Expansionsrate ist.

Da eines der übergreifenden Ziele dieser Dissertation die Untersuchung der Volumenviskosität in Kollisionen von BNS ist, bietet dieses Akkretionsproblem die Möglichkeit, eine erste Intuition für die Gleichungen der relativistischen Volumenviskosität im allgemein relativistischen Kontext aufzubauen, sowie ein Testszenario zu entwickeln, welches für Codetests zukünftiger numerischer Lösungsverfahren ebendieser Gleichungen verwendet werden kann.

Wir benutzen die Zustandsgleichung eines idealen Gases aus Wasserstoffionen, welche im thermodynamischen Gleichgewicht mit Photonen sind. Für die Volumenviskosität verwenden wir eine Formel basierend auf einem Zwei-Fluid Modell [315, 273]. Jedoch verwenden wir für die Relaxationszeit eine Formel die kubisch mit dem Radius ist, d.h. der Entfernung zum Schwarzen Loch, um das Wachstum von Nichtgleichgewichtsbeiträgen zu unterdrücken. Zudem können die entsprechenden Gleichungen in gewöhnliche Differentialgleichungen mit einer hebbaren Singularität überführt werden, deren Lösung mit einer analytischen Rechnung bei der hebbaren Singularität und einer darauf folgenden numerischen Integration erzielt werden kann.

Die Lösung des Problems zeigt, dass für Transportkoeffizienten, welche im Einklang mit der Kausalität der Gleichungen stehen, nur geringe Abweichungen von der nicht viskosen Lösung möglich sind. Zum Beispiel kann die Temperatur in der direkten Umgebung des Ereignishorizontes um bis zu $\sim 19\%$ von der Lösung des per-

fekten Fluids abweichen. Wie erwartet, nimmt die Temperatur für die viskosen Lösungen in der Nähe des Schwarzen Loches zu, was durch den dissipativen Transfer von Bewegungs- zu Wärmeenergie zu erklären ist. Weiterhin nimmt die Schallgeschwindigkeit um ca. 18% in der Nähe des Schwarzen Loches zu, wodurch Werte von ca. 1/2 Mal der Lichtgeschwindigkeit erreicht werden. Interessant ist auch das Verhalten des Nichtgleichgewichtsdrucks Π. Dieser skaliert monoton mit der Magnitude der Volumenviskosität ζ, was zu erwarten ist. In der Nähe des Schwarzen Loches, wo der Betrag der Fluidexpansion Θ ansteigt, haben somit Fluide mit einer höheren Volumenviskosität auch eine höhere Korrektur zum Gleichgewichtsdruck p. Die Relaxationszeit τ hingegen bestimmt, auf welcher Zeitskala der Nichtgleichgewichtsdruck sich dem Wert $-\zeta\Theta$ annähert. Kleine Werte für τ führen dazu, dass $\Pi \approx -\zeta\Theta$, wobei für zu große Werte von τ, Π signifikant von $-\zeta\Theta$ abweichen kann. Wir zeigen ebenfalls, dass die hier erarbeitete Lösung für den Test von Codes geeignet ist, die die Gleichung (1) ohne Annahmen über die Stationarität numerisch lösen.

Volumenviskosität und Kollisionen von binären Neutronensternsystemen

Nachdem wir Gleichung (1) in einem vereinfachten Szenario untersucht haben, ist es in Kapitel 4 an der Zeit, diese Gleichung in einen Code zu implementieren, welcher selbstkonsistent Einsteins Feldgleichungen sowie die Gleichungen der relativistischen Hydrodynamik löst. Dies ist der einzige Weg, die Kollision von BNS zu simulieren, da die Emission von Gravitationswellen bis zu ~ 0.65 Sonnenmassen betragen kann und somit bei einem System von ca. 3 Sonnenmassen nicht zu vernachlässigen ist.

Wir implementieren diese Gleichung in den Code `FIL` [195], welcher numerische Methoden höherer Ordnung sowie robuste Inversionsmethoden für die Primitivvariablen verwendet. `FIL` ist Teil der `Einstein Toolkit` Infrastruktur [178], welche durch den `Carpet` Code [277] adaptive Gitter implementiert.

Besonders erwähnenswert sind die Änderungen, welche durch die Implementierung von Gleichung (1) notwendig sind. Zunächst muss die Inversion für die Primitivvariablen geändert werden, weil die Inklusion des Nichtgleichgewichtsdrucks berücksichtigt werden muss. Wir verwenden eine kleine Änderung der Algorithmen in [124]. Wir können mathematisch zeigen, dass die Existenz und Eindeutigkeit einer Lösung im Prozess der Inversion auch mit der Berücksichtigung der Viskosität Gültigkeit besitzt. Somit besitzt der neue Algorithmus eine ähnliche Robustheit wie der alte. Weiterhin werden zwei Bedingungen implementiert, die sicher stellen, dass sich die Lösung der Inversion in einem physikalischen Bereich befindet. Zunächst gibt es jeweils eine Grenze für den maximalen und minimalen Wert den der Nichtgleichgewichtsdruck annehmen darf. Beide Grenzen stammen von der grundlegenden Annahme, dass der Nichtgleichgewichtsdruck nur eine perturbative Korrektur zum Gleichgewichtsdruck darstellt und deshalb in den ungefähren Bereich $-1 \lesssim \Pi/(e+p) \lesssim 1$ fallen muss, siehe auch [71, 63]. Hierbei ist e die lokale Energiedichte. Die zweite Bedingung erhöht die Relaxationszeit dynamisch während der Simulation, sodass das Prinzip der Kausalität nicht verletzt wird, d.h. Schallwellen dürfen nicht schneller als Licht propagieren.

Ein letzte Modifikation bezieht sich auf den Abfall der Volumenviskosität ζ im Niedrigdichtebereich. In der Regel wird in diesen Bereichen eine geringe Viskosität erwartet, sodass wir eine kubische Abhängigkeit von der Massendichte ρ implementieren, welche zu einem rapiden Abfall in ζ und einem fehlerfreien Übergang zwischen viskoser und nicht viskoser Materie führt.

Um die Implementierung zu testen, simulieren wir zunächst zwei bekannte Testszenarien: Die Dämpfung von perturbativen Oszillationen eines isolierten Neutronensterns [70] sowie die Migration eines instabilen Neutronensterns zu einer stabilen Konfiguration [117]. Der erste Test überprüft die Gleichungen im linearen Bereich und der

zweite Test im nicht linearen.

Die Oszillationen des Neutronensterns werden durch eine Perturbation in der Form der radialen Eigenmoden des Sterns ausgelöst. Untersucht werden Simulationen mit verschiedenen Viskositäten und unter Verwendung verschiedener Auflösungen. Durch das in [70] präsentierte Verfahren kann daraufhin die numerische sowie physikalische Viskosität bestimmt werden. Zunächst lässt sich beobachten, dass mit höherer Auflösung die gemessene Viskosität zu einem Wert nahe der gebrauchten, physikalischen Viskosität konvergiert. Im Rahmen der Unsicherheiten des Messverfahrens folgern wir, dass die Implementierung erfolgreich funktioniert.

Weiterhin lässt sich mit diesem Messverfahren die numerische Viskosität unseres Codes bestimmen. Wir beobachten Werte im Bereich $\lesssim 10^{26}$ g cm^{-1} s^{-1}, was eine sehr optimistische Aussicht für die Simulation physikalischer Viskositäten darstellt, weil diese auf $\gtrsim 10^{27}$ g cm^{-1} s^{-1} geschätzt werden [276, 17].

Bei der Simulation des "Migrationstests" beobachten wir, dass, wie erwartet, die nicht linearen Dichteoszillationen mit höherer Viskosität auch stärker gedämpft werden. Zudem beobachten wir einen leichten Abfall in der zentralen Dichte, was sich durch die zusätzliche dissipative Wärme erklären lässt, welche die viskosen Simulationen erzeugen. Diese zusätzliche Wärme erhöht den Druckgradienten im Inneren des Sterns, wodurch ein weniger kompakter Stern mit gleicher Masse entsteht. Die selbskonsistente Implementierung einer Volumenviskosität erlaubt es uns zusätzlich, die sogenannte inverse Reynolds Zahl zu berechnen

$$\mathcal{R}^{-1} := \frac{\Pi}{e+p}, \tag{2}$$

welche die relative Stärke des Nichtgleichgewichtsdrucks zur Enthalpiedichte misst. Dies ist ein Maß für die relative Stärke von Nichtgleichgewichtsbeiträgen. Wir messen maximale absolute inverse Reynolds Zahlen in einer Höhe von $\sim 1\%$. Es ist bemerkenswert, dass bereits eine geringe inverse Reynolds Zahl dieser Größenordnung zu einer starken Dämpfung der Dichteoszillationen führen kann, siehe z.B. auch [200] für eine zusätzliche Abschätzung. Zudem bestätigen wir in diesen Migrationstests, dass starke Viskositäten die Entwicklung von starken Schockwellen erfolgreich dämpfen. Der größte für die Volumenviskosität verwendete Wert beträgt hierbei 10^{30} g cm^{-1} s^{-1}.

Motiviert durch die Möglichkeit, den Einfluss der Volumenviskosität auf die Emission von Gravitationswellen zu studieren, untersuchen wir im zweiten Teil dieses Projekts Simulationen von Kollisionen von BNS. Dafür führen wir allgemein relativistische hydrodynamische Simulationen unter Einbezug von Gleichung (1) durch. Um den maximalen Einfluss abzuschätzen, den eine realistische Volumenviskosität haben kann, gehen wir davon aus, dass die Viskosität die Werte $\zeta \in [\zeta_0, \zeta_0/2, \zeta_0/5, 0]$ mit $\zeta_0 = 10^{30}$ g cm^{-1} s^{-1} annimmt. Ebenfalls führen wir mehrere Simulationen mit unterschiedlichen Auflösungen durch, um die Auswirkungen der Diskretisierungsfehler abzuschätzen. Wir beobachten qualitativ konsistentes Verhalten, sodass wir nur über die Ergebnisse der hochauflösenden Simulationen berichten.

Wir beginnen mit einer Zusammenfassung der Ergebnisse zur Gravitationswellenemission von Kollisionen von viskosen BNS. Wir stellen fest, dass hohe Volumenviskositäten zu einer Dämpfung und einer Frequenzzunahme in der Emission von Gravitationswellen führen. Beide Effekte hängen mit der Reduktion von quadrupolaren Dichteverformungen zusammen, siehe auch [245], welche durch eine starke Volumenviskosität beeinflusst werden. Große Volumenviskositäten dämpfen effizient die starken Kollisionen der beiden Neutronensternkerne während der ersten Millisekunden nach dem Beginn der Kollision [296, 260]. Dies ist die Ursache der verringerten quadrupolaren Deformationen in der Massendichte. Die Abnahme der Dichteverformungen führt zu einer schwächeren Emission von Gravitationswellen [35, 33, 34],

wodurch jedoch auch weniger Drehimpuls verloren gehen kann. Als Konsequenz führen hohe Volumenviskositäten zu schneller rotierenden hypermassiven Neutronensternen nach der Kollision. Wir beobachten einen Frequenanstieg, welcher für die größte Viskosität bis zu 280 Hz in der dominanten Mode f_2 betragen kann. Weiterhin wird die Gravitationswellenemission für die stärkste Viskosität auf einer Zeitskala von ca. 15 ms effizient gedämpft.

Darüber hinaus stimmt der dynamische Massenauswurf [250, 195, 77, 170] aus Kollisionen von viskosen BNS mit den Ergebnissen zur Gravitationswellenemission überein. Wir stellen fest, dass die dynamisch ausgeworfene Masse in unseren Simulationen im Extremalfall um den Faktor fünf im Vergleich zum nicht viskosen Fall unterdrückt werden kann. Auch dies ist das Ergebnis einer effizienten Dämpfung der anfänglichen Dichteoszillationen und vergleichbar mit den Beobachtungen im Migrationstest. Die geringere kinetische Energie im viskosen Fall macht es schwieriger, Masse zu lösen. Interessanterweise beobachten wir auch, dass die Verteilung der ausgeworfenen Materie entlang der Azimutrichtung zunehmend weniger gleichmäßig ist, wenn die Viskosität erhöht wird. Wir führen dieses Verhalten darauf zurück, dass bei hohen Viskositäten der größte Teil des ungebundenen Materials aus dem ersten Kollisions- und Expansionszyklus der beiden Sterne stammt. Somit wird Materie in eine bevorzugte Richtung ausgeschleudert.

Unsere Ergebnisse deuten darauf hin, dass Viskositäten in der Größenordnung von $\zeta \geq 5 \times 10^{29}$ g cm^{-1} s^{-1} signifikant sein können. Im Vergleich zu den beobachteten Werten in [200] entsteht ein vielversprechendes Bild für die Untersuchung der Volumenviskosität von stark wechselwirkender Kernmaterie durch Kollisionen von BNS. Allerdings werden in [202] effektive Viskositäten in der Größenordnung von $\zeta \lesssim 10^{28}$ g cm^{-1} s^{-1} beobachtet. Bei Werten dieser Größenordnung kann die Volumenviskosität höchstwahrscheinlich die Gravitationswellenemission nicht beeinflussen. Zusätzlich bleibt beim Ziehen von Schlussfolgerungen aus unseren Simulationen ein Vorbehalt bestehen: Aufgrund des Resonanzverhaltens der Volumenviskosität und ihrer starken Temperaturabhängigkeit [17, 10, 16], wird eine realistische Volumenviskositätsverteilung in der Materie des hypermassiven Neutronensterns sehr inhomogen aussehen. In den hier präsentierten Simulationen wurde jedoch die Annahme getroffen, dass die Viskosität im Sterninneren konstant ist. Daher sind die Schlussfolgerungen aus unseren Simulationen optimistische Sichtweisen zu der Fragestellung, ob die Auswirkungen einer realistischen Volumenviskosität tatsächlich beobachtbar sind.

Oberflächen-Magnetfelder in Kollisionen von binären Neutronensternsystemen

Motiviert durch die Modellannahme von Magnetfeldern, welche sich nur an der Oberfläche von Neutronensternen befinden, sogenannten "Oberflächen-Magnetfeldern", wird in Kapitel 5 der Einfluss dieser Magnetfeldtopologie in Kollisionen von BNS untersucht. Solche Magnetfeldkonfigurationen finden Anwendung in der Langzeitentwicklung isolierter Neutronensterne [237, 238, 311], wobei angenommen wird, dass supraleitende Protonen einen Typ-I Supraleiter im Kern des Neutronensterns bilden. Dadurch entwickeln sich die Magnetfelder im Kern auf kurzen Zeitskalen im Vergleich zu der charakteristischen Entwicklungszeit des Neutronensterns und können effizient aus dem Kern verdrängt werden. Die Abschätzungen dieser Zeitskalen unterliegen jedoch großen Schwankungen [233, 232, 138], wodurch sich die Fragestellung ergibt, ob Simulationen von Kollisionen von BNS zur Lösung dieses Problems beitragen können. Insbesondere wird untersucht, ob Magnetfelder, welche sich vor der Kollision ausschließlich nahe der Oberfläche der beiden Sterne befinden, einen Einfluss auf die gesamte Magnetfeldverstärkung bei der Kollision des BNS haben können. Hierfür verwenden wir

globale, hochauflösende Simulationen der allgemein relativistischen Magnetohydrodynamik von BNS mit Methoden höherer Ordnung unter Verwendung des zuvor erwähnten FIL Codes [277, 178, 195].

Unsere Studie umfasst Simulationen von vier Konfigurationen, bei denen wir zwischen zwei verschiedenen Topologien variieren, nämlich der sogenannte "Oberflächenkonfiguration" und der sogenannte "Vollkonfiguration". In der Oberflächenkonfiguration sind nur Oberflächen-Magnetfelder in den Neutronensternen vor der Kollision präsent. Im Gegensatz dazu sind in der Vollkonfiguration auch Magnetfelder im Kern der beiden Sterne vorhanden. Darüber hinaus haben beide Konfigurationen die gleiche anfängliche magnetische Gesamtenergie. Diese beiden Konfigurationen werden mit zwei verschiedenen Auflösungen simuliert, um den Einfluss von Diskretisierungsfehlern abzuschätzen. Wir finden jedoch qualitativ konsistentes Verhalten, sodass wir die Diskussion auf die Simulationen mit höherer Auflösung beschränken.

Zunächst beobachten wir vier verschiedene Stadien in der Entwicklung der Magnetfelder für beide Konfigurationen. Diese sind in aufeinanderfolgender Reihenfolge: die "Kelvin-Helmholtz Instabilitätsetappe" (KHI-Etappe) [168, 221], die "Abstiegsetappe", die "Etappe der turbulenten Verstärkung" und zuletzt die "Windungsetappe" [75, 283, 78]. Die Benennung dieser Stadien erfolgt in Übereinstimmung mit der Physik, welche am relevantesten für die Entwicklung der magnetischen Energie im jeweiligen Zeitabschnitt ist.

Weiterhin beobachten wir, dass obwohl in der Oberflächenkonfiguration die KHI-Etappe effizienter die Verstärkung von Magnetfeldern bewirkt, die endgültige magnetische Energie der Vollkonfiguration um mehr als eine Größenordnung im Vergleich zur Oberflächenkonfiguration größer ist. Wir führen dieses Verhalten auf die verfrühte Beendigung der KHI-Etappe in der Oberflächenkonfiguration zurück, was das Ergebnis zweier Effekte ist.

Erstens, der Mangel an magnetisiertem Material im Inneren der Neutronensterne führt dazu, dass turbulente Strömungen, welche sich von "Außen" nach "Innen" bewegen, keine Möglichkeit haben, die Magnetfeldverstärkung aufrechtzuerhalten, weil sie nicht auf magnetisiertes Material treffen. Und zweitens, zusätzliche Verluste von magnetisiertem Material an der Sternoberfläche führen zu einer ähnlichen Dynamik, bei der wertvolles magnetisiertes Material aus dem Bereich entfernt wird, in dem turbulente Strömungen zu einer Magnetfeldverstärkung führen können. Der erste Effekt kann in der Vollkonfiguration nicht stattfinden, weil der Kern magnetisiert ist. Der zweite Effekt ist in der Vollkonfiguration weniger ausgeprägt, weil der relative Anteil der magnetischen Energie, welcher sich in der Nähe der Oberfläche befindet, d.h. in dem Bereich, welcher aufgrund von dynamischem Massenausstoß am stärksten von Verlusten betroffen ist [250, 195, 77, 170], geringer ist.

Zuletzt beobachten wir, dass durch die geringeren Magnetfeldstärken in der Oberflächenkonfiguration das entsprechende Gravitationswellensignal ca. doppelt so stark wie in der Vollkonfiguration ist. Diese Beobachtung ist das Resultat einer größeren Ausprägung der Achsensymmetrie in der Vollkonfiguration, welche durch starke Magnetfelder begünstigt wird.

Auch wenn die Auflösungen, die wir in dieser Arbeit verwenden, sehr hoch und rechenaufwändig sind, sind sie immer noch nicht hoch genug, um konvergentes Verhalten während der KHI-Etappe zu erreichen [166]. Um diesem Mangel Rechnung zu tragen, benutzen wir zwei verschiedene Auflösungen und schätzen die Auswirkung der Diskretisierungsfehler ab. Wir beobachten, dass das in dieser Arbeit dargestellte Verhalten nur quantitativ durch die Veränderung der Auflösung beeinflusst wird. Wir kommen daher zu dem Schluss, dass unsere Ergebnisse im Rahmen der Unsicherheiten genaue Modelle für die Magnetfeldverstärkung in Kollisionen von BNS darstellen,

welche realistische Oberflächen-Magnetfelder besitzen.

Darüber hinaus haben unsere Erkenntnisse die wichtige Implikation, dass alle astrophysikalischen Prozesse, welche auf starke und geordnete Magnetfelder nach der Kollision von BNS angewiesen sind, verzögert ablaufen könnten. Da sich hinreichend starke Magnetfelder nicht direkt in den ersten Millisekunden nach der Kollision in der Oberflächenkonfiguration aufbauen können, sind auch starke magnetisch dominierte Massenausstöße [231, 268, 203, 75, 58, 78, 199, 82], welche die Kilonova beeinflussen könnten, deutlich unwahrscheinlicher als in der Vollkonfiguration.

Fazit

Mit der Idee, dissipative und scherende Dynamiken in Kollisionen von BNS zu untersuchen, wurde in dieser Dissertation das Ziel verfolgt, neue Effekte zu studieren, welche neue Erkenntnisse über Neutronensternmaterie liefern können. Zum einen wurde der Effekt der Volumenviskosität und zum anderen von Oberflächen-Magnetfeldern untersucht. In beiden Fällen stellen die Untersuchungen in dieser Dissertation vielversprechende aber vorläufige Ergebnisse dar, sodass weitere Studien notwendig sind, um endgültige Aussagen zu treffen. Basierend auf der Grundlage, dass sich gegenwärtige Anstregungen in der Modellierung von Kollsionen von BNS hauptsächlich mit der Zustandsgleichung und der Implementierung von Neutrinophysik befassen, bieten die Resultate dieser Dissertation komplementäre Versuche, die Mikrophysik in Kollisionen von BNS zu untersuchen.

Contents

List of Figures

List of Tables

Chapter 1

Introduction

The advent of the multimessenger era [188], which is landmarked by the unprecedented detection of the binary neutron star (BNS) merger GW170817 through gravity and light, has provided new possibilities to understand the fundamental building blocks of nature [263]. The coincident detection of the gravitational-wave (GW) signal GW170817, the short gamma-ray burst (sGRB) GRB 170817 and the kilonova AT2017gfo [1, 101, 81] is strong evidence for the rich variety of observables BNS mergers provide such that they can be easily considered to be Einstein's richest laboratories [23].

This conclusion is supported by the fact that the physics of neutron stars ranges from nuclear and subnuclear physics as well as quantum chromodynamics (QCD) to general relativity (GR) and high-energy astrophysics. While for some of these areas neutron stars provide complementary data to terrestrial laboratories, e.g., hot and dense QCD, other areas such as the strong-field regime of GR or the origin of heavy elements in the universe must be explored through neutron stars or black holes (BHs) [263].

Considering the evidently wide field of research encompassing neutron star physics in a crude attempt of simplification we can consider it to be a spectrum between fundamental theoretical calculations based on first principles and observational science providing new data on how nature is "actually" behaving. In this sense, this Thesis is a contribution to the middle part of this spectrum where both fundamental theoretical calculations and BNS merger observations meet. By performing numerical simulations of BNS mergers self-consistently and based on first principles we are able to predict BNS merger observables and build a direct link to the assumptions we make in the first place.

Hence, in this Thesis our main goal is to investigate novel processes in the dynamics of BNS mergers which have the potential to offer a window to some of the fundamental areas of physics mentioned above. Specifically, we focus on the dissipative and shearing dynamics of BNS mergers because exactly these dynamical mechanisms have the greatest potential to influence some of the most important observables of BNS mergers, namely the GW emission and the electromagnetic (EM) counterpart.

1.1 Neutron stars

We start by providing a very brief introduction to neutron stars which are covered more extensively in many textbooks, e.g., see [132, 279, 263, 274]. Neutron stars are the collapsed iron or oxygen-neon-magnesium cores of massive stars whose mass exceeds $\sim 8\,M_\odot$. It is believed that if the mass of the progenitor star exceeds $\sim 15-20\,M_\odot$ a BH will be formed [279]. Before collapse the core is stabilized by the electron degeneracy

pressure which balances the inward directed gravitational pull.

However, as soon as the core surpasses its "effective" Chandrasekhar mass limit [317, 67], the self-gravity of the core cannot be balanced anymore and the core starts to collapse on a timescale of several 100 ms [263]. The collapse stops only when nuclear densities on the order of $\sim 2 \times 10^{14}$ g cm^{-3} are reached at which point repulsive nuclear forces are the dominant contribution to the pressure and prevent further collapse. This event marks the formation of nuclear matter and the so-called proto-neutron star (PNS).

The rapid "stiffening" of the equation of state (EOS) at nuclear densities, i.e., matter becomes less compressible, causes infalling matter to form a shock wave which propagates outwards. However, the shock is not able to propagate through the iron core as it looses energy because infalling nuclei photo-dissociate into free nucleons. Eventually, the shocks stalls at ~ 100 km [279, 263]. Simultaneously, the PNS is growing in mass and size reaching radii of ~ 30 km.

Interestingly, during the collapse a large amount of binding energy

$$E_{\text{bind}} \sim \frac{G M_{\text{PNS}}^2}{R_{\text{PNS}}} \sim 10^{53} \left(\frac{M_{\text{PNS}}}{1\ M_\odot}\right)^2 \left(\frac{30\ \text{km}}{R_{\text{PNS}}}\right) \text{erg}, \tag{1.1}$$

is released through the conversion of the kinetic energy of infalling material to heat. This thermal energy is stored below the surface of the PNS which cannot cool down rapidly because maximum temperatures of ~ 10 MeV prevent neutrinos from transporting heat efficiently. At this time the PNS is in thermal and β-equilibrium with neutrinos [279, 263]. Nevertheless, thermal neutrinos and antineutrinos can "diffuse" on timescales of ~ 10 s and cool down the PNS. If the right conditions are met, the outward diffusing neutrinos can deposit a small amount of their energy, $\sim 10^{51}$ erg, behind the stalled shock and lead to a successful supernova explosion [263]. This mechanism is referred to as the delayed neutrino-heating mechanism [44]. Failed explosions lead to substantial amounts of matter which the PNS will accrete until it collapses to a BH eventually.

After a successful explosion the hot PNS cools down on a timescale of $\sim 10^6$ years [263] through neutrinos. Eventually, the PNS becomes a regular "cold" and β-equilibrated neutron star which is smaller in size and has constituents whose thermal energy is much smaller than their respective Fermi energy [279]. As the name suggests, a neutron star consists primarily of neutrons. The reason for this composition is the high Fermi energy of electrons (~ 100 MeV) which easily surpasses the mass difference between neutrons and protons (~ 1.3 MeV) leading to the production of neutrons via inverse β-decay [279].

Currently known neutron stars lie broadly in the mass range between ~ 0.77 [100] and $2.35\ M_\odot$ [266] with a median of $\sim 1.4\ M_\odot$ [217]. Due to the difficulty in measuring neutron star radii accurately through observations and the uncertainties in the nuclear EOS at high densities, neutron star radii are difficult to determine. Recent observations from the Neutron Star Interior Composite Explorer (NICER) place the radius of the neutron star PSR J0030+0451 with a mass of $\sim 1.44\ M_\odot$ between ~ 11.96 km and ~ 14.26 km in the 68% credible region [191] while the $\sim 2.08\ M_\odot$ heavy neutron star, PSR J040+6620, is estimated to have a radius between ~ 12.2 km and ~ 16.3 km in the 68% credible region [192]. Overall, recent studies which constrain the neutron star radius lead to a broad distribution of possible radii between ~ 11 km and ~ 14 km [19, 32, 184, 247, 259, 269, 196, 287, 20, 96, 161].

1.2 Binary neutron stars

Neutron stars can appear in a variety of different systems, e.g., in isolation or in a binary system with a white-dwarf companion [298]. However, the systems most important for this Thesis are binary systems composed of two neutron stars. Such systems have been observed due to the pulsar emission from either one or both companions [153] as well as most recently through GWs [1, 2]. It is quite interesting that the mass distribution of their individual components is very tightly peaked between $\sim 1.1\ M_\odot$ and $\sim 1.5\ M_\odot$ with a median of $1.33\ M_\odot$ [217]. Nevertheless, their formation mechanisms are not fully understood yet, where it is believed that two massive main-sequence stars need to go through the sequence of a first supernova explosion, a "common envelope" evolution and a second supernova explosion in order to create a BNS system, see e.g., [23] for further references.

After formation, the evolution of their orbit is governed by the emission of GWs which remove angular momentum from the system, thereby leading to a coalescence eventually. Using Keplerian equations of motion (EOM) together with the gravitational-radiation reaction based on the quadrupole formula, estimates for the lifetime of observed BNSs can be worked out. Their lifetimes are in the range between $\sim 10^8$ and $\sim 3\times10^9$ yrs which is smaller than the age of the universe $\approx 13.8\times10^9$ yrs [279]. Therefore, BNSs are expected to merge within a Hubble time. The frequency of the emitted GWs can be approximated using Newtonian gravity as [279]

$$f = \frac{1}{\pi}\sqrt{\frac{M}{a^3}} = 10.5\left(\frac{M}{2.8\ M_\odot}\right)^{1/2}\left(\frac{a}{700\ \text{km}}\right)^{-3/2}\ \text{Hz}, \tag{1.2}$$

where M and a are the total mass and the orbital separation of the binary. For a typical binary of mass $2.8\ M_\odot$ the frequency close to merger at a separation of 50 km is $\approx$ 550 Hz.

Overviews over the different stages and timescales of BNS mergers can be found in various reviews, see e.g., [23, 285, 252, 95, 272]. Here, we will focus on the overall evolution outlined in [252] incorporating information from [23] about the total mass of the binary. In general, the total mass of the system dictates at which time in the postmerger, if at all, the merger remnant collapses to a BH. If the total mass of the binary exceeds a certain threshold mass limit [29, 171, 303, 163], the remnant will collapse promptly to a BH already in the very first few milliseconds after merger.

Otherwise, a stable or metastable remnant will be formed. In all cases, the remnant will enter a very violent postmerger phase where the two former neutron stars evolve through a series of collision-and-bounce cycles, see e.g., [296], leading to strong GW emission in a frequency band between 2 and 5 kHz on a timescale of ~ 20 ms. During this phase GWs carry away binding energy and angular momentum leading to an approximately axisymmetric *differentially* rotating remnant. If the mass is below the maximally supported mass of a *uniformly* rotating neutron star, which is $\approx 1.2\ M_{\text{TOV}}$ [56], where M_{TOV} is the maximally supported mass of spherically symmetric non-rotating neutron star [302, 216], the remnant is called a *supramassive* neutron star (SMNS). Otherwise, if the remnant exceeds $\approx 1.2\ M_{\text{TOV}}$, the object is called a *hypermassive* neutron star (HMNS) which must be supported through differential rotation in order avoid collapse to a BH. It is possible that a HMNS is formed after merger which collapses during the first 20 ms post merger implying that the total mass was higher than the maximally supported mass of an approximately axisymmetric differentially rotating HMNS but lower than the threshold mass to prompt collapse, see e.g., [313] for an estimate of the maximum mass of differentially rotating stars.

If the remnant SMNS or HMNS survives the first ~ 20 ms it enters the "viscous"

phase which proceeds on a timescale of $\sim 0.1 - 1$ s. Its evolution is determined by the subtle interplay between magnetic braking, viscous momentum transport and neutrino cooling [120, 115, 123, 170, 121]. In particular, it is believed that the majority of the ejected mass from BNS mergers, which do not collapse promtly, is generated on this timescale [285] such that this "secular ejecta" has a large impact on the kilonova signal [187]. HMNSs are typically *short-lived*, i.e., they collapse on a timescale of $\lesssim 1$ s to a BH, as it is expected that their differential rotation will be removed on this timescale due to an effective turbulent viscosity [104, 244, 286, 280] or magnetic braking [278, 79, 106]. On the other hand, SMNSs are typically *long-lived*, i.e., they do not collapse on a timescale of $\lesssim 1$ s to a BH, because their mass is low enough such that the removal of differential rotation does not immediately lead to an unstable configuration.

Then, after a timescale of ~ 1 s the remnant is either a BH or a SMNS surrounded by a massive torus. In the case of the BH, the torus will be partially accreted and partially ejected as a result of magneto-turbulence [115]. In the case of the SMNS, the spin-down proceeds on a large timescale due to magnetic-dipole radiation [38]. Eventually, also the SMNS will collapse to a BH. Only if the total mass of the binary is lower than $M_{\rm TOV}$, a stable neutron star remnant can be produced.

1.3 Author contributions and overview of the Thesis

This Thesis is divided into five main parts which discuss different aspects of "dissipative and shearing dynamics" in astrophysical compact objects. Many, but not all, results presented in this Thesis are published in the following peer-reviewed articles, which we present together with the author's contributions:

Paper $\mathcal{A}$,

Michail Chabanov, Luciano Rezzolla, and Dirk H. Rischke. "General-relativistic hydrodynamics of non-perfect fluids: 3+1 conservative formulation and application to viscous black hole accretion". In: *Monthly Notices of the Royal Astronomical Society* 505.4 (Aug. 2021), pp. 5910–5940. DOI: 10.1093/mnras/stab1384. arXiv: 2102.10419 [gr-qc],

LR formulated the overall idea of this work while **MC** initiated the investigation of the impact of bulk viscosity on the accretion onto BHs; **MC** carried out all analytical derivations and calculations, implemented the code in BHAC, performed the simulations and the post-process analysis; **MC**, LR and DHR wrote the manuscript together; LR provided useful guidance through all stages of this project;

and Paper $\mathcal{B}$,

Michail Chabanov, Samuel D. Tootle, Elias R. Most, and Luciano Rezzolla. "Crustal Magnetic Fields Do Not Lead to Large Magnetic-field Amplifications in Binary Neutron Star Mergers". In: *Astrophys. J. Lett.* 945.1, L14 (Mar. 2023), p. L14. DOI: 10.3847/2041-8213/acbbc5. arXiv: 2211.13661 [astro-ph.HE],

MC formulated and proposed the idea of this work, implemented the code to initialize crustal magnetic fields and calculate the analysis quantities, performed the simulations and the post-process analysis; **MC** and LR wrote the manuscript together; the simulations make use of the FUKA codes developed and maintained by SDT, as well as the FIL, Antelope and Margherita codes developed and maintained by ERM; LR pro-

vided useful guidance through all stages of this project.

The following is a list of the forthcoming five chapters together with short summaries giving a brief overview of each chapter. Additionally, we provide information about the connections between the articles listed above, i.e., Paper $\mathcal{A}$ and Paper $\mathcal{B}$, and the results presented in this Thesis. A full publication list of the author can be found in the CV which is appended at the end of this Thesis.

Chapter 2

This chapter serves as an introductory chapter to the theoretical and numerical foundations of this Thesis. Specifically, we introduce the equations, which will be solved later in this Thesis, discuss their foundations as well as numerical techniques, that can be employed for the solution. Large portions of this chapter are based on textbooks about the corresponding subjects and Paper $\mathcal{A}$.

Chapter 3

This chapter discusses the impact of bulk viscosity on the accretion onto BHs. As part of the effort to build more realistic models of BNS mergers mentioned later in this Thesis, the results in this chapter mark the first steps towards the inclusion of bulk viscosity in a fully general-relativistic setup. This chapter is based on Paper $\mathcal{A}$.

Chapter 4

In this chapter we continue our effort to study the effects of bulk viscosity in models of BNS mergers. We show how to implement bulk viscosity in fully general-relativistic simulations of neutron stars, how to test our code by measuring the numerical dissipation of neutron star oscillations and get first insights about the effects of bulk viscosity by simulating the violent migration of neutron stars. Then, we move on to full BNS mergers and study the impact of a large but realistic bulk viscosity on their dynamics. The results presented in this chapter are unpublished at the time of submission of this Thesis.

Chapter 5

As will be explained later, BNS mergers are well-known sites of strong magnetic-field amplification which is in agreement with a plethora EM signals associated with them. In this chapter, we challenge the hypothesis that BNS mergers produce strong magnetic-field amplifications by investigating the impact of purely crustal magnetic fields. We also comment on the potential impact of our results on astrophysical observables. This chapter is based on Paper $\mathcal{B}$.

Chapter 6

This is the last chapter and concludes this Thesis by briefly summarizing the main results and contrasting these with current efforts to investigate BNS mergers.

An appendix as well as the bibliography can be found at the end of this Thesis.

1.4 Copyright information

This work includes the reuse of figures and data from Paper $\mathcal{A}$ and Paper $\mathcal{B}$.

For articles published by IOP (*The Astrophysical Journal Letters*), this author has adhered to the guidance provided in IOP's published Authors Rights Policy (see bullet 5).

The publications in *Monthly Notices of the Royal Astronomical Society* under Oxford University Press (OUP) allow the original authors to reuse content in future publications and for academic purposes such as dissertations and course material as listed under OUP's Publication Rights.

1.5 Units, conventions and abbreviations

Unless stated explicitly, we employ units where the speed of light is set to one, i.e., $c = 1$, and the gravitational constant is set to one, i.e., $G = 1$. Moreover, we work in Gaussian units where the vacuum magnetic permeability μ_0 takes the value $\mu_0 = 4\pi c^{-2}$ and magnetic fields have the same dimension as electric fields. The flat spacetime metric, i.e., the Minkowski metric, is denoted by $\eta_{\mu\nu} = \mathrm{diag}[-1, 1, 1, 1]$. Greek indices run over the set $\{0, 1, 2, 3\}$ while Roman indices run over the subset $\{1, 2, 3\}$. Also, we make use of Einstein's summation convention. The symbols $\delta_{\mu\nu} = \delta^{\mu\nu} = \delta^{\mu}{}_{\nu} = \mathrm{diag}[1, 1, 1, 1]$ and $\delta_{ij} = \delta^{ij} = \delta^{i}{}_{j} = \mathrm{diag}[1, 1, 1]$ represent the 4D and 3D Kronecker delta symbol, respectively. Furthermore, we introduce the Levi-Civita tensor

$$\epsilon_{\mu\nu\lambda\delta} := \sqrt{-g}\, \eta_{\mu\nu\lambda\delta}, \tag{1.3}$$

$$\epsilon^{\mu\nu\lambda\delta} := -\frac{1}{\sqrt{-g}}\, \eta^{\mu\nu\lambda\delta}, \tag{1.4}$$

where we define the Levi-Civita symbol through

$$\eta_{\mu\nu\lambda\delta} = \eta^{\mu\nu\lambda\delta} := \begin{cases} +1 & \text{if } [\mu\nu\lambda\delta] \text{ is an even permutation of } 0123, \\ -1 & \text{if } [\mu\nu\lambda\delta] \text{ is an odd permutation of } 0123, \\ 0 & \text{else}, \end{cases} \tag{1.5}$$

and g denotes the determinant of the four-dimensional spacetime metric $g_{\mu\nu}$. We also introduce the definitions

$$T_{(\mu\nu)} := \frac{1}{2}\left(T_{\mu\nu} + T_{\nu\mu}\right), \tag{1.6}$$

and

$$T_{[\mu\nu]} := \frac{1}{2}\left(T_{\mu\nu} - T_{\nu\mu}\right). \tag{1.7}$$

Finally, for later reference, a list of frequently employed abbreviations in this Thesis is provided in Table 1.1.

ADM	Arnowitt-Deser-Misner
BBH	Binary black hole
BDNK	Bemfica-Disconzi-Noronha-Kovtun
BHAC	Black-hole accretion code
BHNS	Black-hole neutron-star binary
BNS	Binary neutron star
BSSNOK	Baumgarte-Shapiro-Shibata-Nakamura-Ohara-Kojima
CFL	Courant-Friedrichs-Lewy
CT	Constrained transport
EM	Electromagnetic
EOM	Equations of motion
EOS	Equation of state
FIL	Frankfurt/IllinoisGRMHD
FUKA	Frankfurt University/KADATH initial data code
GR	General relativity
GRDHD	General-relativistic dissipative hydrodynamics
GRHD	General-relativistic hydrodynamics
GRMHD	General-relativistic magnetohydrodynamics
GW	Gravitational wave
HIC	Heavy-ion collision
HLLE	Harten-Lax-Van Leer-Einfeldt
HMNS	Hypermassive neutron star
HRSC	High-resolution shock-capturing
IMEX	Implicit-explicit
KHI	Kelvin-Helmholtz instability
LES	Large-eddy simulation
LHS	Left-hand side
MIS	Müller-Israel-Stewart
MRI	Magneto-rotational instability
MHD	Magnetohydrodynamics
NICER	Neutron Star Interior Composite Explorer
NR	Numerical relativity
NS	Navier-Stokes
ODE	Ordinary differential equation
PDE	Partial differential equation
PNS	Proto-neutron star
QCD	Quantum chromodynamics
QGP	Quark-gluon plasma
RHS	Right-hand side
sGRB	short gamma-ray burst
SMNS	Supramassive neutron star
TOV	Tolman-Oppenheimer-Volkoff
WRT	With respect to

Table 1.1: List of frequently employed abbreviations

Chapter 2

Theoretical and numerical foundations

2.1 Numerical relativity

Einstein's theory of relativity is imperative to describe neutron stars and high-energy astrophysical phenomena associated with them. An illustrative example of the impact of their high compactness and surface gravity not captured by a purely Newtonian description is the occurance of gravitational lensing which allows an observer to see parts of the star's surface which is oriented in the opposite direction and would be not visible otherwise. In particular, this effect is leveraged by the NASA mission NICER in order to obtain measurements of several neutron star properties, e.g., the shape and location of hot spots, the compactness and the radius [192].

Another and perhaps the most significant illustration of the importance of Einstein's gravity theory for neutron star related phenomena is the emission of GWs by BNS systems. As famously honored by the Nobel Prize in 1993 for the discovery of the Hulse-Taylor pulsar [153], BNS systems lose energy and angular momentum to GWs leading to a decaying orbit which makes a catastrophic coalescence or merger inevitable. The first direct detection of GWs from a BNS system was, however, not possible until decades later. The detection of the BNS merger GW170817 in 2017 was able to provide upper limits on the difference between the speed of gravity and the speed of light [1, 3].

A large portion of this section is dedicated to a brief introduction of the partial differential equations (PDEs) able to describe non-stationary spacetimes. These PDEs need to be solved in order to model isolated and BNS systems dynamically. The numerical solution of these equations belongs to the branch of GR called numerical relativity (NR). A more comprehensive account of the foundations of NR can be found in the books [7, 28, 135, 261, 279].

However, we start by giving a brief introduction to GWs as a particular solution of Einstein's field equations

$$G_{\mu\nu} := R_{\mu\nu} - \frac{1}{2} R g_{\mu\nu} = 8\pi T_{\mu\nu}\,, \tag{2.1}$$

where $\boldsymbol{G}$ is the Einstein tensor, $\boldsymbol{R}$ is the Ricci tensor obtained through contractions of the Riemann tensor $\boldsymbol{\mathcal{R}}$ and R denotes the Ricci scalar which is derived through contractions of $\boldsymbol{R}$

$$R_{\mu\nu} := \mathcal{R}^{\alpha}{}_{\beta\gamma\delta} g_{\alpha}{}^{\gamma}\,, \tag{2.2}$$

$$R := R_{\mu\nu} g^{\mu\nu}\,. \tag{2.3}$$

The rank-two tensor $T_{\mu\nu}$ represents the energy-momentum tensor. Equation (2.1) is a system of ten second-order, nonlinear PDEs in the metric components $g_{\mu\nu}$ only six of which are, however, independent due to the relation $\nabla_\mu G^{\mu\nu} = 0$ [261]. This reduction of degrees of freedom reflects precisely the freedom to choose four arbitrary coordinate functions in order to describe the dynamics and is commonly denoted as gauge freedom.

2.1.1 Gravitational waves

Following [279] Einstein's equations, i.e., Eq. (2.1), allow us to obtain wave solutions in the limit of weak gravitational fields through linearization. We consider the metric to be a superposition of the flat Minkowski metric $\eta_{\mu\nu}$ and a perturbation $\epsilon h_{\mu\nu}$ whose magnitude is denoted by the small parameter ϵ

$$g_{\mu\nu} = \eta_{\mu\nu} + \epsilon h_{\mu\nu} \,. \tag{2.4}$$

Then, the Einstein tensor can be written as

$$G_{\mu\nu} = \frac{\epsilon}{2}\left(-\Box\psi'_{\mu\nu} + \partial_\alpha\partial_\mu\psi'^{\alpha}{}_{\nu} + \partial_\alpha\partial_\nu\psi'^{\alpha}{}_{\mu} - \eta_{\mu\nu}\partial_\alpha\partial_\beta\psi'^{\alpha\beta}\right), \tag{2.5}$$

where we introduced the trace-free perturbation

$$\psi'_{\mu\nu} := h_{\mu\nu} - \frac{1}{2}\eta_{\mu\nu}\eta^{\alpha\beta}h_{\alpha\beta}\,, \tag{2.6}$$

and the standard flat-space wave operator $\Box := -\partial_t^2 + \Delta := -\partial_t^2 + \sum_{i=1}^3 \partial_i^2$. We can now make use of the previously mentioned gauge freedom and choose suitable coordinates which simplify Eq. (2.5) even further. Specifically, we want to eliminate all mixed derivatives which spoil the wave-like nature of Eq. (2.5). This can be done by introducing an infinitessimal coordinate variation $\epsilon\xi^\mu$ on the order of the small parameter ϵ, i.e., $x^\mu \to x^\mu - \epsilon\xi^\mu$, and demanding

$$\eta^{\alpha\beta}\partial_\alpha\psi_{\beta\mu} = 0\,, \tag{2.7}$$

where we have introduced the transformed trace-free metric perturbation

$$\psi_{\mu\nu} := \psi'_{\mu\nu} + \partial_\mu\xi_\nu + \partial_\nu\xi_\mu - \eta_{\mu\nu}\partial_\alpha\xi^\alpha\,. \tag{2.8}$$

This coordinate system is often referred to as Lorenz gauge where each component of ξ^μ reflects one of the four degrees of gauge freedom. Then, assuming that the energy-momentum tensor is of order ϵ as well, we obtain the linearized Einstein's equations in Lorenz gauge

$$\Box\psi_{\mu\nu} = -16\pi\epsilon^{-1}T_{\mu\nu}\,, \tag{2.9}$$

which have the form of inhomogeneous wave equations for the components of $\psi_{\mu\nu}$ in flat spacetime. Additionally, note that the condition in Eq. (2.7) together with the transformation in Eq. (2.8) imply that all coordinate transformations which fulfill the Lorenz gauge condition in Eq. (2.7) at a given time and follow the wave equation

$$\Box\xi_\mu = 0\,, \tag{2.10}$$

will fulfill Eq. (2.7) at all times.

This leads us to the insight that for vacuum, i.e., $T_{\mu\nu} = 0$, only two of the ten different components of $\psi_{\mu\nu}$ are independent which reflect the two dynamical degrees of

freedom of GR [261]. This can be understood if we write down the following solutions of Eqs. (2.9) and (2.10) in vacuum

$$\psi_{\mu\nu}(x^\lambda) = A_{\mu\nu} \exp\left[-i\kappa_\alpha x^\alpha\right], \tag{2.11}$$

$$\xi^\mu(x^\lambda) = C^\mu \exp\left[-i\kappa_\alpha x^\alpha\right], \tag{2.12}$$

respectively, where $A_{\mu\nu}$, C^μ and κ_α are constant and denote the amplitude of $\psi_{\mu\nu}$, the amplitude of ξ^μ as well as the wave four-vector of $\psi_{\mu\nu}$ and ξ^μ, respectively. Using Eq. (2.8) we obtain the following relation

$$A_{\mu\nu} = A'_{\mu\nu} - i\kappa_\mu C_\nu - i\kappa_\nu C_\mu + i\eta_{\mu\nu}\kappa_\alpha C^\alpha, \tag{2.13}$$

which illustrates that the choices made for the vector C_μ can reduce the degrees of freedom of $\psi_{\mu\nu}$ by four. Together with Eq. (2.7) only two independent degrees of freedom remain which are determined by the linearized Einstein's equations in Eq. (2.9). The most convenient gauge for the analysis of GWs represents the *transverse-traceless* (TT) gauge [261] which enforces the conditions $A_{\mu\nu}\kappa^\nu = 0$, $A_{0\mu} = 0$ and $A_\mu{}^\mu = 0$. As an example, if the waves propagate in the z-direction, i.e., $\kappa^\mu = (\kappa^t, 0, 0, \kappa^z)^T$, we obtain

$$\psi_{\mu\nu} = \begin{pmatrix} 0 & 0 & 0 & 0 \\ 0 & h_+ & h_\times & 0 \\ 0 & h_\times & -h_+ & 0 \\ 0 & 0 & 0 & 0 \end{pmatrix}, \tag{2.14}$$

where h_+ and $h_\times$ denote the "plus" and "cross" polarisation amplitudes of the GW, respectively.

In NR simulations the polarisation amplitudes are typically obtained through the Newman-Penrose formalism [211] which connects h_+ and $h_\times$ to components of the Weyl tensor $C_{\alpha\beta\gamma\delta}$, the trace-free part of the Riemann tensor [261]. In particular, at null infinity the curvature scalar ψ_4 is related to the amplitudes through the relation [299]

$$\ddot{h}_+ - i\ddot{h}_\times = \Psi_4, \tag{2.15}$$

where the curvature scalar is defined by

$$\Psi_4 := -C_{\alpha\beta\gamma\delta} n^\alpha \overline{m}^\beta n^\gamma \overline{m}^\delta. \tag{2.16}$$

The set of basis vectors $\{\boldsymbol{l}, \boldsymbol{n}, \boldsymbol{m}, \overline{\boldsymbol{m}}\}$, where the bar denotes the complex conjugate, defines an orthonormal null frame which is constructed from polar orthonormal basis vectors [261]. In numerical simulations with a finite domain Ψ_4 is typically extracted at a finite radius R. Common techniques to extrapolate the signal to null infinity include a fit to a polynomial in $1/R$, propagating the signal by using an analytic formula based on perturbation theory or performing a characteristic evolution [257, 236, 54, 181, 182]. Additionally, the two time integrals, which need to be solved in order to obtain the amplitudes from Eq. (2.15), are typically calculated by using the so-called *fixed frequency integration* (FFI), which removes unphysical secular drifts in the amplitudes [258].

The quantity Ψ_4 is typically decomposed into projections onto $s = -2$ spin-weighted spherical harmonics ${}_{-2}Y_{lm}$ [279]

$$\Psi_4 := \sum_{l,m} \Psi_4^{lm}{}_{-2}Y_{lm}, \tag{2.17}$$

with the inverse relation

$$\Psi_4^{lm} = \oint \mathrm{d}\Omega \Psi_4 \, {}_{-2}\overline{Y}_{lm}\,, \tag{2.18}$$

in order to gain insight about the symmetries of the GW emission and thus the symmtries of the emitting source.

Further below in this Thesis, when examining GWs from BNS mergers, we will make use of the Fourier transform of the *effective* strain [294, 296, 260] defined by

$$\tilde{h}(f) := \sqrt{\frac{\left|\tilde{h}_+(f)\right|^2 + \left|\tilde{h}_\times(f)\right|^2}{2}}\,, \tag{2.19}$$

where $\tilde{h}_+(f)$ and $\tilde{h}_\times(f)$ denote the Fourier transforms of the two polarisation amplitudes, respectively.

2.1.2 3+1 decomposition of spacetime

At the basis of the 3+1 decomposition lies the reintroduction of the notions of space and time. The concept of their unification in a single spacetime achieved by Einstein's theory of special relativity is a milestone in the history of physics but also represents an impractical point of view when for the purpose of obtaining numerical solutions of dynamical systems a Cauchy problem needs to be specified.

The decomposition is achieved by introducing a set of non-intersecting spacelike hypersurfaces whose union defines spacetime and therefore foliates it. Then, a unit timelike four-vector field $\boldsymbol{n}$ can be defined which is always normal to its corresponding hypersurface. As $\boldsymbol{n}$ is a unit vector, i.e., $n_\mu n^\mu = -1$, its integral curves can be viewed as the worldlines of "normal" or "Eulerian" observers. Now, it is possible to decompose physical quantities with respect to the normal observer and obtain projections onto spatial hypersurfaces. In particular, the generic line-element in 3+1 decomposition is given by

$$ds^2 = -(\alpha^2 - \beta_i\beta^i)dt^2 + 2\beta_i dx^i dt + \gamma_{ij} dx^i dx^j\,, \tag{2.20}$$

where α is the so-called lapse function, the purely spatial vector $\boldsymbol{\beta}$, i.e., $\beta^\mu = (0, \beta^i)^T$, is the shift vector, and γ_{ij} denotes the components of the purely spatial metric $\boldsymbol{\gamma}$, defined as

$$\gamma_{\mu\nu} := g_{\mu\nu} + n_\mu n_\nu\,, \tag{2.21}$$

where $\boldsymbol{g}$ is the usual four-metric, and acting as the projection operator onto spatial hypersurfaces. Also, the following identities can be shown: $\beta_i := \gamma_{ij}\beta^j$, $\sqrt{-g} = \alpha\sqrt{\gamma}$, where $g := \det\left(g_{\mu\nu}\right)$ and $\gamma := \det\left(\gamma_{ij}\right)$. The components of $\boldsymbol{n}$ read

$$n^\mu = \frac{1}{\alpha}(1, -\beta^i)^T\,, \qquad\qquad n_\mu = (-\alpha, 0, 0, 0)\,. \tag{2.22}$$

We can now use the timelike unit normal $\boldsymbol{n}$ in order to decompose tensors of various ranks. A rank-one tensor field $\boldsymbol{u}$, i.e., a vector field, can be expressed as

$$u^\mu = (-n_\nu u^\nu)n^\mu + \gamma^\mu{}_\nu u^\nu = W(n^\mu + v^\mu)\,, \tag{2.23}$$

where the expression behind the second equality is commonly used to the define the Lorentz factor $W := (1 - v_i v^i)^{-1/2}$ and $v^\mu := (0, v^i)^T$, a three-velocity measured by the

normal observer, if $\boldsymbol{u}$ is a four-velocity field. Analogously, a symmetric rank-two tensor field $\boldsymbol{T}$ can be written as

$$T^{\mu\nu} = En^\mu n^\nu + S^\mu n^\nu + S^\nu n^\nu + S^{\mu\nu}, \tag{2.24}$$

where

$$E := n_\mu n_\nu T^{\mu\nu}, \tag{2.25}$$
$$S^\mu := -n_\nu \gamma^\mu{}_\alpha T^{\alpha\nu}, \tag{2.26}$$
$$S^{\mu\nu} := \gamma^\mu{}_\alpha \gamma^\nu{}_\beta T^{\alpha\beta}. \tag{2.27}$$

Additionally, we introduce the extrinsic curvature $\boldsymbol{K}$ which plays an important role in the formulations of Einstein's equations in NR

$$K_{\mu\nu} := -\frac{1}{2}\mathscr{L}_{\boldsymbol{n}}\gamma_{\mu\nu} = -\gamma_\mu{}^\lambda \nabla_\lambda n_\nu, \tag{2.28}$$

where $\mathscr{L}_{\boldsymbol{n}}$ represents the Lie derivative along $\boldsymbol{n}$ and $\boldsymbol{\nabla}$ the covariant derivative with respect to the four-metric $\boldsymbol{g}$. It is also convenient to introduce the definition of the acceleration of the normal observer

$$\hat{a}^\mu := n^\nu \nabla_\nu n^\mu = \gamma^{\mu\nu}\partial_\nu \ln(\alpha). \tag{2.29}$$

Finally, we introduce the covariant derivative $\boldsymbol{D}$ with respect to the three-metric $\boldsymbol{\gamma}$ such that $\boldsymbol{D}$ is the fully spatial part of the covariant derivative $\boldsymbol{\nabla}$, i.e., $D_j v^i := \partial_j v^i + {}^{(3)}\Gamma^i{}_{jk} v^k$, where ${}^{(3)}\Gamma^i{}_{jk}$ represent the Christoffel symbols related to the three-metric $\boldsymbol{\gamma}$ [135]

$${}^{(3)}\Gamma^i{}_{jk} := \tfrac{1}{2}\gamma^{il}\left(\partial_j \gamma_{lk} + \partial_j \gamma_{lk} - \partial_l \gamma_{jk}\right). \tag{2.30}$$

2.1.3 ADM equations

A full 3+1 decomposition analogous to the decomposition of tensors in the previous section can now be carried out for the system of PDEs in Eq. (2.1). This is, of course, much more involved because of the occurance of first- and second-order differential operators. Nevertheless, the final result is widely known as the Arnowitt-Deser-Misner (ADM) formulation which represents a system of twelve first-order PDEs supplemented with four additional elliptic PDEs [318, 21, 261]. The evolution equations of the gravitational fields read:

$$\partial_t \gamma_{ij} = -2\alpha K_{ij} + D_i\beta_j + D_j\beta_i, \tag{2.31}$$
$$\begin{aligned}\partial_t K_{ij} = &- D_i D_j \alpha + \beta^k \partial_k K_{ij} + K_{ik}\partial_j \beta^k + K_{kj}\partial_i \beta^k \\ &+ \alpha\left({}^{(3)}R_{ij} + KK_{ij} - 2K_{ik}K^k{}_j\right) + 4\pi\alpha\left[\gamma_{ij}(S-E) - 2S_{ij}\right],\end{aligned} \tag{2.32}$$

where ${}^{(3)}R_{ij}$ is the Ricci tensor with respect to $\boldsymbol{\gamma}$, K is the trace of the extrinsic curvature $\boldsymbol{K}$, $S := S^\mu{}_\mu$ is the projection of the energy-momentum tensor according to Eq. (2.27) and E is the projection of the energy-momentum tensor corresponding to Eq. (2.25).

There are two remarks that are important to make at this point. The first one concerns the prescriptions for the lapse function and the shift vector, the gauge functions, as these are not provided by the ADM formulation but appear at various places in the equations. The previously mentioned freedom of choosing a particular coordinate system defined by four coordinate functions reappears at this point such that it is possible to choose prescriptions that are most suitable. The second remark is about the type of

hyperbolicity of the evolution equations. In particular, the ADM formulation is weakly hyperbolic and therefore not necessarily well-posed which means that the solution is not bound to grow at most exponentially [261]. This is linked to the growth of instabilities during the numerical solution of these equations which yields unphysical results. Hence, alternative formulations have been developed which restore the hyperbolicity of the ADM formulation by removing those parts of the equations responsible for their weak hyperbolicity. Next, we report the four elliptic PDEs.

The first elliptic equation is at the same time the definition of the Hamiltonian constraint H, i.e.,

$$H := {}^{(3)}R + K^2 - K_{ji}K^{ij} - 16\pi E = 0\,, \tag{2.33}$$

where ${}^{(3)}R$ is the Ricci scalar with respect to $\boldsymbol{\gamma}$. The magnitude of H is often used to judge to quality of a NR simulation because numerical errors prohibit the solution to have $H = 0$ and therefore be an exact solution of Einstein's equations. The other three elliptic equations define the momentum contraints M^i, i.e.,

$$M^i := D_j(K^{ij} - \gamma^{ij}K) - 8\pi S^i = 0\,, \tag{2.34}$$

where S^i is the projection of the energy-momentum tensor corresponding to Eq. (2.26).

2.1.4 Conformal traceless formulations

In this subsection we will introduce the famous Baumgarte-Shapiro-Shibata-Nakamura-Ohara-Kojima (BSSNOK) formulation and the Z4c formulation. We will start with the BSSNOK equations.

By having a closer look at the Eqs. (2.31) and (2.32) it is possible to observe that if we substitute Eq. (2.31) for the left-hand side (LHS) of Eq. (2.32) and consider only second-order temporal and spatial derivatives (no mixed temporal and spatial derivatives) of the spatial metric $\boldsymbol{\gamma}$ we arrive at the following relation

$$\partial_t^2 \gamma_{ij} \propto {}^{(3)}R_{ij}\,. \tag{2.35}$$

At this point it is useful to introduce two expressions for the Ricci tensor which can be found in [28]:

$$\begin{aligned}
{}^{(3)}R_{ij} =& \frac{1}{2}\gamma^{kl}\left(\partial_i\partial_l\gamma_{kj} + \partial_k\partial_j\gamma_{il} - \partial_i\partial_j\gamma_{kl} - \partial_k\partial_l\gamma_{ij}\right) \\
&+ \gamma^{kl}\left({}^{(3)}\Gamma^m{}_{il}\,{}^{(3)}\Gamma_{mkj} - {}^{(3)}\Gamma^m{}_{ij}\,{}^{(3)}\Gamma_{mkl}\right), \qquad (2.36)\\
=& -\frac{1}{2}\gamma^{cd}\partial_c\partial_d\gamma_{ij} + g_{c(i}\partial_{j)}\,{}^{(3)}\Gamma^c + {}^{(3)}\Gamma^{c}\,{}^{(3)}\Gamma_{(ij)c} \\
&+ 2g^{ed}\,{}^{(3)}\Gamma^c{}_{e(i}\,{}^{(3)}\Gamma_{j)cd} + \gamma^{cd}\,{}^{(3)}\Gamma^e{}_{id}\,{}^{(3)}\Gamma_{ecj}\,, \qquad (2.37)\\
{}^{(3)}\Gamma^i :=& \gamma^{jk}\,{}^{(3)}\Gamma^i{}_{jk}\,. \qquad (2.38)
\end{aligned}$$

where Eq. (2.36) shows that the Ricci tensor contains four terms with second-order spatial derivatives only one of which has the form of a Laplace operator, i.e., $\gamma^{kl}\partial_k\partial_l$. Equation (2.37) shows that all mixed second-order spatial derivatives, i.e., the second-order spatial derivatives not resembling the Laplace operator, can be absorbed in the derivative of the connection functions ${}^{(3)}\Gamma^i$ defined in Eq. (2.38). Equations (2.36) and (2.37) together with Eq. (2.35) indicate that the wave-nature of the ADM equations (2.31) and (2.32) is spoiled by mixed second-order spatial derivatives which impact the principal part of the equations, thereby preventing it from being hyperbolic.

To overcome this problem the BSSNOK formulation makes use of a conformal and traceless reformulation of the ADM equations together with an introduction of conformal connection functions similar to the ones presented in Eqs. (2.37) and (2.38)

$$\phi := \gamma^{-1/6}, \tag{2.39}$$

$$\tilde{\gamma}_{ij} := \phi^2 \gamma_{ij}, \tag{2.40}$$

$$\tilde{A}_{ij} := \phi^2 \left(K_{ij} - \frac{1}{3}\gamma_{ij} K \right), \tag{2.41}$$

$$\tilde{\Gamma}^i := \tilde{\gamma}^{jk} \tilde{\Gamma}^i_{jk}, \tag{2.42}$$

where ϕ denotes the conformal factor and $\tilde{A}_{ij}$ denotes the conformal and trace-free extrinsic curvature. The conformal connection functions, $\tilde{\Gamma}^i$, are then promoted to new and independent evolution variables such that the new system becomes strongly hyperbolic [207, 282, 27]. The final result reads [261]:

$$\partial_t \tilde{\gamma}_{ij} = -2\alpha \tilde{A}_{ij} + 2\tilde{\gamma}_{k(i}\partial_{j)}\beta^k - \frac{2}{3}\tilde{\gamma}_{ij}\partial_k \beta^k + \beta^k \partial_k \tilde{\gamma}_{ij}, \tag{2.43}$$

$$\begin{aligned}\partial_t \tilde{A}_{ij} =& \phi^2 \left[-D_i D_j \alpha + \alpha \left({}^{(3)}R_{ij} - 8\pi S_{ij} \right) \right]^{\mathrm{TF}} + \beta^k \partial_k \tilde{A}_{ij} + 2\tilde{A}_{k(i}\partial_{j)}\beta^k \\ &+ \alpha \left(\tilde{A}_{ij} K - 2\tilde{A}_{ik}\tilde{A}^k{}_j \right) - \frac{2}{3}\tilde{A}_{ij}\partial_k \beta^k,\end{aligned} \tag{2.44}$$

$$\partial_t \phi = \frac{1}{3}\phi \alpha K - \frac{1}{3}\phi \partial_i \beta^i + \beta^k \partial_k \phi, \tag{2.45}$$

$$\partial_t K = -D_i D^i \alpha + \alpha \left[\tilde{A}_{ij}\tilde{A}^{ij} + \frac{1}{3}K^2 + 4\pi(E+S) \right] + \beta^i \partial_i K, \tag{2.46}$$

$$\begin{aligned}\partial_t \tilde{\Gamma}^i =& \tilde{\gamma}^{jk}\partial_j \partial_k \beta^i + \frac{1}{3}\tilde{\gamma}^{ik}\partial_k \partial_j \beta^j + \frac{2}{3}\tilde{\Gamma}^i \partial_j \beta^j - \tilde{\Gamma}^j \partial_j \beta^i - 2\tilde{A}^{ij}\partial_j \alpha + \beta^j \partial_j \tilde{\Gamma}^i \\ &+ 2\alpha \left(\tilde{\Gamma}^i_{jk}\tilde{A}^{jk} - 3\tilde{A}^{ij}\partial_j \ln \phi - \frac{2}{3}\tilde{\gamma}^{ij}\partial_j K \right) - 16\pi \alpha \tilde{\gamma}^{ij} S_j.\end{aligned} \tag{2.47}$$

The superscript TF indicates that the trace-free part of the bracketed expression is used.

Despite the huge success of the BSSNOK formulation in the modeling of both matter and vacuum spacetimes one desirable feature remains which the equations (2.43)-(2.47) fail achieve. Namely, the BSSNOK equations fail to propagate and damp constraint violations which appear inevitably due to discretization errors in unconstrained evolutions. This can lead to large Hamiltonian constraint violations which can accumulate over time. This behaviour is related to the properties of the PDEs whose constraint subsystem has a zero speed characteristic for the Hamiltonian constraint [42]. A solution to this problem makes use of a covariant extension of Einstein's field equations, namely the Z4 system [49, 50]:

$$R_{\mu\nu} + 2\nabla_{(\mu}\mathcal{Z}_{\nu)} = 8\pi \left(T_{\mu\nu} - \frac{1}{2} T g_{\mu\nu} \right), \tag{2.48}$$

where the evolution equations for the four-vector $\mathcal{Z}_\mu = \Theta n_\mu + Z_\mu$ explicitly include the constraints (2.33) and (2.34). It is easy to realize that solutions with $\mathcal{Z}_\mu = 0$ satisfy the Einstein's equations (2.1). By using the conservation of energy and momentum, i.e., $\nabla_\mu T^{\mu\nu} = 0$, and the Bianchi identities we arrive at a wave-like equation for Z_μ

$$\Box_g \mathcal{Z}_\mu + R_{\mu\nu}\mathcal{Z}^\nu = 0. \tag{2.49}$$

Equation (2.49) ensures that deviations from Einstein's field equations (2.1) propagate along light cones [261, 49]. However, Eq. (2.48) can be further extended. It

would be even more desirable, if constraint violations would not only propagate but also be damped as the simulation progresses. This would ensure that the simulation approaches a true solution of Einstein's equations even if constraint violations were present initially. In other words, it would be desirable if the solutions of Einstein's equations (2.1) become an attractor of the full extended system. This can be achieved by adding suitable damping terms to Eq. (2.48) and leads us to the damped-Z4 formulation which is based on the following extension of Einstein's equations [137]:

$$R_{\mu\nu} + 2\nabla_{(\mu}\mathcal{Z}_{\nu)} - \kappa_1\left[2n_{(\mu}\mathcal{Z}_{\nu)} - (1+\kappa_2)\,g_{\mu\nu}n_\alpha\mathcal{Z}^\alpha\right] = 8\pi\left(T_{\mu\nu} - \frac{1}{2}Tg_{\mu\nu}\right), \tag{2.50}$$

where the constant coefficients κ_1 and κ_2 control the exponential damping time of the constraint violations if $\kappa_1 > 0$ and $\kappa_2 > -1$. Again, we obtain a wave-like equation for Z_μ [261]:

$$\Box_g\mathcal{Z}_\mu + R_{\mu\nu}\mathcal{Z}^\nu = -\kappa_1\nabla^\nu\left[2n_{(\mu}\mathcal{Z}_{\nu)} + \kappa_2 g_{\mu\nu}n_\alpha\mathcal{Z}^\alpha\right], \tag{2.51}$$

which now, however, incorporates a right-hand side (RHS) responsible for damping.

The formulation used in all simulations presented in this Thesis is introduced in [42, 270] and is called the Z4c formulation. Its main goals consist of developing a formulation which is as close as possible to the strongly hyperbolic BSSNOK system (2.43)-(2.47) while at the same time incorporating the constraint propagating and damping behaviour of the damped-Z4 formulation (2.50)-(2.51). Because of the former requirement specific problematic non-principal terms are neglected in the constraint addition leading to a system which is not covariant. Therefore, the Z4c system is not equivalent to the damped-Z4 system [147]. However, the Z4c formulation still benefits from constraint propagation and damping. The evolution equations are

$$\partial_t\tilde{\gamma}_{ij} = -2\alpha\tilde{A}_{ij} + 2\tilde{\gamma}_{k(i}\partial_{j)}\beta^k - \frac{2}{3}\tilde{\gamma}_{ij}\partial_k\beta^k + \beta^k\partial_k\tilde{\gamma}_{ij}, \tag{2.52}$$

$$\begin{aligned}\partial_t\tilde{A}_{ij} =& \phi^2\left[-D_iD_j\alpha + \alpha\left({}^{(3)}R_{ij} - 8\pi S_{ij}\right)\right]^{\mathrm{TF}} + \beta^k\partial_k\tilde{A}_{ij} + 2\tilde{A}_{k(i}\partial_{j)}\beta^k \\ &+ \alpha\left[\tilde{A}_{ij}(\hat{K}+2\Theta) - 2\tilde{A}_{ik}\tilde{A}^k{}_j\right] - \frac{2}{3}\tilde{A}_{ij}\partial_k\beta^k,\end{aligned} \tag{2.53}$$

$$\partial_t\phi = \frac{1}{3}\phi\alpha(\hat{K}+2\Theta) - \frac{1}{3}\phi\partial_i\beta^i + \beta^k\partial_k\phi, \tag{2.54}$$

$$\partial_t\hat{K} = -D_iD^i\alpha + \alpha\left[\tilde{A}_{ij}\tilde{A}^{ij} + \frac{1}{3}(\hat{K}+2\Theta)^2 + \kappa_1(1-\kappa_2)\Theta + 4\pi(E+S)\right] + \beta^i\partial_i\hat{K}, \tag{2.55}$$

$$\begin{aligned}\partial_t\hat{\Gamma}^i =& \tilde{\gamma}^{jk}\partial_j\partial_k\beta^i + \frac{1}{3}\tilde{\gamma}^{ik}\partial_k\partial_j\beta^j + \frac{2}{3}\tilde{\Gamma}^i\partial_j\beta^j - \tilde{\Gamma}^j\partial_j\beta^i - 2\tilde{A}^{ij}\partial_j\alpha + \beta^j\partial_j\hat{\Gamma}^i - 2\alpha\kappa_1\left(\hat{\Gamma}^i - \tilde{\Gamma}^i\right) \\ &+ 2\alpha\left[\tilde{\Gamma}^i_{jk}\tilde{A}^{jk} - 3\tilde{A}^{ij}\partial_j\ln\phi - \frac{1}{3}\tilde{\gamma}^{ij}\partial_j\left(2\hat{K}+\Theta\right) - 8\pi\tilde{\gamma}^{ij}S_j\right],\end{aligned} \tag{2.56}$$

$$\partial_t\Theta = \frac{1}{2}\alpha\left[{}^{(3)}R - \tilde{A}_{ij}\tilde{A}^{ij} + \frac{2}{3}(\hat{K}+2\Theta)^2 - 16\pi E\right] - \alpha\kappa_1(2+\kappa_2)\Theta + \beta^i\partial_i\Theta, \tag{2.57}$$

where we have defined the trace of the extrinsic curvature up to constraint addition, $\hat{K}$, and the new conformal connection functions, $\hat{\Gamma}^i$,

$$\hat{K} := K - 2\Theta, \tag{2.58}$$

$$\hat{\Gamma}^i := \tilde{\Gamma}^i + 2\tilde{\gamma}^{ij}Z_j. \tag{2.59}$$

In addition, the system is constrained by the following relations in order to satisfy

Einstein's equations [147]:

$$\Theta = 0, \tag{2.60}$$

$$Z_i = 0 \Leftrightarrow \hat{\Gamma}^i - \tilde{\Gamma}^i = 0, \tag{2.61}$$

$$\hat{H} :=^{(3)}R - \tilde{A}_{ij}\tilde{A}^{ij} + \frac{2}{3}(\hat{K} + 2\Theta)^2 - 16\pi E = 0, \tag{2.62}$$

$$\tilde{M}^i :=\tilde{D}_j\tilde{A}^{ij} - \frac{2}{3}\tilde{\gamma}^{ij}\partial_j(\hat{K} + 2\Theta) - \frac{4}{3}\tilde{A}^{ij}\partial_j \ln\phi - 8\pi\tilde{\gamma}^{ij}S_j = 0, \tag{2.63}$$

where we have introduced the covariant derivative $\tilde{\boldsymbol{D}}$ associated to the conformal three-metric $\tilde{\gamma}_{ij}$. Equations (2.60) and (2.61) are required for the extended system in order to reduce to Einstein's equations and express the condition $Z_\mu = 0$ while Eqs. (2.62) and (2.63) are generalizations of the Hamiltonian and momentum constraints already introduced in Eqs. (2.33) and (2.34).

2.1.5 Moving puncture gauge conditions

As already mentioned, the formulations of Einstein's equations discussed so far, the ADM, BSSNOK and Z4c formulations, leave the dynamics of the gauge quantities, α and β^i, unspecified. This corresponds to the freedom of choosing an arbitrary coordinate system to describe the evolution of matter and spacetime itself. Thus, their choice can be regarded as gauge fixing for Einstein's equations where physically meaningful observables remain invariant under this choice.

For the purposes of this Thesis, the most important requirement on the gauge conditions is the ability to simulate moving and merging binary black hole (BBH) spacetimes without using singularity excision techniques [8], e.g., these were employed by the first succesful simulation of a BBH coalescence [242], and without holding the BH singularities or "punctures" fixed on the numerical grid. This is done when using a corotating frame implemented by an angular shift vector [8, 57]. Following [261], this can be achieved if the gauge conditions guarantee two requirements:

(i) Singularity-avoiding slicing condition:

The pace at which proper time evolves near the singularity has to be reduced.

(ii) Coordinate distortions due to large spatial curvatures should be counteracted.

Condition (i) is implemented successfully by using the 1+log slicing condition in the form

$$\partial_t\alpha - \beta^k\partial_k\alpha = -2\alpha K. \tag{2.64}$$

Condition (ii) is implemented successfully by using the Gamma driver shift condition

$$\partial_t\beta^i - \beta^j\partial_j = \frac{3}{4}B^i \tag{2.65}$$

$$\partial_t B^i - \beta^j\partial_j B^i = \partial_t\tilde{\Gamma}^i - \beta^j\partial_j\tilde{\Gamma}^i - \eta B^i, \tag{2.66}$$

where the auxiliary variable B^i was introduced. Similar variants of the "moving puncture" gauge presented in Eqs. (2.64) - (2.66) have been employed in the breakthrough BBH simulations of [64, 24].

2.2 Fluids and hydrodynamics

Perhaps one of the best ways to summarize the interplay between spacetime and matter is a quote by John Archibald Wheeler: *"Spacetime tells matter how to move; matter tells spacetime how to curve."* The previous section introduced Einstein's field equations which precisely predict how spacetime curves based on a matter configuration represented by the energy-momentum tensor $T^{\mu\nu}$. This corresponds to the second part of the quote. However, given that the main objective of this Thesis is the exploration of neutron stars and especially BNS mergers, it is important to understand how matter behaves in the presence of strong gravitational fields. Hence, the rest of this chapter is dedicated to the first part of the quote, where we start by giving a very brief introduction to *hydrodynamics* and the so-called *fluid* approximation, see also [261].

The theory of *hydrodynamics* can be understood as an effective theory in the long-wavelength, low-frequency limit of an underlying microscopic theory. By employing kinetic theory for the latter, it is possible to derive the equations of hydrodynamics from the relativistic Boltzmann equation and the method of moments [93]. For example, along this route one arrives at relations which connect the so-called particle distribution function $f = f(t, x, p)$, which is a function of time (t), position (x) and momentum (p), and the energy-momentum tensor

$$T^{\mu\nu} = \int \frac{d^3p}{p_0} f p^\mu p^\nu \,, \tag{2.67}$$

see e.g., [65], thereby showing that the energy-momentum tensor is the second moment of the distribution function [261].

Now, a *fluid* is present if f assumes a very specific form f_0, or at least if the deviation $f - f_0$ is small. Here, f_0 is the so-called equilibrium distribution function which can be the Maxwell-Jüttner distribution function for a classical gas or the Bose-Einstein (Fermi-Dirac) distribution function for a quantum gas of bosons (fermions) [158]. Equivalently, we say that f is close to local thermodynamic equilibrium.

From a physical point of view, it is helpful to think of an ensemble of a large number of particles which can be divided into distinct elements, so-called fluid elements. Their size L is chosen such that each fluid element still contains a sufficiently large number of particles but is homogeneous on scales smaller than L. This means that each element is well approximated by a single number for its density, its temperature and its velocity without the need to consider the substructure of the element. Now, local thermodynamic equilibrium means that thermodynamic transformations applied to each fluid element through an interplay with its neighbours, e.g., compression or expansion, are adiabatic, i.e., the entropy of a fluid element is conserved. Physically this can be achieved through an extremely short mean-free path ℓ of the particles compared to L. This leads us to the definition of the Knudsen number

$$\mathrm{Kn} := \frac{\ell}{L} \,, \tag{2.68}$$

which takes the extremal value $\mathrm{Kn} = 0$ in local thermodynamic equilibrium. Hence, a *fluid* is present, if the Knudsen number is small, while the theory of *hydrodynamics* describes the dynamics of fluids based on a suitable approximation of the Boltzmann equation in the "fluid-limit", i.e., when $f - f_0$ is small.

At this point, it is possible to make a classification of two broad classes of fluids. First, so-called "perfect" fluids are those which are always in local thermodynamic equilibrium, i.e., $\mathrm{Kn} = 0$. Second, so-called "non-perfect" fluids are those for which $\mathrm{Kn} \ll 1$ and $\mathrm{Kn} \neq 0$, which allows for phenomena such as particle diffusion, heat transfer and momentum transfer across the borders of neighbouring fluid elements. Non-perfect fluids are characterised by growing entropy.

2.3 General-relativistic perfect hydrodynamics

The following is a brief review of the equations that describe the evolution of perfect fluids on an arbitrary curved background. More specifically, we focus on a single perfect fluid which is represented by the equations of relativistic perfect hydrodynamics. In later parts of this Thesis we will go beyond this simplifying assumption and also consider the exciting world of non-perfect fluids, which take into account effects from being out of thermodynamic equilibrium, as well as perfect fluids which are ideal conductors and immersed in a coevolving magnetic field. For a more comprehensive introduction we refer to [261].

The energy-momentum tensor for perfect fluids is given by

$$T^{\mu\nu} = T^{\mu\nu}_{\mathrm{pf}} := eu^{\mu}u^{\nu} + ph^{\mu\nu}\,, \tag{2.69}$$

where e denotes the energy density and p the isotropic pressure, both of which are evaluated in the fluid frame. The fluid four-velocity is given by u^{μ} which can also be used to define a projection operator onto hypersurfaces orthogonal to $\boldsymbol{u}$, namely $h_{\mu\nu} := g_{\mu\nu} + u_{\mu}u_{\nu}$. Note that we distinguish between the total energy-momentum tensor $T^{\mu\nu}$ and the form it takes in the specific case of a single perfect fluid $T^{\mu\nu}_{\mathrm{pf}}$. For conserved charges also a charge current can be defined which in the context of neutron stars is typically the baryon number current. Multiplying the baryon number current with a constant baryon mass yields the rest-mass current

$$J^{\mu} = J^{\mu}_{\mathrm{pf}} := \rho u^{\mu}\,, \tag{2.70}$$

where ρ is the rest-mass density, in this case the baryon-mass density, evaluated in the fluid frame. In general, a thermodynamic relation exists connecting the thermodynamic quantities e, p and ρ which is called EOS

$$p = p(\rho, e)\,. \tag{2.71}$$

Having a closer look at the degrees of freedom of the perfect fluid we have introduced so far, we observe that we are left with five undetermined variables, namely ρ, e and three variables for $\boldsymbol{u}$ as we have $u_{\mu}u^{\mu} = -1$. Their evolution is governed by the conservation equations for charge, energy and momentum

$$\nabla_{\mu}J^{\mu} = 0\,, \tag{2.72}$$

$$\nabla_{\mu}T^{\mu\nu} = 0\,. \tag{2.73}$$

Equations (2.72) and (2.73) represent a system of five first-order, nonlinear PDEs which can also be written in flux-conservative form. We recall that a system of PDEs is classified as being in flux-conservative form if it can be represented as

$$\partial_t \boldsymbol{U} + \partial_i \boldsymbol{F}^i(\boldsymbol{U}) = \boldsymbol{S}\,, \tag{2.74}$$

where $\boldsymbol{U}$ is the state vector, $\boldsymbol{F^i}$ are the flux vectors and $\boldsymbol{S}$ is the source vector. The biggest advantage of such a formulation is related to the accurate numerical capture of shock solutions. The nonlinearities in Eqs. (2.72) and (2.73) naturally lead to the appearance of discontinuities which no longer fall into the class of solutions of the equations written down in differential form. Instead, they constitute weak solutions which represent solutions of the weak formulation, i.e., the integral form, of the equations. Now, the importance of a flux-conservative form becomes clear through two theorems. The first one is given in [175] and states that flux-conservative schemes converge to the weak

solution, if they are convergent, and the second one is given in [151] and instead says that numerical schemes not written in a flux-conservative form do not converge to the correct solution, if a shock wave is present in the flow.

Finally, the equations of relativistic perfect hydrodynamics written in a flux-conservative form and typically evolved for BNS merger modeling are given by

$$\boldsymbol{U} = \sqrt{\gamma}\begin{pmatrix} D \\ S_j \\ \tau \end{pmatrix} = \sqrt{\gamma}\begin{pmatrix} \rho W \\ (e+p)\,W^2 v_j \\ (e+p)\,W^2 - p - \rho W \end{pmatrix}, \tag{2.75}$$

$$\boldsymbol{F}^i = \sqrt{\gamma}\begin{pmatrix} V^i D \\ \alpha S^i{}_j - \beta^i S_j \\ \alpha(S^i - v^i D) - \beta^i (E - D) \end{pmatrix}, \tag{2.76}$$

$$\boldsymbol{S} := \sqrt{\gamma}\begin{pmatrix} 0 \\ \frac{1}{2}\alpha S^{ik}\partial_j \gamma_{ik} + S_i \partial_j \beta^i - E\partial_j \alpha \\ \alpha S^{ik} K_{ij} - S^j \partial_j \alpha \end{pmatrix}, \tag{2.77}$$

where we define the coordinate three-velocity $V^j := u^j/u^t = \alpha v^j - \beta^j$, the conserved energy $\tau := E - D$ and the spatial projection of the energy-momentum tensor $S_{ij} := \gamma_{i\mu}\gamma_{jv}T^{\mu v}$, see also Eqs. (2.25)-(2.27). At this point it is helpful to introduce the distinction between conserved and primitive variables. Conserved variables are the entries of the state vector given in Eq. (2.75) and are evolved in time in a numerical hydrodynamics code

$$\boldsymbol{C} := \left\{\sqrt{\gamma}D, \sqrt{\gamma}S_j, \sqrt{\gamma}\tau\right\}. \tag{2.78}$$

Primitive variables represent physically meaningful quantities which are typically needed to compute the flux and source vectors given in Eqs. (2.76) and (2.77) such as the set

$$\boldsymbol{P} := \left\{\rho, p, v^i\right\}. \tag{2.79}$$

In general, the conversion between conserved and primitive variables has to be carried out numerically by using root-finding algorithms, see e.g., [124].

Finally, we define the square of the perfect-fluid sound speed [261] as

$$c_s{}^2 = \left(\frac{\partial p}{\partial e}\right)_\rho + \frac{1}{e+p}\left(\frac{\partial p}{\partial \rho}\right)_e. \tag{2.80}$$

2.3.1 Numerical methods for relativistic hydrodynamics

We start by discussing the possible options of how to represent the solution of a system of PDEs on a discrete numerical grid. There are at least three generic choices. First, it is possible represent the function by using a set of point values which approximate the function at the corresponding set of locations on the grid. The evolution of the pointwise representation of the function is commonly done by using the finite-difference approach. This approach is the easiest to implement but gets more involved if Non-

Cartesian coordinates, e.g., spherical coordinates, are used. Additionally, increasing the formal convergence order of a finite-difference method can also get involved, if the solutions of the system of PDEs naturally develop discontinuities [248, 249, 195].

Second, it is also possible to define cell-averaged values of the function where a set of grid points typically defines the corners of the cells over which the averages are calculated. In this case cell-averaged values are evolved in time which is done by using a finite-volume approach. As this approach makes use of integrals over grid cells it is easily generalizable to a great variation of grid-cell shapes [240, 189]. In other words, it easy to implement different coordinate systems in a finite-volume approach. However, because the formal convergence order of the method is set by the formal convergence order of the technique to evaluate the integrals, high-order finite-volume methods can become very expensive. Typically, in such cases a conversion between cell-averaged and local point values is employed [185].

Finally, it is also possible to represent the function through a finite set of orthogonal basis functions on distinct domains of the grid. This method is named spectral method and involves coefficients which are used to construct the approximated function from the set of basis functions. These coeffcients are then evolved in time. The main advantage of spectral methods is the formal exponential convergence of the solution if the number of basis functions is increased. On the other hand, spectral methods are known to be subject to the Gibb's phenomenon in the presence of large gradients. This means that these methods are ill-suited for the solution in regions where discontinuities can develop [136].

In this Thesis, we will use a point-wise representation of the solution functions and hence make use of a finite-difference scheme to solve hyperbolic equations of the form shown in Eq. (2.74).

The temporal discretization of Eq. (2.74) is achieved by using a semi-discrete/method of lines approach

$$\frac{\mathrm{d}}{\mathrm{d}t} U_i = -\mathcal{D}\left(\hat{F}\right) = -\frac{1}{h}\left(\hat{F}_{i+1/2} - \hat{F}_{i-1/2}\right) + S_i\,, \tag{2.81}$$

where, for simplicity, we have reduced Eq. (2.74) to the case of one spatial dimension x and consider the evolution of only one component of the state vector $\boldsymbol{U}$ denoted by U on a equidistant Cartesian grid. Furthermore, U_i and S_i represent U and S evaluated at the grid point x_i, while the expression $\mathcal{D}\left(\hat{F}\right) := \left(\hat{F}_{i+1/2} - \hat{F}_{i-1/2}\right)/h$ denotes a non-oscillatory approximation of $(\partial_x F)_i$, which is the flux derivative at x_i, with $h := x_{i+1/2} - x_{i-1/2}$. In Equation (2.81) the spatial discretization has been already performed leading to the appearance of the numerical fluxes $\hat{F}_{i\pm1/2}$. The whole equation can now be considered to be discretized in space but still continuous in time which means that the system of PDEs in Eq. (2.74) was cast into a system of ODEs. This also means that time integration methods typically used for the solution of ODEs can also be employed for the solution of Eq. (2.81). In this Thesis, we predominantly make use of the third-order Runge-Kutta method referred to as optimal TVD third-order method in [288]. Additionally, to avoid unstable behaviour the Courant-Friedrichs-Lewy (CFL) condition needs to be fulfilled:

$$\Delta t = C_{\mathrm{CFL}} \frac{h}{\lambda_{\max}}\,, \tag{2.82}$$

with Δt being the timestep, $C_{\mathrm{CFL}} < 1$, and $\lambda_{\max}$ being the maximum of the absolute values of all characteristic velocities.

Next, we focus on the construction of the numerical fluxes $\hat{F}_{i\pm1/2}$. Following [87,

249, 261] we can introduce an auxiliary function H defined by the expression

$$F_i = \frac{1}{h}\int_{x_{i-1/2}}^{x_{i+1/2}} H(\xi)\,\mathrm{d}\xi\,, \tag{2.83}$$

which means that the average of H equals to the point value of the flux F at x_i. Hence, we obtain the pointwise derivative of the flux by

$$(\partial_x F)_i = \frac{H_{i+1/2} - H_{i-1/2}}{h} = \mathcal{D}(H)\,. \tag{2.84}$$

By comparing Eq. (2.84) with Eq. (2.81) we find that the numerical flux is a discrete approximation of the auxiliary function at the borders of the grid cells

$$\hat{F}_{i\pm1/2} = H_{i\pm1/2} + \mathcal{O}(h^q)\,, \tag{2.85}$$

where q is the formal convergence order of our spatial discretization scheme.

Now, how to find an explicit expression for H? Fortunately, we only need an expression for $\hat{F}$ which is an approximation to H to a given order q. Substituting the numerical flux given in Eq. (2.85) into Eq. (2.83) we find that cell averages of the numerical flux $\hat{F}$ can be approximated by cell-centered values of the original flux F

$$\frac{1}{h}\int_{x_{i-1/2}}^{x_{i+1/2}} \hat{F}(\xi)\,\mathrm{d}\xi = F_i + \mathcal{O}(h^q)\,. \tag{2.86}$$

Finally, we are left to calculate the point values $\hat{F}_{i\pm1/2}$ from its cell averages given in Eq. (2.86) up to an error on the order of h^q. This can be achieved by using a Taylor expansion of cell averages in terms of cell-centered point values and a subsequent inversion of the obtained expression. Following [87, 88, 89] the fourth-order formula is given by

$$\hat{F}_{i+1/2} = F_{i+1/2} - \frac{1}{24}\Delta^{(2)}(F_{i+1/2}) + \mathcal{O}\left(h^4\right), \tag{2.87}$$

where we introduced the operation

$$\Delta^{(2)}(F_i) = F_{i-1} - 2F_i + F_{i+1}\,. \tag{2.88}$$

Note that we set out to calculate the point values of $\hat{F}$ from its cell averages, but we used Eq. (2.86) in Eq. (2.87) to directly replace all cell averages of the numerical flux $\hat{F}$ by point values of the original flux F. We have now obtained an high-order approximation of the derivative of the original flux $(\partial_x F)_i$ expressed through a numerical flux $\hat{F}$ which is evaluated at the boundary of the cell and calculated from point values of the original flux.

As already mentioned further above, discontinuous solutions can develop naturally in the system of Eqs. (2.74) - (2.77) even for the case of smooth initial data. This means that particular care needs to be taken in order to obtain numerical solutions which converge to the true solution if the resolution is increased. This requirement leads us to the class of high-resolution shock-capturing (HRSC) methods which can be employed in order to get faithful solutions, see [304] for an overview. In essence, HRSC methods guarantee the upwind property of the scheme which takes into account information about the characteristic structure of the problem [261].

The original idea goes back to Godunov [133] who had the remarkable insight that on a discrete grid, where the solution is approximated as a constant function in each cell, a local Riemann problem arises at interfaces of neighbouring cells. Hence, the

characteristic structure of the problem can be taken into account by solving these local Riemann problems and calculating the interface fluxes $F_{i\pm1/2}$, which are used in Eq. (2.87), based on these solutions. Even though an exact solution to the Riemann problem in perfect-fluid hydrodynamics exists, see e.g., [261], high computational costs arise when computing this solution for each interface in a multidimensional code because it cannot be given in a closed analytic form. Therefore, approximate solutions have been developed which are numerically cheap to evaluate but nevertheless yield accurate results.

Here, we introduce the Harten-Lax-Van Leer-Einfeldt (HLLE) solver [143, 109] which assumes that only two waves develop from an initial discontinuous state giving rise to a *Riemann fan* which consists only of three states. Assuming the two waves propagate with velocities λ_L and λ_R, the approximate solution to the Riemann problem takes the form [261]

$$U(t,x) = \begin{cases} U_L & \text{if} \quad x/t < \lambda_L, \\ U^{\text{HLLE}} & \text{if} \quad \lambda_L < x/t < \lambda_R, \\ U_R & \text{if} \quad x/t > \lambda_R, \end{cases} \tag{2.89}$$

where U_L (U_R) is the state at the cell interface calculated from an interpolation based on a left-biased (right-biased) stencil. For example, assuming a representation of the solution using constant functions in each cell, the states U_L and U_R at the interface $x_{i+1/2}$ are given by U_i and U_{i+1}, respectively. The wave velocities are given by

$$\lambda_L = \min\left(0, \lambda_-(U_L), \lambda_-(U_R)\right), \tag{2.90}$$

$$\lambda_R = \max\left(0, \lambda_+(U_L), \lambda_+(U_R)\right), \tag{2.91}$$

where λ_- (λ_+) is lowest (highest) characteristic velocity. The middle state U^{HLLE} is given by

$$U^{\text{HLLE}} = \frac{\lambda_R U_R - \lambda_L U_L + F_L - F_R}{\lambda_R - \lambda_L}, \tag{2.92}$$

where we have introduced the fluxes $F_L := F(U_L)$ and $F_R := F(U_R)$. Finally, the application of the Rankine-Hugoniot conditions [261] gives rise to the following flux formula

$$F^{\text{HLLE}} = \begin{cases} F_L & \text{if} \quad x/t < \lambda_L, \\ F_* & \text{if} \quad \lambda_L < x/t < \lambda_R, \\ F_R & \text{if} \quad x/t > \lambda_R, \end{cases} \tag{2.93}$$

with

$$F_* := \frac{\lambda_R F_L - \lambda_L F_R + \lambda_R \lambda_L (U_R - U_L)}{\lambda_R - \lambda_L}. \tag{2.94}$$

In this Thesis we employ a discretization which guarantees the upwind property of Eq. (2.81) by employing the approximate HLLE Riemann solver presented in Eq. (2.93) to calculate the original interface fluxes in Eq. (2.87).

Finally, the last piece missing in the HRSC scheme is the calculation of U_L and U_R at each interface given the set of cell-centered states U_i. Here, we employ the WENO-Z method [52] by using the proposed coeffcients and stencils from [89]. Note that as opposed to the common reconstruction of point values from cell averages in finite-volume schemes, in this case point values at cell interfaces are reconstructed from point values at cell centers [87].

In this Thesis we make use of the fourth-order finite-difference HRSC GRMHD code FIL [195] which employs the Eulerian conservative high-order (ECHO) scheme

[89] whose methods we introduced in this subsection. In the following, we briefly summarize the solution procedure of FIL in the correct order for a single perfect-fluid on an one-dimensional Cartesian grid:

C2P Given the set of cell-centered conservative variables $\boldsymbol{C}$ at time t compute the corresponding primitive variables $\boldsymbol{P}$ at cell centers.

REC Reconstruct the primitive variables at the left and right cell interfaces using the WENO-Z method. These are two non-oscillatory interpolations from cell-centered primitives $\boldsymbol{P}$ to primitives at cell interfaces $\boldsymbol{P}_{L/R}$.

HLLE Compute the HLLE flux F^{HLLE} in Eq. (2.93) from the left and right primitive variables defined at cell interfaces $\boldsymbol{P}_{L/R}$.

DER Compute the numerical flux $\hat{F}$ used in Eq. (2.81) by using the fourth-order formula in Eq. (2.87) and replacing the original interface flux with the corresponding HLLE flux F^{HLLE}.

RK3 Evolve Eq. (2.81) to the time $t + \Delta t$ using the third-order Runge-Kutta method mentioned previously.

2.4 General-relativistic dissipative hydrodynamics

In this section we will introduce non-perfect fluids and the broader subject of general-relativistic dissipative hydrodynamics (GRDHD). In simplified terms, the aim of this subject is the faithful inclusion of dissipative effects such as viscous dissipation and heat conduction in the relativistic continuum equations presented in Section 2.3. Typically, these dissipative effects stem from microphysical processes which together with gradients in the macroscopic fluid variables lead to deviations from local thermodynamic equilibrium. As an example, we discuss the appearance of a microphysical bulk viscosity due to violations of chemical equilibrium in Subsection 4.1.2.

Apart from that, it is also interesting to mention that dissipative effects may arise from a very different source. Due to the limitations in computational power NR simulations can only be performed with finite resolutions which are typically above the scale at which turbulence is physically quenched off. Mathematically, this corresponds to an *implicit* filtering operation which neglects the contributions from unresolved scales to the resolved ones [68, 69]. These contributions from unresolved scales are similar to dissipative terms and arise when the filtering operation is applied to nonlinear terms in the original set of equations. Different approaches exist to model such subgrid-scale contributions in NR simulations. Noteworthy examples include the purely hydrodynamical general-relativistic large-eddy simulations (LESs) presented in [244, 246, 254, 251] which aim to model the magneto-turbulent fluid state encountered after merger, the previously mentioned LES from [310, 6] which focus on magnetic-field amplification and the again purely hydrodynamical schemes shown in [103, 286, 115, 122, 105] which target among other effects angular-momentum transport and mass ejection on long timescales.

Furthermore, although applications of GRDHD in NR simulations have a only started in the past few years, this is not the case for the modeling of heavy-ion collisions (HICs). Specifically, the special-relativistic evolution of the quark-gluon plasma (QGP), which is the hot and dense strongly interacting matter created in HICs, is described by relativistic dissipative hydrodynamics. Therefore, a large amount of literature on this subject already exists, see e.g., [267, 60, 186] for some reviews. It is noteworthy that simulations of the relativistic dissipative hydrodynamics of HICs allow us to extract

the magnitudes of bulk and shear viscosity from the experimental data [39] giving rise to the conclusion that the QGP behaves like a near-perfect fluid.

2.4.1 A brief overview

In this subsection we give a brief overview over the different formulations of GRDHD that have been proposed over the years. We start by the general distinction of *first-order* and *second-order* theories. In simplified terms, the class of first-order theories can be viewed as formulations which generalize the non-relativistic Navier-Stokes (NS) equations, in which the dissipative quantities are proportional to first-order gradients of the perfect-fluid hydrodynamic variables, such as e.g., pressure, rest-mass density and fluid velocity [108, 174]. While this approach has the advantage of recovering the correct non-relativistic limit, it was shown that a large class of these first-order theories is plagued by instabilities and acausal behaviour because of the partially parabolic nature of the equations [148, 150, 91].

In order to counter this drawback, the class of second-order theories was developed which is characterised by the inclusion of terms which are of second-order in the deviations from perfect-fluid hydrodynamics. As mentioned above, for first-order theories these deviations take the form of first-order gradients of the perfect-fluid variables. Therefore, the newly included second-order terms can be second-order gradients of the perfect-fluid variables or expressions which are quadratic in first-order gradients. Additionally, it is possible to promote the dissipative currents such as the bulk-viscous pressure, the heat current or the shear-stress tensor to independent fluid variables of first-order in the deviations from perfect-fluid hydrodynamics. Then, the second-order terms may also include first-order gradients of the dissipative currents or terms quadratic in the dissipative currents. The idea to promote dissipative currents to independent fluid variables goes back to the formulations proposed by [204, 157, 158] such that these formulations are often referred to as Müller-Israel-Stewart (MIS) theories.

There are multiple ways to formulate second-order theories and in this overview we will focus on three specific examples. The first approach to second-order theories makes use of the entropy current by extending its definition. The logic is that all terms of second-order or less in dissipative currents, which are allowed by symmetry, should be added to the entropy current. Then, the second-law of thermodynamics naturally leads to hyperbolic relaxation-type equations for the dissipative currents [149, 206, 160]. The second approach, instead, starts directly from the definitions of the dissipative currents. Similar to the first approach, the idea is to add all terms of second-order or less in gradients of the perfect-fluid variables, which are allowed by symmetry, to the definitions of the dissipative currents [22]. Finally, the third approach derives the equations of second-order relativistic dissipative hydrodynamics from kinetic theory. By applying the method of moments to the Boltzmann equation [158, 45, 92, 93, 159] it is possible to derive an infinite system of coupled EOM for the moments of the deviation of the full distribution function from its equilibrium form mentioned before. In particular, a systematic power-counting scheme was proposed in [93] which rigorously makes use of the Knudsen number in Eq. (2.68) and defines the relativistic Reynolds number. This allows for a systematic truncation at an arbitrary order [94].

We conclude this overview by commenting a very exciting and recent development regarding first-order theories. It was shown by the works of [37] and [173], but see also [308, 99, 152, 293], that the acausal behaviour of first-order theories can be removed by changing the so-called "hydrodynamic frame". In practice, the definition of the hydrodynamic frame is equivalent to the definitions of the perfect-fluid variables, i.e., the pressure, rest-mass density and fluid velocity, when the fluid is in an out-of-

equilibrium state. In equilibrium these quantities admit a unique definition but out of equilibrium ambiguity arises which makes it possible to choose a frame which leads to PDEs with the most desirable properties. This class of first-order theories is referred to as Bemfica-Disconzi-Noronha-Kovtun (BDNK) theory and first numerical investigations paint a promising picture [224, 223, 222, 25] regarding their applicability.

2.4.2 GRDHD via the entropy current

In this subsection, we will give a brief introduction to the equations of GRDHD which can be derived from the entropy current. Our fundamental assumption is that the rest-mass density current J^μ and the energy-momentum tensor $T^{\mu\nu}$ continue to give a valid description of the fluid even if its state is out of thermodynamic equilibrium. Hence, the conservation equations, i.e., Eqs. (2.72) and (2.73), continue to hold. We make the separation between perfect-fluid variables and dissipative currents which constitute the perfect and non-perfect (dissipative) parts of the conserved currents, respectively,

$$T^{\mu\nu} = T^{\mu\nu}_{\mathrm{pf}} + T^{\mu\nu}_{\mathrm{npf}}, \tag{2.95}$$

$$J^{\mu} = J^{\mu}_{\mathrm{pf}} + J^{\mu}_{\mathrm{npf}}, \tag{2.96}$$

where $T^{\mu\nu}_{\mathrm{pf}}$ is given in Eq. (2.69) and J^{μ}_{pf} is given in Eq. (2.70). Additionally, as in perfect-fluid hydrodynamics, the system is complemented by an EOS of the form in Eq. (2.71). The non-perfect terms $T^{\mu\nu}_{\mathrm{npf}}$ and J^{μ}_{npf} can be written in their most general form assuming the "Eckart frame" (this means we explicitly choose an hydrodynamic frame) [108, 71]

$$T^{\mu\nu}_{\mathrm{npf}} = \Pi h^{\mu\nu} + 2q^{(\mu}u^{\nu)} + \pi^{\mu\nu}, \tag{2.97}$$

$$J^{\mu}_{\mathrm{npf}} = 0, \tag{2.98}$$

where Π is the bulk-viscous pressure, q^μ is the heat current, which is orthogonal to the fluid four-velocity, i.e., $q^\mu u_\mu = 0$, and finally, $\pi^{\mu\nu}$ is the shear-stress tensor and has the following properties: It is symmetric $\pi^{\mu\nu} = \pi^{\nu\mu}$, purely spatial $\pi^{\mu\nu}u_\mu = 0$, and trace-free $\pi^{\mu}{}_{\mu} = 0$. Furthermore, we make use of the definition $b^{\langle\mu\rangle} := h^{\mu}{}_{\nu}b^{\nu}$ as the projection of the contravariant components of an arbitrary vector b^ν in the direction orthogonal to $\boldsymbol{u}$, and $b^{\langle\mu\nu\rangle} := (h_\alpha{}^{(\mu}h^{\nu)}{}_\beta - \frac{1}{3}h^{\mu\nu}h_{\alpha\beta})b^{\alpha\beta}$ as the symmetric and trace-free projection of an arbitrary rank-2 tensor $b^{\mu\nu}$ in the direction orthogonal to $\boldsymbol{u}$.

If we count the number of independent variables we arrive at 14, but currently we have specified only five evolution equations (Eqs. (2.72), (2.73) and (2.71)) which means that nine additional evolution equations are required to close the system. These equations determine the evolution of the dissipative currents Π, q^μ and $\pi^{\mu\nu}$. By following [157, 149], we can write down the most general entropy current which is quadratic in the dissipative currents

$$\mathcal{S}^\mu = su^\mu + \frac{q^\mu}{T} - \left(\beta_0\Pi^2 + \beta_1 q_\alpha q^\alpha + \beta_2\pi_{\alpha\beta}\pi^{\alpha\beta}\right)\frac{u^\mu}{2T} + \alpha_0\frac{\Pi q^\mu}{T} + \alpha_1\frac{q_\alpha\pi^{\alpha\mu}}{T}, \tag{2.99}$$

where the physical meaning of the coefficients $\alpha_0, \alpha_1, \beta_0, \beta_1, \beta_2$ will become clear below, T is the temperature and s is the entropy density. From the second law of thermody-

namics, $\nabla_\mu \mathcal{S}^\mu \geq 0$, the following set of constitutive equations is obtained

$$\tau_{\Pi}\dot{\Pi} = \Pi_{\rm NS} - \Pi - \frac{1}{2}\zeta\Pi T\nabla_\mu\left(\frac{\tau_\Pi u^\mu}{\zeta T}\right) + \alpha_0\zeta\nabla_\mu q^\mu + \gamma_0\zeta T q^\mu\nabla_\mu\left(\frac{\alpha_0}{T}\right), \tag{2.100}$$

$$\tau_q\dot{q}^{\langle\mu\rangle} = {q_{\rm NS}}^\mu - q^\mu - \frac{1}{2}\kappa T^2 q^\mu\nabla_\nu\left(\frac{\tau_{\rm q} u^\nu}{\kappa T^2}\right) + \kappa T\Bigg[\alpha_0\nabla^{\langle\mu\rangle}\Pi + \alpha_1\nabla_\nu\pi^{\nu\langle\mu\rangle} + (1-\gamma_0)\Pi T\nabla^{\langle\mu\rangle}\left(\frac{\alpha_0}{T}\right) + (1-\gamma_1)T\pi^{\mu\nu}\nabla_\nu\left(\frac{\alpha_1}{T}\right)\Bigg], \tag{2.101}$$

$$\tau_\pi\dot{\pi}^{\langle\mu\nu\rangle} = {\pi_{\rm NS}}^{\mu\nu} - \pi^{\mu\nu} - \frac{1}{2}\eta T\pi^{\mu\nu}\nabla_\lambda\left(\frac{\tau_\pi u^\lambda}{\eta T}\right) + 2\alpha_1\eta\nabla^{\langle\mu}q^{\nu\rangle} + 2\gamma_1\eta T q^{\langle\mu}\nabla^{\nu\rangle}\left(\frac{\alpha_1}{T}\right), \tag{2.102}$$

where we have introduced two new coefficients, γ_0 and γ_1, which come frome the ambiguity when working out the terms which involve the products Πq^μ and $q_\alpha\pi^{\alpha\mu}$. We have also introduced the so-called "comoving derivative" $\dot{\boldsymbol{A}} := (\boldsymbol{u}\cdot\boldsymbol{\nabla})\boldsymbol{A} = u^\mu\nabla_\mu\boldsymbol{A}$, where $\boldsymbol{A}$ can be an arbitrary tensor field. Such a comoving derivative usually occurs together with a so-called "relaxation time" for the corresponding dissipative current, which are defined as

$$\tau_{\Pi} := \beta_0\zeta\,, \qquad \tau_q := \beta_1\kappa T\,, \qquad \tau_\pi := 2\beta_2\eta\,, \tag{2.103}$$

where ζ is the bulk viscosity, κ the heat conductivity, η the shear viscosity. The coefficients introduced in Eq. (2.103) are always positive or zero and set the timescales over which non-equilibrium effects push the equations of GRDHD towards the relativistic NS solution.

The acausal and unstable NS extension of GRDHD leads to the following expressions [108, 174]

$$\Pi_{\rm NS} = -\zeta\Theta\,, \tag{2.104}$$

$${q_{\rm NS}}^\mu = -\kappa T\left(\nabla^{\langle\mu\rangle}\ln T + a^\mu\right), \tag{2.105}$$

$${\pi_{\rm NS}}^{\mu\nu} = -2\eta\sigma^{\mu\nu}\,, \tag{2.106}$$

which denote the NS values or quantities. The expressions Θ, a^μ and $\sigma^{\mu\nu}$ denote the fluid expansion, the kinematic fluid four-acceleration and the fluid shear tensor, respectively. References and their definitions can be found in Appendix B.

Furthermore, if the entropy current contains only first-order dissipative currents, i.e., $\beta_0 = \beta_1 = \beta_2 = \alpha_0 = \alpha_1 = 0$, then [261]:

$$\Pi = \Pi_{\rm NS}\,, \tag{2.107}$$

$$q^\mu = {q_{\rm NS}}^\mu\,, \tag{2.108}$$

$$\pi^{\mu\nu} = {\pi_{\rm NS}}^{\mu\nu}\,. \tag{2.109}$$

We close this subsection by introducing the definitions of the relativistic inverse Reynolds numbers based on the convention of [93]

$$\mathcal{R}_{\Pi}^{-1} := \frac{\Pi}{p+e}, \quad \mathcal{R}_q^{-1} := \frac{\sqrt{q_\mu q^\mu}}{p+e}, \quad \mathcal{R}_\pi^{-1} := \frac{\sqrt{\pi_{\mu\nu}\pi^{\mu\nu}}}{p+e}\,. \tag{2.110}$$

From Eq. (2.110) it becomes clear that the Reynolds number measures the relative importance of inertial forces compared to viscous or dissipative forces. Furthermore, we can now make a precise definition of first-order $\mathcal{O}_1$ and second-order $\mathcal{O}_2$ terms:

$$\mathcal{O}_1 := \mathcal{O}\left(\mathcal{R}_i^{-1}\right) \quad \text{or} \quad \mathcal{O}(\mathrm{Kn})\,, \tag{2.111}$$

$$\mathcal{O}_2 := \mathcal{O}\left(\mathcal{R}_i^{-2}\right) \quad \text{or} \quad \mathcal{O}\left(\mathcal{R}_i^{-1}\mathrm{Kn}\right) \quad \text{or} \quad \mathcal{O}\left(\mathrm{Kn}^2\right). \tag{2.112}$$

First-order gradients of perfect-fluid variables, such as Θ or $\dot{e}/e$ are typically viewed as being of order $\mathcal{O}(\mathrm{Kn})$ because they involve gradients of macroscopic variables. This means that they are formally of order $1/L$ where L is the same macroscopic length scale used in the definition of the Knudsen number in Eq. (2.68). Thus, multiplying these terms by a microscopic length scale ℓ would make them formally be of first-order in Knudsen number.

For the remainder of this Thesis we will only need a truncated version of the evolution equation for the bulk-viscous pressure Π because we neglect heat currents and viscous shear stresses, i.e., we set $q^\mu = 0 = \pi^{\mu\nu}$. Thus, Equations (2.100) and (2.110) can be simplified to

$$\tau_\Pi \dot{\Pi} = \Pi_{\mathrm{NS}} - \Pi\,, \tag{2.113}$$

$$\mathcal{R}^{-1} := \mathcal{R}_\Pi^{-1} = \frac{\Pi}{e+p}\,. \tag{2.114}$$

Then, the conservation Eqs. (2.72) and (2.73) applied to the current in Eq. (2.96) and the total energy-momentum tensor for a pure bulk-viscous fluid, i.e., we apply $q^\mu = 0 = \pi^{\mu\nu}$ in Eq. (2.95), lead to the following new definitions of the state, flux and source vector, respectively:

$$\boldsymbol{U} = \sqrt{\gamma}\begin{pmatrix} D \\ S_j \\ E-D \\ D\Pi \end{pmatrix} = \sqrt{\gamma}\begin{pmatrix} \rho W \\ (e+p+\Pi)\,W^2 v_j \\ (e+p+\Pi)\,W^2 - p - \Pi - \rho W \\ \rho W \Pi \end{pmatrix}, \tag{2.115}$$

$$\boldsymbol{F}^i = \sqrt{\gamma}\begin{pmatrix} V^i D \\ \alpha S^i{}_j - \beta^i S_j \\ \alpha(S^i - v^i D) - \beta^i (E-D) \\ V^i D\Pi \end{pmatrix}, \tag{2.116}$$

$$\boldsymbol{S} = \sqrt{\gamma}\begin{pmatrix} 0 \\ \frac{1}{2}\alpha S^{ik}\partial_j \gamma_{ik} + S_i \partial_j \beta^i - E\partial_j \alpha \\ \alpha S^{ik} K_{ij} - S^j \partial_j \alpha \\ -\left(\alpha D/\tau_\Pi W\right)\left[\zeta\left(\vartheta + \Lambda - KW\right) + \Pi\right] \end{pmatrix}, \tag{2.117}$$

where we used the expressions

$$\Theta = \vartheta + \Lambda - KW\,, \tag{2.118}$$

$$\vartheta := D_i\left(W v^i\right) = \frac{\partial_i\left(\sqrt{\gamma} W v^i\right)}{\sqrt{\gamma}}\,, \tag{2.119}$$

$$\Lambda := \frac{1}{\alpha}\left(\partial_t - \mathscr{L}_\beta\right) W + W v_i \hat{a}^i\,, \tag{2.120}$$

to decompose the source terms of Eq. (2.113) such that the appearance of temporal and spatial derivatives becomes evident, see also [71] for a systematic derivation of the 3+1 split of the equations of GRDHD. Additionally, we remark that for the general case, where heat fluxes and viscous shear stresses are not set to zero, the more complex definitions for the conservative variables $\boldsymbol{C}$, see [71], require a more complex inversion procedure, see e.g., [297, 90, 286, 102, 105].

Finally, we define the square of the sound speed including modifications from bulk viscosity [36, 71, 62] as

$$c_s'^2 = \frac{\zeta}{\tau_\Pi}\frac{1}{e+p+\Pi} + \left(\frac{\partial p}{\partial e}\right)_\rho + \frac{1}{e+p+\Pi}\left(\frac{\partial p}{\partial \rho}\right)_e , \tag{2.121}$$

which becomes the standard expression for the perfect-fluid speed of sound in the inviscid limit $\lim_{\Pi,\zeta\to 0} c_s'^2 = {c_s}^2$, see Eq. (2.80).

2.4.3 Numerical methods for GRDHD

In this subsection we will introduce the numerical methods typically used for the solution of second-order MIS-type GRDHD. An example for such a theory modeling a pure bulk-viscous fluid is given in Eqs. (2.115)-(2.117). This set of equations serves as a good example because the methods necessary for the solution of Eqs. (2.115)-(2.117) can also be applied with minor non-conceptual modifications in order to solve more extended sets of second-order MIS-type GRDHD equations.

Most importantly, as can be seen from Eqs. (2.115)-(2.117) the newly included evolution equations for the dissipative currents have an advective term, which is represented by the definition of the corresponding flux component in Eq. (2.116), and a corresponding source term in Eq. (2.117). So far, this structure corresponds to the structure of the equations of perfect-fluid hydrodynamics presented in Section 2.3. However, a major difference appears when inspecting the source term of the evolution equation for the bulk-viscous pressure Π more closely. Namely, temporal and spatial derivatives of the primitive fluid variables, more specifically the fluid four-velocity u^μ, are present. As can be seen from the first three components of Eq. (2.117), the evolution equations stemming from the conservation of charge, energy and momentum have only derivatives of the metric in their source terms.

Usually, the occurance of time derivatives on the RHS of Eq. (2.74) can be avoided by writing the system of PDEs in the form

$$\boldsymbol{\mathcal{A}}^\mu \partial_\mu \boldsymbol{\Phi} = \boldsymbol{\mathcal{S}} , \tag{2.122}$$

where $\boldsymbol{\mathcal{A}}^\mu$, $\boldsymbol{\Phi}$ and $\boldsymbol{\mathcal{S}}$ are vectors and $\boldsymbol{\Phi}$ ($\boldsymbol{\mathcal{S}}$) represents a state (source) vector. For example, the system in Eqs. (2.115)-(2.117) can be written in such a form with $\boldsymbol{\mathcal{A}}^\mu$ being symmetric, $\boldsymbol{\mathcal{A}}^0$ being positive definite and $\boldsymbol{\Phi} = (\rho, e, u^i, \Pi)$ [36]. However, as discussed in Section 2.3 the system in Eq. (2.122) is not in a flux-conservative form and therefore not suitable to obtain discontinuous solutions in the perfect-fluid limit. Hence, many authors choose to solve the system in Eqs. (2.115)-(2.117) instead and discretize the time derivative in the source term using backward finite-differencing [103, 194, 193, 297, 275, 90, 286, 281, 102, 105].

In addition, the spatial derivatives in the source term of Eq. (2.117) constitute a so-called non-conservative product whose discretization is the subject of path-conservative numerical schemes [228, 107]. However, the most common approach in the modeling of the QGP and dissipative effects in neutron stars makes use of simple finite-difference operators similar to the discretization of the time deriative [103, 194, 193, 297, 275, 90, 286, 281, 102, 105]. We note that recently a fully flux-conservative method based on

stiff-relaxation has been developed which shows promising results in the modeling of shocks. However, its characteristic structure has not been investigated so far [197] which makes it unclear whether causality and stability are guaranteed.

The appearance of derivatives in the sources leads us to the more fundamental issue of how to model large gradients, and specifically shocks, in GRDHD. In principle, the inability of Eqs. (2.122) to model discontinuities does not constitute a conceptual problem because large gradients of hydrodynamic fields, i.e., large changes over small length scales compared to the system size, imply that the Knudsen number is large. Going back to the overview presented in Subsection 2.4.1 the theory of hydrodynamics can be understood as an effective theory in the long-wavelength, low-frequency limit of an underlying microscopic theory quantified by the two small parameters: Knudsen number and relativistic inverse Reynolds number. It follows that this underlying assumption is violated, if gradients become too large and especially if a discontinuity develops. This means that, strictly speaking, hydrodynamics is not applicable to describe the behaviour of matter when passing through a strong shock, and as a consequence the system in Eq. (2.122) or equally (2.115)-(2.117) should not be solved in these regions. On the other hand, in practice, it is not feasible to solve the full Boltzmann equation neither in the full domain nor in localized regions, which means that hydrodynamics is used to describe the solution at shock fronts.

Then, the question arises whether the equations of GRDHD, e.g., Eqs. (2.115)-(2.117), can develop discontinuities starting from smooth initial data such as the equations of perfect-fluid hydrodynamics do. Obviously, this is the case in the limit of vanishing viscosities, i.e., $\zeta \to 0, \eta \to 0, \kappa \to 0$, and as a consequence numerical schemes solving Eq. (2.122) will fail to provide convergent solutions in this limit. This means that a flux-conservative form, see Eq. (2.74), must be employed to capture the perfect-fluid limit of GRDHD correctly.

Furthermore, investigations of the equations of GRDHD with non-zero transport coefficients, i.e., $\zeta \neq 0, \eta \neq 0, \kappa \neq 0$, show that above a maximum upstream Mach number the solutions of the MIS theory become multiple-valued because the characteristic velocity is exceeded [215]. Effectively, this result shows that continuous shock solutions exist only for low upstream Mach numbers in the MIS theory. On top of that, a recent work shows that the system in Eqs. (2.115)-(2.117) can develop non-smooth or "unphysical" solutions in a finite time, see [98] for a precise definition of "unphysical", starting from smooth initial data [98]. Again, as a consequence of these two results numerical schemes solving Eqs. (2.122) will fail to provide convergent solutions for strong shocks which can develop naturally.

However, it is important to note that the construction of a weak solution in the sense discussed in Section 2.3 is usually not possible for the MIS theory [215, 128, 98] which constitutes a serious practical problem. Effectively, this means that strong shocks can form in GRDHD but, in contrast to the hydrodynamics of perfect fluids, it is unclear how the evolution of the dissipative fluid can be continued beyond shock formation. This also means that well-informed numerical schemes can't be constructed in order to *capture* these shocks.

For the sake of completeness, we will mention two ideas that could inspire the construction of numerical schemes which circumvent this problem. First, the same problem occurs in the modeling of Newtonian gas flow based on moment equations [305]. There, a regularization scheme is applied which effectively adds higher-order gradient terms that transform the nature of the PDEs from hyperbolic to parabolic [292, 305, 256]. The new parabolic nature of the PDEs implies that information can propagate at an infinite speed which means that the characteristic velocity cannot be exceeded. Hence, discontinuities cannot form and the system admits arbitrary strong continu-

ous shock solutions. In a relativistic context, as already discussed in Subsection 2.4.1, parabolic equations violate causality which implies thermodynamic instability [126]. Thus, this approach is unfavourable. The second approach takes also advantage of the insight that modifications of the charactersitic velocities could lead to a system which *avoids* the formation of discontinuities. More specifically, it was shown that for the case of the BDNK theory, see 2.4.1 for references, a suitable choice of free parameters exists which increases one of the characterstic speeds to the speed of light such that, again, all shocks become continuous [118, 224, 119].

Finally, we mention briefly that small relaxation times in the general system presented in Eqs. (2.100)-(2.102) lead to so-called *stiff* equations which require an implicit or mixed implicit-explicit (IMEX) time update [229]. These methods are commonly employed in resistive MHD [218, 97, 265, 85] and radiation hydrodynamics [314, 197, 253]. In the context of GRDHD, IMEX methods have been employed [105, 197, 63] but also the Strang splitting method [85] together with piecewise exact solutions [297] has been used.

2.5 General-relativistic ideal magnetohydrodynamics

In this section we will give a brief introduction to the equations of ideal general-relativistic magnetohydrodynamics (GRMHD) which describe fluids with an infinite conductivity and immersed in coevolving magnetic fields by following [26, 89, 111, 279, 240, 195]. We start by recalling the two Maxwell's equations

$$\nabla_\mu F^{\mu\nu} = -4\pi \mathcal{J}^\nu , \tag{2.123}$$

$$\nabla_\mu {}^*F^{\mu\nu} = 0 , \tag{2.124}$$

where $F^{\mu\nu}$ is the Faraday tensor and ${}^*F^{\mu\nu}$ denotes its dual. The quantity $\mathcal{J}^\mu = \rho_e n^\mu + J^\mu$ describes the EM current four-vector [26] where ρ_e and J^μ are the charge density and current. The Faraday tensor can be written in two equivalent forms

$$F^{\mu\nu} = \nabla^\mu \mathcal{A}^\nu - \nabla^\nu \mathcal{A}^\mu , \tag{2.125}$$

$$= n^\mu E^\nu - n^\nu \mathrm{E}^\mu + \epsilon^{\mu\nu\lambda\delta} B_\lambda n_\delta , \tag{2.126}$$

where $\mathcal{A}^\mu = \Phi n^\mu + A^\mu$ is the magnetic four-vector potential with A^μ being purely spatial and Φ the EM scalar potential measured in the Eulerian frame [111]. The fields E^μ and B^μ denote the electric and magnetic fields, respectively, as measured by the Eulerian observer given by n^μ and are purely spatial $n_\mu E^\mu = n_\mu B^\mu = 0$ [279]. The tensor $\epsilon^{\mu\nu\lambda\delta}$ is the fully-antisymmetric Livi-Civita tensor defined in Eq. (1.4). Equations (2.125) and (2.126) can be combined to yield

$$B^i = \frac{1}{\sqrt{\gamma}} \eta^{ijk} \partial_j A_k , \tag{2.127}$$

where η^{ijk} denotes the standard three-dimensional Levi-Civita symbol [26, 111]. Additionally and following [279], the dual Faraday tensor can be written as

$${}^*F^{\mu\nu} := \frac{1}{2} \epsilon^{\mu\nu\lambda\delta} F_{\lambda\delta} , \tag{2.128}$$

$$= -\left(n^\mu B^\nu - n^\nu B^\mu + \epsilon^{\mu\nu\lambda\delta} E_\lambda n_\delta \right) . \tag{2.129}$$

Analogously, we can also define the electric and magnetic fields in the fluid frame

$$e^\mu := F^{\mu\nu} u_\nu , \tag{2.130}$$

$$b^\mu := u_\mu {}^*F^{\mu\nu} , \tag{2.131}$$

respectively. In the ideal MHD approximation electric fields vanish in the fluid frame

$$e^{\mu} = 0\,, \tag{2.132}$$

which leads together with Eqs. (2.123) and (2.124) to an overdetermined system such that it is sufficient to consider only the homogeneous Maxwell's equations given by Eq. (2.124), e.g., the electric field in the Eulerian frame E^{μ} can be expressed through velocities and magnetic fields and does not need to be evolved [279]

$$E^{i} = -\frac{1}{\sqrt{\gamma}}\eta^{ijk}v_{j}B_{k}\,. \tag{2.133}$$

It is also useful to recall the relations transforming Eulerian magnetic fields to comoving magnetic fields and vice versa [279, 240]

$$b^{0} = \frac{W}{\alpha}v_{i}B^{i}\,, \tag{2.134}$$

$$b^{i} = \frac{1}{W}B^{i} + \frac{\alpha}{W}b^{0}u^{i}\,. \tag{2.135}$$

Furthermore, we can also rewrite the Faraday tensor and its dual in terms of e^{μ} and b^{μ} and subsequently set $e^{\mu} = 0$

$$F^{\mu\nu} = \epsilon^{\mu\nu\lambda\delta}b_{\lambda}u_{\delta}\,, \tag{2.136}$$

$${}^{*}F^{\mu\nu} = b^{\mu}u^{\nu} - b^{\nu}u^{\mu}\,. \tag{2.137}$$

At this point, equations (2.124) and (2.137) allow us derive an evolution equation for the EM energy density in the fluid frame in the ideal MHD approximation. In particular, it interesting to consider the sources and sinks of EM energy in order to understand the mechanisms by which energy can be transferred between the EM and the kinetic sector. An application to local Newtonian simulations of the magnetised Kelvin-Helmholtz instability (KHI) can be found in [213] while an application to the magnetised KHI in global simulations of BNS mergers can be found in [74]. The derivation is simple and can be carried out by calculating the projections $0 = u_{\nu}\nabla_{\mu}(b^{\mu}u^{\nu} - b^{\nu}u^{\mu})$ and $0 = h_{\lambda\nu}\nabla_{\mu}(b^{\mu}u^{\nu} - b^{\nu}u^{\mu})$. The final result reads

$$\nabla_{\mu}\left(e_{\rm mag}u^{\mu}\right) = \frac{1}{4\pi}b^{\mu}b^{\nu}\sigma_{\mu\nu} - \frac{1}{3}\Theta e_{\rm mag}\,, \tag{2.138}$$

where we have introduced the definition:

$$e_{\rm mag} := p_{\rm mag} := b^{2}/8\pi = b_{\mu}b^{\mu}/8\pi\,. \tag{2.139}$$

The quantity $e_{\rm mag}$ is the comoving EM energy density, $p_{\rm mag}$ is the comoving EM pressure and Θ as well as $\sigma_{\mu\nu}$ are defined in Appendix B. From Eq. (2.138) we see that local increases and decreases of EM energy density can only be due to two processes which are highly connected to the flow properties of the fluid. More specifically, only if shearing motion or expansion/compression is present in the fluid, the EM energy density can be affected and energy transfer is possible. For convenience we will introduce a separate definition for the RHS of Eq. (2.138):

$$s_{\rm mag} := \frac{1}{4\pi}b^{\mu}b^{\nu}\sigma_{\mu\nu} - \frac{1}{3}\Theta e_{\rm mag}\,. \tag{2.140}$$

The EM component of the energy-momentum tensor in the ideal MHD approximation reads

$$T^{\mu\nu}_{\rm em} := \frac{1}{4\pi}\left(F^{\mu\lambda}F^{\nu}{}_{\lambda} - \frac{1}{4}g^{\mu\nu}F_{\lambda\delta}F^{\lambda\delta}\right), \tag{2.141}$$

$$= e_{\rm mag}u^{\mu}u^{\nu} + p_{\rm mag}h^{\mu\nu} - \frac{1}{4\pi}b^{\mu}b^{\nu}. \tag{2.142}$$

The magnetic pressure can also be expressed in terms of the Eulerian magnetic field B^i

$$p_{\rm mag} = \frac{1}{8\pi}\left(B^2/W^2 + (v_iB^i)^2\right). \tag{2.143}$$

Next, we will rewrite the homogeneous Maxwell's equations (2.124) in order to obtain PDEs for the evolution of the magnetic fields. Following [26] and using Eqs. (2.125) and (2.126) together with Eq. (2.124) it is possible to derive the following equations:

$$\partial_i\left(\sqrt{\gamma}B^i\right) = 0, \tag{2.144}$$

$$\partial_t A_i = \sqrt{\gamma}\,\eta_{ijk}V^jB^k - \partial_i\left(\alpha\Phi - \beta^jA_j\right), \tag{2.145}$$

$$\partial_t\left(\sqrt{\gamma}B^i\right) = -\partial_j\left[\sqrt{\gamma}\left(V^jB^i - V^iB^j\right)\right]. \tag{2.146}$$

Note that Eqs. (2.145) and (2.146) do not depend on E^i as the ideal MHD approximation has already been applied in the derivation. Equation (2.144) expresses the divergence-free or "no-monopoles" constraint on the magnetic fields. The subsequent equations (2.145) and (2.146) are different versions of the magnetic induction equation expressed either using the vector potential or the magnetic field directly, respectively. If the evolution equation for the vector potential (2.145) is chosen, a suitable EM gauge condition needs to be supplemented which yields a constitutive relation for the scalar potential Φ. A suitable relation is provided by the "generalized Lorenz gauge condition" [110, 114]

$$\nabla_{\mu}\mathcal{A} = \xi n_{\mu}\mathcal{A}^{\mu}, \tag{2.147}$$

which prevents spurious magnetic fields from appearing on refinement boundaries. The constant parameter ξ has dimensions 1/Length and controls the damping time of EM gauge modes. This gauge condition yields an evolution equation for Φ:

$$\partial_t\left(\sqrt{\gamma}\Phi\right) = -\partial_j\left(\alpha\sqrt{\gamma}A^j - \sqrt{\gamma}\beta^j\Phi\right) - \xi\alpha\sqrt{\gamma}\Phi. \tag{2.148}$$

In this Thesis we will use Eqs. (2.145) and (2.148) supplemented with Eq. (2.127) in order to obtain the evolution of the magnetic fields. We will explain the reasons for our choice in the following subsection.

Finally, we need to consider that the system contains a single perfect fluid as well as EM fields which means that the total energy-momentum tensor takes the form

$$T^{\mu\nu} = T^{\mu\nu}_{\rm pf} + T^{\mu\nu}_{\rm em},$$

$$= (e + e_{\rm mag})u^{\mu}u^{\nu} + (p + p_{\rm mag})h^{\mu\nu} - \frac{1}{4\pi}b^{\mu}b^{\nu}. \tag{2.149}$$

Then, the conservation Eqs. (2.72) and (2.73) applied to the current in Eq. (2.70) and the total energy-momentum tensor for ideal magnetohydrodynamics in Eq. (2.149) lead to

the following new definitions of the state, flux and source vector, respectively:

$$\boldsymbol{U} = \begin{pmatrix} \sqrt{\gamma} D \\ \sqrt{\gamma} S_j \\ \sqrt{\gamma} \tau \\ A_j \\ \sqrt{\gamma} \Phi \end{pmatrix} = \begin{pmatrix} \sqrt{\gamma} \rho W \\ \sqrt{\gamma} \left[(e+p) W^2 v_j + B^2 v_j - (v_i B^i) B_j \right] \\ \sqrt{\gamma} \left\{ (e+p) W^2 - p + \frac{1}{2} \left[B^2 (1+v^2) - (v_i B^i)^2 \right] - \rho W \right\} \\ A_j \\ \sqrt{\gamma} \Phi \end{pmatrix}, \tag{2.150}$$

$$\boldsymbol{F}^i = \begin{pmatrix} \sqrt{\gamma} V^i D \\ \sqrt{\gamma} \left(\alpha S^i{}_j - \beta^i S_j \right) \\ \sqrt{\gamma} \left[\alpha (S^i - v^i D) - \beta^i (E - D) \right] \\ 0 \\ \sqrt{\gamma} \left(\alpha A^i - \Phi \beta^i \right) \end{pmatrix}, \tag{2.151}$$

$$\boldsymbol{S} = \begin{pmatrix} 0 \\ \sqrt{\gamma} \left(\frac{1}{2} \alpha S^{ik} \partial_j \gamma_{ik} + S_i \partial_j \beta^i - E \partial_j \alpha \right) \\ \sqrt{\gamma} \left(\alpha S^{ik} K_{ij} - S^j \partial_j \alpha \right) \\ \sqrt{\gamma} \eta_{jik} V^i B^k - \partial_j \left(\alpha \Phi - A_i \beta^i \right) \\ -\sqrt{\gamma} \xi \alpha \Phi \end{pmatrix}. \tag{2.152}$$

Note that we have included the evolution Eqs. (2.145) and (2.148) in the definitions (2.150) - (2.152) in order to present the complete set equations employed in this Thesis. However, we remark that due to the staggering of the EM fields, see Subsection 2.5.1, their discretization procedure differs from the discretization of the fluid components of the state vector, i.e., $\boldsymbol{C}$, see Eq. (2.78) and [111] for further details. Additionally, the more complex definitions for the conservative variables $\boldsymbol{C}$, which follow from Eq. (2.150), require a significantly more complex inversion procedure, see e.g., [219, 290, 195, 164].

2.5.1 Numerical methods for GRMHD

We start by discussing the advantages and disadvantages of using Eq. (2.145) or (2.146) for the solution of Maxwell's equations, thereby giving a brief overview of the numerical methods commonly employed in GRMHD. The choice between Eqs. (2.145) and (2.146) is mainly made by judging which set of equations is best suited to fulfill the constraint presented in Eq. (2.144). Starting from the induction equation for the magnetic fields (2.146), a naive free evolution would violate the divergence-free constraint. A customary approach from Newtonian MHD [86] adopts a constraint damping technique similar to the damped-Z4 formulation for Einstein's equations introduced in Subsection 2.1.4, see also [240] for implementation details. This leads to propagating and damped constraint violations. However, the solenoidal condition can also be

maintained to machine precision by making use of constrained transport (CT) methods. If the initial condition for the magnetic fields is divergence-free, then CT methods employ specific discretization techniques of Eq. (2.146) in order preserve Eq. (2.144). In general, this discretization technique amounts to the definition of so-called staggered magnetic fields, i.e., magnetic fields defined at cell interfaces. Examples for CT methods are the flux-interpolated CT method presented in [306] and the upwind CT method developed in [180] and [89]. However, both of these methods fail to work if adaptive mesh refinement (AMR) is used without special care because the interpolation methods which translate data between different refinement levels, i.e., prolongation and restriction operators, need to be constraint-preserving as well [214]. Constraint-preserving prolongation and restriction operators can be derived for staggered magnetic fields and have been applied successfully to simulations of accretion disks [214]. On the other hand, the use of the vector potential (2.145) allows a simpler approach to maintaining the solenoidal constraint even with AMR. By using Eq. (2.127) together with finite-difference operators which are defined such that the divergence of a curl is zero to machine precision, Eq. (2.144) is fulfilled automatically even when using AMR without constraint-preserving interpolation methods [88, 111]. Unfortunately, this method is subject to the generation of spurious magnetic fields. However, suitable gauge conditions such as the one shown in Eq. (2.148) are able to minimize this effect.

Simulations in this Thesis which involve magnetic fields, i.e., $B^i \neq 0$, solve Eq. (2.145). Therefore, we will now focus on the discretization methods for Eq. (2.145) and (2.148). Similar to Eq. (2.81), Equation (2.145) can be written in the following semi-discrete form [88, 89]

$$\frac{\mathrm{d}}{\mathrm{d}t} A_i = -\mathcal{E}_i \,, \tag{2.153}$$

where we drop the gauge terms for simplicity and introduce the magnetic flux

$$\mathcal{E}_i := -\sqrt{\gamma}\,\eta_{ijk} V^j B^k \,, \tag{2.154}$$

which is present in the induction Eq. (2.145). As opposed to Eq. (2.81), we don't need to calculate derivatives at this level such that it is sufficient to provide high-order approximations of V^j and $\sqrt{\gamma}B^k$ in Eq. (2.154). However, as the magnetic field is calculated from Eq. (2.127), we need to indroduce a numerical vector potential $\hat{A}_i$ in order to obtain high-order approximations of $\sqrt{\gamma}B^k$ which gives rise to the following formula

$$\sqrt{\gamma} B^i = \eta^{ijk} \mathcal{D}_j \hat{A}_k \,, \tag{2.155}$$

where $\mathcal{D}_j$ is the same numerical operator already introduced in Eq. (2.81) but in the direction $i \in \{x, y, z\}$. At this point it is important to understand the locations at which the quantities appearing in Eq. (2.155) are defined. The staggering of magnetic fields is based on Stokes' theorem which converts the surface integral of the curl of a vector field into a line integral of the same vector field. Naturally, this leads to magnetic fields defined at cell surfaces and vector potentials defined at cell edges [88]. A summary of the storage locations of various quantities involved in the solution of Eqs. (2.150) - (2.152) can be found in Table 2.1 taken from [111]. The staggering procedure implies the following form of the x-component of Eq. (2.155)

$$\left[\sqrt{\gamma} B^x\right]_{i+1/2,j,k} = \frac{\left[\hat{A}_z\right]_{i+1/2,j+1/2,k} - \left[\hat{A}_z\right]_{i+1/2,j-1/2,k}}{h_y} - \frac{\left[\hat{A}_y\right]_{i+1/2,j,k+1/2} - \left[\hat{A}_y\right]_{i+1/2,j,k-1/2}}{h_z} \,, \tag{2.156}$$

Variable(s)	storage location
Metric terms, $\boldsymbol{C}$, $\boldsymbol{P}$	(i,j,k)
B^x	$(i+\frac{1}{2},j,k)$
B^y	$(i,j+\frac{1}{2},k)$
B^z	$(i,j,k+\frac{1}{2})$
A_x	$(i,j+\frac{1}{2},k+\frac{1}{2})$
A_y	$(i+\frac{1}{2},j,k+\frac{1}{2})$
A_z	$(i+\frac{1}{2},j+\frac{1}{2},k)$
Φ	$(i+\frac{1}{2},j+\frac{1}{2},k+\frac{1}{2})$

Table 2.1: Storage locations of fluid and magnetic variables
Storage locations of various variables employed in the solution of the system in Eqs. (2.150) - (2.152). The conservative variables $\boldsymbol{C}$ are defined in Eq. (2.78) while the primitive variables $\boldsymbol{P}$ are defined in Eq. (2.79).This table is reused from [111].

where h_x, h_y and h_z denote the cell sizes in the x, y, and z direction, respectively, and the $[\cdot]_{a,b,c}$ symbol denotes the evaluation of the corresponding quantity at the grid location given by the triple index (a,b,c).

Now, following the ideas from Subsection 2.3.1 we can introduce helper functions for the numerical vector potential components and require that their *line averages* correspond to the point values of the original vector potential evaluated at cell edges, see Table 2.1. Ultimately, we arrive at expressions similar to Eq. (2.87) where the fourth-order approximations of the numerical vector potential are given by [88, 195]

$$\hat{A}_x = A_x - \frac{1}{24}\Delta_y^{(2)}(A_x) - \frac{1}{24}\Delta_z^{(2)}(A_x) + \mathcal{O}\left(h^4\right), \tag{2.157}$$

$$\hat{A}_y = A_y - \frac{1}{24}\Delta_z^{(2)}\left(A_y\right) - \frac{1}{24}\Delta_x^{(2)}\left(A_y\right) + \mathcal{O}\left(h^4\right), \tag{2.158}$$

$$\hat{A}_z = A_z - \frac{1}{24}\Delta_x^{(2)}(A_z) - \frac{1}{24}\Delta_y^{(2)}(A_z) + \mathcal{O}\left(h^4\right), \tag{2.159}$$

where the operation $\Delta_i^{(2)}$ applies the operation in Eq. (2.88) in the direction $i \in \{x,y,z\}$. The high-order approximations of the magentic field in Eq. (2.155) satisfy the discrete version of Eq. (2.144), i.e., the discrete version of the solenoidal constraint, at cell centers to machine precision [88].

Next, an appropriate upwind flux is needed which takes into account the staggering of the magnetic fields. In particular, the magnetic fluxes $\mathcal{E}_i$ are computed at cell edges which constitute intersections of two surfaces. Hence, in contrast to a discontinuity between two states, see Subsection 2.3.1, which can be thought of as the zero-dimensional intersection between two lines, now a one-dimensional intersection between two surfaces is present. This gives rise to four states determining the solution of the Riemann problem [88, 180]. Then, the HLLE solver introduced in Subsection 2.3.1 can be generalized to yield [111]

$$\begin{aligned}\mathcal{E}_z^{\text{HLLE}} =& \frac{\lambda_x^R\lambda_y^R\mathcal{E}_z^{LL} + \lambda_x^R\lambda_y^L\mathcal{E}_z^{LR} + \lambda_x^L\lambda_y^R\mathcal{E}_z^{RL} + \lambda_x^L\lambda_y^L\mathcal{E}_z^{RR}}{(\lambda_x^R+\lambda_x^L)(\lambda_y^R+\lambda_y^L)} \\ &+ \frac{\lambda_x^R\lambda_x^L}{\lambda_x^R+\lambda_x^L}\left(\sqrt{\gamma}_R B_R^y - \sqrt{\gamma}_L B_L^y\right) - \frac{\lambda_y^R\lambda_y^L}{\lambda_y^R+\lambda_y^L}\left(\sqrt{\gamma}_R B_R^x - \sqrt{\gamma}_L B_L^x\right)\end{aligned} \tag{2.160}$$

where we introduced the quantities $\mathcal{E}_z^{ab}$ with $a,b \in \{L,R\}$ denoting that the reconstruction is performed from the a-side in x-direction and from the b-side in y-direction. The symbols $\sqrt{\gamma}_{L(R)}B_{L(R)}^y$ are reconstructed from the left (right) state in the x-direction

while the symbols $\sqrt{\gamma}_{L(R)} B^x_{L(R)}$ are reconstructed from the left (right) state in the y-direction. The characteristic speeds are given by

$$\lambda_x^L = \min\left(0, \lambda_x^-(U_{LL}), \lambda_x^-(U_{LR}), \lambda_x^-(U_{RL}), \lambda_x^-(U_{RR})\right), \tag{2.161}$$

$$\lambda_x^R = \max\left(0, \lambda_x^+(U_{LL}), \lambda_x^+(U_{LR}), \lambda_x^+(U_{RL}), \lambda_x^+(U_{RR})\right), \tag{2.162}$$

where the symbols U_{ab} with $a, b \in \{L, R\}$ denote that the state is reconstructed from the a-side in x-direction and from the b-side in y-direction. We also introduce the lowest (highest) characteristic speed in the x-direction by λ_x^- (λ_x^+). The formulas for $\mathcal{E}_x^{\mathrm{HLLE}}$ and $\mathcal{E}_y^{\mathrm{HLLE}}$ can be obtained by suitable permutations. Finally, the reconstruction to cell edges, i.e., the interpolation procedure to obtain the set of states $\{U_{LL}, U_{LR}, U_{RL}, U_{RR}\}$ is performed using the same WENO-Z method already mentioned in Subsection 2.3.1.

The code we employ in this Thesis, namely FIL, makes use of the methods described in this subsection together with the methods described in Subsection 2.3.1 to solve the system presented in Eqs. (2.150)-(2.152). As already mentioned, this is the so-called ECHO scheme which takes the following brief schematic form for ideal GRMHD [89, 195]:

DER-B Compute an high-order approximation of the staggered magnetic fields using Eq. (2.155) together with Eqs. (2.157)-(2.159).

C2P Interpolate staggered magentic fields to cell centers. Given the set of cell-centered conservative variables $\boldsymbol{C}$ at time t compute the corresponding primitive variables $\boldsymbol{P}$ at cell centers.

REC-F Reconstruct the primitive variables at the left and right cell interfaces using the WENO-Z method. These are two non-oscillatory interpolations from cell-centered primitives $\boldsymbol{P}$ to primitives at cell interfaces $\boldsymbol{P}_{L/R}$.

HLLE-F Compute the HLLE flux F^{HLLE} in Eq. (2.93) from the left and right primitive variables defined at cell interfaces $\boldsymbol{P}_{L/R}$.

DER-F Compute the numerical flux $\hat{F}$ used in Eq. (2.81) by using the fourth-order formula in Eq. (2.87) and replacing the original interface flux with the corresponding HLLE flux F^{HLLE}.

REC-B Reconstruct magnetic fields and primitive variables from cell interfaces to cell edges using the WENO-Z method. These are four non-oscillatory interpolations.

HLLE-B Compute the HLLE magnetic flux $\mathcal{E}^{\mathrm{HLLE}}$ in Eq. (2.160).

RK3 Evolve Eq. (2.81) and Eq. (2.153) to the time $t + \Delta t$ using the third-order Runge-Kutta method mentioned previously.

Chapter 3

Viscous black-hole accretion

The set of GRDHD equations presented in Eqs. (2.100) - (2.102) adds arguably a new layer of complexity in the possible behaviour of the fluid under investigation. On top of that, this set of equations is not commonly investigated in a general-relativistic setup making its application to neutron star physics a challenging endeavour. Thus, before moving on to dynamical spacetimes with neutron stars we start by developing an intuition for second-order GRDHD in a general-relativistic setup by solving the problem of spherically symmetric accretion onto BHs for a viscous fluid described by Eq. (2.113). Additionally, this setup can be used as a test scenario by numerical codes simulating non-perfect fluids on curved backgrounds. We also evaluate this possibility by testing the GRDHD implementation of the code BHAC [71] with this solution.

Although viscous BH accretion solutions are not extensively explored, the solutions for the case of perfect fluids are well known. In this case the spherically symmetric accretion onto nonrotaing BHs is commonly modeled using the famous "Michel solution" [190] and "Bondi-Hoyle solution" [51], but see [212] as well. Both of these solutions are commonly employed as testbeds for general-relativistic hydrodynamics (GRHD) and GRMHD codes [144, 240, 314]. The effects of shear viscosity which arise from magneto-turbulence have been considered for the first time by [307]. However, in this case a prescription in terms of general-relativistic NS equations was used. To the best of our knowledge, the problem of stationary, spherically symmetric accretion of bulk-viscous fluids onto nonrotating BHs using the second-order equations of GRDHD has not been solved before.

In this investigation we first solve the corresponding system of ODEs which yields a solution that we use as initial data for an evolution in our extended version of the GRMHD code BHAC, see [71] for details on the implementation.

We use an EOS which models a combination of ionised non-relativistic hydrogen and photons [261]

$$p = p_{\mathrm{M}}(1+\alpha), \tag{3.1}$$

where p_{M} denotes the pressure of the matter component, which is modeled as an ideal gas, while the contribution from the photons is kept constant using the parameter α. We can manipulate Eq. (3.1) in order to find that the EOS of the total mixture becomes similar to the ideal gas EOS where the effective adiabatic index γ_e can be obtained from:

$$p = (\gamma_e - 1)(e - \rho), \tag{3.2}$$

with $\gamma_e = 1 + 2(1+\alpha)/[3(1+2\alpha)]$. We remark that e is the total energy density of the fluid, while ρ is the rest-mass density of the matter component made up of hydrogen

ions. The temperature can be calculated from the matter component of the ideal fluid EOS, i.e., $p_{\mathrm{M}} = 2(k_{\mathrm{B}}/m_{\mathrm{p}})\rho T$, which yields:

$$T = \frac{1}{2(1+\alpha)} \frac{m_{\mathrm{p}}}{k_{\mathrm{B}}} \frac{p}{\rho}, \tag{3.3}$$

where m_{p} denotes the proton mass and k_{B} the Boltzmann constant. We remark that due to charge neutrality the presence of electrons needs to be considered such that a factor 2 appears in the denominator. Furthermore, we follow [315] as well as [273] and employ the radiative bulk viscosity of our two-component fluid

$$\zeta = 4\zeta_0 \sigma_{\mathrm{SB}} T^4 \tau_{\mathrm{mfp}} \left(\frac{4}{3} - \gamma_e\right)^2, \tag{3.4}$$

where σ_{SB} is the Stefan-Boltzmann constant and $\tau_{\mathrm{mfp}} := m_{\mathrm{p}} \rho^{-1} \sigma_{\mathrm{T}}^{-1}$ the mean-free path for radiation in the fluid, with σ_{T} being the Thomson scattering cross-section. We use the dimensionless constant ζ_0 in order to explore the impact of low and high bulk viscosities. The relaxation time τ_{Π} is chosen to be set by the formula:

$$\tau_{\Pi} = \tau_0 \frac{M}{|\dot{M}|} \left(\frac{r}{2M}\right)^3, \tag{3.5}$$

where r denotes the circumference radius in Schwarzschild coordinates, M the mass of the BH, $\dot{M}$ the accretion rate, and τ_0 is a dimensionless parameter to investigate the impact of short and long relaxation times. We remark that in Eq. (3.5) the relaxation time is proportional to the radius to the power of three. In order to prevent the rapid growth of non-equilibrium effects near the sonic point, which can yield unphysical solutions, we find that the relaxation time needs to increase as a function of radius to a sufficiently high power.

3.1 GRDHD in spherical symmetry

In this section, we introduce the equations of GRDHD in spherical symmetry in the presence of a Schwarzschild BH. The equations of GRDHD are given by Eqs. (2.72) and (2.73) together with the definitions in Eqs. (2.95) and (2.96) and $q^\mu = 0 = \pi^{\mu\nu}$. Then, the system is closed by Eq. (2.113) and an EOS. Moreover, we demand the solution to be spherically symmetric, i.e., all variables are restricted to depend only on time, t, as well as the circumference radius, r, and the fluid four-velocity is given by $u^\mu = (u^t, u, 0, 0)^T$. Furthermore, we want to obtain a stationary solution such that the t-dependence is removed as well and we end up with a coupled, nonlinear system of ODEs in the radial Schwarzschild coordinate r:

$$\frac{d\rho}{dr} = -\frac{\rho}{r} \frac{M/(\mathcal{E}^2 r) - \Pi r/\left[(\rho h + \Pi)\tau_{\Pi} u\right] - 2u^2/\mathcal{E}^2}{c_s'^2 - u^2/\mathcal{E}^2}, \tag{3.6}$$

$$\frac{du}{dr} = \frac{u}{r} \frac{M/(\mathcal{E}^2 r) - \Pi r/\left[(\rho h + \Pi)\tau_{\Pi} u\right] - 2c_s'^2}{c_s'^2 - u^2/\mathcal{E}^2}, \tag{3.7}$$

$$\frac{d\Pi}{dr} = -\frac{\Pi\left(c_s'^2 - u^2/\mathcal{E}^2\right)/(u\tau_{\Pi}) + \zeta\left[M/(\mathcal{E}^2 r) - \Pi r/\left[(\rho h + \Pi)\tau_{\Pi} u\right] - 2u^2/\mathcal{E}^2\right]/(\tau_{\Pi} r)}{c_s'^2 - u^2/\mathcal{E}^2}, \tag{3.8}$$

$$\frac{dh}{dr} = -\frac{\rho h + \Pi}{\rho r} \frac{\left[c_s'^2 - (\zeta/\tau_{\Pi} - \Pi)/(\rho h + \Pi)\right]\left[M/(\mathcal{E}^2 r) - \Pi r/\left[(\rho h + \Pi)\tau_{\Pi} u\right] - 2u^2/(\mathcal{E}^2)\right]}{c_s'^2 - u^2/\mathcal{E}^2}, \tag{3.9}$$

Model	ζ_0	$\tau_0\,[10^{-12}]$
low-ζ	160	1.0
medium-ζ	16,000	1.0
high-ζ	104,000	1.0
low-τ_{Π}	16,000	0.06
high-τ_{Π}	16,000	50

Table 3.1: Parameters for viscous black-hole accretion
This table summarizes the parameters ζ_0 and τ_0 for the various models employed in this study. This table has been reused from [71].

where $\mathcal{E} := u_t = -\sqrt{1-2M/r+u^2}$ and $h := (e+p)/\rho$ denotes the specific enthalpy. The system has two conserved quantities, namely, the mass-accretion rate $\dot{M}$ and the "viscous" Bernoulli constant $\mathcal{B}$

$$\dot{M} := 4\pi\rho u r^2, \tag{3.10}$$
$$\mathcal{B} := (\rho h + \Pi)\mathcal{E}/\rho. \tag{3.11}$$

We remark that in the inviscid limit we obtain the behaviour $\lim_{\Pi\to 0}\mathcal{B} = \mathcal{B}_{\rm pf} := h\mathcal{E} = hu_t$, where $\mathcal{B}_{\rm pf}$ denotes the relativistic inviscid Bernoulli constant.

By using the defintions of the constants $\dot{M}$ and $\mathcal{B}$, the quantities ρ and Π can be eliminated and expressed in terms of u, h and r alone

$$\rho = \dot{M}/(4\pi u r^2), \tag{3.12}$$
$$\Pi = \rho\mathcal{B}/\mathcal{E} - \dot{M}h/(4\pi u r^2), \tag{3.13}$$

so that the viscous speed of sound becomes

$$c_s'^2 = (\gamma_e - 1)\frac{\mathcal{B}-\mathcal{E}}{\mathcal{B}} + \frac{\zeta}{\tau_{\Pi}}\frac{4\pi\mathcal{E}ur^2}{\mathcal{B}\dot{M}}, \tag{3.14}$$

and Eqs. (3.7) and (3.9) simplify to

$$\frac{du}{dr} = \frac{u}{r}\,\frac{M/(\mathcal{E}^2 r) - (\mathcal{B}-\mathcal{E}h)r/\left(\mathcal{B}\tau_{\Pi}u\right) - 2c_s'^2}{c_s'^2 - u^2/\mathcal{E}^2}, \tag{3.15}$$

$$\frac{dh}{dr} = -\frac{1}{r}\,\frac{[(\gamma_e-1)(\mathcal{B}-\mathcal{E})/\mathcal{E} + (\mathcal{B}-h\mathcal{E})/\mathcal{E}]\left[M/(\mathcal{E}^2 r) - (\mathcal{B}-\mathcal{E}h)r/\left(\mathcal{B}\tau_{\Pi}u\right) - 2u^2/\mathcal{E}^2\right]}{c_s'^2 - u^2/\mathcal{E}^2}. \tag{3.16}$$

Equations (3.15)–(3.16) cannot be solved analytically. We discuss their solution in detail in Appendix A.

3.2 Investigated models

We employ models where the sonic point is located at $r_s = 200M$, the BH mass equals $M = 3M_{\odot}$, and the ratio between matter and radiation is set by $\alpha = 1$, which then results in $\gamma_e = 1.4\overline{4}$. In addition, the conserved quantities assume values which correspond to their inviscid values computed at $r_s = 200M$, i.e., $\dot{M} = -0.01582$ and $\mathcal{B} = -1.00192$. We remark that in the perfect-fluid case we can make use of a polytropic form of the EOS,

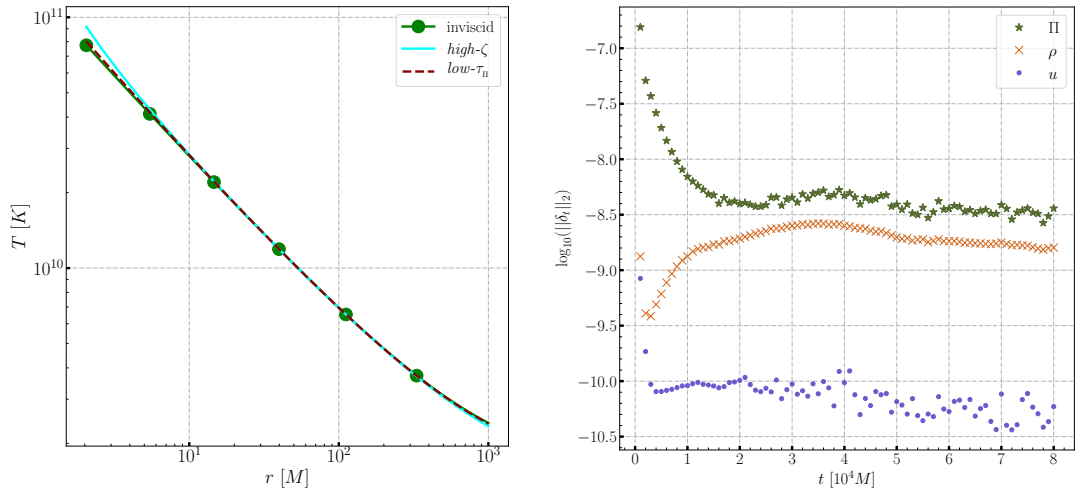

Figure 3.1: Temperature profile and L_2-norm of the relative time variation in viscous black-hole accretion
Left: This panel shows profiles of the temperature as a function of the circumference radius in units of M. Filled circles show the solution for $\zeta_0 = 0$, the solid line denotes the solution for the *high-*ζ model and the dashed line denotes the solution for the *low-*τ model. *Right*: This panel shows the L_2-norm of the relative time variation δ_t as a function of time for the following quantities: The rest-mass density ρ (crosses), the bulk-viscous pressure Π (stars) and the fluid four-velocity u (filled circles). All data points are shown for the *medium-*ζ model. This figure has been reused from [71].

i.e., $p = k\rho$, because the accretion process for an inviscid fluid is isentropic. Then, the polytropic constant k of the inviscid fluid is given by $k = 2(1+\alpha)T_\infty \rho_\infty^{1-\gamma_e}$. For our choice of r_s the asymptotic values for density and temperature are $\rho_\infty = 2\times10^{-9}\,\mathrm{g\ cm^{-3}}$ and $T_\infty = 1.5\times10^5\,\mathrm{K}$[1], respectively. We calculate five models which differ by their values for ζ_0 and τ_0. The parameters are presented in Table 3.1. The parameters are chosen such that we can investigate the impact of high and low bulk viscosities as well as relaxation times while not violating causality, i.e., $c_s' < 1$ holds everywhere in the domain.

3.3 Impact of bulk viscosity on black-hole accretion

The left panel of Fig. 3.1 shows the inviscid solution for the temperature profile together with the solutions from the models *high-*ζ and *low-*τ at time $t = 10{,}000\,M$. In the right panel of Fig. 3.1 we show the logarithm of the L_2-norm of the relative time variation δ_t for the rest-mass density ρ, the primitive fluid four-velocity u and the bulk-viscous pressure Π as a function of time for the *medium-*ζ model. For each quantity ϕ, the relative time variation is defined as $\delta_t\phi(t) := 1 - \phi(t-10\,M)/\phi(t)$.

From the right panel of Fig. 3.1 we observe that larger variations in time are present at the beginning of the simulation. However, these variations decay on a timescale of $\sim 10^4\,M$ by approximately one order of magnitude such that an approximately stationary state is reached after $\sim 10^4\,M$. The remaining small values of the time variation are attributed to small-scale oscillations which are generated by perturbations from the outer boundary of the numerical domain. Furthermore, we perform a (global) self-convergence test which recovers the formal convergence order of the second-order finite-volume code BHAC, i.e., ≈ 2 [240]. Additionally, local self-convergence tests show that for small radii, i.e., close to the BH event horizon, the convergence order is very close to two while for large radii we observe oscillations around two.

[1] The units employed in the code are such that $m_\mathrm{p}/k_\mathrm{B} = 1$ and $k = 1$.

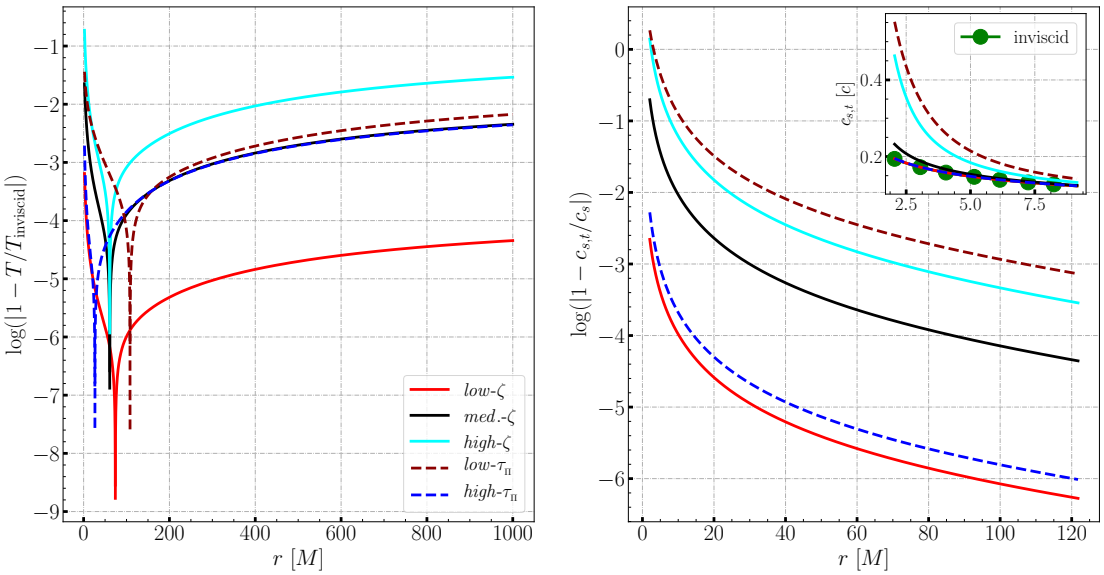

Figure 3.2: Relative differences in temperature and viscous sound speed in viscous black-hole accretion
Left: This panel shows the relative differences in temperature between the viscous models and the inviscid model. *Right*: This panel shows the relative differences in the viscous speed of sound between the viscous models and the inviscid model. The inset shows the actual value of the viscous speed of sound close to the event horizon. This figure has been reused from [71].

The left panel of Fig. 3.2 presents the radial profiles of the relative difference between the temperature for the various viscous models and the inviscid solution. By looking at the solid lines which denote the *low-*, *medium-*, and *high-*ζ models, we find that the viscous fluid is hotter near the BH event horizon and colder at large radii close to the end of the simulation domain. The highest temperature difference observed can be found in the *high-*ζ model where the temperature at the horizon can be up to $\sim 18\%$ larger than in the inviscid model. We observe similar behaviour for the dashed lines, which refer to the *low-* and *high-*τ_Π models.

In the right panel of Fig. 3.2 we show the corresponding relative difference in terms of the viscous sound speed close to the BH event horizon. We observe that for the *low-*τ_Π model the difference can be as large as a factor of ~ 3 while for the *high-*ζ model we observe values up to ~ 2.3. This means the models reach viscous sound speeds as high as 0.5 and 0.4, respectively (see inset).

Overall, our simulations confirm that the inclusion of large viscosities leads to more dissipative heating close to the BH and, therefore, to higher temperatures. Also, as expected, larger viscosities and lower relaxation times lead to larger deviations from the inviscid solution which manifest as larger deviations in temperature and viscous speed of sound.

Next, we explore the behaviour of the bulk-viscous pressure in our simulations which is a measure of out-of-equilibrium contributions according to Eq. (2.114). Figure 3.3 shows radial profiles of the inverse Reynolds number $\mathcal{R}^{-1} = \Pi/(\rho h)$ (left panel, solid and dashed lines) and of the bulk-viscous pressure normalized to its corresponding NS value $\Pi/\Pi_{\rm NS}$ (right panel, solid and dashed lines). We observe that for large radii the quantity $\Pi/\rho h$ has small values which are on the order of $\sim 10^{-4}$ to $\sim 10^{-7}$. When moving further inside its magnitude decreases even further until a turning point is reached at around $\sim 100\,M$. Then, the inverse Reynolds number starts to increase sharply until it reaches the BH event horizon. This behaviour is similar for all investigated models. However, quantitative differences arise in the magnitude of the inverse Reynolds

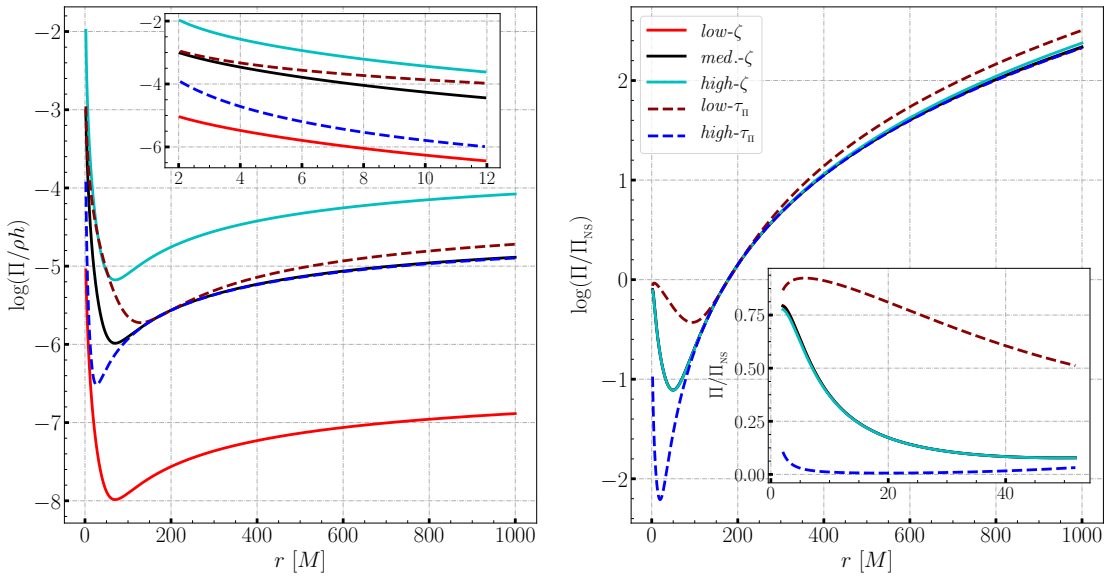

Figure 3.3: Inverse relativistic Reynolds number and bulk-viscous pressure over Navier-Stokes value in viscous black-hole accretion
Left: Shown are the profiles of the inverse Reynolds number, i.e., the ratio between the bulk-viscous pressure and the enthalpy density, as a function of circumference radius. The inset presents a zoom-in to the event horizon. *Right*: Shown are the profiles of the ratio between the bulk-viscous pressure and its NS value as a function of the circumference radius. This figure has been reused from [71].

number and the location of the turning point. More specifically, we observe that larger bulk viscosities ζ lead in general to larger values of the inverse Reynolds number while smaller relaxation times τ_Π lead in general to a turning point which is located at a larger radius. It is also interesting to note that smaller relaxation times lead to larger inverse Reynolds numbers close to the BH event horizon than larger relaxation times. Our observations confirm the expectation that the coefficient of the bulk viscosity controls the magnitude of out-of-equilibrium contributions while the relaxation time controls the timescale on which the bulk-viscous pressure evolves. This interpretation is suported by the right panel of Fig. 3.3 which confirms that small relaxation times yield bulk-viscous pressures which are closer to their NS values. Hence, the relaxation time controls the timescale on which the bulk-viscous pressure converges towards its NS value, e.g., for the models *low*-ζ, *medium*-ζ, and *high*-ζ, the bulk-viscosity pressure reaches nearly $\sim 80\%$ of the NS value close to the BH horizon, while the corresponding value for the *high*-τ_Π model is considerably smaller and of the order of $\sim 10\%$. Instead, the *low*-τ_Π model is able to reach a maximum of $\sim 92\%$ but not exactly at the event horizon. This feature is absent in the solutions of the ODEs such that we attribute it to cancellation errors in BHAC.

Finally, we note that the behaviour of our solutions close to the event horizon is reminiscent of the late-time behaviour of longitudinally expanding fluids, such as the Bjorken flow [47, 90, 156, 155]. In both cases, it can be observed that the fluid tends to converge towards its NS value. However, in the accretion solutions presented here the fluid is driven out of equilibrium close to the BH horizon while in the late-time behaviour of the Bjorken flow the fluid thermalizes. Nevertheless, if the velocity of the solution is reversed, we obtain outflowing solutions [144] which are similar to the Bjorken flow.

3.4 Summary and outlook

In this chapter we have investigated for the first time the problem of stationary, spherically symmetric accretion of bulk-viscous fluids onto nonrotating BHs using a second-order GRDHD formalism. First, we solve this problem by integrating the non-trivial set of ODEs presented in Section 3.1. Then, this solution is used as our initial data for a simulation of this problem using our extension of the GRMHD code BHAC [71].

By varying the bulk viscosity coefficient and the relaxation time we are able to observe differences of up to $\lesssim 19\%$ for the temperature and $\sim 200\%$ for the sound speed between the viscous and the inviscid case. Furthermore, we find that the bulk-viscous pressure can show variations of approximately three orders of magnitude near the event horizon. We attribute this behaviour to the strong compression that the fluid is subject to when falling onto the BH close to the event horizon. This leads to an increase in inverse Reynolds number which means that the fluid is driven out of thermodynamic equilibrium. Additionally, we have been able to verify that the role of the relaxation time is to set the timescale on which the bulk-viscous pressure assumes its NS value.

By performing tests of the stationarity of the problem together with an assessment of self-convergence we are able to suggest this problem as an useful testbed for GRDHD codes which aim at the inclusion of dissipative effects in BNS mergers. However, we remark that one caveat remains. Although the BHAC simulations reach a quasi-stationary state, the simulations do not converge to the reference solutions with increasing grid resolution because of errors which stem from the finite boundaries of the domain. We plan to investigate this issue in a future work.

Finally, this work yields the possibilty of investigating the equations of GRDHD in a simple but non-trivial general-relativistic setup. Further ideas which arise from our work include the investigation of the behaviour of the solution at large distances from the BH. Given that the growth of out-of-equilibrium contributions is suppressed in our approach by using the $\tau_{\Pi} \propto r^3$ dependence of the relaxation time, it would be interesting to understand the origin of this problem in more detail as well as whether it can be cured by including terms of higher-order in Kn and $\mathcal{R}^{-1}$ in the EOM. This idea leads us directly to the next possibility of extending this work by systematically studying the impact of higher-order terms on viscous BH accretion. Last but not least, given the common features we observe between the solution of the viscous accretion problem and the late-time behaviour in the Bjorken flow, it would be interesting to study whether even deeper similarities exist. It would be particularly exciting to explore the existence of an universal attractor for outflowing solutions which was shown to be present for a longitudinally expanding QGP [145].

Chapter 4

Bulk viscosity in binary mergers

4.1 Bulk viscosity in neutron stars

Binary neutron star mergers are very violent and nonlinear phenomena, especially during the first few milliseconds after the collision, and present ideal sites for non-equilibrium hydrodynamic effects (dissipative effects) to take place, see e.g., [23, 230, 59] for some reviews. This, however, depends crucially on the magnitude of the microphysical transport coefficients, e.g., the bulk viscosity, shear viscosity and heat conductivity. The appearance of a microphysical bulk viscosity in BNS mergers has been investigated in the simplified setup of harmonic density oscillations where realistic oscillation frequencies have been used [17, 10, 16]. Results from these studies provide a classification of the thermodynamic conditions under which bulk viscosity becomes important. Furthermore, the results shown in [9] suggest that these conditions might indeed be present in BNS mergers. This paves the way for the inclusion of a realistic bulk viscosity in BNS merger simulations. The consequences of such an inclusion are numerous but most importantly, bulk-viscous damping of strong density oscillations right after the collision might lead to a modification of the postmerger GW signal and is potentially observable through GW detectors. This exciting idea motivates us to study bulk viscosity in BNS mergers.

The microphysical origin of bulk viscosity in BNS mergers is the violation of weak chemical equilibrium (β-equilibrium) through the violent collision process [12, 11, 141]. Specifically, assuming that cold neutron stars are made up of *npe*-matter, i.e., they consist only of neutrons, protons and electrons, and neglecting the appearance of muons for simplicity, see also [179, 16], different conditions for chemical equilibrium exist which are based on the weak chemical reactions among the constituents of the neutron star matter. Following [141] these reactions are β-processes under various thermodynamic conditions which can be broadly grouped into electron-capture reactions and neutron-decay reactions. First, we distinguish between "neutrino-transparent" [13] and "neutrino-trapped" matter [15]. This is important as the mean-free path of neutrinos becomes shorter than the radius of the neutron star for temperatures $\gtrsim 5$ MeV [17] which means that they can participate as reactants in the reactions. Accordingly, for temperatures below ~ 5 MeV it can be assumed that neutrinos freely escape the neutron star.

4.1.1 β-equilibrium under neutron star merger conditions

The easiest neutrino-transparent case occurs for "cold" matter where the temperature is assumed to be less than a few hundred keV. The chemical reactions are the two

direct Urca reactions

$$p + e^- \to n + \nu_e\,, \tag{4.1}$$
$$n \to p + e^- + \overline{\nu}_e\,, \tag{4.2}$$

and the four modified Urca reactions

$$p + p + e^- \to p + n + \nu_e\,, \tag{4.3}$$
$$p + n \to p + p + e^- + \overline{\nu}_e\,, \tag{4.4}$$
$$n + p + e^- \to n + n + \nu_e\,, \tag{4.5}$$
$$n + n \to n + p + e^- + \overline{\nu}_e\,. \tag{4.6}$$

The distinction between direct and modified Urca processes is necessary as in the $T \to 0$ limit the former are forbidden below the direct Urca threshold density since the electron and proton Fermi momenta are not large enough to account for the neutron Fermi momentum [12]

$$p_{Fn} > p_{Fp} + p_{Fe}\,. \tag{4.7}$$

Hence, below the direct Urca threshold density the kinematically allowed modified Urca reactions provide the leading order contribution to the β-equilibration rate. However, above the threshold density the equilibration rate is dominated by direct Urca processes which are several orders of magnitude faster than the modified Urca reactions [12]. It is interesting to note that none of the reactions presented in Eqs. (4.1)-(4.2) and Eqs. (4.3)-(4.6) are the exact inverse of any other. Hence, the principle of detailed balance does not apply [12, 141] and the condition for β-equilibrium needs to be generalized to

$$\mu_n - \mu_p - \mu_e = \mu_\delta\,, \tag{4.8}$$

where μ_n, μ_p, μ_e and μ_δ are the neutron, proton, electron and "offset" chemical potentials. As it turns out, for our case of "cold" matter, i.e., $T \lesssim \mathcal{O}(100\,\text{keV})$, the neutron-decay and electron-capture rates balance for both direct and modified Urca processes leading to $\mu_\delta \lesssim 1$ MeV [12]. This means that we recover the standard cold β-equilibrium condition

$$\mu_n - \mu_p - \mu_e \approx 0\,, \tag{4.9}$$

which becomes exact for $T \to 0$.

For temperatures in the range $\mathcal{O}(100\,\text{keV}) \lesssim T \lesssim 5$ MeV we still assume that neutrinos freely escape the neutron star. However, modified Urca neutron-decay and electron-capture rates no longer balance below the direct Urca threshold such that μ_δ cannot be neglected. In particular, it was found that 5 MeV $\lesssim \mu_\delta \lesssim$ 23 MeV [12]. Following [141] we call matter under these conditions "warm" matter.

Finally, above the neutrino-trapping temperature neutrinos can start to participate as reactants in neutron-decay and electron-capture reactions such that the important reactions become the following direct Urca reactions

$$p + e^- \leftrightarrow n + \nu_e\,, \tag{4.10}$$
$$n \leftrightarrow p + e^- + \overline{\nu}_e\,. \tag{4.11}$$

Note that in this case of so-called "hot" matter the reactions proceed in both directions such that the principle of detailed balance yields the equilibrium condition

$$\mu_n - \mu_p - \mu_e = -\mu_{\nu_e}\,, \tag{4.12}$$

where μ_{ν_e} denotes the electron-neutrino chemical potential.

4.1.2 Bulk viscosity from violations of chemical equilibrium

In the previous subsection we have identified three distinct β-equilibrium conditions, namely Eqs. (4.9), (4.8) and (4.12) for cold, warm and hot matter, respectively. These conditions have a specific temperature range associated to them. Furthermore, also the baryon density plays an important role in selecting which reactions are dominant in setting the β-equilibration rate. As a next step, we can now assume, motivated by the violent expansion and compression cycles observed in BNS merger simulations, that the corresponding β-equilibrium condition is violated by an amount μ_Δ

$$\mu_n - \mu_p - \mu_e - \mu_\delta = \mu_\Delta \,, \tag{4.13}$$

where in cold matter $\mu_\delta \approx 0$ while in hot matter $\mu_\delta = -\mu_{\nu_e}$, and that the density has small-amplitude oscillations around a fixed background, i.e.,

$$n_i = n_{i,0} + \delta n_i \,, \tag{4.14}$$

$$\delta n_i \propto \exp\left[i\omega t\right] , \tag{4.15}$$

where n_i is the number density of the respective particle species with $j \in (n, p, e, \nu_e)$. We can further split the perturbations into an equilibrium and non-equilibrium contribution

$$\delta n_i = \delta n_{i,\mathrm{eq}} + \delta n_i' , \tag{4.16}$$

respectively. For simplicity, we restrict the discussion to the case of hot matter, such that $\mu_\delta = -\mu_{\nu_e}$, and follow [17]. As the matter is oscillating, a periodic production of neutrons and protons via the reactions (4.10) and (4.11), respectively, can drive violations of chemical equilibrium and therefore determines μ_Δ. In the limit of small deviations from the equilibrium condition in Eq. (4.12), i.e., $\mu_\Delta/T \ll 1$, which is also referred to as the "subthermal regime", see also [14] for the so-called "suprathermal regime", the net direct Urca rate is given by

$$\Gamma_\Delta := \Gamma_p - \Gamma_n \approx \left.\frac{\partial\left(\Gamma_p - \Gamma_n\right)}{\partial \mu_\Delta}\right|_{\mu_\Delta = 0} \mu_\Delta = \lambda \mu_\Delta , \quad \lambda > 0 \,, \tag{4.17}$$

where Γ_p and Γ_n are the proton and neutron production rates, respectively, and λ denotes the relaxation rate, e.g., see [15]. Due to these flavor-changing reactions the number densities are not conserved but evolve according to

$$\partial_t \delta n_i = -\theta n_{i,0} \pm \lambda \mu_\Delta \,, \tag{4.18}$$

with a plus sign for $i \in (p, e)$ and a minus sign for $i \in (n, \nu_e)$. The quantity θ is the non-relativistic expansion $\theta := \partial_i v^i$. Now, the viscosity can be derived by splitting the total pressure into an equilibrium and non-equilibrium contribution and assuming that the deviations from equilibrium are small

$$p = p_{\mathrm{eq}} + \Pi \approx p_{\mathrm{eq}} + \sum_i \left.\frac{\partial p}{\partial n_i}\right|_{n_{i,0} + \delta n_{i,\mathrm{eq}}} \delta n_i' = p_{\mathrm{eq}} - \zeta_{\mathrm{eff}} \theta \,, \tag{4.19}$$

where we used the NS definition of the non-equilibrium pressure Π [108, 174] and ζ_{eff} denotes the "effective" bulk viscosity. The final result is the standard resonant form of the bulk viscosity for harmonic density oscillations with frequency ω

$$\zeta_{\mathrm{eff}}(\omega) = \frac{\gamma}{\omega^2 + \gamma^2} \left.\frac{n_B^2 (\partial \mu_\Delta / \partial n_B)_{Y_n}^2}{(\partial \mu_\Delta / \partial n_n)_{n_B}}\right|_{\mu_\Delta = 0} , \tag{4.20}$$

where n_B is the conserved baryon number density, $Y_n := n_n/n_B$ is the neutron fraction and $\gamma := (\partial\Gamma_\Delta/\partial n_n)_{n_B} = (\partial\mu_\Delta/\partial n_n)_{n_B}\lambda$ is the equilibration rate. The second factor in Eq. (4.20) is fully determined by the EOS while the first factor expresses the frequency dependence of ζ_{eff}. If we consider ω to be fixed and vary γ, ζ_{eff} reaches its resonant maximum if $\gamma = \omega$, i.e., the oscillation frequency of density perturbations matches the equilibration rate of the weak chemical reactions,

$$\zeta_{\max}(\omega) := \frac{1}{2\omega}\left.\frac{n_B^2(\partial\mu_\Delta/\partial n_B)^2_{Y_n}}{(\partial\mu_\Delta/\partial n_n)_{n_B}}\right|_{\mu_\Delta=0}. \tag{4.21}$$

In the "fast" limit, i.e., $\gamma \gg \omega$, which corresponds to the physical scenario where chemical equilibration happens almost instantaneously compared to the evolution timescale of the fluid, we find

$$\zeta := \zeta_{\text{eff}}(\omega/\gamma \ll 1) = \frac{1}{\gamma}\left.\frac{n_B^2(\partial\mu_\Delta/\partial n_B)^2_{Y_n}}{(\partial\mu_\Delta/\partial n_n)_{n_B}}\right|_{\mu_\Delta=0}. \tag{4.22}$$

4.1.3 Simulating bulk viscosity in neutron stars

In this subsection we connect the results about the emergence of a microphysical bulk viscosity presented in Subsection 4.1.2 with the formulation of GRDHD shown in Section 2.4. In particular, we follow the analytical investigations from [125, 69, 62] which connect bulk-viscous hydrodynamics in the absence of shear viscosity and heat conduction, i.e., $\eta = \kappa = 0$, to a chemically reacting multi-fluid. As presented in [125, 62], in the limit of small deviations from weak equilibrium, i.e., $\mu_\Delta/T \ll 1$ but see also [127] for a more recent result on large deviations, a chemically reacting multi-fluid with one independent particle fraction can be mapped mathematically to the MIS-theory of a bulk-viscous single fluid which behaves according to Eq. (2.113).

This mapping is accurate to second-order in μ_Δ/T which translates to second-order accuracy in inverse Reynolds number $\mu_\Delta^2 \propto \Pi^2 \propto \mathcal{R}^{-2}$. As we will consider only fluids with vanishing shear viscosity and heat conductivity in the rest of this Thesis, we make use of the definition of the inverse Reynolds number in Eq. (2.114). Note that Eq. (2.113) can be obtained from the more general Eq. (2.100). In the example discussed in Section 4.1.2 we considered a fluid consisting of *npe*-matter with trapped neutrinos. These are four particle fractions, however, not all of them are independent since the conditions of baryon number conservation, $n_B = n_p + n_n$ and $\nabla_\mu(n_B u^\mu) = 0$, lepton number conservation, $n_L = n_e + n_\nu$ and $\nabla_\mu(n_L u^\mu) = 0$, and charge neutrality, $n_p = n_e$, hold. These conditions restrict the system to only one independent particle fraction or "reaction coordinate" such that the results from [125] are directly applicable.

By mapping Eq. (4.20) to Eq. (116) of [125]

$$\zeta_{\text{eff}}(\omega) = \zeta\frac{1}{1+\tau_\Pi^2\omega^2}, \tag{4.23}$$

we are able to confirm that the bulk viscosity ζ in Eq. (2.113) is given by Eq. (4.22) and the relaxation time is simply the inverse of the equilibration rate γ, i.e.,

$$\tau_\Pi = \frac{1}{\gamma} = (\partial\Gamma_\Delta/\partial n_n)^{-1}_{n_B} = (\partial\mu_\Delta/\partial n_n)^{-1}_{n_B}\lambda^{-1}. \tag{4.24}$$

This mathematical duality has many consequences but most importantly, as long as deviations from chemical equilibrium are small, we are able to model the more general

chemically reacting multi-fluid by a simple MIS-type bulk-viscous fluid. This has the advantage that results regarding the causality and stability of the MIS-theory apply [36].

A recent study implementing direct and modified Urca reactions in a full NR simulation has shown that many regions in the postmerger reach the bulk-viscous regime such that using Eq. (2.113) is indeed a valid approach [202]. Another investigation has provided first clues about the impact of fast equilibration on the GW signal [140]. Finally, a recent study has compared a bulk-viscous fluid with transport coefficients obtained through the previously mentioned mathematical duality to the corresponding multi-fluid. The investigation has shown that the MIS approach performs reasonably well when considering simple oscillations and the migration of TOV stars [63]. Motivated by these results, we will implement Eq. (2.113) in full NR simulations and study the impact of bulk viscosity on the postmerger evolution.

4.2 Numerical implementation of a causal bulk viscosity

In this section we introduce the novel methods implemented in the high-order and HRSC code FIL [195, 201] which allow us to solve the system in Eqs. (2.115)-(2.117) for BNS mergers.

4.2.1 Discretization

All flux terms appearing in Eq. (2.116) are discretized following the ECHO scheme presented in Subsection 2.3.1. As discussed in Subsection 2.4.3, spatial derivatives occuring in Eq. (2.117) in the component belonging to the evolution of Π are discretized using fourth-order central finite differences.

The temporal derivative is calculated through first-order backward differencing with respect to (WRT) the previous timestep. For example, let us assume we employ Heun's second-order method with two stages and the solution should be advanced from t to $t+\Delta t$. We also assume that the solution at $t-\Delta t$ is available. Then, the first stage employs the following approximation of the time derivative of the Lorentz factor

$$\partial_t W|_t \approx \frac{W(t)-W(t-\Delta t)}{\Delta t}, \tag{4.25}$$

while in the second stage we use

$$\partial_t W|_{t+C\Delta t} \approx \frac{W(t+C\Delta t)-W(t)}{C\Delta t}, \tag{4.26}$$

where $C=1$ for Heun's method. For higher-order multi-stage methods only C needs to be adjusted for each stage separately.

4.2.2 Primitive inversion and limiting

As already mentioned in Chapter 2, typical methods for the solution of the equations of relativistic hydrodynamics involve the conversion between the conserved variables, i.e., $\boldsymbol{C}$, see Eq. (2.78), and the primitive variables, $\boldsymbol{P}$, see Eq. (2.79), which has to be carried out numerically by using root-finding algorithms. In this Thesis we augment the purely hydrodynamical algorithm from [124] already provided by FIL in order to include the bulk-viscous pressure Π. As will be shown, almost all desirable properties can be transferred to the viscous case if a suitable limiting procedure is employed. In the following we briefly review the most notable steps of the inversion algorithm presented in [124], thereby highlighting the modifications which arise from the inclusion

of the bulk-viscous pressure. At this stage we omit all details related to the handling of the density floor, the finite range of the EOS table as well as all rescalings that follow from the bounds on the conserved and primitive variables. All of these steps are not influenced by the inclusion of bulk viscosity except that an atmosphere value for Π needs to be specified which we choose to be $\Pi_{\rm atmo} = 0$.

As in [124], we start by introducing the following definitions

$$a' = \frac{p+\Pi}{\rho(1+\epsilon)}, \quad h' = h + \frac{\Pi}{\rho}, \quad z = Wv\,, \tag{4.27}$$

$$q = \frac{\tau}{D}, \quad r = \frac{S^i S_i}{D}, \quad k = \frac{r}{1+q}, \tag{4.28}$$

which yield the following relations:

$$z = \frac{r}{h'}, \quad \rho = \frac{D}{W}, \quad W = \sqrt{1+z^2}, \tag{4.29}$$

and most crucially

$$\epsilon = Wq - zr + W - 1\,, \tag{4.30}$$

$$h' = (1+\epsilon)(1+a') = (W - zk)(1+q)(1+a')\,. \tag{4.31}$$

These expressions are exactly the same as in [124] if a and h would be replaced by a' and h', respectively. The quantity ϵ denotes the specific internal energy.

Limiting

We impose the same requirements which have been already formulated in [124] for the case of perfect fluids on the viscous fluid of our simulations. This means that the matter should satisfy the dominant energy condition and the viscous sound speed, see Eq. (2.121) for the definition, has to be smaller than the speed of light

$$0 \leq a' \leq 1\,, \tag{4.32}$$

$$0 \leq {c_s'}^2 \leq 1\,. \tag{4.33}$$

Because the bulk-pressure Π is treated as an evolved, independent quantity, the fluid can easily evolve into states which violate the conditions in Eqs. (4.32) and (4.33). Hence, we formulate the following limiting strategy in order to avoid large out-of-equilibrium contributions in the fluid:

(i) If $\Pi < 0$ and $\Pi < \alpha p$ with $-1 \leq \alpha \leq 0$, set $\Pi = \alpha p$. Note that for these ranges of α the condition in Eq. (4.32) is automatically fulfilled. We typically choose $\alpha = -0.9$ in order to avoid regions where the fluid is pressure-less.

(ii) If $\Pi > 0$ and $a' > 1$, set $\Pi = e - p$.

(iii) If ${c_s'}^2 > {c_{\rm max}}^2$, set

$$\tau_\Pi = \frac{\zeta}{\rho h'} \frac{1}{{c_{\rm max}}^2 - \left(\frac{\partial p}{\partial e}\right)_\rho - \frac{1}{h'}\left(\frac{\partial p}{\partial \rho}\right)_e}\,, \tag{4.34}$$

where $0 \leq {c_{\rm max}}^2 \leq 1$.

Bounds for the conserved variables

Again following [124] we find the same lower bound on q, if the specific internal energy ϵ is required to be positive

$$q = h'W - 1 - \frac{p+\Pi}{W\rho} \geq \epsilon \geq \epsilon_{\min}\,, \tag{4.35}$$

where $\epsilon_{\min}$ denotes the minimum specific internal energy in the whole table. Additionally, we can also confirm that the relations and bounds for the total momentum density in terms of k remain almost unchanged, if bulk viscosity is included, i.e.,

$$k(v,a') = v\frac{1+a'}{1+v^2a'}, \quad \frac{\partial}{\partial a'}k(v,a') \geq 0\,, \tag{4.36}$$

$$0 \leq \frac{1}{2}k \leq v \leq k \leq \frac{2v}{1+v^2} < 1\,. \tag{4.37}$$

These relations are based on the dominant energy condition which is expressed through bounds on a'. By using a limit on the maximum fluid velocity $v_{\max}$ we automatically obtain

$$k < k_{\max} = \frac{2v_{\max}}{1+{v_{\max}}^2}\,. \tag{4.38}$$

Root finding, existence and uniqueness

We use the same root-finding function as in [124] except that we substitute $\tilde{h}(z)$ by $\tilde{h'}(z)$, i.e., our root-finding function takes the form

$$f(z) = z - \frac{z}{\tilde{h'}(z)}\,, \tag{4.39}$$

where the tilde has the same meaning as in [124]. Furthermore, the limits on Π are imposed at this stage. This means we impose the requirements (i) and (ii) when computing $\tilde{a'}(z)$. In addition, from Eq. (4.37) we find that the bracketing interval remains unchanged as well, i.e.,

$$z_- = \frac{k/2}{\sqrt{1-k^2/4}}, \quad z_+ = \frac{k}{\sqrt{1-k^2}}\,. \tag{4.40}$$

Moreover, it is possible to show that $f(z)$ has one unique solution by following the steps outlined in [124] and replacing $\tilde{h}$ and $\hat{a}$ by $\tilde{h'}$ and $\hat{a'}$, respectively. There is only one notable difference: Due to the fact the we limit Π during the root-finding process, Π can only be considered constant, if the limiter is never applied. This leads to three separate cases, for each of which uniqueness can be established independently. Overall, this leads to different expressions for the quantity B defined in

$$\frac{df}{dz} = 1 - v^2 B\,, \tag{4.41}$$

$$B = \hat{a'}\left[1 + \frac{\partial \ln(1+\hat{a'})}{\partial \ln(1+\epsilon)}\right] + \frac{\partial \ln(1+\hat{a'})}{\partial \ln(\rho)}\,. \tag{4.42}$$

If Π is assumed to be constant, then we obtain

$$B_\Pi = \left.\frac{\partial p}{\partial e}\right|_\rho + \frac{1}{h'}\left.\frac{\partial p}{\partial \rho}\right|_e \leq {c_s'}^2 \leq 1\,. \tag{4.43}$$

If Π is limited from below, then we obtain

$$B_{(\mathrm{i})} = (1-\alpha)\left\{ \left.\frac{\partial p}{\partial e}\right|_{\rho} + \frac{\rho}{(1-\alpha)p + e} \left.\frac{\partial p}{\partial \rho}\right|_{e} \right\} \leq {c_s}^2 \leq 1\,. \tag{4.44}$$

Finally, if Π is limited from above, then we obtain

$$B_{(\mathrm{ii})} = a' = 1\,. \tag{4.45}$$

Comment

In this paragraph we want to give an estimate for the minimum and maximum inverse Reynolds numbers achievable by our scheme. As an example, we use the simple ideal gas EOS, i.e., $p = (\gamma - 1)\rho\epsilon$. We assume that the pressure can be written additionally as $p = K\rho^{\gamma}$ and the specific internal energy is given by $\epsilon = \frac{K\rho^{\gamma-1}}{\gamma-1}$. Then, the minimum inverse Reynolds number is given by (i):

$$\mathcal{R}^{-1} = \frac{\Pi}{\rho h} = \frac{\alpha p}{e+p} = \alpha \frac{1}{K^{-1}\rho^{1-\gamma} + 1 + (\gamma-1)^{-1}}. \tag{4.46}$$

A typical choice for test simulations of neutron stars is $\gamma = 2$, $K = 100$ and $\rho = 0.00128$ which yields $\mathcal{R}^{-1} \simeq -0.1$ for $\alpha = -0.9$. For the same setup the maximum inverse Reynolds number is given by (ii):

$$\mathcal{R}^{-1} = \frac{\Pi}{\rho h} = \frac{e-p}{e+p} = \frac{(\gamma-1)\rho^{1-\gamma}/K - \gamma + 2}{(\gamma-1)\rho^{1-\gamma}/K + \gamma}. \tag{4.47}$$

Using the same choice for γ, K and ρ we find $\mathcal{R}^{-1} \simeq 0.8$. These estimates show that our scheme is well-suited to simulate out-of-equilibrium processes which are close to the boundaries which denote the theoretical range of applicability of second-order GRDHD, i.e., $-1 \lesssim \mathcal{R}^{-1} \lesssim 1$.

4.2.3 Transport coefficients and transition to inviscid fluid

The scope of this is work to examine, for the first time, the impact of a causal bulk viscosity prescription on BNS merger simulations. Hence, at this stage we are mainly interested in the general, qualitative behaviour of bulk-viscous BNS mergers. Thus, we decide to keep the buk viscosity as well as the relaxation time constant in our simulations. This allows us the explore the most extreme case of a large but realistic bulk viscosity and study systematically the impact of the magnitude of ζ.

However, as BNS mergers lead to violent shocks which propagate outward through a decreasing density profile, a constant value for the bulk viscosity, which is applicable and realistic in the high-density regions, will lead to large inverse Reynolds numbers at sufficiently low densities. As a consequence, the limiting procedure described in Subsection 4.2.2 will be applied consistently. However, bulk viscosity is expected to decrease with decreasing density, see e.g., [17], which motivates us to implement a smooth transition zone between the high-density bulk viscosity ζ_h and the low-density bulk viscosity ζ_l which we typically chose to be $\zeta_l = 0$. The high-density zone which has $\zeta = \zeta_h$ occupies matter with densities $\rho \geq \rho_h$ while the region with densities $\rho \leq \rho_l$ has the bulk viscosity ζ_l. The functional behaviour of the bulk viscosity in the transition zone defined as the density interval $\rho_l < \rho < \rho_h$ is expressed through a cubic polynomial

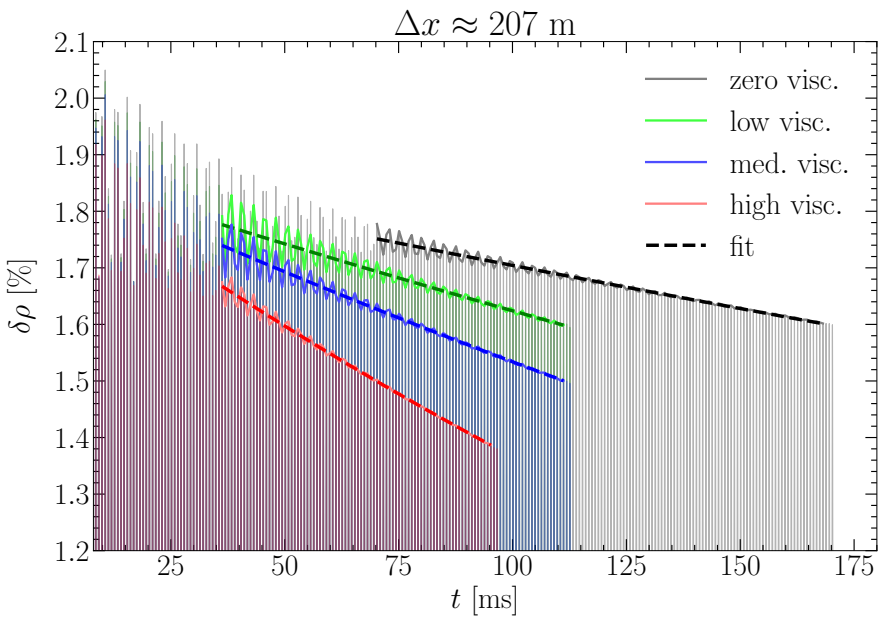

Figure 4.1: Central rest-mass density oscillations of perturbed viscous neutron stars Shown in solid thin lines is the timeseries of the quantity $\delta\rho$ which denotes the normalized central density of the corresponding star, where the large-scale density drift has been removed from the data, see item 1 in Subsection 4.3.1. Shown in solid thick lines is the amplitude of $\delta\rho$ estimated by using the local maxima of the signal, see item 2. Finally, dashed lines denote fitting functions to the amplitude of $\delta\rho$, see item 3. Overall, we show only data for the highest resolution but for all viscosities.

which ensures continuity of ζ and $\mathrm{d}\zeta/\mathrm{d}\rho$ at ρ_h and ρ_l. Overall, our prescription can be summarized as follows:

$$\zeta(\rho) = \begin{cases} \zeta_l & \text{if} \quad \rho \le \rho_l\,, \\ a\rho^3 + b\rho^2 + c\rho + d & \text{if} \quad \rho_l < \rho < \rho_h\,, \\ \zeta_h & \text{if} \quad \rho \ge \rho_h\,, \end{cases} \tag{4.48}$$

where the coeffcients of the cubic polynomial are given by

$$a = \frac{2(\zeta_l - \zeta_h)}{(\rho_h - \rho_l)^3}\,, \tag{4.49}$$

$$b = \frac{3(\zeta_l + \zeta_h)(\zeta_h - \zeta_l)}{(\rho_h - \rho_l)^3}\,, \tag{4.50}$$

$$c = \frac{6\rho_h\rho_l(\zeta_l - \zeta_h)}{(\rho_h - \rho_l)^3}\,, \tag{4.51}$$

$$d = \frac{\left[(3\rho_h\rho_l^2 - \rho_l^3)\zeta_h + (\rho_h^3 - 3\rho_h^2\rho_l)\zeta_l\right]}{(\rho_h - \rho_l)^3}\,. \tag{4.52}$$

Additionally, we specify the relaxation time to be constant as well by using a prescription with a linear interpolation in the transition zone

$$\tau_\Pi(\rho) = \begin{cases} \tau_l & \text{if} \quad \rho \le \rho_l\,, \\ \tau_h - (\tau_h - \tau_l)(\rho_h - \rho)/(\rho_h - \rho_l) & \text{if} \quad \rho_l < \rho < \rho_h\,, \\ \tau_h & \text{if} \quad \rho \ge \rho_h\,. \end{cases} \tag{4.53}$$

We typically choose τ_h to be $\sim 1.1\Delta t_{\mathrm{min}}$ and τ_l to be $\sim 1.1\Delta t_{\mathrm{max}}$, where Δt_{min} and Δt_{max} are the minimum and maximum timesteps in the simulation, respectively. If

the neutron stars are fully covered by the highest refinement level and the dynamical/hydrodynamical timescale is well-resolved by $\Delta t_{\rm min}$, this prescription for the relaxation time ensures that $\Pi \simeq \Pi_{\rm NS} = -\zeta\Theta$. On top of that, these choices for τ_{Π} avoid stiff source terms. Note that at the same time causality is guaranteed through Eq. (4.34).

4.3 Numerical experiments with isolated neutron stars

After having discussed our implementation strategy in the previous section, i.e., Section 4.2, we now move on to the first numerical experiments involving isolated neutron stars in order to test the implementation. Specifically, we investigate the damping of radial eigenmode perturbations and the migration of neutron stars in this section.

4.3.1 Numerical viscosity in neutron star simulations

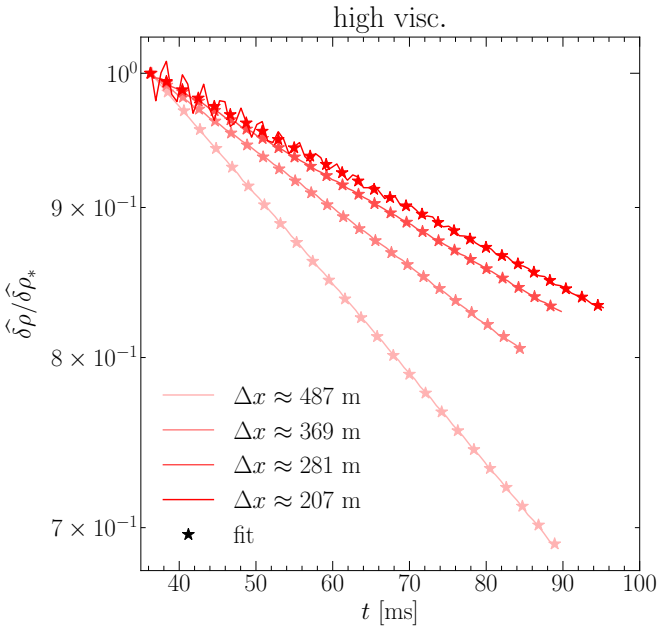

Figure 4.2: Amplitude of central rest-mass density oscillations of perturbed viscous neutron stars
Solid lines show the quantity $\widehat{\delta\rho}/\widehat{\delta\rho}_*$ which denotes the reduced timeseries of the local maxima of $\delta\rho$, i.e., $\widehat{\delta\rho}$, see Section 4.3.1, normalized by its first value $\widehat{\delta\rho}_*$. We show only data for the high viscosity case but for all employed numerical resolutions. Symbols denote fitting functions to $\widehat{\delta\rho}/\widehat{\delta\rho}_*$.

In this test problem we set out to measure the numerical and the physical viscosity of our code. The procedure has been layed out in [70] and we follow it for the most part except of some minor differences. We use simulations of isolated TOV stars using a simple hybrid polytropic EOS, i.e., $p = K\rho^{\Gamma} + (\Gamma_{\rm th} - 1)\rho\epsilon_{\rm th}$ with $K = 100$, $\Gamma = 2$, $\Gamma_{\rm th} = 1.1$ and a central density of $\rho_c = 1.28 \times 10^{-3}\ M_{\odot}^{-2} \approx 7.91 \times 10^{14}$ g cm^{-3} which yields a $M = 1.4\ M_{\odot}$ star. This configuration is well-explored with well-known pulsation frequencies [117]. We use such a low $\Gamma_{\rm th}$ because we have found that the drift of the central density ρ_c can be reduced, if $\Gamma_{\rm th}$ assumes values close to 1. Our measurement procedure is based on the damping of the oscillations of ρ_c which means that we want to reduce unwanted secondary effects by reducing the density drift. This is in contrast to [70] where integrals of the velocity profile have been employed.

Furthermore, we initialize the stars by using a perturbation in the form of the fundamental radial eigenmode which produces oscillations in the central density on the order of $\sim 2\%$, e.g., see Fig. 4.1. This ensures that our simulations remain in the linear regime of the coupled hydrodynamic and gravitational equations. The perturbation equations are solved by using the `PizzaTOV` thorn which solves the Sturm-Liouville boundary value problem [172] and is part of the `Einstein Toolkit`. Overall, we carry out 16 simulations which correspond to four different bulk viscosities and four different resolutions. We vary the bulk viscosity between $\zeta_h \in \{0, \sim 4.3\times10^{25}, \sim 9.42\times10^{25}, \sim$

$1.98 \times 10^{26}\}$ g s^{-1} cm^{-1}, which are denoted as zero, low, medium and high viscosity cases, respectively. The resolution on the finest refinement level varies between $\Delta x \in \{\sim 207, \sim 281, \sim 369, \sim 487\}$ m. Furthermore, we set $\zeta_l = 0$, $\rho_h \approx 1.28 \times 10^{-4}\, M_\odot^{-2} \approx 7.91 \times 10^{13}$ g cm^{-3} and $\rho_l \approx 1.28 \times 10^{-7}\, M_\odot^{-2} \approx 7.91 \times 10^{10}$ g cm^{-3}.

Measurement procedure

Following [70] and [83] the rate of change of the kinetic energy of a weakly pulsating star E, i.e., the magnitude of the pulsation is small such that linear perturbation theory is applicable, is given by

$$\frac{\mathrm{d}E}{\mathrm{d}t} = -4\pi \int_0^R \mathrm{d}r r^2 \phi^6 \zeta |\Theta|^2 , \tag{4.54}$$

where ϕ is the conformal factor and R the radius of the neutron star. Then, if the pulsation energy E is known, the damping time $\overline{\tau}$ can be simply estimated through

$$\overline{\tau} = -2E \left\langle \frac{\mathrm{d}E}{\mathrm{d}t} \right\rangle^{-1} , \tag{4.55}$$

where $\langle \cdot \rangle$ denotes the time-average over one pulsation cycle.

Expanding E and $\mathrm{d}E/\mathrm{d}t$ to leading order in the post-Newtonian expansion, see [70] for details, we obtain the following expressions

$$E = 4\pi \int_0^R \mathrm{d}r r^2 \frac{1}{2} \rho_0 v'^2 \left(1 + \mathcal{O}(c^{-2})\right), \tag{4.56}$$

$$\frac{\mathrm{d}E}{\mathrm{d}t} = -4\pi \int_0^R \mathrm{d}r r^2 \zeta |\Theta|^2 \left(1 + \mathcal{O}(c^{-2})\right), \tag{4.57}$$

where $v' = v - v_0 = v$ is the Newtonian three-velocity perturbation in the radial direction with $v_0 = 0$ being the background velocity which is zero in our case. Analogously, ρ_0 is the background density profile of the TOV solution.

Assuming a harmonic form of the perturbation, i.e., $v' \propto \exp[i\omega t + ikr]$, where ω is the angular frequency of the pulsation mode and k is the wavenumber, we obtain

$$\left\langle |\Theta|^2 \right\rangle \propto k^2 \left\langle v' \right\rangle = k^2 v'^2_{\mathrm{max}}/2 . \tag{4.58}$$

The quantity v'_{max} is a function of radius. Analogously to the simple harmonic oscillator, the energy oscillates between kinetic and potential energy. Therefore E can be estimated by substituting v'_{max} for v'. Then, by using the definition of the speed of sound $c_s^2 = \omega^2/k^2$ we obtain

$$E = 2\pi \int_0^R \mathrm{d}r r^2 \rho_0 v'^2_{\mathrm{max}} \left(1 + \mathcal{O}(c^{-2})\right), \tag{4.59}$$

$$\left\langle \frac{\mathrm{d}E}{\mathrm{d}t} \right\rangle \sim -2\pi \frac{\omega^2}{c_s^2} \zeta \int_0^R \mathrm{d}r r^2 v'^2_{\mathrm{max}} \left(1 + \mathcal{O}(c^{-2})\right). \tag{4.60}$$

Finally, by using Eq. (4.55) we find a formula which relates the damping time of radial pulsations $\overline{\tau}$ to the bulk viscosity ζ

$$\zeta = 2 \frac{1}{\overline{\tau}} \frac{c_s^2}{\omega^2} \overline{\rho_0} , \tag{4.61}$$

where

$$\overline{\rho_0} := \frac{\int_0^R \mathrm{d}r r^2 v'^2_{\max} \rho_0}{\int_0^R \mathrm{d}r r^2 v'^2_{\max}}, \tag{4.62}$$

is the eigenmode-averaged background density. In practice, ω can be obtained from the simulations by measuring the pulsation frequency, $\overline{\rho_0}$ can be obtained from the initial data by calculating the integrals in Eq. (4.62) and c_s^2 can be simply evaluated at $\overline{\rho_0}$ by using the EOS. This means that we are left with the determination of $\overline{\tau}$ in order to calculate ζ through Eq. (4.61).

As already mentioned above, we use the central density ρ_c to measure the damping time $\overline{\tau}$. In order to do so, we make use of the following simple recipe:

1. **Make use of a high-order low-pass Butterworth filter in order to remove global drifts of the central density from the signal.**

   As can be seen from Fig. 4.1 our simulations have a typical length on the order of $T \sim \mathcal{O}(100\ \mathrm{ms})$ which yields a minimum resolved frequency of $f_{\min} \sim 0.01$ kHz. We choose the cutoff-frequency on the order of $f_c \sim 0.1$ kHz and a $n = 4$ filter, where n denotes the order of the Butterworth filter. The frequency of the fundamental mode is $f_F \sim 1.44$ kHz, see e.g., [117], which means that our cutoff-frequency is more than an order of magnitude lower than the frequency we want to resolve. Thus, the choices $f_c \sim 0.01$ kHz and $n = 4$ ensure that we obtain the density drift without contributions from higher frequencies. Then, we subtract the drift from the original data and obtain a signal which oscillates around zero. Additionally, we normalize the "drift-free" signal by the initial central density $\rho_c(t = 0)$. We define the "drift-free" and normalized signal as $\delta\rho$ which is shown in Fig. 4.1 in solid thin lines for the simulations with the highest resolution.

2. **Calculate the local maxima of the signal.**

   Now, we assume that the signal is composed of a sum of damped sinusoids, i.e.,

   $$\delta\rho \approx \sum_k A_k \exp[-t/\overline{\tau}_k] \sin[2\pi f_k t - \phi_k], \tag{4.63}$$

   where the index k runs over all excited eigenmodes, i.e., F, $H1$, $H2$, ..., A_k denotes the initial normalized amplitude, $\overline{\tau}_k$ denotes the damping time, f_k the frequency and ϕ_k the phase shift of the k-th excitation. First, we tried a matched filtering approach by fitting $\delta\rho$ with a function of the form presented in Eq. (4.63). We varied the amount of sinusoids in the sum but were not able to find satisfying results with this approach.

   Hence, we resorted to the calculation of the local maxima of the signal in order to obtain data which can be fitted to a simple exponential function. The main caveat in this approach is that it is not possible to distinguish between different excitation modes with different damping times. This means that it is necessary select only those parts of the timeseries of $\delta\rho$ which are dominated by a single eigenmode; the F-mode in our case. This is not a problem for lower-resolution simulations as the overtone modes have a shorter damping time due to more efficient numerical damping.

   Therefore, for lower-resolution simulations the "pollution" of the signal is reduced such that almost all of $\delta\rho$ is dominated by the F-mode. However, as numerical damping decreases with increasing resolution also the contributions from excited overtone modes become non-negligible. This can be seen in Fig. 4.1 where

for $t \lesssim 50$ ms the evolution of the local maxima is highly oscillatory due to contributions from overtone modes. A naive computation of the local maxima together with a subsequent fitting procedure results in an underestimation of $\overline{\tau}_F$ because overtone modes have shorter damping times than the fundamental mode. Thus, for higher-resolution simulations we make only use of approximately the last half of the signal where the contributions from the overtone modes can be neglected. We show thick solid lines which connect the local maxima in Fig. 4.1 in order to visualize the utilised part of $\delta\rho$. The timeseries of the utilised local maxima of $\delta\rho$ is defined as $\widehat{\delta\rho}$ and the first value in this sequence is defined as $\widehat{\delta\rho}_*$.

3. **Fit the logarithm of the local maxima to a linear function in time.**

   In this step we additionally normalize $\widehat{\delta\rho}$ by $\widehat{\delta\rho}_*$ and fit the values of $\log[\widehat{\delta\rho}/\widehat{\delta\rho}_*]$ to a linear function in time. The results are shown in Figs. 4.1 and 4.2. Dashed lines in Fig. 4.1 and the star symbols in Fig. 4.2 represent the fits, respectively. To avoid overcrowding Fig. 4.2, we only show $\widehat{\delta\rho}/\widehat{\delta\rho}_*$ for the high viscosity case. Different color intensities in Fig. 4.2 show different resolutions and solid lines connect the original data points of $\widehat{\delta\rho}/\widehat{\delta\rho}_*$.

From Fig. 4.1 we observe that larger viscosities lead to stronger damping of the fundamental mode, as expected. From Fig. 4.2 we observe convergent behaviour in the slopes of the linear fits. This is expected because increased numerical resolution leads to a decrease in numerical damping such that the measured damping time converges to the damping time related to the physical viscosity, see Eq. (4.61). Finally, we observe oscillatory behaviour in the data presented for the highest resolution in Fig. 4.2. As already discussed, these oscillations stem from contributions of overtone modes and do not significantly impact the calculation of $\overline{\tau}_F$.

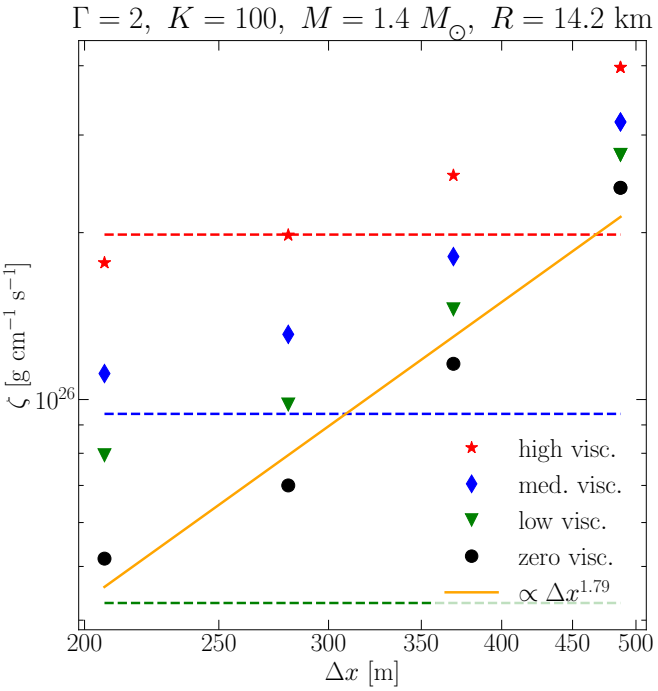

Figure 4.3: Numerical viscosity of perturbed viscous neutron stars with $M = 1.4\ M_\odot$
Summary of the results on the measurement of the numerical viscosity denoted by different symbols. The measured viscosities are given as a function of the grid resolution and have been calculated from Eq. (4.61). Dashed lines show the values of the employed physical viscosities and the solid line shows a linear fit of $\log[\zeta]$ as a function of $\log[\Delta x]$ for the zero viscosity case. The parameters of the TOV solution are given in the title.

Results on the numerical viscosity measurement

Here we present the results of the numerical viscosity measurement. Figure 4.3 shows the values of ζ obtained through Eq. (4.61) for all 16 simulations denoted by different symbols. Additionally, we present the values of the employed physical bulk viscosities in dashed lines and a linear fit of $\log[\zeta]$

as a function of $\log[\Delta x]$ for the zero viscosity case by using a solid line.

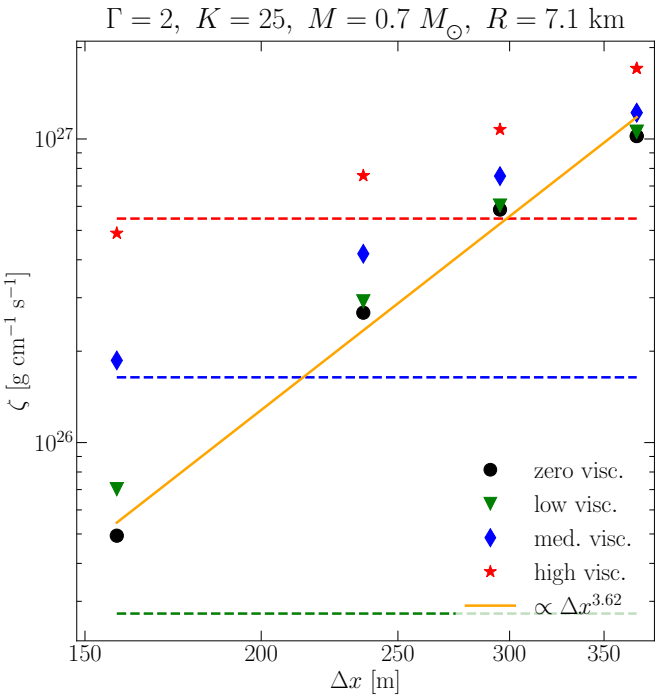

Figure 4.4: Numerical viscosity of perturbed viscous neutron stars with $M = 0.7\ M_\odot$
Shown is the same as in Fig. 4.3 but for a different TOV solution whose parameters are given in the title of this figure. In particular, this solution has a smaller mass and radius than the solution used in Fig. 4.3.

There is a number of observations that can be made: First, we observe that the measured bulk viscosity for the medium and high viscosity case approximately converges to its physical value which confirms our implementation of Eq. (2.113) in FIL. For the high viscosity case the measured value in the highest resolution simulation is even smaller than the physical bulk viscosity. This can be explained by considering that we setup the bulk viscosity by employing a transition zone, e.g., see Eq. (4.48). Thus, our choices of ζ_l, ρ_l and ρ_h lead to a lower bulk viscosity in the outer, low-density regions of the star than in the inner, high-density regions. Considering that the radial fundamental mode has larger velocities closer to the surface of the star than in the high-density interior we arrive at the conclusion that the constant-viscosity approximation made to derive Eq. (4.61) does not longer hold and leads to an underestimation of the constant bulk viscosity in the inner regions of the star.

Second, we observe slow convergence of the low viscosity case. We attribute this behaviour to the slow convergence observed also for the zero viscosity case. The FIL code employs 4th-order accurate methods, see [195], while the employed time integrator is of order three, e.g., see Subsection 2.3.1, which means that the observed convergence order of ~ 1.79 is far below the formal one. It is important to remark that the discretization of Θ in Eq. (2.113) does not impact the convergence order for the zero viscosity case as $\zeta = 0$. We explain this behaviour through the influence of discretization errors from the neutron star surface whose large density and pressure gradients manifest as effective discontinuities in the numerical solution leading to a reduction of the observed convergence order.

Because of the reduced convergence order found in Fig. 4.3 it is interesting to compare to another numerical viscosity measurement performed during an earlier development stage of our bulk-viscous extension of FIL. In that case, we employed a different isolated TOV solution with $K = 25$, $\Gamma = 2$, $\Gamma_{\rm th} = 2$ and a central density of $\rho = 5.12 \times 10^{-3}\ M_\odot^{-2} \approx 3.16 \times 10^{15}$ g cm^{-3} which yields a $M = 0.7\ M_\odot$ star. We vary the bulk viscosity between $\zeta_h \in \{0, \sim 2.73 \times 10^{25}, \sim 1.64 \times 10^{26}, \sim 5.47 \times 10^{26}\}$ g s^{-1} cm^{-1}, which are denoted as zero, low, medium and high viscosity cases, respectively. The resolution on the finest refinement level varies between $\Delta x \in \{\sim 158, \sim 236, \sim 295, \sim 369\}$ m. Furthermore, instead of employing the cubic polynomial in Eq. (4.48), ζ is set to zero sharply for $\rho < \rho_l = \rho_h = 2.56 \times 10^{-4}\ M_\odot^{-2} \approx 1.58 \times 10^{14}$ g cm^{-3}.

Figure 4.4 presents the numerical viscosity measurement for the old setup by making use of the same measurement procedure already used for Fig. 4.3. The main difference between Fig. 4.3 and Fig. 4.4 can be found in the measurement of the convergence order for the zero viscosity cases.

We were able to obtain a convergence order of ~ 3.62 for the old setup which is consistent with the formal convergence order of our numerical schemes. Comparing the radii of the old and new TOV solutions another difference becomes evident: The radius of the old setup is approximately half the size of the radius of the new, more realistic setup. This also implies that effectively, if the same resolution is used for both setups, the star of the old setup is covered by only half the number of points that the star in the new setup is covered with. This means that the old setup employs effectively a lower resolution than the new setup even though the grid spacing on the finest refinement level is the same in both cases. Hence, we suspect that the old setup leads to a measured convergence order closer to the formal one because the damping of the density oscillations is dominated by discretization errors not originating from the surface due to the lower effective resolution.

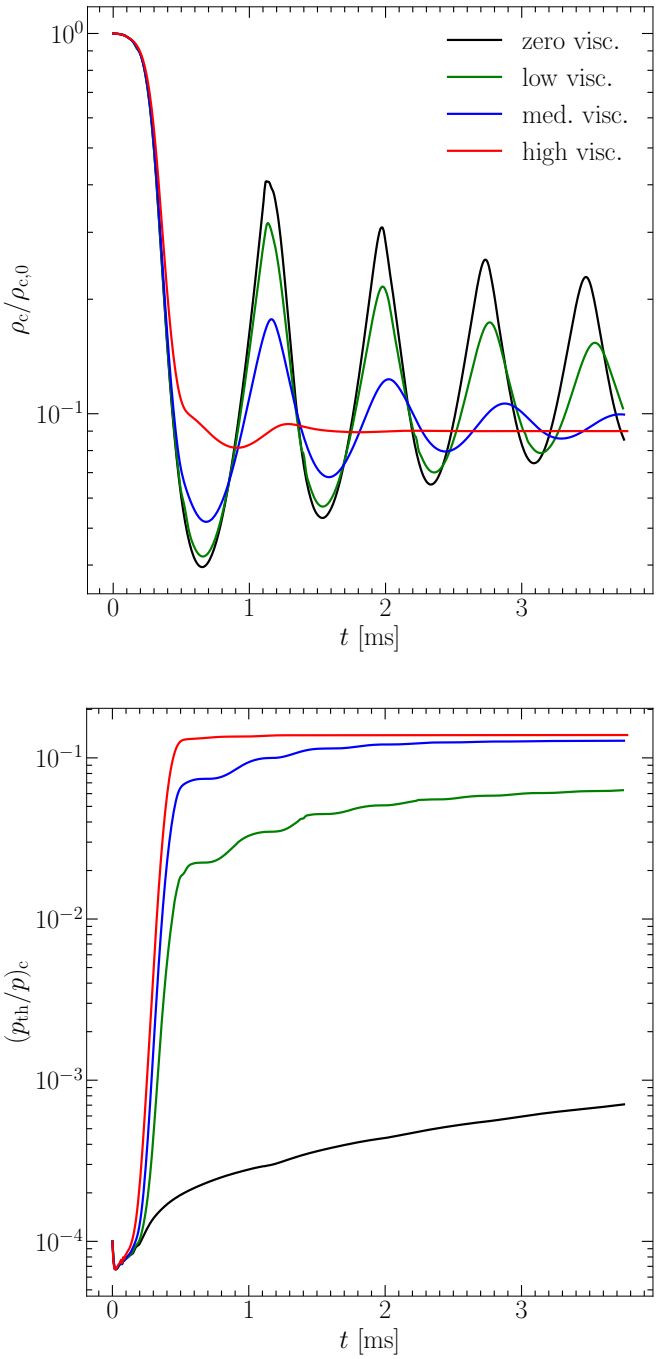

Figure 4.5: Central rest-mass density and thermal pressure over total pressure in migrating viscous neutron stars
Shown are the normalized central density (top panel) and the ratio of the thermal pressure over the total pressure (bottom panel) in the center of the migrating neutron star as a function of time for all viscosity cases.

4.3.2 Migration of viscous neutron stars

In this test problem we simulate a migrating TOV star [117] with four different values for the bulk viscosity, i.e., $\zeta_h \in \{0, 8\times10^{27}, 4\times10^{28}, 8\times10^{29}, 10^{30}\}\,\mathrm{g\,s^{-1}\,cm^{-1}}$ which are denoted as zero, low, medium and high viscosity cases, respectively. As before, we use a standard polytropic EOS with a hybrid thermal component and choose $K = 100$ and $\Gamma = \Gamma_{\mathrm{th}} = 2$. As in [117] the stars are initial-

ized to have a central rest-mass density of $\rho_c = 8 \times 10^{-3}$ which results in an ADM mass of $M = 1.447\,M_\odot$. Furthermore, the computational grid has outer boundaries at $64\,M_\odot \simeq 95\,\mathrm{km}$ in the three spatial directions and we employ a z-symmetry in the equatorial plane. We use four refinement levels with a factor of two refinement; the last level, which has a width of $24\,M_\odot$, has a grid spacing of $\Delta x = 0.25\,M_\odot \simeq 370\,\mathrm{m}$.

We start by describing the evolution of the characteristic central quantities shown in Fig. 4.5. The top panel shows the evolution of the central rest-mass density normalized by its initial value at $t = 0$ for all five cases in different colors. First, as expected, the magnitude of ζ has a strong influence on the damping time of the nonlinear central density oscillations. Higher values of the bulk viscosity lead to more efficient damping of density oscillations.

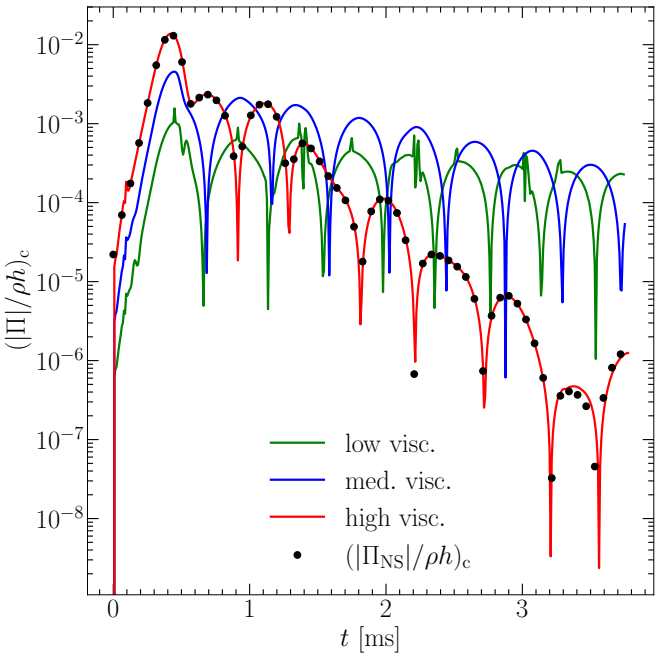

Figure 4.6: Absolute inverse relativistic Reynolds number in migrating viscous neutron stars
Shown is the absolute inverse Reynolds number, i.e., the ratio of the absolute value of the bulk-viscous pressure over the enthalpy density, in the center of the migrating neutron star for all viscosity cases. The black symbols denote the ratio of the absolute NS value over the enthalpy density at the same location for the high viscosity case.

Additionally, the average values around which these oscillations occur decrease with increasing bulk viscosity. This can be understood by looking at the bottom panel in Fig. 4.5 which shows the evolution of the thermal pressure component $p_{\rm th} := (\Gamma_{\rm th} - 1)\rho\epsilon_{\rm th}$ in the center over the total pressure in the center. Higher values for ζ lead to a more rapid initial increase and higher asymptotic values in $(p_{\rm th}/p)_c$. As a result, the oscillating TOV stars with a larger value for the bulk viscosity have larger thermal support in the center which causes changes in their overall structure. This leads to less compact asymptotic states and a lower central rest-mass density.

Figure 4.6 shows the absolute value of the relativistic inverse Reynolds number $\mathcal{R}^{-1} = \Pi/\rho h$ in the center of the stars. By comparing to the top panel of Fig. 4.5 we observe that a viscous flow with $|\mathcal{R}^{-1}| \gtrsim 10^{-2}$, which is realized in the high viscosity case, has a large influence on the evolution of the central rest-mass density. Additionally, the black filled markers show the inverse Reynolds number computed from the NS value $\Pi_{\rm NS} = -\zeta\Theta$. We observe good agreement between the true bulk-viscous pressure Π and $\Pi_{\rm NS}$ which means that our simulations deviate only weakly from a first-order formulation of relativistic dissipative hydrodynamics. Nevertheless, the simulations presented here are causal.

Now, we move on to the evolution of shock waves commonly observed in migration tests. Our results are presented in Fig. 4.7 where a spacetime diagram of the evolution of the first three shock fronts on the x-axis is shown. We note that the trajectories presented here might not include the location of the shock fronts at all times as our tracking algorithm is designed to track only forward moving shocks having a coordi-

nate velocity derivative below a certain threshold. However, this does not influence our conclusions as those parts of the shock trajectories which are not visible in Fig. 4.7 constitute only small segments.

First, we observe that a larger value for the bulk viscosity leads to a shock front which develops at larger distances from the core. In order to understand this, we need to describe briefly the generic mechanism of shock-front formation. Prior to the development of the shock front, the neutron star is contracting and matter at larger distances is radially infalling. As soon as the contraction of the neutron star is decelerated as the result of increasing pressure gradients, radially infalling material hits the neutron star surface and gets shocked. Consequently, an outward propagating shock is generated as soon as the shock is strong enough to overcome the ram pressure generated by the radially infalling material.

Now, this process is influenced by the presence of viscosity. As can be seen in Fig. 4.5, viscosity damps the violent density oscillations which occur in the star and produces heat. This also changes the overall structure of the neutron star as discussed previously. The changes in the neutron star structure can be appreciated in Fig. 4.8 which shows spacetime diagrams of the coordinate velocity on the x-axis, i.e., v^x, for the zero (left half) and medium viscosity case (right half). Additionally, we use black contour lines to plot the evolution of the density contours at $\rho \in 4.5\times\{10^{14}, 10^{12}, 10^{10}, 10^{8}\}\,\mathrm{g\,cm^{-3}}$ with solid, dashed, solid and again dashed linestyles, respectively. Note that the inner solid contour line corresponds to ρ_h and the outer solid contour line is chosen to be ρ_l, see Eq. (4.48). The colored markers denote the locations of the first three shock fronts for each of the two simulations, respectively.

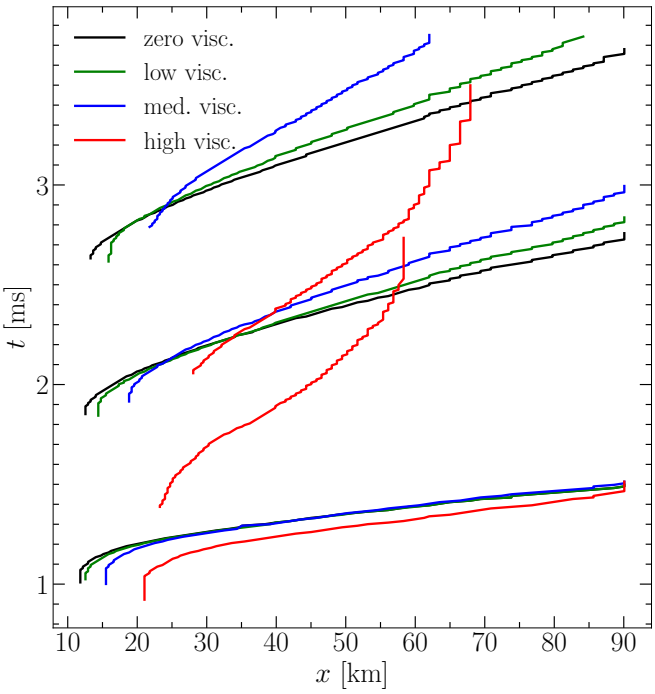

Figure 4.7: Shock-front evolution in migrating viscous neutron stars
Spacetime diagram of the evolution of the shock fronts on the x-axis which develop at the neutron star surface as a result of the violent nonlinear oscillations during the migration of the star. Different colors denote different viscosities.

We observe in Fig. 4.8 that the inner solid density contour line of the zero viscosity case reaches larger values in x than the cooresponding density contour line in the medium viscosity case. This indicates that the neutron star in the medium viscosity case has a less compact core which can be explained by the additional thermal support observed in Fig. 4.5. At the same time a larger density gradient is present in the outer layers of the medium viscosity case. Also, the inner dashed density contour line is located further out than in the zero viscosity case. As a result, the pressure gradient in the outer layers of the medium viscosity star is increased which means that the neutron star surface and the location where the shock forms have moved outwards in

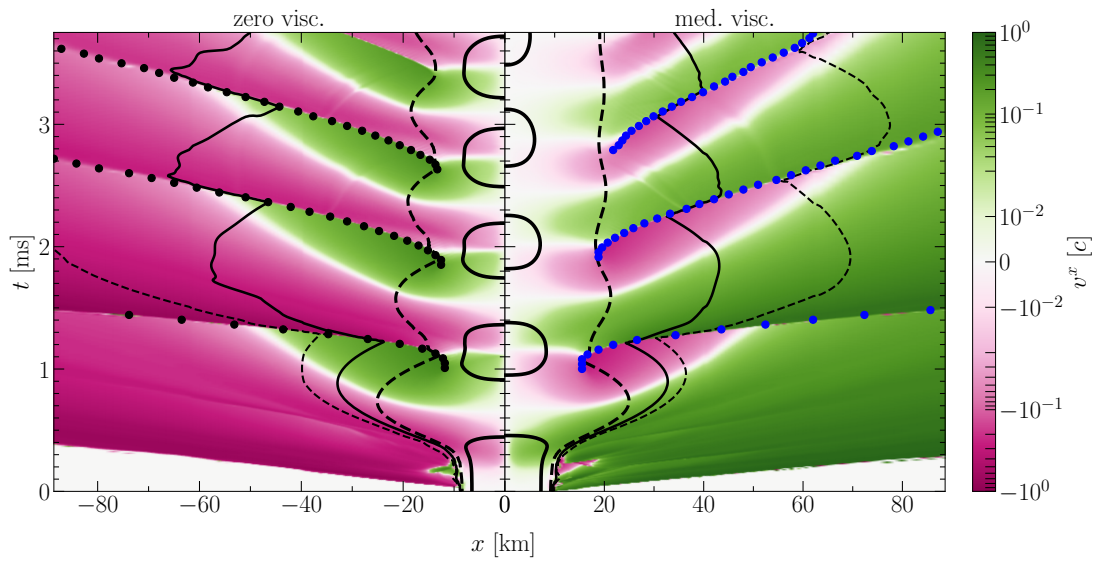

Figure 4.8: Fluid velocity evolution in migrating viscous neutron stars
The color code shows spacetime diagrams of the evolution of the Eulerian three-velocity in x-direction, i.e., v^x, on the x-axis for the zero viscosity (left panel) and medium viscosity (right panel) cases. The symbols denote the evolution of the corresponding shock fronts already presented in Fig. 4.7. The inner solid, inner dashed, outer solid and outer dashed lines denote density contours at $\rho = 4.5\times\{10^{14}, 10^{12}, 10^{10}, 10^{8}\}\,\mathrm{g\,cm^{-3}}$, respectively. Note that the inner solid line represents ρ_h while the outer solid corresponds to ρ_l, see Eq. (4.48).

comparison to the zero viscosity case.

Second, we observe that larger values for the bulk viscosity lead to less energetic shock waves, especially when considering the second and third shock wave. This can be seen in Fig. 4.7 when concentrating on the second shock wave for each value of the bulk viscosity. Clearly, the velocities of the shock fronts decrease with higher ζ. In the high viscosity case the shock front of the second wave even stops propagating when it reaches $\sim 60\,\mathrm{km}$. The reason for this behaviour is mainly related to the damping of the neutron star oscillations due to viscosity. For the viscous cases matter is still radially infalling and being shocked at the neutron star surface. But due to the increased dissipative transfer of radial kinetic energy to thermal energy in the neutron star a lower energy budget is available to accelerate the shock. Additionally, most of the shock waves are propagating through viscous material in the beginning which further increases dissipation of kinetic energy.

4.4 Bulk viscosity in binary merger simulations

4.4.1 Simulation setup

In this section we discuss the simulations of BNS mergers with a constant causal bulk viscosity prescription. We use the initial data setup presented in Appendix C which produces a long-lived SMNS remnant. Similar to the numerical experiments with isolated stars, we employ a hybrid EOS of the form $p = p_{\mathrm{cold}} + \rho\epsilon_{\mathrm{th}}(\Gamma_{\mathrm{th}} - 1)$ where the cold part is modeled by a cold, β-equilibrated slice of the TNTYST EOS [301]. We choose $\Gamma_{\mathrm{th}} = 1.7$ which corresponds to the optimal value found in [116]. We simulate four different values for the bulk viscosity ζ which is given by $\zeta_h \in \{\zeta_0, \zeta_0/2, \zeta_0/5, 0\}$ with $\zeta_0 = 10^{30}$ g cm^{-1} s^{-1}. The value of ζ_0 corresponds approximately to the highest bulk viscosity observed in the [200]. In accordance with the magntiude of ζ the simulations

are labeled as high, medium, low and zero viscosity. We choose $\rho_h \approx 4.52 \times 10^{14}$ g cm^{-1} and $\rho_l \approx 1.13 \times 10^{12}$ g cm^{-1}. Besides, we have set $\tau_h \approx 2.7 \times 10^{-4}$ ms.

All reported simulations are performed with a resolution of $\Delta x \sim 0.17\ M_\odot \approx 260$ m on the sixth refinement level. We have also performed simulations with a lower resolution of $\Delta x \sim 0.25\ M_\odot \approx 370$ m for the zero, low and high viscosity case. We observe qualitatively consistent behaviour such that we only report the results of the high-resolution simulations. In addition, the computational grid has outer boundaries at $1000\,M_\odot \simeq 1476$ km in the three spatial directions and we employ a z-symmetry in the equatorial plane. We use six refinement levels with factor of two refinement. The last level, which has a width of 70 $M_\odot$ in order to ensure that only inviscid matter is passing refinement boundaries, is centered at the center of the domain when the separation between the "barycenters" of the two stars is $\lesssim 9\ M_\odot$.

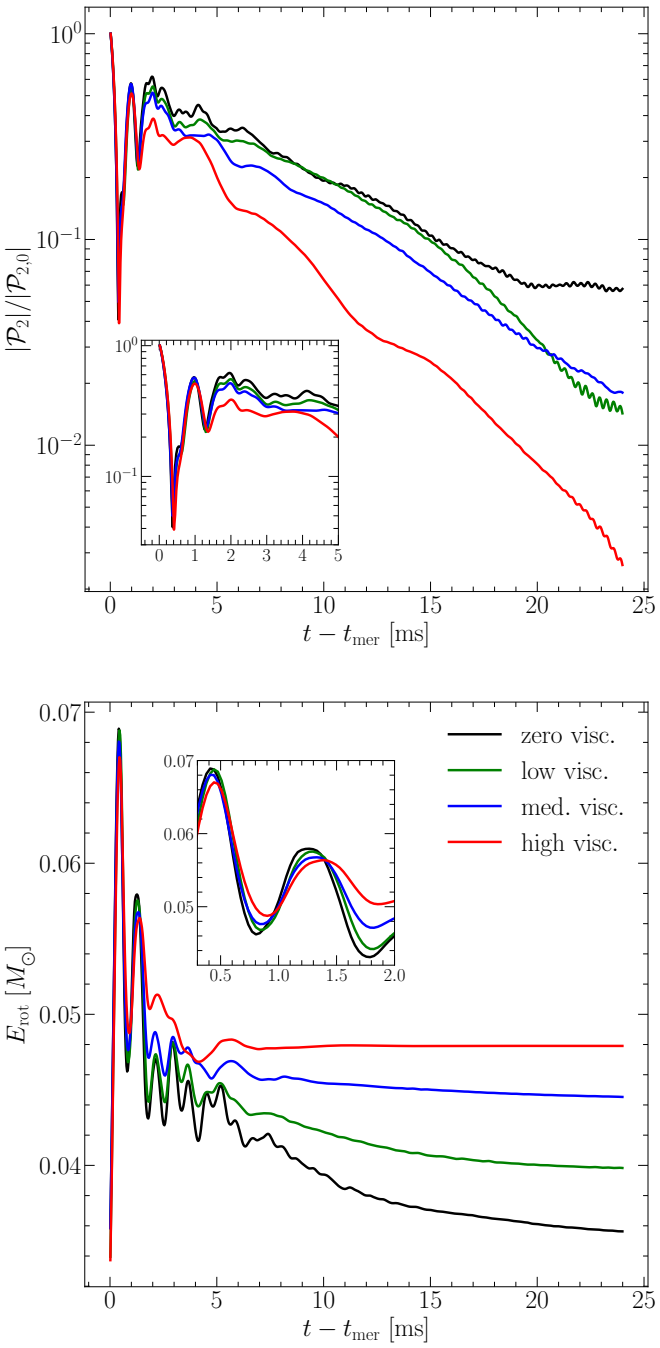

Figure 4.9: Rest-mass density deformations and rotational energy in viscous neutron star mergers *Top*: Normalized $m = 2$ mode of the density distribution, see Eq. (4.64), for all configurations. The red, blue, green and black lines denote the high, medium, low and zero viscosity cases, respectively. *Bottom*: Rotational kinetic energy, see Eq. (4.65), for the same configurations.

4.4.2 Structural and rotational properties

We start by describing the overall evolution of the binaries by focussing on the structural and the rotational properties of the SMNS. Differences in the SMNS structure can be measured by using a modal decomposition of the density similar to [245]

$$\mathcal{P}_i := \int \rho W e^{-im\phi} \sqrt{\gamma}\, dx dy dz. \tag{4.64}$$

We show the quantity $\mathcal{P}_2/\mathcal{P}_{2,0}$, i.e., the $m = 2$ mode of the density distribution normalized by its value at $t = t_{\rm mer}$, in the top panel of Fig. 4.9. We observe that $\mathcal{P}_2/\mathcal{P}_{2,0}$ is monotonically affected by the magnitude of the

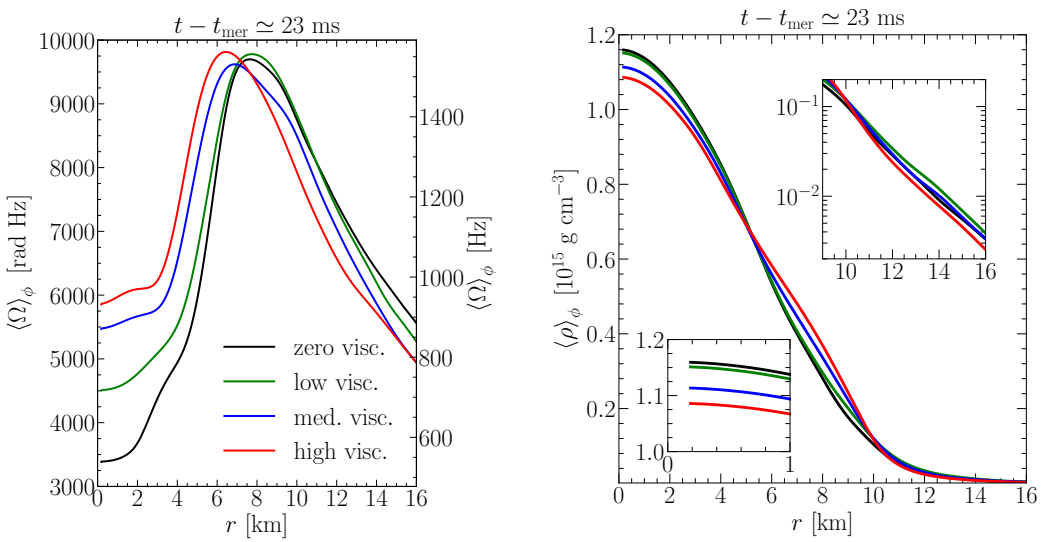

Figure 4.10: Angular velocity and rest-mass density profiles in viscous neutron star mergers
Left (Right): ϕ-averages in the equatorial plane of the angular velocity (rest-mass density) as a function of the coordinate radius $r := (x^2 + y^2)^{1/2}$ at $t - t_{\rm mer} \approx 23$ ms. Shown are the zero, low, medium and high viscosity cases in black, green, blue and red, respectively.

bulk viscosity which enhances the decrease of the $m = 2$ deformation of the SMNS with time. Given that this mode, the so-called bar-mode, is mainly responsible for GW losses [291], we also expect the GW amplitude to be affected in a similar way. At this point, however, we observe that strong bulk viscosities lead to decreased $m = 2$ density deformations which means that a more axisymmetric SMNS is produced. To analyse the rotational properties of the SMNS we employ the rotational kinetic energy, which we approximate as

$$E_{\rm rot} := \frac{1}{2} \int \rho h v^\phi u_\phi \sqrt{\gamma}\, dx dy dz. \tag{4.65}$$

The quantity $u^\phi := -W\beta^\phi/\alpha + W v^\phi$ denotes the ϕ-component of the fluid four-velocity. Furthermore, the quantities β^ϕ and v^ϕ are the ϕ-component of the shift vector and the the Eulerian three-velocity, respectively. The rotational energy is shown in the bottom panel of Fig. 4.9.

We observe two important effects. First, initial oscillations of $E_{\rm rot}$ appearing in the first $\lesssim 2$ ms after merger are damped stronger with higher viscosities, e.g., see the inset in the bottom panel of Fig. 4.9. Second, we find that the final amount of rotational energy depends monotonically on the value of the bulk viscosity where higher bulk viscosities lead to a higher $E_{\rm rot}$ at the end of the simulations. The damping of the oscillations can be explained naturally by considering that the origin of these oscillations are periodic collisions of the two neutron star cores in the postmerger. Bulk viscosity leads to damping of fluid expansion and compression and therefore directly affects such periodic core bounces through strong nonlinear damping. Further evidence for this process is provided by the inset in the left panel of Fig. 4.9 which shows reduced deformations in the corresponding time interval. The behaviour of the final rotational energy of the SMNS indicates that strong bulk viscosities are able to efficiently decrease losses of kinetic rotational energy. This is not suprising as the main mechanism by which rotational energy is lost in the postmerger phase is the emission of GWs sourced by rotating $m = 2$ density deformations. Due to their reduction a larger portion of the rotational kinetic energy can be conserved until the end of the simulations.

We show further evidence for this mechanism in Fig. 4.10, where the left (right) panel shows ϕ-averages in the equatorial plane of the angular velocity (rest-mass density) as a function of the coordinate radius $r := (x^2 + y^2)^{1/2}$ at $t - t_{\rm mer} \approx 23$ ms. At this time, we observe higher angular velocities with higher bulk viscosity in the region $r \lesssim 7$ km, while the opposite trend, i.e., lower angular velocity with higher bulk viscosity, is realized for 7 km $\lesssim r$. The different angular velocity profiles are the consequence of the efficient damping of $m = 2$ density deformations as these are important in order to transport angular momentum efficiently to large radii r, see also [210]. Thus, reduced deformations lead to less efficient angular momentum redistribution. On top of that, the increased centrifugal and thermal support in the innermost regions of the SMNS leads to a redistribution of matter inside the SMNS core which can be seen in the rest-mass density profiles shown in the right panel. The density is decreased (increased) in the inner (outer) core, i.e., $r \lesssim 5$ km (5 km $\lesssim r$).

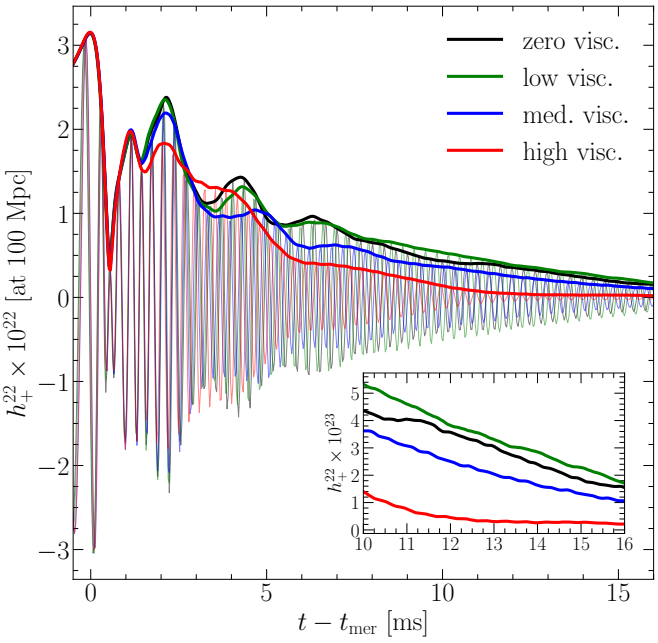

Figure 4.11: Gravitational-wave strain in viscous neutron star mergers
Gravitational-wave strain in the $\ell = 2, m = 2$ mode of the + −polarisation extracted at ~ 740 km and normalized to a distance of 100 Mpc. Shown are the configurations zero (black line), low (green line), medium (blue line) and high (red line) viscosity. Thick solid lines report the corresponding amplitudes.

4.4.3 Gravitational-wave emission

Next, we report the emitted postmerger GW signal in Fig. 4.11. We start by focussing on GW damping. Overall, we observe a strong damping of the $\ell = 2, m = 2$ mode of the GW signal with higher viscosities which is explained by the efficient decrease of the $m = 2$ deformation, see e.g., Fig. 4.9.

More precisely, we observe that for $t - t_{\rm mer} \lesssim 1$ ms all three signals are very similar and start to deviate only afterwards. This time corresponds approximately to half a collision-and-bounce cycle of the stellar cores after which the cores reach a maximum separation. This can be observed in Fig. 4.11 where at $t - t_{\rm mer} \approx 1$ ms the second local maximum in the signal is reached. Afterwards, the three signals start to differ in amplitude but not in phase until $t - t_{\rm mer} \lesssim 2.5$ ms, which is a clear sign of the impact of bulk viscosity. Higher bulk viscosities lead to stronger dissipation of the radial kinetic energy stored in the colliding motions of the stellar cores. At $t - t_{\rm mer} \approx 2.5$ ms we observe that the waveforms aquire a phase difference which can be understood by looking at the power-spectral density of the postmerger GW signal shown in Fig. 4.12.

Overall, we observe that the highest peak of the spectral density, f_2, is shifting monotonically to higher frequencies, e.g., the difference between the zero and high viscosity case is $\Delta f_{\rm zero,high} \approx 280$ Hz. This value is approximately twice as larger as the frequency shifts observed in [140] and [202] where weak chemical equilibration has been implemented either in the instantaneous equilibration limit, i.e., $\Gamma \to \infty$, with

Γ being the reaction rate, or by using Urca rates self-consistently in the simulations, respectively. This behaviour can be understood by keeping in mind that higher viscosities lead to a decreased $m = 2$ deformation of the SMNS as shown in the top panel of Fig. 4.9. Smaller deformations of the SMNS cause two effects both of which lead to a spin-up of the SMNS core.

First, the interaction between the high-density bar-mode and the surrounding isotropic low-density matter leads to spiral-wave winds and mass ejection on dynamical timescales [210, 252]. But, this interaction leads not only to dynamical mass ejection. More generically, the redistribution of angular momentum to larger distances from the SMNS core is caused, as mentioned before. Effectively, this means that higher rotational frequencies can be realized in the "inner" regions of SMNS if the development of the high-density bar-mode is suppressed due to large bulk viscosities.

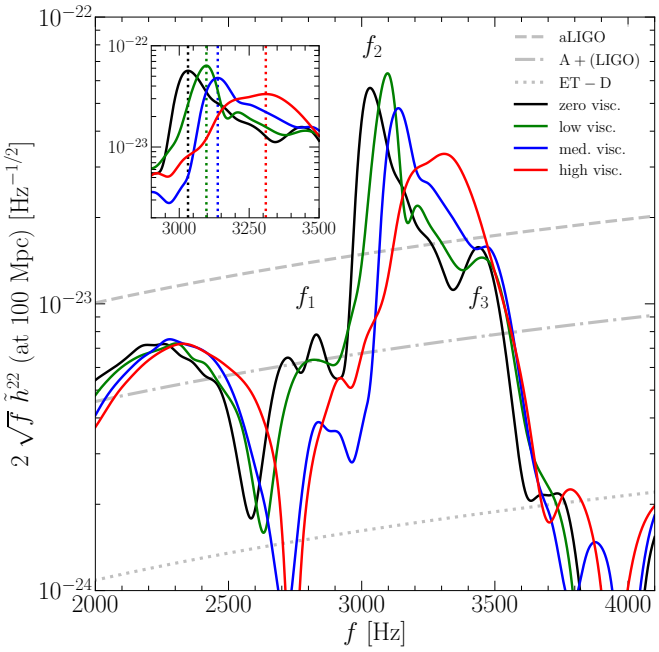

Figure 4.12: Gravitational-wave power spectral density in viscous neutron star mergers
Power spectral density of the $\ell = 2, m = 2$ mode of the + –polarisation extracted at ~ 740 km and normalized to a distance of 100 Mpc for the configurations zero (black line), low (green line), medium (blue line) and high (red line) viscosity. Grey lines denote sensitivity curves of a selection of GW detectors [146, 61].

Second and perhaps most importantly, the decrease in GW emission shown in Fig. 4.11 leads to a decrease in angular momentum losses through GWs. Effectively, this means that higher rotational frequencies can be realized in the SMNS if the moment of inertia is kept fixed. Then, higher rotational frequencies will also lead higher frequencies in the GW spectrum.

Additionally, we observe in Fig. 4.12 that the neighbouring peaks, i.e., the local maxima denoted by f_1 and f_3 in Fig. 4.12, are decreasing with increasing bulk viscosity as well. Assuming that these peaks are the result of the nonlinear coupling between the rotating non-axisymmetric bar-mode and the quasi-radial mode excited through the collision [291, 296], the decrease can be explained by bulk-viscous damping of the quasi-radial mode.

Furthermore, as can be seen in the top panel of Fig. 4.9 a low viscosity also leads to a decrease of the $m = 2$ deformation, which, however, is very weak. At the same time, a low viscosity leads to a weak spin-up of the SMNS core shown in the left panel of Fig. 4.10. For the low viscosity case both of these effects, i.e., the decrease of the $m = 2$ deformation and the spin-up of the SMNS core, lead to comparable but counteracting effects on the damping of gravitational waves. While the reduced $m = 2$ deformation decreases GW emission, the spin-up leads to an increased emission. Both of these effects become comparable for the low viscosity case, which leads to the amplitude of the $\ell = 2, m = 2$ mode being equal to and at certain times even higher than the amplitude from the zero viscosity case. Note that non-monotonic behaviour has been observed before in general-relativistic LESs of BNS mergers [244] where extra terms in

the hydrodynamic equations take the form of a shear-viscous tensor.

To conclude the discussion about the GW emission from viscous BNS mergers we briefly mention the impact of bulk viscosity on the cummulative energy emitted by GWs $E_{\rm GW}$. Figure 4.13 shows the emitted GW energy (solid lines) together with dimensionless spin of the SMNS remnant $\chi_{\rm rem}$ (dashed lines) defined by

$$\chi_{\rm rem} := \frac{J_{\rm ADM} - J_{\rm GW}}{(M_{\rm ADM} - E_{\rm GW})^2}, \tag{4.66}$$

where $M_{\rm ADM}$ and $J_{\rm ADM}$ are the initial ADM mass and angular momentum, respectively, and $J_{\rm GW} \approx J^z_{\rm GW}$ is the radiated angular momentum approximated by its z-component (see, e.g., [226]).

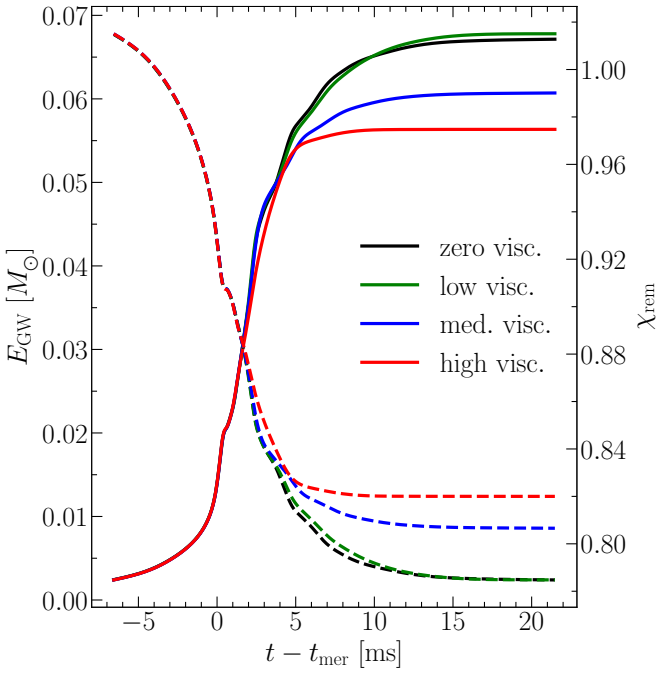

Figure 4.13: Radiated energy and remnant spin in viscous neutron star mergers
Evolution of the radiated GW energy (solid lines) and of the dimensionless spin of the SMNS remnant (dashed lines) for the four configurations considered. Both quantities are measured at ~ 740 km.

Higher bulk viscosities lead to less energy losses due to GW emission. Again, it is interesting to consider the low viscosity case as we observe non-monotonic behaviour which corresponds to our previous discussion about GW damping in the low viscosity case. In essence, our previous discussion is directly related to the non-monotonicity observed here. We recall that the effect of reduced $m = 2$ density deformations is comparable to the effect of the spin-up of the SMNS core resulting in an increased radiated energy.

4.4.4 Thermal properties

In this subsection we discuss the impact of bulk viscosity on the thermal properties of BNS mergers. We start by reporting the maximum rest-mass density (top panel of Fig. 4.14) and the thermal energy

$$E_{\rm th} := \int \rho \epsilon W \sqrt{\gamma}\, dxdydz, \tag{4.67}$$

(bottom panel of Fig. 4.14).

First, from the inset in the top panel of Fig. 4.14 we observe that the strong density oscillations which occur in the first ~ 5 ms after merger are damped efficiently in the cases with strong bulk viscosities. This is not suprising as these oscillations are related to expansion and compression cycles of the newly formed SMNS. It is precisely the kinetic energy stored in fluid expansion and compression which is dissipated through bulk viscosity. Furthermore, we observe that a larger bulk viscosity leads to a less dense SMNS core at the end of our simulations at around $t - t_{\rm mer} \approx 24$ ms. This effect is similar to the increase in the kinetic rotational energy observed previously, e.g., see Fig. 4.9 and

Fig. 4.10. Hence, this can be explained by the additional centrifugal support which is present for larger bulk viscosities.

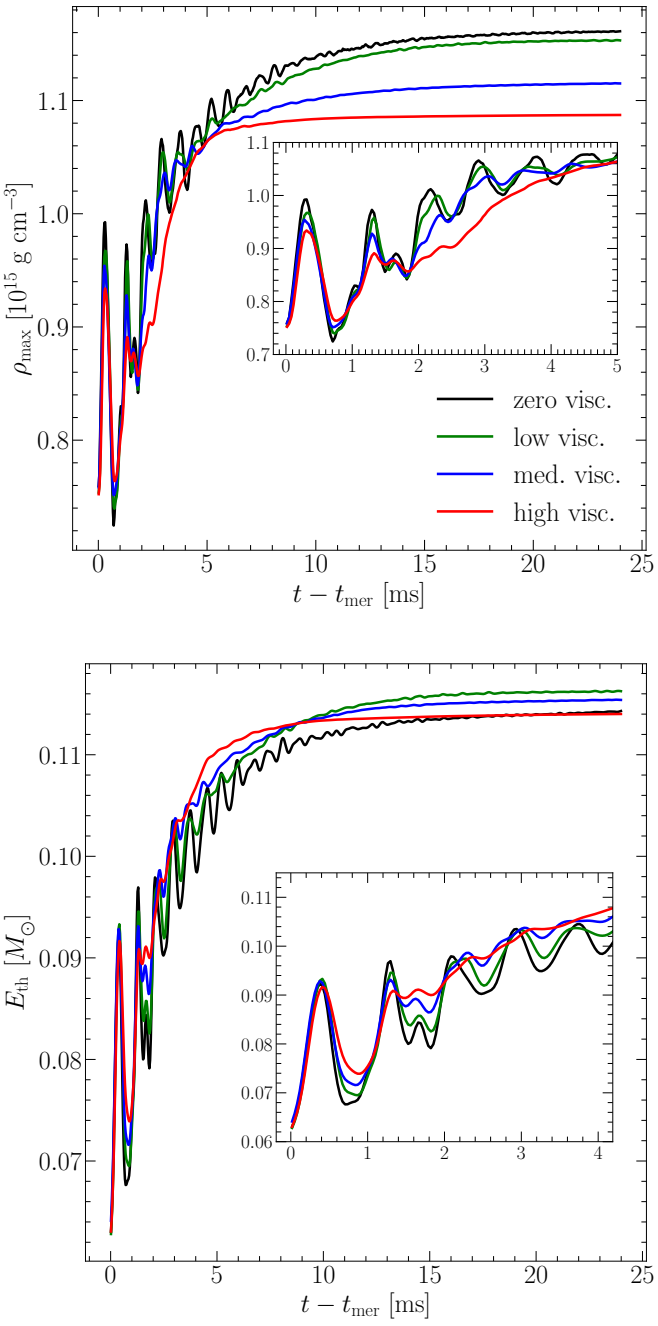

Figure 4.14: Maximum rest-mass density and thermal energy in viscous neutron star mergers
Top: Maximum rest-mass density in the postmerger phase for the zero (black line), low (green line), medium (blue line) and high (red line) viscosity case. The inset shows a zoom-in for the first five milliseconds. *Bottom*: Same as *Top* but for the total thermal energy defined in Eq. (4.67).

Second, from the bottom panel of Fig. 4.14 we find that larger bulk viscosities lead to a larger overall thermal energy in the first $\sim$ 5 ms after merger. As observed before, during the first $\sim$ 5 ms after merger the damping of large density oscillations is most efficient such that also the dissipation of kinetic into thermal energy is most efficient. Thus, larger bulk viscosities lead to larger thermal energies during that time. However, after the first five milliseconds other effects need to be taken into account in order to explain the evolution of $E_{\rm th}$. While the dissipation of kinetic into thermal energy leads to an increase in thermal energy the aforementioned decrease in central rest-mass density leads to a decrease in thermal energy. Both of these effects are competing on a timescale larger than five milliseconds which leads to the non-monotoic behaviour observed in $E_{\rm th}$ at the end of our simulations. In particular, we see that the decrease in central density of the medium and high viscosity cases leads to *lower* final thermal energies than in the low viscosity case which has the largest final thermal energy. The final thermal energy of the high viscosity case is even below the inviscid case.

Finally, we show the total kinetic energy in the z-direction

$$E_z := \frac{1}{2}\int \rho h v^z u_z \sqrt{\gamma}\, dx dy dz, \tag{4.68}$$

in Fig. 4.15. In order to strengthen the claim that during the first $\sim$ 5 ms after the merger most of the bulk-viscous energy dissipation is taking place we can make use of E_z. This

is illustrative as the kinetic energy in the z-direction is generated purely by strong oscillations and shocks coming from the collision of the binary and is therefore subject to bulk-viscous damping. Here, we see very clearly that the behaviour is monotonic and larger bulk viscosities lead to a smaller E_z. Additionally, we also verify that most of the kinetic energy is dissipated during the first ~ 5 ms after merger.

Furthermore, we can also evaluate "how viscous" the fluid is or in other words, how large the deviations from thermodynamic equilibrium are by measuring the relativistic Reynolds number $\mathcal{R}$ defined in Eq. (2.114). We present the quantity $|\mathcal{R}^{-1}|$ measured in the center of the grid for the first ~ 5 ms after merger in the top panel of Fig. 4.16 while the quantity $|\Pi|/p$ measured in the center of the grid for the same time interval is shown in the bottom panel. We present time-series for all simulations and additionally show the quantities $(|\Pi|_{\text{NS}}/\rho h)_c$ and $(|\Pi|_{\text{NS}}/p)_c$ denoted by dashed lines in both panels, see also Eq. (2.104). The NS values are presented only for the high viscosity case to avoid overcrowding the figure.

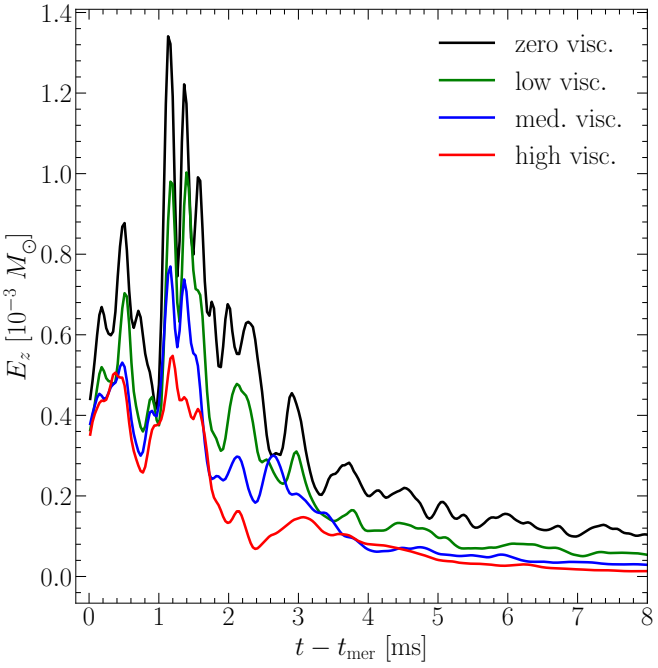

Figure 4.15: Kinetic energy in viscous neutron star mergers
Total kinetic energy in the z-direction defined in Eq. (4.68) for all viscosity cases considered in this investigation.

Both panels show qualitatively the same unsurprising behaviour: Larger bulk viscosities lead to a larger inverse Reynolds number as well as larger viscous contributions to the total pressure. It is interesting to note that for the high viscosity case the inverse Reynolds number reaches values above $\sim 1\%$ which corresponds to a bulk-viscous pressure that is $\sim 20\%$ of the equilibrium pressure. This happens right after merger when the strongest density oscillations are present. Afterwards, both quantities decrease but remain of this order until $t - t_{\text{mer}} \approx 1.5$ ms.

Then, both quantities drop sharply by approximately two orders of magnitude and, after further decrease, reach values of around $(|\Pi|/\rho h)_c \approx 10^{-5}$ and $(|\Pi|/p)_c \approx 10^{-4}$ at $t - t_{\text{mer}} \approx 5$ ms. This provides further evidence that bulk-viscous dissipation works very efficiently in the first five milliseconds after merger; Figure 4.16 even suggests that during the first 1.5 ms after merger bulk-viscous dissipation is having the biggest impact on the merger.

The measurement of the relativistic Reynolds number enables us to compare off-equilibrium contributions in BNS mergers to the viscous contributions in another relativistic fluids, namely the QGP encountered in HICs. Following the results presented in [202], we first observe that the order-of-magnitude estimates obtained in that study through post-process calculations agree with our findings for the highest viscosity case. This is not suprising as [202] present the maximum inverse Reynolds number over the whole domain which is likely found where the bulk viscosity ζ reaches its maximum. Since our high viscosity case makes use of a constant value for ζ which corresponds

to the highest value found in [202], it is natural to expect similar inverse Reynolds numbers if the underlying fluid motion does not vary significantly.

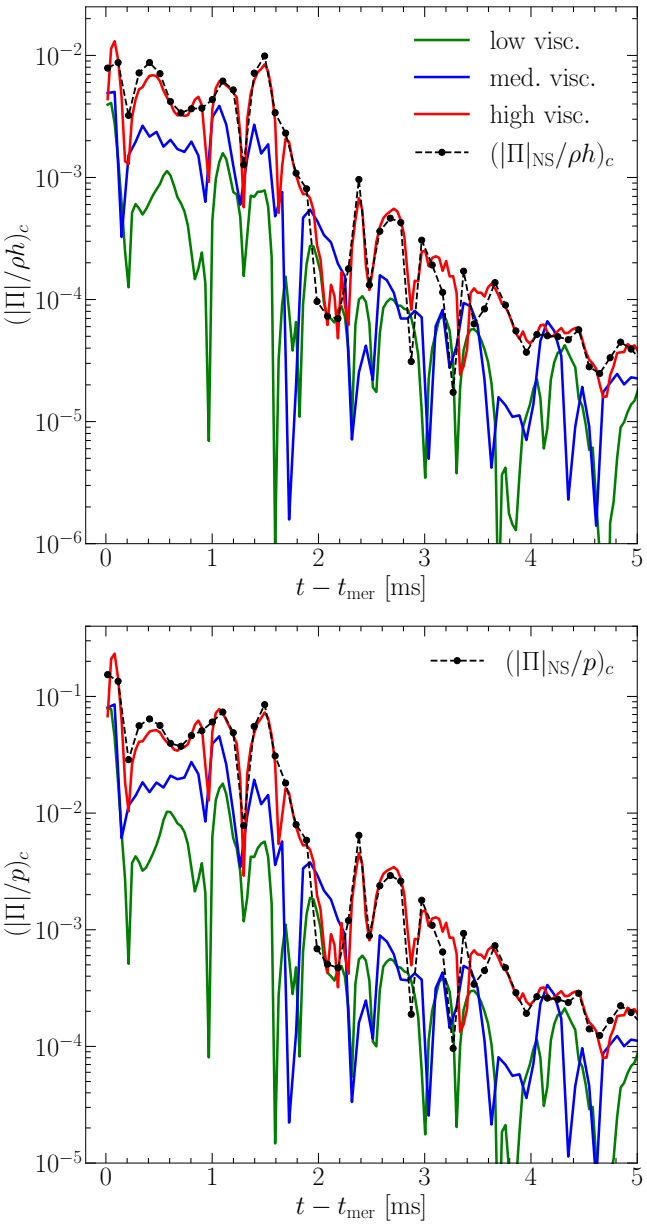

Figure 4.16: Relativistic inverse Reynolds number and bulk-viscous pressure over equation of state pressure in viscous neutron star mergers
Top: Absolute inverse Reynolds number, i.e., the ratio of the absolute bulk-viscous pressure over the enthalpy density, for all viscosity cases in different solid lines. The black dashed line denotes the same quantity but calculated from the NS value. *Bottom*: Same as *Top* but for the ratio of the absolute bulk-viscous pressure over the EOS pressure.

Second, as observed in [202] we find that the inverse Reynolds number in HICs is approximately one order of magnitude higher than in BNS mergers suggesting that the QGP is further away from thermodynamic equilibrium than the high-density matter encountered in a SMNS shortly after merger.

Next, we report sections of the temperature distribution (top row) and the distribution of the quantity Π/p (bottom row) in the equatorial plane at $t - t_{\rm mer} \approx 4.22$ ms for the low (left column), medium (middle column) and high viscosity (right column) cases. The solid line denotes a density contour at $\rho = \rho_h \approx 4.52 \times 10^{14}$ g cm^{-1} while the dashed line denotes a density contour at $\rho = \rho_l \approx 1.13 \times 10^{12}$ g cm^{-1}. During this time the strong damping of density oscillations and thus the dissipation of oscillatory kinetic energy into thermal energy has almost ended, as discussed previously. However, the SMNS has not settled into an approximately axisymmetric state yet where the rotational energy density has been redistributed. Thus, during this time the thermal energy is not yet affected by the indirect influence of matter redistribution due to centrifugal forces.

As discussed previously, this indirect influence leads to non-monotonicity in the thermal energy at the end of the simulations. On the other hand, this means that we should be able to observe higher temperatures for higher bulk viscosities during this time because all configurations have a similar compactness as can be observed in Fig. 4.14, where all configurations have a comparable maximum rest-mass density at $t - t_{\rm mer} \approx 4.22$ ms. Indeed, we observe that the temperature distributions shown

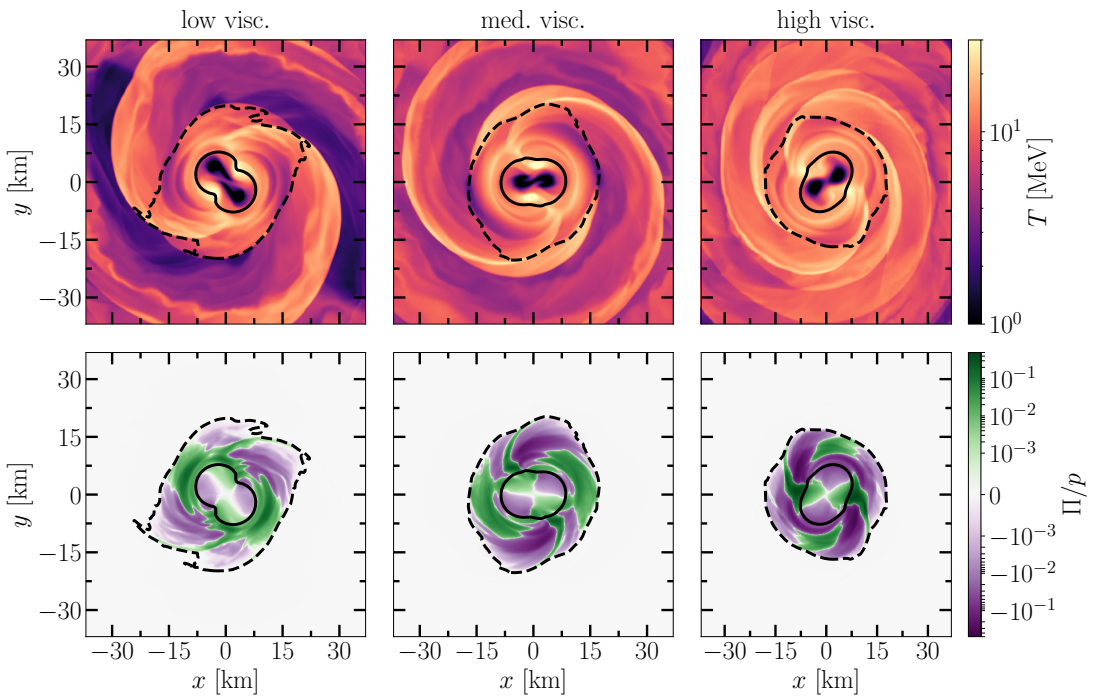

Figure 4.17: Cross-sections of temperature and bulk-viscous pressure over equation of state pressure in viscous neutron star mergers
The color code shows cross-sections of the temperature T (top row) and of the ratio of the bulk-viscous pressure Π over the EOS pressure p in the (x, y) plane. The snapshots are taken at $t - t_{\rm mer} = 4.22$ ms. Shown are the low viscosity (left column), medium viscosity (middle column) and high viscosity (right column) cases.

in the top row of Fig. 4.17 look more homogeneous and feature less "cold" material, i.e., $T \lesssim 5$ MeV, if the bulk viscosity is large.

Two effects are important in order to understand this behaviour. First, as already mentioned, higher bulk viscosities lead to more dissipation of kinetic into thermal energy which leads to an increase in temperature if the fluid is not expanding simultaneously (adiabatic cooling might dominate the temperature evolution). Second, the decrease in kinetic energy is affecting the redistribution and ejection of loosely bound matter through shock waves. This means that in addition to the increased dissipative heating due to bulk viscosity the SMNS is also less efficient in transporting heated matter through shock waves. Both of these effects lead to the relatively homogeneous distribution of temperature in the outer layers of the SMNS for the high viscosity case shown in the top right panel of Fig. 4.17.

In addition, the lower row shows how the bulk-viscous pressure is distributed. First, given that ρ_l marks the value of the rest-mass density below which we set $\zeta = \zeta_l = 0$, e.g., see Eq. (4.48), we observe that the bulk-viscous pressure Π becomes vanishingly small for densities below ρ_l. Furthemore, we observe that $|\Pi|/p$ reaches its maximum value in the transition zone $\rho_l < \rho < \rho_h$, i.e., between the dashed and the solid line. The largest values of $|\Pi|$ are reached in regions with densities higher than ρ_h because these regions have the largest oscillations and bulk viscosities. Nevertheless, the largest values of $|\Pi|/p$ are sensitive to the rapid decrease in pressure in the outer layers of the SMNS which is the reason for $|\Pi|/p$ reaching its maximum at $\rho < \rho_h$.

We also observe that even though the distributions of Π/p are subject to different density oscillations, overall, larger bulk viscosities lead to larger bulk viscous pressures as one would intuitively expect. We recall that this was not the case for the viscous

migration test reported in Fig. 4.6 as the high viscosity case was extremely efficient in the damping of density oscillations.

Last but not least, the distributions of Π/p resemble quadrupolar structures for $\rho_h \leq \rho$ and $\rho_l < \rho < \rho_h$ for all cases. This can be explained by considering the $m = 2$ bar-mode deformation of the SMNS and its interaction with the surrounding matter. It is useful to recall that $\Pi \sim -\zeta\Theta$ in our simulations. This means that regions with $\Pi < 0$ are expanding while regions with $\Pi > 0$ are compressing. First, we observe that one of the intersections between negative and positive bulk-viscous pressure is connecting the two temperature "hot spots" [142] which also correspond to the two largest eddies that developed during the merger. Then, the other intersection separating negative and positive Π regions is found approximately orthogonal to the first intersection connecting the hot spots.

As the SMNS is rotating counter-clockwise in Fig. 4.17 we observe that the regions of the SMNS which are located immediately above either of the two hot spots are always compressing (positive Π) while the regions below either of the two hot spots are expanding (negative Π). As the two eddies located at the two temperature hot spots have the same orientation as the rotation axis of the SMNS, i.e., both rotate counter-clockwise, matter above the hot spots must have a postive Π and matter below a negative Π. The reason for this is that the rotating motions of the eddies compress matter in front of them because of the drag towards the SMNS. Correspondingly, matter behind the eddies expands because of the drag away from the SMNS.

Finally, we discuss sections of the rest-mass density distribution (left half panels) and the distribution of the temperature (right half panels) in the (xz) plane at $t - t_{\rm mer} \approx 23$ ms for the zero (upper left), low (upper right), medium (lower right) and high viscosity (lower left) cases in Fig. 4.18. The solid line denotes a density contour at $\rho = \rho_h \approx 4.52 \times 10^{14}$ g cm^{-1}, the dashed line denotes a density contour at $\rho = \rho_l \approx 1.13 \times 10^{12}$ g cm^{-1} and the dash-dotted line denotes a low-density contour at $\rho \approx 1.85 \times 10^{10}$ g cm^{-1} which covers the envelope of the SMNS or torus. This figure helps us to understand the impact of large bulk viscosities on the overall structure of the long-lived SMNS and torus when a quasi-stationary state is reached. First, we observe that the torus has a smaller extent, if the bulk viscosity is increased. Also, the SMNS has a less oblate shape with larger bulk viscosities which is related to the less efficient angular momentum transport to the outer layers of the remnant. In general, large bulk viscosities prevent neutron star matter from reaching large radii which leads to an overall more compact envelope and an higher concentration of angular momentum at smaller radii.

Second, focussing on the temperature distributions, we find that the low-density funnel above the SMNS has overall lower temperatures with larger bulk viscosities. At this point it is important to remark that large temperatures in the funnel region are most likely the consequence of using a hybrid EOS with an ideal gas law because a comparable study using fully tabulated hot EOSs did not show this behaviour [244]. However, since we are interested in learning about the qualitative impact that large bulk viscosities have in the postmerger phase, it is still interesting to compare the temperature distributions for the different cases to understand how bulk viscosity can impact the funnel region. In our case, large temperatures in the funnel region stem from bound shock-heated material which accumulates above the SMNS. As bulk viscosity tends to damp violent nonlinear density oscillations of the SMNS, which are a primary source of shock waves, larger bulk viscosities tend to produce weaker shock waves and therefore less efficient shock-heating in the funnel region.

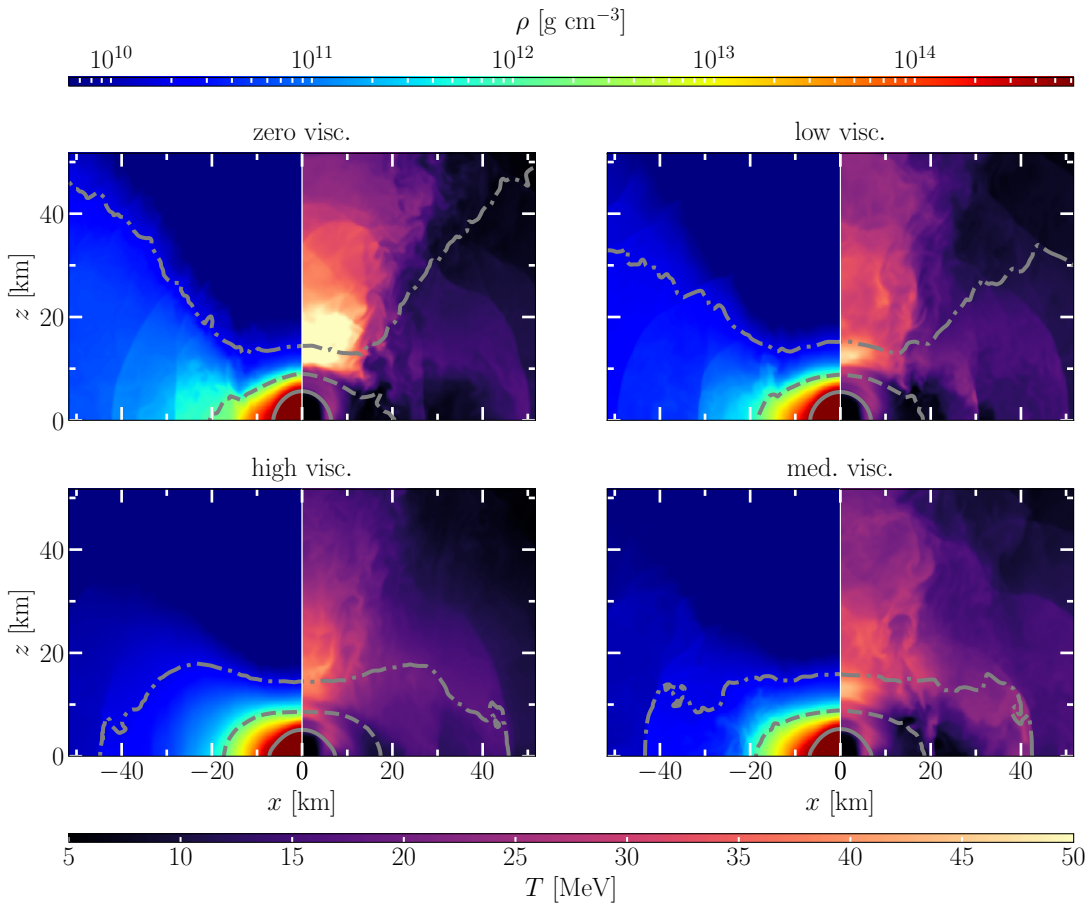

Figure 4.18: Cross-sections of rest-mass density and temperature at small distances in viscous neutron star mergers
Left (Right) half of each panel: The color code shows cross-sections of the rest-mass density ρ (temperature T) in the (x,z) plane. The snapshots are taken at $t - t_{\rm mer} = 23$ ms. Shown is the zero viscosity case in the upper left panel, the low viscosity case in the upper right panel, the medium viscosity case in the lower right panel and the high viscosity case in the lower left panel. The solid line denotes a density contour at $\rho = \rho_h \approx 4.52 \times 10^{14}$ g cm^{-1}, the dashed line denotes a density contour at $\rho = \rho_l \approx 1.13 \times 10^{12}$ g cm^{-1} and the dash-dotted line denotes a low-density contour at $\rho \approx 1.85 \times 10^{10}$ g cm^{-1}.

4.4.5 Dynamical mass ejection

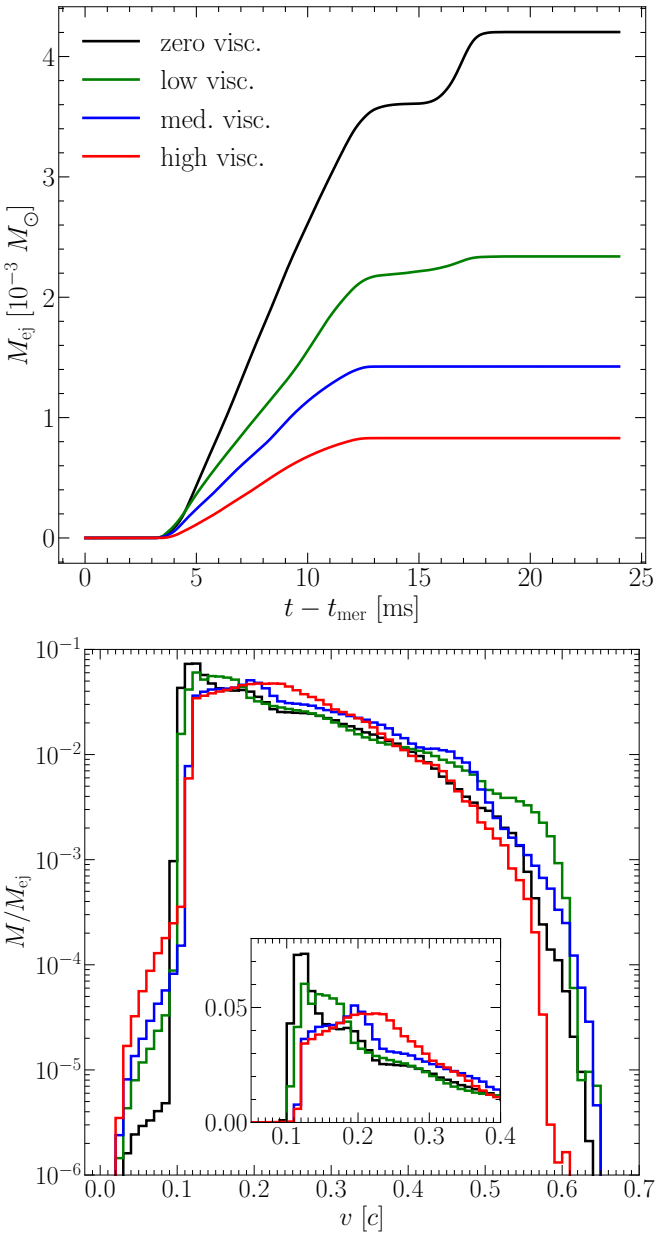

Figure 4.19: Mass and velocity distribution of dynamical ejecta in viscous neutron star mergers
Top: Cummulative ejected mass from the Bernoulli criterion. The detector is placed at ~ 517 km for all viscosity cases. *Bottom*: Distribution of ejected mass in velocity $v = \sqrt{v_i v^i}$ at the end of our simulations. The inset shows a zoom-in around the mean of the distribution.

In this subsection we discuss the impact of large bulk viscosities on the dynamical mass ejection in our simulations. We start by showing to total unbound material passing through a detector at ~ 517 km and calculated by using the Bernoulli criterion, i.e., material is classified as being unbound if $-hu_t - h_\infty > 0$ with h_∞ being the minimum specific enthalpy of the cold EOS table employed, see also [121]. The top panel of Fig. 4.19 shows the cummulative unbound mass as a function of $t - t_{\rm mer}$ while the bottom panel shows the velocity distribution of the total unbound material at the end of the simulations for all cases.

First, we observe a clear impact of bulk viscosity on the total unbound material from the top panel. Large bulk viscosities suppress dynamical mass ejection. For the high viscosity case the total ejecta mass is only $\sim$ 20% of the mass measured for the zero viscosity case. The impact of bulk viscosity on the velocity distributions is less severe. We observe that large bulk viscosities tend to suppress ejecta with velocities below ~ 0.2 and above ~ 0.5 compared to the less viscous cases.

As can be seen from the inset in the bottom panel of Fig. 4.19, the majority of the distribution tends to shift slightly to higher velocities. Correspondingly, the median of the distribution is shifting to higher velocities as well. The suppression of the *slow* ejecta component as well as the shift of the distribution to higher velocities is most likely sourced by the same effect. We suspect that the slow ejecta, more precisely, ejecta with $v \lesssim 0.2$, observed in the zero and low viscosity cases stems from marginally unbound material which could be powered by shocks which propagate through it. Large viscosities would naturally suppress this type of ejecta due to less efficient shock-heating, see also the discussion on Figs. 4.17 and 4.18. As a consequence,

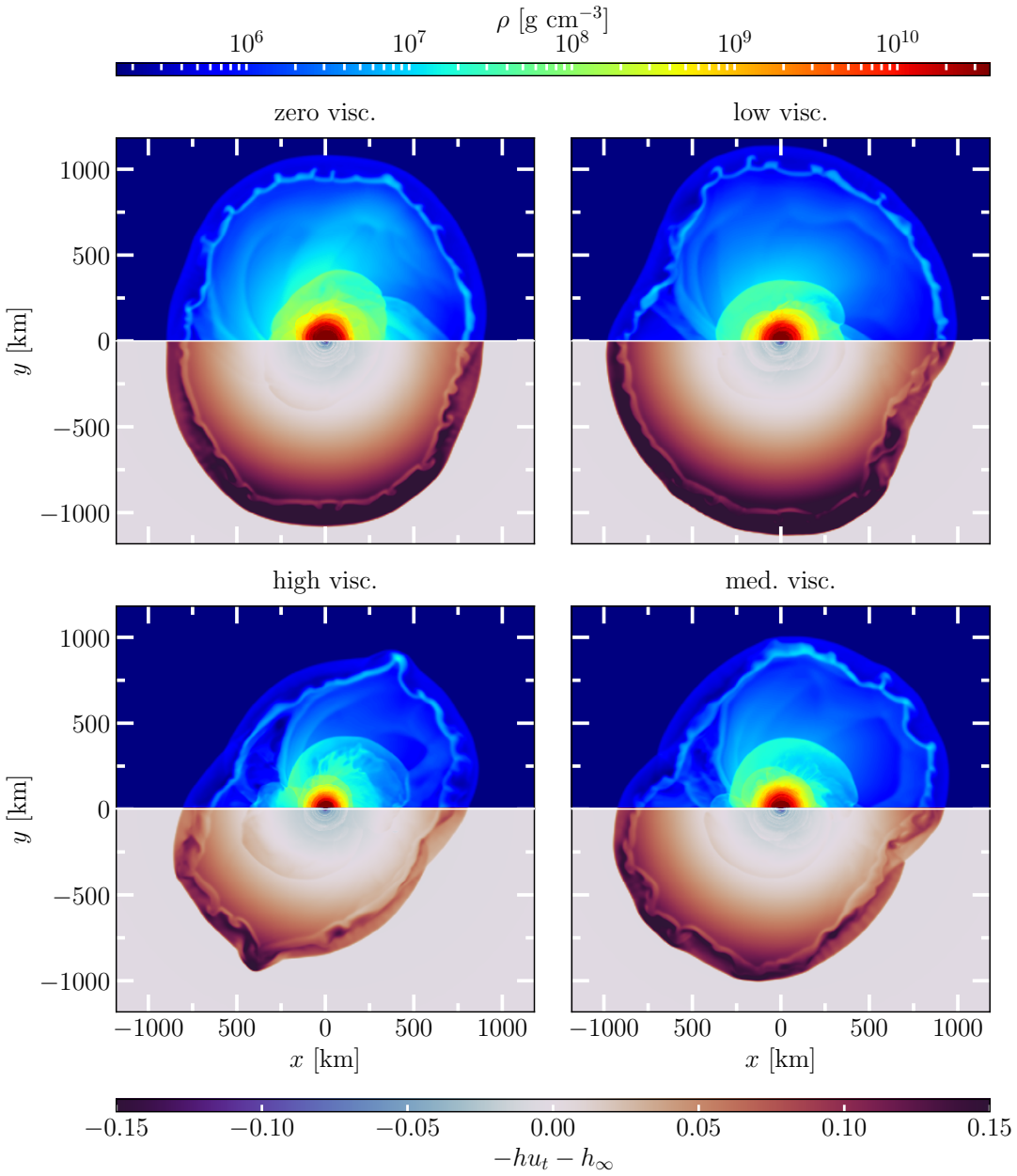

Figure 4.20: Cross-sections of rest-mass density and Bernoulli criterion in viscous neutron star mergers
Top (Bottom) half of each panel: The color code shows cross-sections of the rest-mass density ρ (Bernoulli criterion $-hu_t - h_\infty$) in the (x, y) plane. The snapshots are taken at $t - t_{\text{mer}} = 7.11$ ms. Shown is the zero viscosity case in the upper left panel, the low viscosity case in the upper right panel, the medium viscosity case in the lower right panel and the high viscosity case in the lower left panel.

the distribution of the ejecta in v shifts to higher velocities as only the marginally unbound material with low velocities is affected by this mechanism.

The suppression of the *fast* ejecta component is the direct result of strong viscous damping of density oscillations. The fast ejecta component originates from the first bounces of the two neutron star cores. As bulk viscosity tends to damp these violent collisions the energy reservoir powering the ejection of fast matter is dissipated more efficiently leading to a reduction of fast unbound matter.

Next, we will discuss the geometric distribution of the dynamical ejecta in the ϑ and ϕ-directions on the detector. Figure 4.20 shows the rest-mass density (top half panels) and the quantity $-hu_t - h_\infty$ (bottom half panels) at $t - t_{\rm mer} \approx 7.11$ ms for all configurations in the equatorial plane. We observe that an increase in bulk viscosity leads to a more asymmetric or less spherical shape of the outermost ejecta front which is at the same time a major component of the overall dynamical ejecta. This means that bulk viscosity tends to increase the selection of a preferred direction of the dynamical ejecta in the ϕ-direction. In our case, mass ejection tends to be increased for the angles $\phi \approx \pi/4$ and $\phi \approx 5\pi/4$. This finding is further supported by the Mollweide projections of the total dynamical ejecta presented in Fig. 4.21. Solid lines denote contour lines at 0.006%. For the medium and high viscosity case we observe pockets of low mass ejection in the equatorial plane with less than 0.006% of $M_{\rm ej}$. On the other hand, we also observe that the medium and high viscosity cases tend to reach higher fractions of their $M_{\rm ej}$ inside the contour lines which means that these distributions are less uniform than the distributions for the zero and low viscosity cases. Additionally, we observe low mass ejection in the polar direction for all cases which is in agreement with the findings from other NR simulations, see e.g., [77]. This effect can easily be explained by considering that the dynamical ejecta consists of a tidally ejected component and a shock-heated component [285]. The tidally ejected component is weakly affected by bulk viscosity in our simulations as we set $\zeta = 0$ in low-density matter which is more likely to get unbound through tidal forces. In contrast, as already explained above together with Fig. 4.18, strong bulk viscosities reduce shock-heating. Hence, the first bounce of the two neutron star cores powers significantly more matter ejection than all subsequent bounces, if the bulk viscosity is large. Therefore, matter is ejected primarily in the direction of the first bounce for the high viscosity case while for the zero viscosity case matter ejection from the subsequent core bounces tends to symmetrise the distribution along the ϕ-direction.

To conclude this subsection, we present the same quantities as in Fig. 4.18 focussing now, however, on the distributions at large distances from the SMNS in Fig. 4.22. As already observed in Fig. 4.18, we find that large bulk viscosities lead to a significantly more compact envelope or torus. We attribute this observation to the less efficient transport of matter to large distances which is a direct effect of large bulk viscosities. Also, it is important to note that the matter shown in Fig. 4.22 is primarily bound. The temperature distributions at large distances are comparable for all cases which indicates that the impact of bulk viscosity on the thermal properties of matter located at large distances from the SMNS is weak.

4.5 Summary and outlook

The results presented in this chapter can be broadly grouped into results on numerical aspects of the inclusion of bulk viscosity in NR simulations (Sections 4.2 and 4.3) and the impact of bulk viscosity on BNS mergers (Section 4.4). Thus, in the following we divide this section into two summaries and overviews. The first summary and overview is based on Sections 4.2 and 4.3 and concludes about the numerical aspects of the

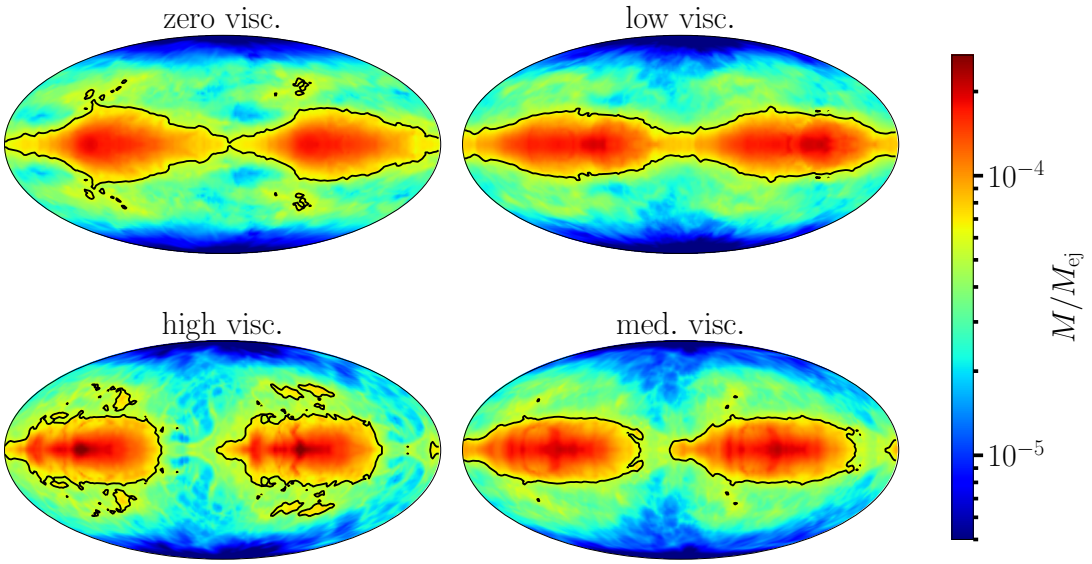

Figure 4.21: Mollweide projections of ejected mass in viscous neutron star mergers
The color code shows Mollweide projections of the cummulative ejected mass measured by using the Bernoulli criterion at the end our simulations. Shown is the zero viscosity case in the upper left panel, the low viscosity case in the upper right panel, the medium viscosity case in the lower right panel and the high viscosity case in the lower left panel. Solid lines denote contour lines at 0.006%.

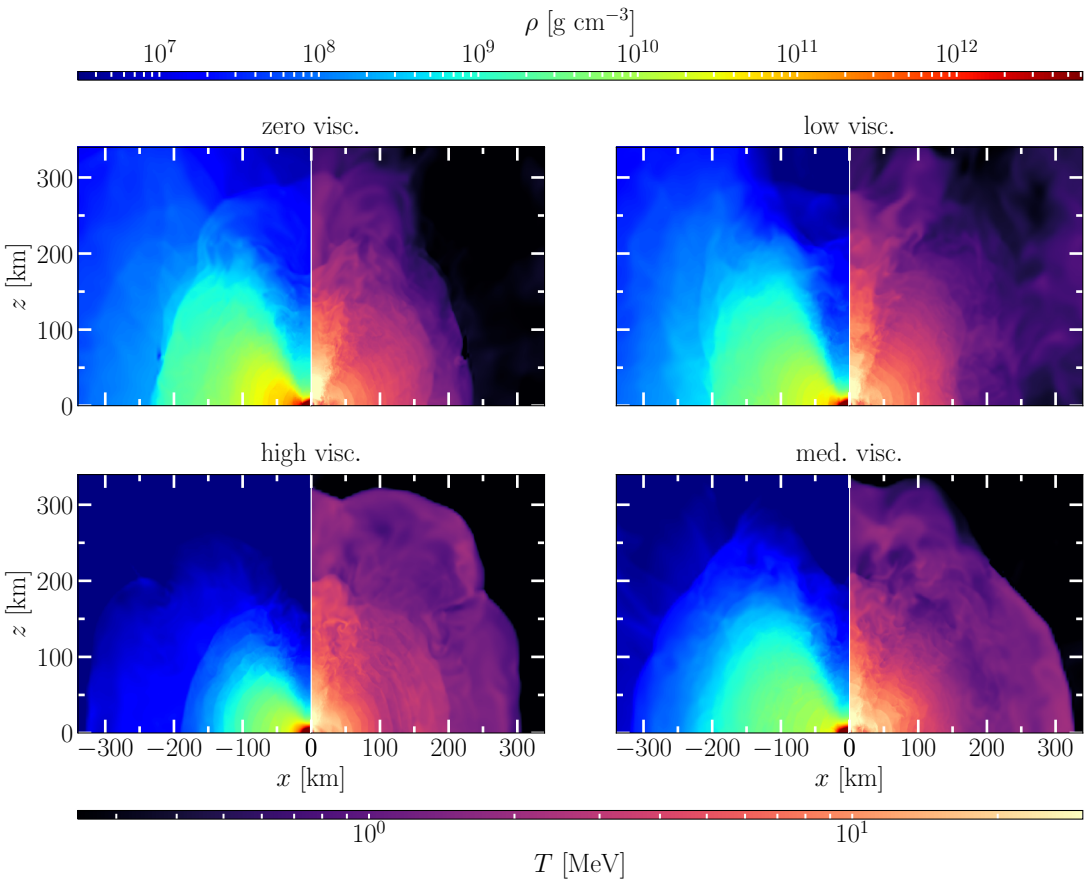

Figure 4.22: Cross-sections of rest-mass density and temperature at large distances in viscous neutron star mergers
Same as Fig. 4.18 but for a much larger domain focussing on the envelope of the remnant.

inclusion of bulk viscosity in NR simulations. The second summary and overview is based on Section 4.4 and concludes about the impact of bulk viscosity in BNS mergers.

4.5.1 Numerical aspects of the inclusion of bulk viscosity in numerical relativity

In this chapter we have presented a new implementation strategy to include the effects of bulk viscosity in NR simulations. The strategy is heavily based on the implementation developed in [71] with a few differences to account for the more complex dynamics of neutron stars. To summarize, the discretization of the fluxes is based on high-order HRSC methods while the discretization of the sources makes use of standard finite-difference methods. Additionally, we employ a modified version of the C2P algorithm proposed in [124]. Our modification preserves the existence and uniqueness properties of the root-finding function, thereby making it highly robust. We also make use of a limiting procedure based on the dominant energy condition and on causality. Finally, we employ a cubic fall-off of the bulk viscosity coefficient $\zeta \propto \rho^3$ in low-density regions which ensures a smooth transition between viscous and inviscid matter.

As a first test case we consider the measurement of numerical viscosity and calculate the damping time of the radial fundamental eigenmode of an isolated TOV solution. By evolving stars with different physical bulk viscosities and different resolutions we were able to observe convergent behaviour in the measured viscosity. Specifically, we observe that the measured viscosity is converging to the employed physical viscosity when we increase the numerical resolution. However, the convergence order is strongly affected by the size of the neutron stars due to the relative importance of discretization errors originating from the ill-balanced surface. In a representative setup we obtained numerical viscosities $\lesssim 10^{26}$ g cm^{-1} s^{-1} which is a promising finding considering that realistic viscosities can reach values of $\gtrsim 10^{27}$ g cm^{-1} s^{-1} [276, 17] in isolated stars as well as BNS mergers.

As a second test case we simulate the violent migration of unstable neutron stars to the stable branch. In contrast to the first test case, this scenario tests the implemented equations in a nonlinear and fully general-relativistic regime. We observe the expected behaviour that the damping of the nonlinear density oscillations is increased for larger bulk viscosities. Additionally, dissipative heating leads to a decrease of the central rest-mass density because the contribution of the thermal pressure in the neutron star core increases. The contribution can reach values of up to $\sim 10\%$ of the total pressure for the highest viscosity case. Also, we observe inverse Reynolds numbers on the order $\sim 1\%$ for the highest viscosity considered. Furthermore, we find good agreement between the values of the bulk-viscous pressure and its NS value which indicates that our simulations are in the NS regime of the equations. Finally, this test case allows us to provide evidence that our scheme is able to handle the transition between a viscous neutron star and an inviscid low-density exterior. This is an important ability as it allows us to study the impact of bulk viscosity on mass ejection in BNS merger simulations. We show that shock waves which originate at the neutron star surface located in viscous matter propagate without any disturbance through the transition region between viscous and inviscid matter. This allows us to observe that higher viscosities lead to weaker shock waves in the second and third bounce of the neutron star. It is due to the efficient dissipation of kinetic energy into heat that a lower amount of energy is transferred to the shock wave for higher bulk viscosities.

Finally, we plan to extend our numerical scheme in two important ways. First, the simulations performed so far make use of a simplified hybrid EOS which makes it easy to calculate the thermodynamic derivatives in Eq. (4.34). In order to use a more realistic temperature-dependent EOS we need to provide tabulated data for these deriva-

tives which is straightforward but technical. Along the same lines, we plan to implement realistic temperature-dependent bulk viscosities and relaxation times given by Eqs. (4.22) and (4.24). And second, short relaxation times as well as the explicit time integration procedure currently employed could lead to stiff source terms which require very short timesteps in the numerical solution. Hence, the simulations could become unfeasible due to the increasing computational costs. In order to solve this problem we will consider more sophisticated numerical methods including mixed implicit-explicit (IMEX) time integrators [218, 97, 314, 197, 198]

4.5.2 Impact of bulk viscosity on binary mergers

Motivated by the possibility of studying the impact of realistic bulk viscosities on the postmerger GW emission from BNS mergers we perform fully general-relativistic simulations employing a causal MIS-type model for the inclusion of a relativistic bulk viscosity. In order to estimate the maximum impact a realistic bulk viscosity can have we perform several simulations with varying constant bulk viscosities assuming the values $\zeta \in \{\zeta_0, \zeta_0/2, \zeta_0/5, 0\}$ with $\zeta_0 = 10^{30}$ g cm^{-1} s^{-1}. We also carry out several simulations with different resolutions in order to estimate the impact of discretization errors. We observe qualitatively consistent behaviour such that we only report the results from the high-resolution simulations.

We start by summarizing the results on the GW emission from viscous BNS mergers. We find that high bulk viscosities lead to damping and a frequency increase in the GW emission. Both of these effects are related to the decrease of $m = 2$ density deformations as a result of a strong bulk viscosity. Large bulk viscosities efficiently damp the violent collisions of the two neutron star cores during the first few milliseconds after the merger. This leads to reduced $m = 2$ density deformations. The decrease of density deformations causes weaker angular momentum losses through GW emission and weaker angular momentum transport to large radii. Effectively, larger bulk viscosities lead to faster rotating SMNS cores in the postmerger phase which leads to the frequency increase in the GW signal. For $\zeta = 10^{30}$ g cm^{-1} s^{-1} we observe efficient GW damping on a timescale of $t - t_{\rm mer} \lesssim 15$ms and an increase of f_2 compared to the inviscid case by $\Delta f_{\rm zero,high} \approx 280$ Hz.

We also observe non-monotonic behaviour in the GW emission for $\zeta = 2{\times}10^{29}$ g cm^{-1} s^{-1}. For this magnitude of the viscosity the impact of reduced density deformations and SMNS core spin-up seems to be comparable such that the energy emitted by GWs increases compared to the inviscid case.

Additionally, moving on to the thermal properties of viscous BNS mergers, we find that for large viscosities the increase of the total thermal energy due to dissipative heating is counteracted by the lower density of the SMNS core. These lower densities are the result of the additional centrifugal support in the SMNS core mentioned above. We also observe a more uniform temperature distribution and less efficient shock-heating in the SMNS remnant. We attribute this behaviour to the dissipation of kinetic energy into heat and, as a result, a less efficient kinetic-energy transfer from the fast-rotating deformed SMNS core to the matter making up its envelope. This energy transfer is suppressed for large viscosities due to the damping of density oscillations and the reduction of $m = 2$ deformations. Furthermore, we measure inverse Reynolds numbers on the order of $\sim 1\%$ in the center of the SMNS directly after the merger for the highest viscosity considered. This corresponds to bulk-viscous pressures, which are approximately $\sim 20\%$ of the total EOS pressure. Overall, the remnant of a viscous BNS merger has a less extended envelope and at the same time a less dense core.

Finally, the dynamical mass ejection from viscous BNS mergers is in agreement with

the overall results presented so far. We find that the dynamically ejected mass in our simulations is suppressed by a factor of approximately five for the high viscosity case when compared to the inviscid case. Again, this is the result of efficient dissipation of kinetic energy which makes it hard to unbind mass. Interestingly, we also find that the distribution of ejected matter along the azimuthal direction becomes increasingly less uniform with increasing viscosities. We attribute this behaviour to the fact that for large viscosities most of the unbound material stems from the first collision-and-expansion cycle of the two stars. Thus, matter is ejected in a preferred direction.

Our results imply that viscosities on the order of $\zeta \geq 5 \times 10^{29}$ g cm^{-1} s^{-1} can significantly impact the GW emission. Compared to the values observed in [200] this creates a promising picture for studying the bulk viscosity of nuclear matter through BNS collisions. However, in [202] effective viscosities on the order of $\zeta \lesssim 10^{28}$ g cm^{-1} s^{-1} have been extracted. Values of this order will most likely not be able to influence the GW emission. Additionally, one caveat remains when drawing conclusions from our simulations: Due to the resonant behaviour of the bulk viscosity and its strong temperature dependence, which is the result of neutrino trapping, large values of ζ will most likely appear only in small localized regions in the SMNS [9, 200]. Hence, the conclusions drawn from our simulations represent an optimistic viewpoint. Most likely the impact of a realistic, density and temperature-dependent bulk viscosity with a resonant value equal to the values sampled in this work will be reduced compared to the corresponding case presented here.

Apart from using a more realistic EOS and more realistic transport coefficients, this study could be extended to a greater variety of EOSs, total masses and mass ratios in order to sample these parameter spaces. Furthermore, so far we haven't closely investigated the impact of bulk viscosity on the inspiral GW signal. It would be interesting to explore the damping of tidal deformations or resonant density oscillations as the result of bulk viscosity during the inspiral. Finally, another potential site for the influence of a microphysical bulk viscosity could be the tidal disruption of BHNSs. Can a large bulk viscosity "save" the neutron star from being tidally disrupted? We leave these investigations for future work.

Chapter 5

Crustal magnetic fields in binary mergers

5.1 Magnetic fields in neutron stars

The role of magnetic fields is indisputable when discussing observational phenomena related to single neutron stars. Such phenomena include radio emission and spin-down from pulsars [239, 154], thermal emission and neutron star cooling which is intimately linked to the evolution magnetic fields in the neutron star [241, 239], the emission of non-thermal radiation from highly magnetised neutron stars, so-called magnetars, as well as the observation of "hot spots" on the neutron star surface through the NASA mission NICER [191, 264, 84], potential associations with the emission of fast radio bursts [80, 48] and many more. Thus, our ability to understand many of these observations depends crucially on our understanding of the topology and strength of the magnetic fields of neutron stars. Arguably, understanding magnetic fields in isolated neutron stars presents on its own already a formidable challenge. But on top that, detailed knowledge of this subject might accelerate progress on other fundamental questions related to neutron star physics, e.g., constraining the neutron star EOS. However, even though magnetic fields participate in a wide variety of observational phenomena of neutron stars a coherent theory of pulsar magnetospheres is still missing, see [43] for a review. Many models still rely on the simplifying assumption of a centered dipolar field configuration. Recently, this assumption has been challenged by NICER observations suggesting more complex, multipolar field topologies [46, 319]. In spite of its simplicity the dipolar field component is expected to dominate the observed spin-down of pulsars due to the weaker fall-off in distance compared to higher-order mutlipoles. Hence, by using simple formulas relating the period P, the period time derivative $\dot{P}$ and the angle between the rotation axis and the orientation of the magnetic dipole the strength of the dipolar component of the surface magnetic field $B_{\rm p}$ can be inferred. These values are typically overlaid in the famous P-$\dot{P}$ diagram and range from $\sim 10^8$ G to $\sim 10^{14}$ G [154], where magnetars fall in the class of $B_{\rm p} \gtrsim 10^{13}$ G.

But not only observations of isolated neutron stars are subject to the influence of strong magnetic fields. At least since the advent of multimessenger astronomy for BNS mergers marked by the coincident detection of GWs, GW170817 [1], a sGRB, GRB 170817A [1], and a kilonova signal, AT2017gfo [101, 81], strong evidence exists that large magnetic fields are necessary to account for these observations. This conclusion is based on a large amount of investigations exploring the ability of magnetic fields to drive large amounts of "slow", i.e., sub- and mildly relativistic, outflow [167, 289, 166, 115, 75, 121] as well as power ultrarelativitsic outflows in the form of so-called jets [177, 18, 262, 220, 169, 205, 76, 209, 208, 134].

Already early studies of BNS mergers identified a mechanism to amplify the magnetic field during such collisions efficiently. Namely, magnetohydrodynamic turbulence which is triggered by the onset of the KHI in the first few milliseconds after merger can lead to magnetic-field growth by several orders of magnitude [243, 130, 168, 6]. The KHI itself is developing as a result of the unstable shear layer which is present right at the onset of the merger between both stars. The dispersion relation for the linear Kelvin-Helmholtz modes at an interface of a simplified but representative setup [300] can be written as

$$\omega_{\pm} = k\Delta V \left(\frac{\rho_+ \pm i(\rho_+\rho_-)^{1/2}}{\rho_+ + \rho_-} \right), \tag{5.1}$$

where the quantities ω, k, ΔV, ρ_+ and ρ_- denote the angular frequency, the wavenumber, the difference in velocity at the interface and the two densities separated at the interface, respectively. From Eq. (5.1) it becomes evident that the linear Kelvin-Helmholtz modes with a positive imaginary part (the perturbation is proportional to $\propto \exp[i(kx - \omega t)]$) are unstable with a growth rate of

$$\mathrm{Im}\left[\omega_+\right] = k\Delta V \frac{(\rho_+\rho_-)^{1/2}}{\rho_+ + \rho_-}. \tag{5.2}$$

As the growth rate in Eq. (5.2) is proportional to the wavenumber k which is inversely proportional to the wavelength of the perturbation λ, i.e., $\mathrm{Im}[\omega_+] \propto k \propto \lambda^{-1}$, we find that small spatial perturbations of the interface grow faster than large ones. This finding has very important implications for the numerical modeling of magnetic-field amplification in BNS mergers. First, we assume that in reality all perturbations with $k \gtrsim (2\pi R)^{-1}$, where R denotes the radius of the neutron star, are triggered and keep in mind that the growth rate of the magnetic field is determined by the growth rate of the KHI. As a consequence, we are left with the conclusion that due to an unavoidable finite resolution in numerical simulations an upper bound for k, which is approximately the inverse of the grid spacing, i.e., $k_{\mathrm{max}} \approx (2\pi\Delta x)^{-1}$, determines the overall observed growth rate of magnetic fields in the numerical modeling. In reality we would expect effects from microphysical transport, such as shear and bulk viscosity [276], a large but finite conductivity and parasitic instabilities [213] or the backreaction of strong magnetic fields [213, 221] to determine k_{max}. This means that a faithful modeling of turbulent magnetic-field amplification can only be achieved at very high resolutions and, therefore, very high computational costs. However, so-called subgrid-scale modeling techniques exist which try to circumvent this problem by altering the EOM through additional terms. Simulations employing such extra terms fall in the class of LESs and their goal is to include the small-scale, dynamo-driven, magnetic-field amplification into *global* high-resolution GRMHD simulations with affordable resolutions [131, 219, 244, 66, 309, 310, 6, 284]. It is important to mention also *local* high-resolution simulations of the KHI in a magnetised fluid which provide evidence of saturation and convergence of the growth of the magnetic energy [213, 320].

A generally accepted picture of how magnetic fields are amplified, how magnetoturbulence develops and the saturation of the magnetic-field growth in a BNS merger is still missing. However, there exists broad consensus that the turbulent amplification process should stop when small-scale magnetic fields are strong enough to backreact on the fluid and therefore resist further amplification by quenching the KHI. This means that magnetic energy and kinetic energy are in equipartition on the smallest scales which is sometimes referred to as "local" equipartition. This mechanism yields "magnetar-strength" fields on the order $\gtrsim 10^{16}$ G [243, 177, 129]. Recently, a high-order and high-resolution global LES of merging magnetised neutron stars was able to

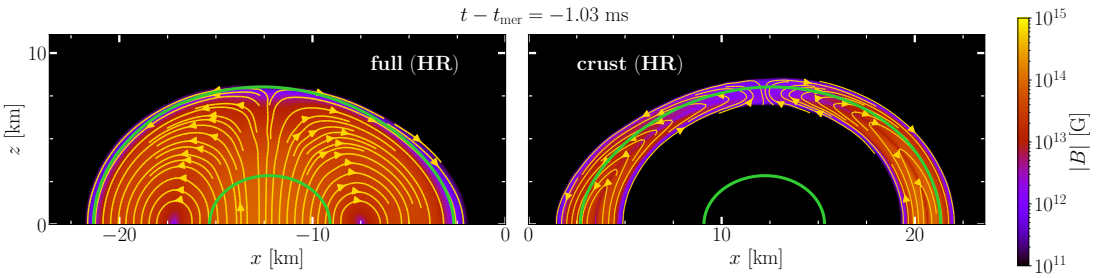

Figure 5.1: Initial full- and crust-configuration magnetic-field topology
The color code shows cross-sections of the magnetic-field strength $|B|$ in the (x, z) plane. The snapshots are taken from the HR simulations ~ 1 ms before merger. Yellow lines denote magnetic-field lines. On the left we show the full-configuration while on the right we show the crust-configuration. This figure has been reused from [74].

demonstrate this expectation [221], where the amplification of the averaged magnetic field saturated to approximately 10^{16} G.

Another interesting question is about the role played by the properties of the initial or seed magnetic field. In particular, does it matter which strength or topology the seed field has? Some initial investigations in this direction have been undertaken by [129, 165, 271], but most recently [5] have shown that the topology of the seed field is destroyed in the first milliseconds of the postmerger phase. Thus, the outcome depends only weakly on the configuration considered, e.g., dipoles with different strengths, misaligned dipoles, and even a multipolar structure. A common assumption in all of these studies is that the magnetic field is confined to the neutron star and permeates the whole stellar structure, i.e., the whole star is assumed to be magnetised. However, a number of investigations studying the long-term evolution of newly born neutron stars by exploring the rotational, thermal, and magnetic properties simulate configurations where the magnetic field is present only in the crust [237, 238]. The underlying assumption is that above a certain threshold density neutrons become superfluid and protons become superconducting. Then, if the stellar core is a type-I superconductor most of the magnetic flux in the core of the neutron star will be expelled on a very short timescale [311], much shorter than the typical timescales on which BNSs merge which are determined by orbital decay through GW emission [113]. However, it is important to point out that the timescales on which magnetic fields are evolving in the neutron star interior are highly uncertain and can vary up to several orders of magnitude [233, 232, 138]. Nevertheless, it is interesting to investigate whether BNS mergers together with their observations have predicting power in distinguishing configurations where the magnetic fields in the stellar cores have been expelled or have decayed from those where the whole neutron stars are magnetised.

Therefore, in this chapter we will present BNS merger simulations of magnetised neutron stars with two different magnetic-field topologies. Specifically, we distinguish between the "crust-configuration", where magnetic fields are located only close to the neutron star surface, and the "full-configuration", where magnetic fields are present everywhere in the neutron star, i.e., the core and the crust of the neutron star are magnetised.

5.2 Simulation setup

In order to study the impact of crustal magnetic fields in BNS mergers, we carry out GRMHD simulations in a fully dynamical spacetime. Hence, we solve self-consistently

Model	Δx [m]	$R_{\rm in}$ [$M_\odot$]	A_b	g_w [$M_\odot^{-2}$]	g_r [$M_\odot$]	$p_{\rm co}$ [$M_\odot^{-2}$]	n
full (HR)	70	0	0.028	0	0.0	1.0×10^{-8}	1.00
full (LR)	105	0	0.028	0	0.0	1.0×10^{-8}	1.00
crust (HR)	70	5	0.131	4	6.1	1.0×10^{-8}	0.85
crust (LR)	105	5	0.120	4	6.1	1.6×10^{-7}	0.85

Table 5.1: Parameters for initial magnetic fields
This table provides important information about the models we simulate in this work. Going from the left column to the right column we show the cell size on the highest refinement level as well as the seed magnetic-field parameters employed in Eq. (5.3) to initialize the magnetic field, respectively. This table has been reused from [74].

Einstein's equations by employing the Z4c formulation presented in Eqs. (2.52)-(2.57) together with the moving puncture gauges in Eqs. (2.64)-(2.66). Furthermore, magnetic and fluid fields are evolved by assuming the ideal MHD approximation and solving the evolution of the vector potential. Thus, we solve the system presented in Eqs. (2.150)-(2.152).

As before, we make use of the high-order HRSC code `FIL` [195, 201, 111] which employs the publicly available `Einstein Toolkit` [178] infrastructure including the fixed mesh-refinement code `Carpet` [277]. `FIL` employs fourth-order accurate finite-difference stencils in Cartesian coordinates to solve the system in Eqs. (2.52)-(2.57). The system of fluid and EM equations is solved via the ECHO scheme presented in Subsection 2.5.1. In addition, we use the temperature-dependent EOS `TNTYST` [301] and the initial data calculated as in Appendix C.

We use seven refinement levels and a computational domain which ranges from $-1000\,M_\odot \simeq -1476\,$km to $1000\,M_\odot \simeq 1476\,$km in all three spatial dimensions. The last level is added shortly before merger and has a width of 32 $M_\odot$. Besides, we make use of a z-symmetry in the equatorial plane. In order to estimate the influence of discretization errors on our results we employ two different resolutions which are $\Delta x \sim 0.047\ M_\odot \approx 70\,$m and $\Delta x \sim 0.071\ M_\odot \approx 105\,$m on the seventh refinement level. The former resolution is labeled as high-resolution (HR) and the latter is denoted as low-resolution (LR).

We make use of the same analytic function for both configurations, i.e., the crust- and full-configuration, in order to initialize the vector potential

$$A_i = A_b\,[-(x^j - x^j_{\rm NS})\epsilon_{ij}]\exp[-g_w(r-g_r)^2]\max(p-p_{\rm co},0)^n, \tag{5.3}$$

for $i \in \{x,y\}$ and $A_z = 0$, where $x^j_{\rm NS}$ denote the coordinate centers of the two stars ($x^3_{\rm NS} = z_{\rm NS} = 0$), $r := \sqrt{\delta_{ij}(x^i - x^i_{\rm NS})(x^j - x^j_{\rm NS})}$, and ϵ_{ij} is the Levi-Civita symbol. The outer boundary of the magnetised region is determined by the cut-off pressure $p_{\rm co} \approx 6\times10^{-5}\times p_c$, where p_c is the central pressure. The inner boundary of the magnetised region is set by the parameter $R_{\rm in}$, such that $A_i = 0$, if $r < R_{\rm in}$ (see Table 5.1 for a comprehensive account of the employed seeding parameters).

Using such a prescription for the magnetic-field seed, i.e., Eq. (5.3) and Table 5.1, we obtain magnetic-field configurations which are characterised by closed poloidal loops around a neutral line which is located at $\simeq 0.52\ R_{\rm NS}$ for the full-configurations and at $\simeq 0.87\ R_{\rm NS}$ for the crust-configurations. The topolgy shortly before merger is il-

Model	$\lvert B\rvert^{\rm seed}_{\rm max}$ [G]	$t^{\rm KHI}_{\rm end}-t_{\rm mer}$ [ms]	$t^{\rm D}_{\rm end}-t_{\rm mer}$ [ms]	$t^{\rm TA}_{\rm end}-t_{\rm mer}$ [ms]
full (HR)	1.04×10^{14}	2.46	3.48	7.13
full (LR)	1.04×10^{14}	1.77	5.15	10.1
crust (HR)	2.36×10^{14}	0.90	3.59	5.09
crust (LR)	2.26×10^{14}	1.82	3.54	11.5

Table 5.2: Characterising information about the full- and crust-configuration
This table provides important information about the models we simulate in this work. Going from the left column to the right column we show the maximum magnetic-field strength after initialization, $\lvert B\rvert^{\rm seed}_{\rm max}$, as well as the end time of the different stages discussed in the text, i.e., $t^{\rm KHI}_{\rm end}$, $t^{\rm D}_{\rm end}$ and $t^{\rm TA}_{\rm end}$, respectively. This table has been reused from [74].

lustrated in Fig. 5.1. In the HR (LR) case the magnetised crust of the crust-configuration is resolved by $\gtrsim 17$ ($\gtrsim 11$) gridpoints.

Furthermore, we provide additional information about the simulations presented in this chapter in Table 5.2. From left to right, Table 5.2 shows the the initial maximum magnetic-field strength $\lvert B\rvert^{\rm seed}_{\rm max}$ and the times characterising the different stages of our simulations, namely, the end of the KHI-driven stage $t^{\rm KHI}_{\rm end}$, the end of the decay stage $t^{\rm D}_{\rm end}$, and the end of the turbulent-amplification stage $t^{\rm TA}_{\rm end}$.

5.3 Overall evolution of magnetic fields

We start this section by discussing the overall common dynamics of the magnetic fields in both configurations with particular focus on the evolution of the total EM energy in the whole computational domain

$$E_B := \frac{1}{8\pi}\int (E^2+B^2)\sqrt{\gamma}dxdydz, \tag{5.4}$$

where $B^2 := B_iB^i$ ($E^2 := E_iE^i$) is the square modulus of the magnetic (electric) field in the Eulerian frame. We present the evolution of E_B in the top panel of Fig. 5.2 for all simulated configurations where blue lines represent the full-configurations and red lines the crust-configurations. Solid lines represent HR simulations while dashed lines denote LR simulations. In order to compare simulations with the same initial EM energy budget we set the initial EM energy to $\sim 3\times10^{44}$ erg for all configurations which corresponds to a maximum initial magnetic-field strength of $\sim 10^{14}$ G ($\sim 2.4\times10^{14}$ G) for the full-configuration (crust-configuration; see also Table 5.2).

The evolution of E_B can be divided into four distinct stages all of which are characterized by different processes which influence the evolution of the total EM energy. The first stage of the evolution, or "KHI-driven stage", starts at $t-t_{\rm mer}\approx -0.6$ ms (-0.6) and ends at $t-t_{\rm mer}\approx 2.46$ ms (0.9) for the full-configuration (crust-configuration). The KHI-driven stage is initiated due to the development of the KHI at the shear layer between both stars which are strongly deformed due to tidal forces. An example of overturning eddies which stem from the KHI can be observed in the first column of Fig. 5.3 which shows cross-sections of the norm of the magnetic field $|B| := \sqrt{B^iB_i}$ in the (x,y) plane at time $t-t_{\rm mer}=-0.12$ ms for the full- (top row) and crust-configuration (bottom row). The cross-sections are obtained at $z\simeq 1$ km $\lesssim 0.115\ R_{\rm NS}$ which is chosen such

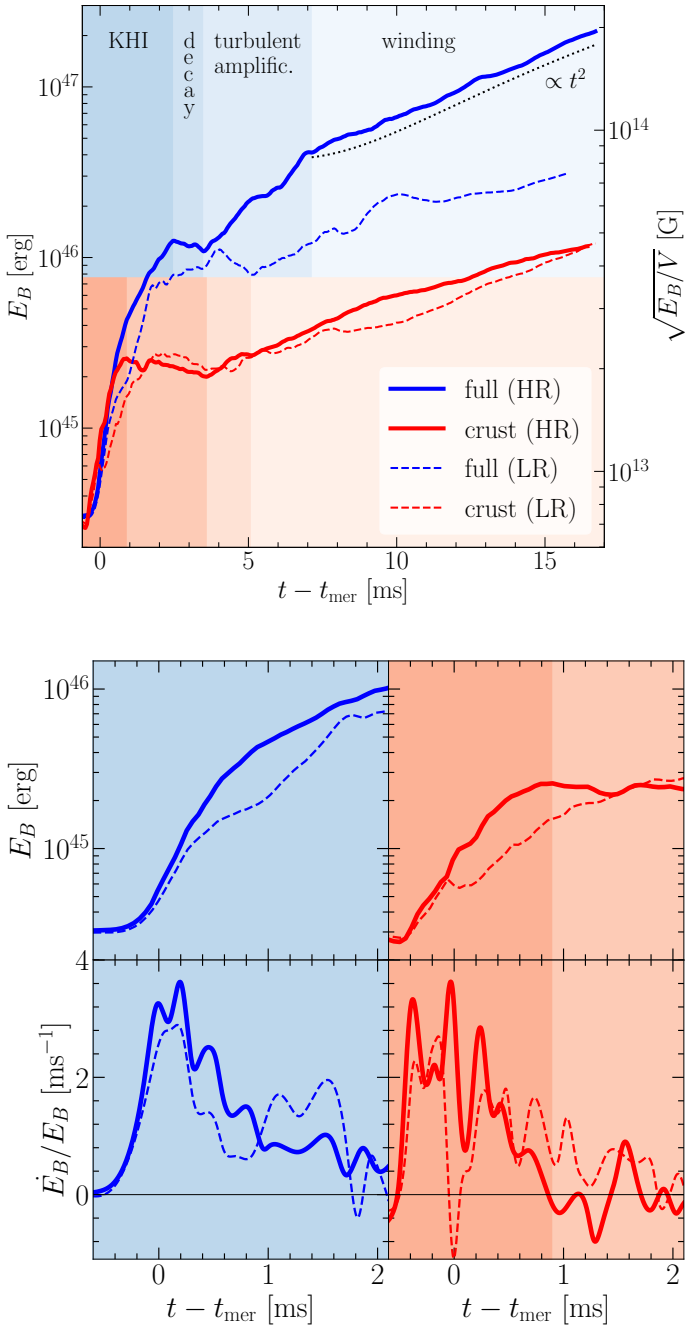

Figure 5.2: Total magnetic energy and magnetic-energy growth rate for the full- and crust-configuration
Upper panel: This panel shows the evolution of the total magnetic energy E_B for all configurations. Blue lines denote the full-configurations while red lines denote the crust-configurations. Solid lines denote the HR simulations while dashed lines denote the LR simulations. Also, we use different shadings in order to highlight the different stages for the HR full-configuration (top half of upper panel) and the HR crust-configuration (bottom half of upper panel). Additionally, we add a black dotted line which is a quadratic fit to the data of the HR full-configuration during the winding stage in order to highlight the similarity. However, we move the black dotted line slightly downwards for better visualization. Finally, V is the volume of a reference neutron star with a radius of 11 km. *Lower panel, top*: Shown is the same as in the upper panel of this figure with the only difference that $t - t_{\rm mer} \lesssim 2$ ms. *Lower panel, bottom*: Shown is the same as in the top half of the lower panel but instead of showing the total magnetic energy the growth rate $\dot{E}_B/E_B$ is shown. This figure has been reused from [74].

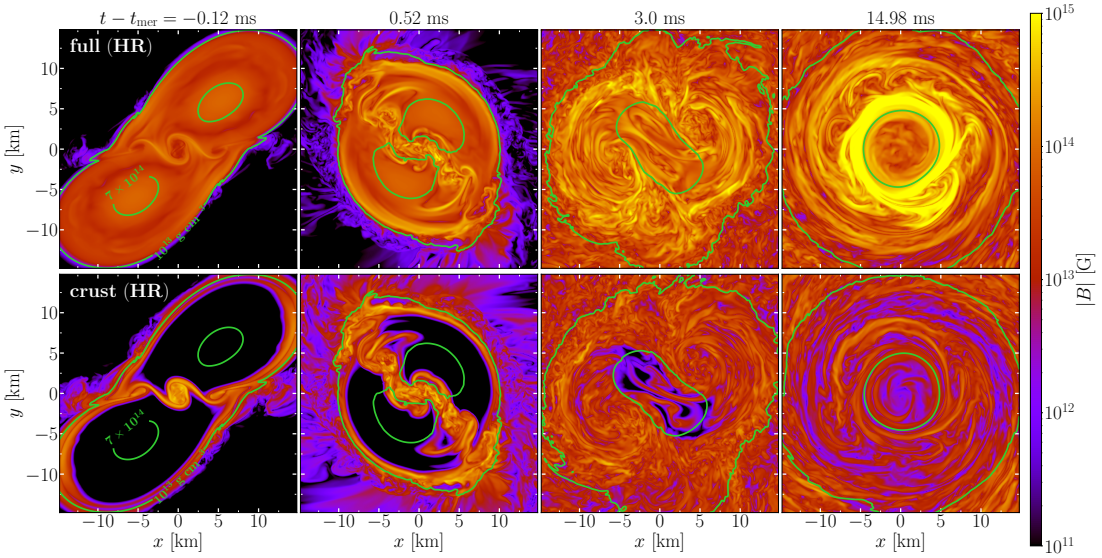

Figure 5.3: Cross-sections of magnetic-field strength for the full- and crust-configuration
The color code shows cross-sections of the magnetic-field strength $|B|$ in the (x, y) plane. The snapshots are taken at four different times from the HR simulations. The upper panels show the full-configuration while the lower panels show the crust-configuration. This figure has been reused from [74].

that the influence of the boundary conditions in the equatorial plane are minimized. Furthermore, after the linear stage of the KHI the development of turbulence occurs which extends also to regions other than the immediate viccinity of the shear layer. For example, the second column of Fig. 5.3 shows a snapshot at $t - t_{\rm mer} = 0.52\,$ms and highlights how turbulent motions start to develop also closer to the stellar interior.

During the second stage of the evolution, or "decay stage", the total EM energy shows a constant evolution or even a weak decay. This behaviour can be attributed to a number factors. First, during this stage large magnetic pressure gradients are present which stem from the magnetic field amplification of the previous stage. These gradients contribute to the expansion of matter in the SMNS such that work is done *on* the fluid *by* the magnetic fields which leads to an overall decrease in E_B. In addition, due to the development of an effective turbulent viscosity and the emission of GWs the periodic collisions and bounces of the two neutron star cores are damped. As a consequence, the production of shear layers in the fluid is suppressed. These shear layers are important as they serve as the basis for the development of the KHI which amplifies the magentic field. This means that in this stage KHI-driven turbulent motion ceases to be produced efficiently as the kinetic energy in the remnant is reduced and redistributed. It is interesting to note that the developed turbulence has not yet penetrated the SMNS core. This results in weak magnetic fields in the SMNS core for the crust-configuration and the preservation of the initial large-scale coherence of the magnetic fields in the SMNS core for the full-configuration, e.g., see the third column of Fig. 5.3 at $t - t_{\rm mer} = 3\,$ms. The decay stage ends for the full-configuration (crust-configuration) at $t - t_{\rm mer} = 3.48\,$ms (3.59).

In the third stage, or "turbulent-amplification stage", we observe that the total EM energy is growing again. This means that a new process of magnetic-field amplification has been activated and is strong enough to contribute to the growth of E_B, see also [289]. At the same time we observe that the violent and nonlinear early postmerger phase in which the cores of both neutron stars collide periodically has ended, see [296]

for a toy model. We link the amplification during this stage to turbulent motions which arise when the SMNS is changing its structure to a more axisymmetric one. It is also important to note that this behaviour is not associated with the growth of the magneto-rotational instability (MRI) but nevertheless leads to a significant amplification of the poloidal component of the magnetic field up to $t - t_{\rm mer} = 7.13\,$ms (5.09) for the full-configuration (crust-configuration).

Finally, the last and longest stage of the evolution of E_B, or "winding-stage", starts when the turbulence is not increasing anymore. This means that the evolution of E_B is not dominated by turbulence on small-scales but rather large-scale shearing motions in the SMNS are the source of energy increase. More specifically, due to the infinite-conductivity condition of ideal MHD large-scale differential rotation leads to magnetic winding and the characteristic linear-in-time growth of the magnetic field, see also [278, 79, 106, 167]. This behaviour is present until the end of our simulations, e.g., see the final part of the top panel of Fig. 5.2. Additional evidence is given by the highly magnetised ring that can be seen in the upper panel of the last column of Fig. 5.3. The location of the ring corresponds to the radius where the angular velocity shows the steepest gradient which marks the area of strongest differential rotation. Furthermore, it is important to note that even though we don't observe saturation of EM energy growth it is expected that the winding stage terminates when the EM energy budget becomes comparable to the budget of differential kinetic energy. This sets a threshold for the maximum EM energy achievable through magnetic winding. Additionally, it is possible that the evolution of E_B saturates already after the KHI-driven stage such that all subsequent stages might be absent. This could be the result of additional terms in the MHD equations, see [131, 221], large initial magnetic fields or even higher resolutions [166]. This means that the 4-stage classification presented here even though applicable to our simulations with moderate magnetic fields may fail to hold for other simulations and evolutions present in the literature [131, 221, 166].

5.4 Evolution of crustal magnetic fields

In this section we focus specifically on the differences between the full- and crust-configuration which eventually determine the final magnetic-field amplification. The first and probably most striking difference between both configurations is the duration of the KHI-driven stage. This stage is significantly shorter in the crust-configuration which leads to a weaker magnetic-field amplification by a factor of > 3 after the KHI-driven stage has ended for both configurations. We will investigate this behaviour further below in more detail. In addition, the crust-configuration exhibits a longer decay stage and a shorter turbulent amplification than the full-configuration, see also Table 5.2. All in all, this leads to the result that E_B differs by more than one order of magnitude between both configurations at the beginning of the winding stage. During the winding stage both configurations show similar growth rates of the EM energy such that the difference in E_B is preserved until the simulations end. Apart from that, it is interesting to look into the question of why the KHI-driven amplification is weaker in the crust-configuration than in the full-configuration. This behaviour can be attributed to two effects. First, due to the different magnetic-field topologies naturally there is less magnetised matter in the crust-configuration which is affected by turbulence than in the full-configuration. Second, because in the crust-configuration the magnetised matter is located predominantly in those regions having a lower density (i.e., $\rho \lesssim 10^{13}\,{\rm gm/cm^3}$) and near the stellar surface, a larger portion of it is subject to dynamical ejection and mass-shedding what ultimately removes it from the regions where it can be used for magnetic-field amplification due to turbulence. In the full-

configuration, however, both of these effects are suppressed.

We will now discuss the evolution of E_B during the first two stages in more detail by using also the bottom panel of Fig. 5.2. The upper row of the bottom panel of Fig. 5.2 shows the same as the top panel of Fig. 5.2 but is restricted to a window in time with $t - t_{\rm mer} \lesssim 2\,$ms. The lower row of the bottom panel of Fig. 5.2 shows the growth rate $\dot{E}_B/E_B$ for the same time window. First, we observe that E_B is growing exponentially and reaches its maximum growth rate in $\lesssim 0.7\,$ms (0.2) for the full-configuration (crust-configuration). The maximum growth rate is similar for both configurations for the same resolution. Also, the magnetic-field amplification is much more efficient in the crust-configuration which manifests as more rapid changes of E_B. This behaviour stems from the fact that all of the initial EM energy participates directly in the amplification process as it is exactly the two crusts of the neutron stars which are subject to the KHI. In contrast, the initial EM energy is distributed over the whole extent of both stars for the full-configuration such that it is always only a fraction of E_B that is amplified. The evolution after the maximum of $\dot{E}_B/E_B$ is similar for both configurations. The growth rate declines until it reaches values below zero which indicates the end of the KHI-driven stage. However, it is interesting to have a closer look at the short variations which occur during this decline in growth rate.

We find that the variations occur with a typical period of $\simeq 0.25 - 0.35\,$ms. If we assume that the largest eddies present in the simulation have a characteristic eddy-rotation velocity of $\sim 0.15\,c$ we are able to estimate that the lengthscale of such eddies is $\sim 1.8 - 2.5\,$km. This number is broadly consistent with the size of the largest eddies produced across all simulations. In addition, the observed period of the variations is approximately half the period of the bounces of the two stellar cores which is $\sim 0.77\,$ms. These observations lead to the following picture: The colliding motions of the two neutron star cores generate turnovers of the shear layer between the stars which produce the largest eddies present in the soon-to-be SMNS. These largest eddies drag magnetic flux tubes into rotation such that periodic variations in the growth rate develop. We conclude that lasting magnetic-field amplification depends crucially on the development of magnetic turbulence in all regions of the SMNS. In the crust-configuration magnetic-field amplification continues when the turbulence extends beyond the neutron star crust to the stellar interior but is weakened because of the mixing of magnetised and unmagnetised material. Together with losses of magnetised material at the surface of the SMNS this effect explains the faster decay of $\dot{E}_B/E_B$ in the crust-configuration compared to the full-configuration which benefits from a fully magnetised stellar interior.

Finally, Fig. 5.4 provides evidence for the loss of important magnetised material at the SMNS surface which ultimately leads to the early termination of the KHI-driven stage in the crust-configuration. Figure 5.4 shows snapshots of representative quantities at $t - t_{\rm mer} = 0.52$ ms for the full- (top row) and crust-configuration (bottom row). In particular, we show $|B|/[10^{15}\,\mathrm{G}]$, the density-weighted spatial projection of the kinematic vorticity

$$\left|\rho\omega_{\perp}^{xy}\right| := \rho\gamma^{x}{}_{\mu}\gamma^{y}{}_{\nu}\omega^{\mu\nu}\,, \tag{5.5}$$

and the amplification source term defined in Eq. (2.140) from left to right, respectively. The quantity $\omega^{\mu\nu}$ denotes the kinematic vorticity, see Appendix B. As already mentioned in Section 2.5, $s_{\rm mag}$ can be used to measure local sources $s_{\rm mag} > 0$ and sinks $s_{\rm mag} < 0$ of magnetic energy.

First, when comparing the magnetic-field strength $|B|$ shown in the left column between both configurations we find that the crust-configuration has stronger magnetic fields than the full configuration. This observation can naturally be explained by the

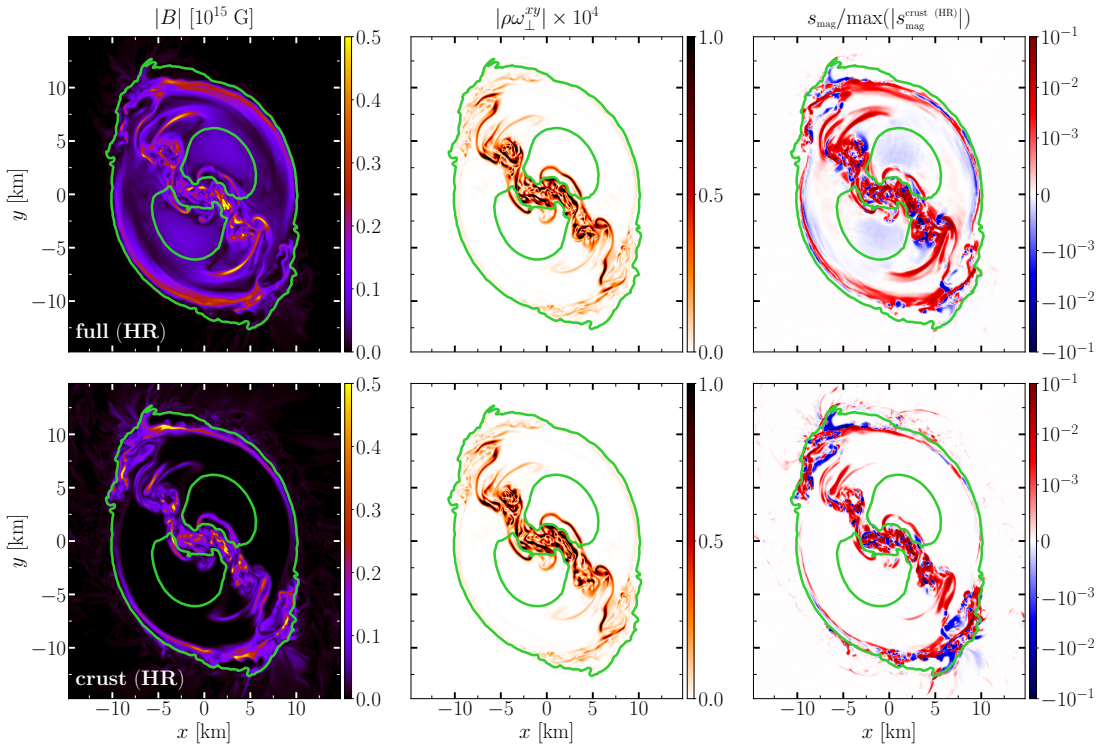

Figure 5.4: Cross-sections of magnetic-field strength, vorticity and amplification source term for the full- and crust-configuration
The color code shows cross-sections of the magnetic-field strength $|B|$ (left column), of the density-weighted xy-component of the kinematic vorticity $|\rho\omega_{\perp}^{xy}|$ (middle column), and of the amplification source term $s_{\rm mag}$ (right column) in the (x, y) plane. The snapshots are taken at $t - t_{\rm mer} = 0.52$ ms. The upper panels show the HR full-configuration while the lower panels show the HR crust-configuration. This figure has been reused from [74].

fact that the initial magnetic-field strength is higher for the crust-configuration than for the full-configuration, e.g., see Table 5.2, and the more efficient magnetic-field amplification during the KHI-driven stage in the crust-configuration, see e.g., Fig. 5.2 and the corresponding discussion further above in this section. In addition, we observe that the strongest magnetic fields in the crust-configuration are located near the stellar surface marked by the green density contour line at $\rho = 10^{13}$ g cm^{-3}. This implies that the evolution of a large portion of the total magnetic energy in the crust-configuration depends on the evolution of the low-density matter located near the stellar surface of the SMNS. For example, any dynamical process which leads to the ejection matter located at lower densities can potentially remove large amounts of magnetic energy from the regions of the SMNS which will be subject to turbulence. Second, the middle column shows that the vorticity looks almost identical between both configurations. Vorticity is mainly concentrated in all regions of the SMNS which are connected to the shear layer that developed in the first few fractions of a millisecond after the merger. In particular, we observe also a larger amount of vorticity in the low-density region near the stellar surface which marks both ends of the shear layer. On the other hand, vorticity falls-off rapidly in the high-density region of the newly formed SMNS. The reason why the vorticity looks almost identical for both configurations is related to the relative importance of magnetic fields when compared to the purely hydrodynamic evolution. This can be quantified through the so-called plasma beta quantity $\beta := p/p_{\rm mag}$ which measures the relative strength between fluid pressure p and the magnetic pressure $p_{\rm mag}$. Even though we observe turbulence and the corresponding magnetic-field amplification in the low-density region of the SMNS which naturally corresponds to lower fluid pressures, the magnetic-field strengths obtained in these simulations are not high enough to yield $\beta \lesssim 10^3$. This means that the evolution of the matter in our simulations is mainly hydrodynamical where magnetic fields lead only to small perturbations which, however, are barely visible in the middle column of Fig. 5.4. Finally, when having a look at the right column of Fig. 5.4 we find that for both configurations the sources of magnetic energy are more pronounced than the sinks. This is expected as the snapshots are taken at a time where the total EM energy is growing. Furthermore, we also observe that many of the important sources of magnetic energy in the crust-configuration are located near the SMNS surface. All in all, Fig. 5.4 supports the hypothesis that the loss of precious magnetised matter at the SMNS surface is an important process by which an early termination of magnetic-field amplification is realized in the crust-configuration. More specifically, Fig. 5.4 shows that a large portion of magnetic energy together with its important sources are located in the low-density region of the SMNS close to the stellar surface where turbulence is developing. Naturally, together with the dynamical ejection of mass from these regions important magnetised material is removed from the regions of the SMNS where further turbulent amplification could increase the magnetic energy in the crust-configuration. This contributes to an early termination of magnetic-field amplification.

5.5 Gravitational-wave emission

In this section we will discuss how the GW signal is influenced by the different magnetic-field configurations. Figure 5.5 shows the emitted $\ell = 2$, $m = 2$ mode of the +-polarised GW strain measured at $\sim$ 740 km and assuming that the merger is located 100 Mpc away from the observer. The full-configuration is shown in blue while the crust-configuration is shown in red. The signal for both configurations looks almost the same in the first two milliseconds after merger. This corresponds to the time when the KHI is most active. However, for $t - t_{\rm mer} \gtrsim 2$ ms the two signals start to differ sig-

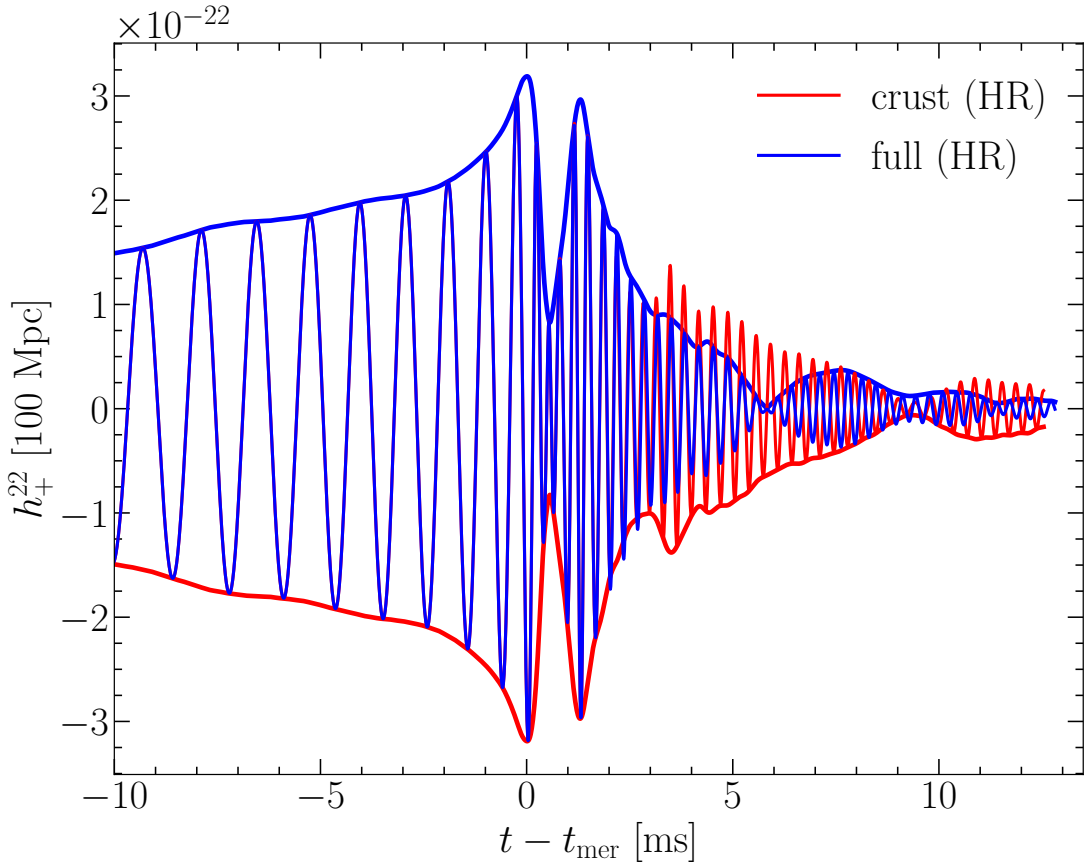

Figure 5.5: Gravitational-wave strain for the full- and crust-configuration
Shown is the $\ell = 2, m = 2$ mode of the gravitational-wave strain for the + –polarisation. The signal is extracted at ∼ 740 km and normalized to a luminosity distance of 100 Mpc. Blue lines denote the HR full-configuration while red lines denote the LR crust-configuration. The thick lines highlight the corresponding amplitudes. This figure has been reused from [74].

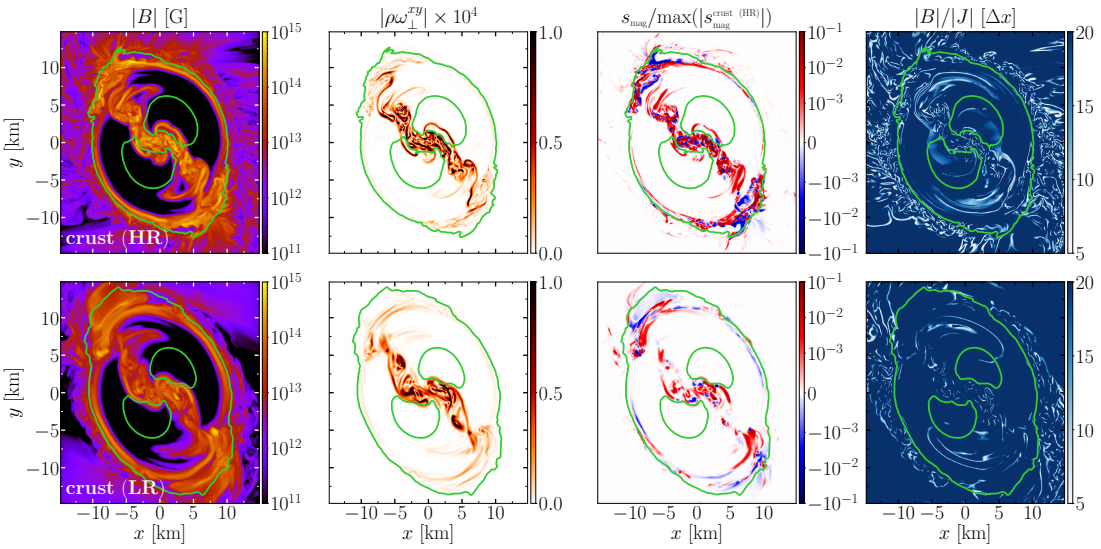

Figure 5.6: Cross-sections of magnetic-field strength, vorticity, amplification source term and characteristic length-scale for the full- and crust-configuration
The color code shows cross-sections of the magnetic-field strength $|B|$ (first column), of the density-weighted xy-component of the kinematic vorticity $|\rho\omega_\perp^{xy}|$ (second column), of the amplification source term $s_{\rm mag}$ (third column), and of the characteristic length-scale of the magnetic field, i.e., $|B|/|J|$, in the units of the grid spacing Δx (fourth column) in the (x, y) plane. The snapshots are taken at $t - t_{\rm mer} = 0.52$ ms. The upper panels show the HR crust-configuration while the lower panels show the LR crust-configuration. This figure has been reused from [74].

nificantly. In particular, the amplitude of the strain of the full-configuration decays much stronger than the amplitude of the crust-configuration. This also means that less gravitational energy is emitted for $t - t_{\rm mer} \gtrsim 2$ ms for the full-configuration than for the crust-configuration. There are two reasons for this effect. The first one is related to the increased magnetic energy in the full-configuration which comes at the expense of the kinetic energy reservoir. Less kinetic energy which is predominantly stored as rotational kinetic energy means slower rotation which directly affects the magnitude of the emitted GW strain. The second reason is related to the $m = 2$ density-deformations of the SMNS which are affected by the strong magnetic fields in the full-configuration. Strong magnetic fields lead to a more axisymmetric SMNS in the full-configuration which weakens the emitted GW signal.

5.6 Impact of resolution

Due to the dependence of the growth rate of the KHI on the grid resolution also the achievable final magnetic energy in the KHI-driven stage depends on grid resolution [168]. This makes a quantification of the impact of resolution on the results shown in the previous sections inevitable. In this section we will contrast the low-resolution and high-resolution versions of the crust-configuration in addition to the results already presented in Fig. 5.2. We will not concentrate on the full-configuration as in this case the evolutions for both resolutions are very similar. Also, the evolution of BNS mergers with magnetic fields which have been seeded in the whole stellar volume (as done in the full-configuration) has been discussed already extensively by a number of papers, e.g., see [195] for a case with larger magnetic-field strengths but lower resolutions compared to the simulations in this Thesis. Even though the resolutions employed in this work are still not high enough for a rigorous convergence study, the observed evolu-

tions provide evidence for being numerically consistent, i.e., numerical errors decrease with increasing resolution. In particular, Fig. 5.6 shows snapshots of representative quantities for the high-resolution (top row) and the low-resolution (bottom row) simulations at $t - t_{\rm mer} = 0.52$ ms and $t - t_{\rm mer} = 0.59$ ms, respectively. The different times are due to the difference in phase evolution resulting from the different resolutions. As in Fig. 5.4, the first three columns from the left report $|B|/[\mathrm{G}]$, the density-weighted spatial projection of the kinematic vorticity, see Eq. (5.5), and the amplification source term defined in Eq. (2.140), respectively. The fourth column, on the other hand, shows the characteristic length-scale of the Eulerian magnetic field, i.e., $|B|/|J|$, and is expressed in units of the grid spacing Δx, see Eq. (15) of [213]. Here, $J := \sqrt{J^i J_i}$ and the spatial current is estimated as

$$J^i \simeq \frac{1}{4\pi\alpha\sqrt{\gamma}} \eta^{ijk} D_j (\alpha B_k) \,. \tag{5.6}$$

Expression (5.6) can be deduced from Eq. (21) of [26] which denotes the Ampère-Maxwell equation in the 3+1 formalism

$$\partial_t E^i = \frac{1}{\sqrt{\gamma}} \eta^{ijk} \, D_j (\alpha B_k) - 4\pi\alpha J^i + \alpha K E^i + \mathcal{L}_\beta E^i \,. \tag{5.7}$$

From the ideal MHD approximation which results in Eq. (2.133) we find that for non-relativistic flows $E_i \sim \mathcal{O}(v_i) \ll 1$ and the charge current in Eq. (5.7) can be expressed by Eq. (5.6). The first column of Fig. 5.6 shows that the high-resolution simulation suffers from larger losses of magnetised material at the SMNS surface. This is most pronounced at both ends of the turbulent shear layer which also mark the regions where dynamical mass ejection will take place due to violent collisions of the neutron star cores. The second column compares the densitised vorticity for high- and low-resolution and shows that the high-resolution simulation features higher vorticities. In addition, the high-resolution simulation shows more small-scale features and variations as one would expect from a finer grid structure. However, the broad region of high vorticity is almost identical for both resolutions except of the region at both ends of the turbulent shear layer which has notably higher vorticity values in the high-resolution simulation as compared to its low-resolution counterpart. The third column shows that stronger sinks (higher in magnitude but negative) of magnetic energy can be found in the high-resolution simulation. More specifically, these large sinks are located at both ends of the turbulent shear layer which correlates with the location where precious magnetised material is lost. Finally, the fourth column clearly shows a "cloud" of low-density and magnetised material which has a very small characteristic length-scale. This "cloud" is surrounding the SMNS and originates from mass losses at the SMNS surface and is less pronounced in the low-resolution simulation. To summarize, Fig. 5.6 demonstrates how a higher resolution for the crust-configuration can lead to enhanced losses of important magnetised material at the SMNS surface eventually leading to an early termination of magnetic-field amplification in the KHI-driven stage.

5.7 Summary and outlook

Motivated by the common modeling assumption of *crustal* magnetic fields in the long-term evolution of isolated neutron stars, we have explored the hypothesis whether seed magnetic fields which are confined to a small region near the stellar surface have an impact on the total magnetic-field amplification in BNS mergers. We have used high-resolution, global, and high-order GRMHD simulations of BNS mergers with different

seed magnetic-field topologies in order to investigate this hypothesis. Our study includes simulations of four binaries where we vary between two different topologies, namely the crust-configuration and the full-configuration. In the crust-configuration the magnetic field is seeded only near the stellar surface while in the full-configuration the whole star, including the core, is magnetised. Additionally, both topologies have the same initial total magnetic energy. These two setups are simulated at two different resolutions in order to estimate the influence of discretization errors. However, we find qualitatively consistent behaviour such that we focus the discussion for the most part on the simulations with higher resolutions.

First, we observe four different stages of magnetic-field evolution for both configurations, namely the KHI-driven stage, the decay stage, the turbulent-amplification stage and the winding stage. These stages are named in agreement with the main physical process determining the magnetic-energy evolution in the corresponding stage. Second, although in the crust-configuration the KHI-driven stage is more efficient in amplifying the magnetic fields as a result of larger initial magnetic-field strengths, the final magnetic energy of the full-configuration is more than one order of magnitude larger when compared to the crust-configuration. We attribute this behaviour to the early termination of the KHI-driven stage in the crust-configuration which is the result of two effects: the lack of magnetised material in the neutron-star interior and losses of magnetised material at the stellar surface. On the one hand, magnetic-field amplification cannot be sustained in the crust-configuration due to the fact that the turbulent motions, which amplify the magnetic field, move into regions which are unmagnetised in the crust-configuration. This cannot happen in the full-configuration as such regions do not exist. On the other hand, magnetic-field amplification in the crust-configuration could continue due to turbulent motions in the outer regions of the newly formed SMNS. However, this possibility is prevented as well due to the ejection of magnetised material at the stellar surface. And third, as a result of the lower magnetic-field strengths in the crust-configuration we observe that the corresponding GW signal is approximately two times stronger than in the full-configuration. We attribute this behaviour to the lower degree of axisymmetry in the crust-configuration.

Even though the resolutions we employ in this work are very high and computationally expensive, they are still not high enough in order to reach convergent behaviour during the KHI-driven stage. In order to accomodate for this short-coming we employ two different resolutions and estimate the impact of the discretization errors. We find that the behaviour presented in this work is affected only quantitatively by varying the resolution. Thus, we conclude that our results are reasonably accurate models for the magnetic-field amplification in BNS mergers with crustal and full magnetic fields.

Furthermore, our findings have the important implication that future observations of magnetar-strength magnetic fields in the merger remnant disfavour purely crustal premerger magnetic-field topologies. In particular, the launching of sub-relativistic magnetised outflows on short timescales after the merger might not be possible if the magnetic-field topology is a purely crustal one. This opens up a new avenue of constraining the magnetic-field topology of old coalescing BNSs using observations of the SMNS remnant.

Finally, this study could be continued in many interesting directions. To name only a few, it would interesting to investigate the final magnetic energy as a function of the volume fraction endowed with magnetic field before merger. Such an investigation might provide clues about the maximum radius of an unmagnetised neutron star core which is still compatible with magnetar-strength magnetic fields in the postmerger. Additionally, it would be interesting to investigate the impact of crustal magnetic fields on the mass ejection from BNS mergers. It is not trivial whether crustal magnetic

fields increase or decrease the ejected mass. That is because crustal magnetic-field topologies might increase the magnetic pressure in low-density regions of the early postmerger but might fail to produce significant magnetic pressures later on due to the lower amplification. Also, a deeper investigation of the turbulent properties of the postmerger crustal magnetic field could provide interesting information about the development of magneto-turbulence in different regions of the neutron stars. We leave these investigations for future work.

Chapter 6

Conclusions

In this Thesis we have pursued the overall goal to investigate dissipative and shearing effects in BNS mergers in order to identify new avenues to constrain hot and dense neutron star matter through BNS mergers. To do so, we have chosen two promising effects which might have an observable impact on the dynamics of BNS mergers.

The first effect is the dissipation of kinetic energy due to bulk viscosity in the violent early postmerger phase of a BNS merger. The bulk viscosity stems from out-of-thermodynamic equilibrium nuclear reactions, i.e., direct and modified URCA processes, which can happen on comparable timescales as the nonlinear density oscillations in the postmerger phase [17]. Given the novelty of the modeling of dissipative effects in a fully general-relativistic setting, we have decided to start our investigation of bulk viscosity by exploring the behaviour of the corresponding equations in a simplified setup first.

Hence, in Chapter 3 we have studied the problem of spherically symmetric BH accretion of a bulk-viscous fluid [71]. We have obtained solutions by solving the corresponding system of ODEs and a suitable parametrization which prevents large out-of-thermodynamic equilibrium contributions at large radii. The parameters are chosen such that the fluid is causal at all radii which limits the deviations of the viscous solution from the inviscid one. We observe only small deviations between the two cases for the most extreme bulk viscosities and relaxation times we have considered. Nevertheless, to the best of our knowledge, our calculations represent the first stationary accretion solution of a MIS-type bulk-viscous fluid onto a Schwarzschild BH. This is the first step in the process of investigating bulk viscosity in BNS mergers as we have developed a sufficiently simple, general-relativistic solution which can serve as a test case for GRDHD codes.

Motivated by these results we have moved on and developed a robust scheme to include the effects of the aforementioned MIS-type bulk viscosity in fully dynamical general-relativistic simulations of BNS mergers in the first part of Chapter 4. We have tested the implementation by measuring the numerical and physical viscosity of our code and achieved convergent results. However, as also already observed by [70], we find that the numerical viscosity can be dominated by discretization errors at the neutron star surface which leads to a degraded convergence order compared to the formal convergence order of the code. Our code represents one of a few NR codes taking into account the effects of viscosity and being able to simulate BNS mergers self-consistently [103, 244, 286, 105].

In the second part of Chapter 4 we have explored, for the first time, the impact of bulk viscosity on the BNS merger dynamics. Given the novelty of this study we decided to have a simplified description of bulk viscosity by setting it to a constant value inside the neutron stars. Varying its value within the allowed range [200] has

allowed us to gain systematically a first qualitative and quantitative understanding of the most extreme scenarios. Our main findings are:

1. Large bulk viscosities can efficiently damp the GW emission by suppressing quadrupolar density deformations, see also [280] for a similar observation related to shear viscosity.

2. Large bulk viscosities can lead to a shift in the dominant frequency f_2 of the GW signal which can be of $\simeq 9\%$ or $\simeq 280\,\mathrm{Hz}$, see also [140, 202] which report frequency shifts which are by approximately a factor 2 smaller.

3. Large bulk viscosities impact the secondary peaks, f_1 and f_3, of the postmerger PSD by reducing their power, see also [296] for an inviscid toy model.

4. Large bulk viscosities lead to a change in the SMNS structure by increasing the angular velocity in the SMNS core and therefore the total rotational kinetic energy.

5. Large bulk viscosities suppress the dynamical mass ejection and enhance the anisotropy in the outflow.

The main caveat of our study is the employment of a constant bulk viscosity which in reality is expected to vary as a function of density and temperature. Nevertheless, our observations have numerous implications for future observations of BNS mergers. Most importantly, given the strong impact of bulk viscosity on the postmerger GW signal, upcoming third-generation GW detectors such as the Einstein Telescope [146] and the Cosmic Explorer [112] might be able to provide meaningful upper limits on the bulk viscosity through observations of the postmerger GW signal. Additionally, universal relations involving the measurements of the f_2 frequency which are used to deduce the properties of the EOS (see, e.g., [31, 295, 41, 296, 259, 30, 35, 40, 34, 53, 176, 55]) need to be properly adjusted in order to account for shifts in f_2 due to bulk viscosity. Also, the EM counterpart from a BNS merger might be affected by large bulk viscosities due to its influence on the rotational energy of the remnant and the dynamically ejected mass. We reserve an investigation of the links between a large bulk viscosity and the corresponding kilonova signal for future studies where data from the kilonova accompanying GW170817 [252] will be used. Overall, given the tight relation between the magnitude of the bulk viscosity and the EOS, meaningful upper limits on the bulk viscosity might therefore add novel constraints on the EOS of hot and dense neutron star matter.

The second effect investigated in this Thesis, which might yield novel constraints on the physics of neutron star matter, is the amplification of crustal magnetic fields in BNS mergers. In Chapter 5 we provide first evidence that magnetic fields which are located only close to the neutron star surface lead to weaker magnetic fields and smaller total magnetic energies compared to the standard case where magnetic fields are present also in the core of the neutron stars [74]. These results have been obtained by performing computationally expensive high-resolution GRMHD simulations of BNS mergers.

The main caveat of our study, as is the case with most simulations of BNS mergers, is the high but still insufficient resolution to fully capture the shearing dynamics of the KHI [320, 166, 221]. Nevertheless, the outcome of our investigation has important implications for the outcome of BNS mergers due to the role magnetic fields play in the postmerger phase. Numerous studies have shown how strong large-scale helical magnetic fields can launch mildly relativistic polar outflows [231, 268, 203, 75, 58, 78, 199, 82] which serve as a possible explanation for the massive blue kilonova component observed in AT2017gfo [252]. The generation of such magnetic-field structures

is sensitive to the strength and topology of the magnetic fields in the early postmerger phase. As a consequence, the timescales on which these outflows are generated can be prolonged as a result of magnetic fields which are not strong enough in the first ten milliseconds after the merger.

Hence, polar outflows which originate from an early postmerger phase are in tension with purely crustal initial magnetic field topologies. Going back to our initial goal of finding new avenues to constrain the physics of neutron star matter, this finding suggests that the neutron star cores could not have been type-I superconductors which have expelled most of their magnetic flux on a sufficiently short timescale, if early magnetised outflows are observed. Our study suggests that the superconducting properties of dense nuclear matter could be tested in high-resolution simulations of BNS mergers for the most extreme cases.

All in all, this Thesis provides promising results on the influence of realistic dissipative and shearing effects in BNS mergers. Although promising, further studies are needed in order to clarify the role of a realistic bulk viscosity and crustal magnetic fields in BNS mergers and overcome the shortcomings of our first investigations.

Appendix

A Calculation of viscous black-hole accretion

This section contains important details about the solution of the viscous BH accretion problem.

Singular point analysis and integration

The sonic point r_s is defined as the radius at which the fluid velocity is surpassing the speed of sound. This radius is given by the condition $u^2/\mathcal{E}^2 = c_s'^2$. Therefore, the sonic point is a singular point of the system of ODEs given in Eqs. (3.15) and (3.16). We start solving the problem by choosing the sonic point r_s. In the following, we will describe our integration method which starts directly at r_s. This allows us to integrate inward (i.e., the supersonic portion) and outward (i.e., the subsonic portion) from there such that we can employ analytical results on the fluid properties and their derivatives at the sonic point.

In the inviscid case, the constants of motion $\dot{M}$ and $\mathcal{B}_{\text{pf}}$ are already determined by the choice of a sonic point [144]. We calculate these values from r_s and reuse them for the viscous solution, e.g., $\mathcal{B} = \mathcal{B}_{\text{pf}}(r_s)$. This allows us to compute the initial values $u_s := u(r_s)$ and $h_s := h(r_s)$ as the first step of the viscous solution in the following way: Given that the singularity at r_s must be removable for the solution to be regular, we obtain from Eqs. (3.15) and (3.16) the conditions

$$0 = \frac{M}{\mathcal{E}^2 r} - \frac{\mathcal{B} - \mathcal{E}h}{\mathcal{B}} \frac{r}{\tau_{\Pi} u} - 2c_s'^2 , \tag{A.1}$$

$$0 = c_s'^2 - \frac{u^2}{\mathcal{E}^2} . \tag{A.2}$$

The values u_s and h_s can now be calculated by using a numerical root-finding procedure with the help of Mathematica [316]. At this point we find multiple solutions and choose the accreting solution by enforcing $u_s < 0$ and $h_s > 1$, which was found to provide a unique solution for constant ζ and τ_{Π}.

Finally, in order to start the numerical integration at r_s we need to have accurate values for the derivatives du/dr and dh/dr which do not come from the evaluation of the RHS of Eqs. (3.15) and (3.16). Although the solution is regular at r_s, numerical errors make the evaluation of the RHS at r_s unreliable and behave singularly. Hence, the first step in the integration (inward and outward) makes use of analytically calculated values for the RHS. We follow the work of [183] (but see also [255, 4]) and assume u, r and h to be functions of an additional parameter ξ, i.e., $u = u(\xi), r = r(\xi), h = h(\xi)$. Then, Eqs. (3.15) and (3.16) which are written symbolically in the form $du/dr = A/B$ and $dh/dr = C/B$, respectively, can be rewritten in the form $du/d\xi = A$, $dr/d\xi = B$, and

$dh/d\xi = C$:

$$\frac{dr}{d\xi} = r\left(c_s'^2 - \frac{u^2}{\mathcal{E}^2}\right), \tag{A.3}$$

$$\frac{du}{d\xi} = u\left(\frac{M}{\mathcal{E}^2 r} - \frac{\mathcal{B}-\mathcal{E}h}{\mathcal{B}}\frac{r}{\tau_\Pi u} - 2c_s'^2\right), \tag{A.4}$$

$$\frac{dh}{d\xi} = -\left[(\gamma_e - 1)\frac{\mathcal{B}-\mathcal{E}}{\mathcal{E}} + \frac{\mathcal{B}-h\mathcal{E}}{\mathcal{E}}\right]\left[\frac{M}{\mathcal{E}^2 r} - \frac{\mathcal{B}-\mathcal{E}h}{\mathcal{B}}\frac{r}{\tau_\Pi u} - 2\frac{u^2}{\mathcal{E}^2}\right]. \tag{A.5}$$

We remark that ξ is not physically meaningful and should be viewed as a mathematical parameter. However, it is helpful to think of the solution at r_s as having two branches: one branch for the supersonic portion and one for the subsonic portion, and the solution at r_s is given in the limit $\xi \to \pm\infty$[1].

Note that solutions of the original system, i.e., Eqs. (3.15) and (3.16), are now given by the trajectories of the solutions of the extended system, i.e., Eqs. (A.3)–(A.5), in the *phase space*, i.e., the (u, h, r)-space. Hence, the solutions of the original system describe the so-called *phase paths* of Eqs. (A.3)–(A.5). Then, the solution at the sonic point (u_s, h_s) corresponds to the so-called *equilibrium point* (u_s, h_s, r_s) of the extended system (the equilibrium point is defined by the conditions $du/d\xi = dh/d\xi = dr/d\xi = 0$).

In order to obtain values for the RHS analytically, we can linearise the extended system of Eqs. (A.3)–(A.5) at the equilibrium point, i.e., $u \approx u_s + \delta u$, $h \approx h_s + \delta h$ and $r \approx r_s + \delta r$, to obtain a local solution [162]. Using the ansatz $\delta u = \delta_u \exp(\lambda\xi)$, $\delta h = \delta_h \exp(\lambda\xi)$ and $\delta r = \delta_r \exp(\lambda\xi)$ we obtain an eigenvalue problem. The result is a set of three eigenvalues $\{\lambda_1, \lambda_2, \lambda_3\}$ and eigenvectors with the properties $\lambda_1 < 0$, $\lambda_2 > 0$ and $\lambda_3 \approx 0$. The corresponding set of local solutions is then

$$\delta u_1(\xi) = (\delta_u)_1 \exp(\lambda_1\xi);\ \delta h_1(\xi) = (\delta_h)_1 \exp(\lambda_1\xi);\ \delta r_1(\xi) = (\delta_r)_1 \exp(\lambda_1\xi), \tag{A.6}$$

$$\delta u_2(\xi) = (\delta_u)_2 \exp(\lambda_2\xi);\ \delta h_2(\xi) = (\delta_h)_2 \exp(\lambda_2\xi);\ \delta r_2(\xi) = (\delta_r)_2 \exp(\lambda_2\xi), \tag{A.7}$$

where $((\delta_u)_i, (\delta_h)_i, (\delta_r)_i)$ denotes the i-th eigenvector which corresponds to the i-th eigenvalue λ_i. We note that the linearised solution of the extended system must pass through the equilibrium point (u_s, h_s, r_s) such that we find that $\delta u_i(\xi) = \delta h_i(\xi) = \delta r_i(\xi) = 0$ only in the limit $\xi \to +\infty$ or $\xi \to -\infty$. In particular, we find that in the limit $\xi \to +\infty$ the set in Eq. (A.6) reaches the equilibrium point while in the limit $\xi \to -\infty$ the set in Eq. (A.7) passes through the equilibrium point. We neglect the set of eigenvectors which correspond to λ_3 because $\lambda_3 \approx 0$. Furthermore, superpositions between different sets of eigenvectors are not allowed because they reach the equilibrium point for different limits of ξ. The RHS of Eqs. (3.15) and (3.16) at the sonic point is then given by $(du/dr)_s = (\delta_u)_i/(\delta_r)_i$ and $(dh/dr)_s = (\delta_h)_i/(\delta_r)_i$ for $i \in \{1, 2\}$. We choose the eigenvalue whose eigenvector yields $(du/dr)_s > 0$.

We are now able to start the numerical integration of the ODEs. The first step on either side of the sonic point, i.e., at $r_l = r_s - \Delta r$ and $r_r = r_s + \Delta r$, is calculated by using simple forward and backward finite differencing where we employ the analytical solutions to estimate the RHS of Eqs. (3.15) and (3.16). After the first step, we employ a fourth-order L-stable singly diagonally implicit Runge-Kutta (SDIRK) method (see Table 6.5. of [139] and the corresponding Butcher tableau). The implicit equation appearing in this method is solved by using a fixed-point iteration method. The s-stage

[1] This condition is the result of the form of the perturbation which behaves as $\sim e^{\lambda\xi}$, where λ is a constant eigenvalue that can be either positive or negative, and that it vanishes at the sonic point; see also below.

1/4	1/4				
3/4	1/2	1/4			
11/20	17/50	−1/25	1/4		
1/2	371/1360	−137/2720	15/544	1/4	
1	25/24	−49/48	125/16	−85/12	1/4
	25/24	−49/48	125/16	−85/12	1/4

Table A.1: Butcher tableau for a *L*-stable SDIRK method of order 4

Runge-Kutta method has the form

$$y_{n+1} = y_n + \Delta r \sum_{i=1}^{s} b_i k_i \,, \tag{A.8}$$

$$k_i = f\left(r_n + c_i \Delta r, y_n + h \sum_{j}^{s} a_{ij} k_j \right), \qquad i = 1, \ldots, s \,, \tag{A.9}$$

where the coefficients $\{c_i, a_{ij}, b_i\}$ are given in the form of Butcher tableaus in Table A.1. We use 700,000 points for the integration and concentrate resolution wherever it is most needed, i.e., near the sonic point and close to the BH event horizon.

B Decomposition of the gradients of the fluid four-velocity

This section introduces various definitions related to the decomposition of the gradients of the fluid four-velocity and is based on [235, 234, 261, 71]. The "irreducible decomposition" is given by

$$\nabla^\mu u^\nu = \omega^{\mu\nu} + \sigma^{\mu\nu} + \frac{1}{3}\Theta h^{\mu\nu} - u^\mu a^\nu \,, \tag{B.1}$$

where Θ is the so-called "fluid expansion" and defined as

$$\Theta := \nabla_\mu u^\mu \,, \tag{B.2}$$

a^μ is the so-called "kinematic fluid four-acceleration" and given by

$$a^\mu := u^\lambda \nabla_\lambda u^\mu \,, \tag{B.3}$$

$\sigma^{\mu\nu}$ is the so-called "fluid shear tensor" and defined by

$$\sigma^{\mu\nu} := \nabla^{\langle\mu} u^{\nu\rangle} = \nabla^{(\mu} u^{\nu)} + a^{(\mu} u^{\nu)} - \frac{1}{3}\Theta h^{\mu\nu} \,, \tag{B.4}$$

and finally, $\omega^{\mu\nu}$ is the so-called "kinematic fluid vorticity"

$$\omega^{\mu\nu} := \nabla^{[\mu} u^{\nu]} + u^{[\mu} a^{\nu]} . \tag{B.5}$$

C Initial data for binary neutron star simulations

The initial data for all simulations of BNS mergers, which are presented in this Thesis, is computed using the FUKA codes [227]. We compute irrotational equal-mass binaries with a total ADM mass of $\sim 2.55\ M_\odot$ at a separation of $\sim 30\ M_\odot \approx 44\,\mathrm{km}$. Furthermore, we employ a cold, β-equilibrated slice of the TNTYST EOS, which has a maximum mass of $M_{\mathrm{TOV}} = 2.21\ M_\odot$ [301]. Note that the ADM mass of this binary is smaller than the maximally supported mass of a uniformly rotating neutron star described by the TNTYST EOS which can approximated as $M_{\mathrm{max}} \approx 1.2 \times M_{\mathrm{TOV}} \approx 2.65\ M_\odot$ [56]. Therefore, we expect the resulting SMNS remnant to be long-lived. Furthermore, these choices for the binary parameters are well-represented in the set of observed BNS systems [217].

Bibliography

[1] B. P. Abbott et al. "GW170817: Observation of Gravitational Waves from a Binary Neutron Star Inspiral". In: *Phys. Rev. Lett.* 119.16, 161101 (Oct. 2017), p. 161101. DOI: 10.1103/PhysRevLett.119.161101. arXiv: 1710.05832 [gr-qc].

[2] B. P. Abbott et al. "GW190425: Observation of a Compact Binary Coalescence with Total Mass $\sim 3.4\ M_{\odot}$". In: *Astrophys. J. Lett.* 892.1, L3 (Mar. 2020), p. L3. DOI: 10.3847/2041-8213/ab75f5. arXiv: 2001.01761 [astro-ph.HE].

[3] Benjamin P. Abbott et al. "Gravitational Waves and Gamma-Rays from a Binary Neutron Star Merger: GW170817 and GRB 170817A". In: *Astrophys. J. Lett.* 848.2 (2017), p. L13. DOI: 10.3847/2041-8213/aa920c. arXiv: 1710.05834 [astro-ph.HE]. URL: https://doi.org/10.3847%2F2041-8213%2Faa920c.

[4] N. Afshordi and B. Paczyński. "Geometrically Thin Disk Accreting into a Black Hole". In: *Astrophys. J.* 592.1 (July 2003), pp. 354–367. DOI: 10.1086/375559. arXiv: astro-ph/0202409 [astro-ph].

[5] Ricard Aguilera-Miret, Daniele Viganò, and Carlos Palenzuela. "Universality of the Turbulent Magnetic Field in Hypermassive Neutron Stars Produced by Binary Mergers". In: *Astrophys. J. Lett.* 926.2 (2022), p. L31. DOI: 10.3847/2041-8213/ac50a7. arXiv: 2112.08406 [gr-qc].

[6] Ricard Aguilera-Miret et al. "Turbulent magnetic-field amplification in the first 10 milliseconds after a binary neutron star merger: Comparing high-resolution and large-eddy simulations". In: *Phys. Rev. D* 102.10, 103006 (Nov. 2020), p. 103006. DOI: 10.1103/PhysRevD.102.103006. arXiv: 2009.06669 [gr-qc].

[7] Miguel Alcubierre. *Introduction to* $3+1$ *Numerical Relativity*. Oxford, UK: Oxford University Press, 2008. DOI: 10.1093/acprof:oso/9780199205677.001.0001.

[8] Miguel Alcubierre et al. "Dynamical evolution of quasi-circular binary black hole data". In: *Phys. Rev. D* 72.4 (2005), p. 044004. eprint: gr-qc/0411149.

[9] M. G. Alford et al. "Viscous Dissipation and Heat Conduction in Binary Neutron-Star Mergers". In: *Phys. Rev. Lett.* 120 (4 Jan. 2018), p. 041101. DOI: 10.1103/PhysRevLett.120.041101. eprint: 1707.09475 (gr-qc).

[10] Mark G. Alford and Alexander Haber. "Strangeness-changing Rates and Hyperonic Bulk Viscosity in Neutron Star Mergers". In: *arXiv e-prints*, arXiv:2009.05181 (Sept. 2020), arXiv:2009.05181. arXiv: 2009.05181 [nucl-th].

[11] Mark G. Alford, Alexander Haber, Steven P. Harris, and Ziyuan Zhang. "Beta Equilibrium Under Neutron Star Merger Conditions". In: *Universe* 7.11 (Oct. 2021), p. 399. DOI: 10.3390/universe7110399. arXiv: 2108.03324 [nucl-th].

[12] Mark G. Alford and Steven P. Harris. "Beta equilibrium in neutron star mergers". In: *Phys. Rev. C* 98.6 (2018), p. 065806. DOI: 10.1103/PhysRevC.98.065806. arXiv: 1803.00662 [nucl-th].

[13] Mark G. Alford and Steven P. Harris. "Damping of density oscillations in neutrino-transparent nuclear matter". In: *arXiv e-prints*, arXiv:1907.03795 (July 2019), arXiv:1907.03795. arXiv: 1907.03795 [nucl-th].

[14] Mark G. Alford, Simin Mahmoodifar, and Kai Schwenzer. "Large amplitude behavior of the bulk viscosity of dense matter". In: *J. Phys.* G37 (2010), p. 125202. DOI: 10.1088/0954-3899/37/12/125202. arXiv: 1005.3769 [nucl-th].

[15] Mark Alford, Arus Harutyunyan, and Armen Sedrakian. "Bulk viscosity of baryonic matter with trapped neutrinos". In: *arXiv e-prints*, arXiv:1907.04192 (July 2019), arXiv:1907.04192. arXiv: 1907.04192 [astro-ph.HE].

[16] Mark Alford, Arus Harutyunyan, and Armen Sedrakian. "Bulk Viscosity of Relativistic npeμ Matter in Neutron-Star Mergers". In: *Particles* 5.3 (Sept. 2022), pp. 361–376. DOI: 10.3390/particles5030029. arXiv: 2209.04717 [astro-ph.HE].

[17] Mark Alford, Arus Harutyunyan, and Armen Sedrakian. "Bulk Viscous Damping of Density Oscillations in Neutron Star Mergers". In: *Particles*, arXiv:2006.07975 (June 2020), arXiv:2006.07975. DOI: 10.3390/particles3020034. arXiv: 2006.07975 [nucl-th]. URL: http://dx.doi.org/10.3390/particles3020034.

[18] M. Anderson et al. "Magnetized Neutron-Star Mergers and Gravitational-Wave Signals". In: *Phys. Rev. Lett.* 100.19, 191101 (May 2008), p. 191101. DOI: 10.1103/PhysRevLett.100.191101. arXiv: 0801.4387 [gr-qc].

[19] E. Annala, T. Gorda, A. Kurkela, and A. Vuorinen. "Gravitational-Wave Constraints on the Neutron-Star-Matter Equation of State". In: *Phys. Rev. Lett.* 120.17, 172703 (Apr. 2018), p. 172703. DOI: 10.1103/PhysRevLett.120.172703. arXiv: 1711.02644 [astro-ph.HE].

[20] Eemeli Annala et al. "Evidence for quark-matter cores in massive neutron stars". In: *Nature Physics* 16.9 (June 2020), pp. 907–910. DOI: 10.1038/s41567-020-0914-9.

[21] R. Arnowitt, S. Deser, and C. W. Misner. "Republication of: The dynamics of general relativity". In: *General Relativity and Gravitation* 40 (Sept. 2008), pp. 1997–2027. DOI: 10.1007/s10714-008-0661-1. eprint: gr-qc/0405109.

[22] Rudolf Baier et al. "Relativistic viscous hydrodynamics, conformal invariance, and holography". In: *Journal of High Energy Physics* 2008.04 (Apr. 2008), pp. 100–100. DOI: 10.1088/1126-6708/2008/04/100. URL: https://doi.org/10.1088%2F1126-6708%2F2008%2F04%2F100.

[23] Luca Baiotti and Luciano Rezzolla. "Binary neutron-star mergers: a review of Einstein's richest laboratory". In: *Rept. Prog. Phys.* 80.9 (2017), p. 096901. DOI: 10.1088/1361-6633/aa67bb. arXiv: 1607.03540 [gr-qc].

[24] John G. Baker et al. "Gravitational wave extraction from an inspiraling configuration of merging black holes". In: *Phys. Rev. Lett.* 96 (2006), p. 111102. eprint: gr-qc/0511103.

[25] Hans Bantilan, Yago Bea, and Pau Figueras. "Evolutions in first-order viscous hydrodynamics". In: *Journal of High Energy Physics* 2022.8, 298 (Aug. 2022), p. 298. DOI: 10.1007/JHEP08(2022)298. arXiv: 2201.13359 [hep-th].

[26] T. W. Baumgarte and S. L. Shapiro. "General Relativistic Magnetohydrodynamics for the Numerical Construction of Dynamical Spacetimes". In: *Astrophys. Journal* 585 (Mar. 2003), pp. 921–929. DOI: 10.1086/346103. eprint: arXiv:astro-ph/0211340.

[27] T. W. Baumgarte and S. L. Shapiro. "Numerical integration of Einstein's field equations". In: *Phys. Rev. D* 59.2, 024007 (Jan. 1999), p. 024007. DOI: 10.1103/PhysRevD.59.024007. eprint: gr-qc/9810065.

[28] T. W. Baumgarte and S. L. Shapiro. *Numerical Relativity: Solving Einstein's Equations on the Computer*. Cambridge, UK: Cambridge University Press, 2010. DOI: 10.1017/cbo9781139193344.

[29] A. Bauswein, T. W. Baumgarte, and H.-T. Janka. "Prompt Merger Collapse and the Maximum Mass of Neutron Stars". In: *Phys. Rev. Lett.* 111.13, 131101 (Sept. 2013), p. 131101. DOI: 10.1103/PhysRevLett.111.131101. arXiv: 1307.5191 [astro-ph.SR].

[30] A. Bauswein and H.-T. Janka. "Measuring Neutron-Star Properties via Gravitational Waves from Neutron-Star Mergers". In: *Phys. Rev. Lett.* 108.1, 011101 (Jan. 2012), p. 011101. DOI: 10.1103/PhysRevLett.108.011101. arXiv: 1106.1616 [astro-ph.SR].

[31] A. Bauswein, H.-T. Janka, K. Hebeler, and A. Schwenk. "Equation-of-state dependence of the gravitational-wave signal from the ring-down phase of neutron-star mergers". In: *Phys. Rev. D* 86.6, 063001 (Sept. 2012), p. 063001. DOI: 10.1103/PhysRevD.86.063001. arXiv: 1204.1888 [astro-ph.SR].

[32] A. Bauswein, O. Just, H.-T. Janka, and N. Stergioulas. "Neutron-star Radius Constraints from GW170817 and Future Detections". In: *Astrophys. J. Lett.* 850, L34 (Dec. 2017), p. L34. DOI: 10.3847/2041-8213/aa9994. arXiv: 1710.06843 [astro-ph.HE].

[33] A. Bauswein and N. Stergioulas. "Unified picture of the post-merger dynamics and gravitational wave emission in neutron star mergers". In: *Phys. Rev. D* 91.12, 124056 (June 2015), p. 124056. DOI: 10.1103/PhysRevD.91.124056. arXiv: 1502.03176 [astro-ph.SR].

[34] A. Bauswein, N. Stergioulas, and H.-T. Janka. "Exploring properties of high-density matter through remnants of neutron-star mergers". In: *European Physical Journal A* 52, 56 (Mar. 2016), p. 56. DOI: 10.1140/epja/i2016-16056-7. arXiv: 1508.05493 [astro-ph.HE].

[35] A. Bauswein, N. Stergioulas, and H.-T. Janka. "Revealing the high-density equation of state through binary neutron star mergers". In: *Phys. Rev. D* 90.2, 023002 (July 2014), p. 023002. DOI: 10.1103/PhysRevD.90.023002. arXiv: 1403.5301 [astro-ph.SR].

[36] Fábio S. Bemfica, Marcelo M. Disconzi, and Jorge Noronha. "Causality of the Einstein-Israel-Stewart Theory with Bulk Viscosity". In: *Phys. Rev. Lett.* 122 (22 June 2019), p. 221602. DOI: 10.1103/PhysRevLett.122.221602. URL: https://link.aps.org/doi/10.1103/PhysRevLett.122.221602.

[37] Fábio S. Bemfica, Marcelo M. Disconzi, and Jorge Noronha. "Nonlinear causality of general first-order relativistic viscous hydrodynamics". In: *Phys. Rev. D* 100 (10 Nov. 2019), p. 104020. DOI: 10.1103/PhysRevD.100.104020. URL: https://link.aps.org/doi/10.1103/PhysRevD.100.104020.

[38] Paz Beniamini and Wenbin Lu. "Survival Times of Supramassive Neutron Stars Resulting from Binary Neutron Star Mergers". In: *Astrophys. J.* 920.2, 109 (Oct. 2021), p. 109. DOI: 10.3847/1538-4357/ac1678. arXiv: 2104.01181 [astro-ph.HE].

[39] Jonah E. Bernhard, J. Scott Moreland, and Steffen A. Bass. "Bayesian estimation of the specific shear and bulk viscosity of quark-gluon plasma". In: *Nature Physics* 15.11 (Aug. 2019), pp. 1113–1117. DOI: 10.1038/s41567-019-0611-8.

[40] S. Bernuzzi, T. Dietrich, and A. Nagar. "Modeling the Complete Gravitational Wave Spectrum of Neutron Star Mergers". In: *Phys. Rev. Lett.* 115.9, 091101 (Aug. 2015), p. 091101. DOI: 10.1103/PhysRevLett.115.091101. arXiv: 1504.01764 [gr-qc].

[41] S. Bernuzzi et al. "Quasiuniversal Properties of Neutron Star Mergers". In: *Phys. Rev. Lett.* 112.20, 201101 (May 2014), p. 201101. DOI: 10.1103/PhysRevLett.112.201101. arXiv: 1402.6244 [gr-qc].

[42] Sebastiano Bernuzzi and David Hilditch. "Constraint violation in free evolution schemes: comparing BSSNOK with a conformal decomposition of Z4". In: *Phys. Rev. D* 81 (2010), p. 084003. DOI: 10.1103/PhysRevD.81.084003. arXiv: 0912.2920 [gr-qc].

[43] V. S. Beskin. "Radio pulsars: already fifty years!" In: *Physics Uspekhi* 61.4 (Apr. 2018), pp. 353–380. DOI: 10.3367/UFNe.2017.10.038216. arXiv: 1807.08528 [astro-ph.HE].

[44] H. A. Bethe and J. R. Wilson. "Revival of a stalled supernova shock by neutrino heating". In: *Astrophys. J.* 295 (Aug. 1985), pp. 14–23. DOI: 10.1086/163343.

[45] B. Betz, D. Henkel, and D. H. Rischke. "From kinetic theory to dissipative fluid dynamics". In: *Progress in Particle and Nuclear Physics* 62.2 (Apr. 2009), pp. 556–561. DOI: 10.1016/j.ppnp.2008.12.018. arXiv: 0812.1440 [nucl-th].

[46] A. V. Bilous et al. "A NICER View of PSR J0030+0451: Evidence for a Global-scale Multipolar Magnetic Field". In: *Astrophys. J. Lett.* 887.1, L23 (Dec. 2019), p. L23. DOI: 10.3847/2041-8213/ab53e7. arXiv: 1912.05704 [astro-ph.HE].

[47] J. D. Bjorken. "Highly relativistic nucleus-nucleus collisions: The central rapidity region". In: *Phys. Rev. D* 27 (Jan. 1983), pp. 140–151. DOI: 10.1103/PhysRevD.27.140.

[48] C. D. Bochenek et al. "A fast radio burst associated with a Galactic magnetar". In: *Nature* 587.7832 (Nov. 2020), pp. 59–62. DOI: 10.1038/s41586-020-2872-x. arXiv: 2005.10828 [astro-ph.HE].

[49] C. Bona, T. Ledvinka, C. Palenzuela, and M. Zácek. "General-covariant evolution formalism for numerical relativity". In: *Phys. Rev. D* 67.10, 104005 (May 2003), p. 104005. DOI: 10.1103/PhysRevD.67.104005. eprint: gr-qc/0302083.

[50] C. Bona and C. Palenzuela. "Dynamical shift conditions for the Z4 and BSSN formalisms". In: *Phys. Rev. D* 69.10, 104003 (May 2004), p. 104003. DOI: 10.1103/PhysRevD.69.104003. eprint: gr-qc/0401019.

[51] H. Bondi. "On spherically symmetrical accretion". In: *Mon. Not. R. Astron. Soc.* 112 (Jan. 1952), p. 195. DOI: 10.1093/mnras/112.2.195.

[52] R Borges, M Carmona, B Costa, and W Don. "An improved weighted essentially non-oscillatory scheme for hyperbolic conservation laws". In: *Journal of Computational Physics* 227.6 (Mar. 2008), pp. 3191–3211. ISSN: 00219991. DOI: 10.1016/j.jcp.2007.11.038. URL: http://linkinghub.elsevier.com/retrieve/pii/S0021999107005232.

[53] S. Bose et al. “Neutron-Star Radius from a Population of Binary Neutron Star Mergers”. In: *Phys. Rev. Lett.* 120.3, 031102 (Jan. 2018), p. 031102. DOI: 10.1103/PhysRevLett.120.031102. arXiv: 1705.10850 [gr-qc].

[54] M. Boyle and A. H. Mroué. “Extrapolating gravitational-wave data from numerical simulations”. In: *Phys. Rev. D* 80.12, 124045 (Dec. 2009), p. 124045. DOI: 10.1103/PhysRevD.80.124045. arXiv: 0905.3177 [gr-qc].

[55] Matteo Breschi et al. “Constraints on the Maximum Densities of Neutron Stars from Postmerger Gravitational Waves with Third-Generation Observations”. In: *Phys. Rev. Lett.* 128.16, 161102 (Apr. 2022), p. 161102. DOI: 10.1103/PhysRevLett.128.161102. arXiv: 2110.06957 [gr-qc].

[56] C. Breu and L. Rezzolla. “Maximum mass, moment of inertia and compactness of relativistic stars”. In: *Mon. Not. R. Astron. Soc.* 459 (June 2016), pp. 646–656. DOI: 10.1093/mnras/stw575. arXiv: 1601.06083 [gr-qc].

[57] B. Brügmann, W. Tichy, and N. Jansen. “Numerical Simulation of Orbiting Black Holes”. In: *Phys. Rev. Lett.* 92.21, 211101 (May 2004), p. 211101. DOI: 10.1103/PhysRevLett.92.211101. eprint: gr-qc/0312112.

[58] M. Bugli, J. Guilet, and M. Obergaulinger. “Three-dimensional core-collapse supernovae with complex magnetic structures - I. Explosion dynamics”. In: *Mon. Not. R. Astron. Soc.* 507.1 (Oct. 2021), pp. 443–454. DOI: 10.1093/mnras/stab2161. arXiv: 2105.00665 [astro-ph.HE].

[59] Eric Burns. “Neutron star mergers and how to study them”. In: *Living Reviews in Relativity* 23.1, 4 (Dec. 2020), p. 4. DOI: 10.1007/s41114-020-00028-7. arXiv: 1909.06085 [astro-ph.HE].

[60] Wit Busza, Krishna Rajagopal, and Wilke van der Schee. “Heavy Ion Collisions: The Big Picture and the Big Questions”. In: *Annual Review of Nuclear and Particle Science* 68.1 (2018), pp. 339–376. DOI: 10.1146/annurev-nucl-101917-020852. eprint: https://doi.org/10.1146/annurev-nucl-101917-020852. URL: https://doi.org/10.1146/annurev-nucl-101917-020852.

[61] Craig Cahillane and Georgia Mansell. “Review of the Advanced LIGO Gravitational Wave Observatories Leading to Observing Run Four”. In: *Galaxies* 10.1 (Feb. 2022), p. 36. DOI: 10.3390/galaxies10010036. arXiv: 2202.00847 [gr-qc].

[62] Giovanni Camelio et al. “Simulating bulk viscosity in neutron stars I: formalism”. In: *arXiv e-prints*, arXiv:2204.11809 (Apr. 2022), arXiv:2204.11809. arXiv: 2204.11809 [gr-qc].

[63] Giovanni Camelio et al. “Simulating bulk viscosity in neutron stars II: evolution in spherical symmetry”. In: *arXiv e-prints*, arXiv:2204.11810 (Apr. 2022), arXiv:2204.11810. arXiv: 2204.11810 [gr-qc].

[64] Manuela Campanelli, Carlos O. Lousto, Pedro Marronetti, and Yosef Zlochower. “Accurate evolutions of orbiting black-hole binaries without excision”. In: *Phys. Rev. Lett.* 96 (2006), p. 111101. eprint: gr-qc/0511048.

[65] C. Y. Cardall, E. Endeve, and A. Mezzacappa. “Conservative 3+1 general relativistic Boltzmann equation”. In: *Phys. Rev. D* 88.2, 023011 (July 2013), p. 023011. DOI: 10.1103/PhysRevD.88.023011. arXiv: 1305.0037 [astro-ph.HE].

[66] Federico Carrasco, Daniele Viganò, and Carlos Palenzuela. “Gradient subgrid-scale model for relativistic MHD large-eddy simulations”. In: *Phys. Rev. D* 101.6, 063003 (Mar. 2020), p. 063003. DOI: 10.1103/PhysRevD.101.063003. arXiv: 1908.01419 [astro-ph.HE].

[67] B.W. Carroll and D.A. Ostlie. *An Introduction to Modern Astrophysics*. Pearson Addison-Wesley, 2007. ISBN: 9780805304022.

[68] T. Celora, N. Andersson, I. Hawke, and G. L. Comer. "Covariant approach to relativistic large-eddy simulations: The fibration picture". In: *Phys. Rev. D* 104.8, 084090 (Oct. 2021), p. 084090. DOI: 10.1103/PhysRevD.104.084090. arXiv: 2107.01083 [gr-qc].

[69] T. Celora et al. "Formulating bulk viscosity for neutron star simulations". In: *Phys. Rev. D* 105.10, 103016 (May 2022), p. 103016. DOI: 10.1103/PhysRevD.105.103016. arXiv: 2202.01576 [astro-ph.HE].

[70] P. Cerdá-Durán. "Numerical viscosity in hydrodynamics simulations in general relativity". In: *Classical and Quantum Gravity* 27.20, 205012 (Oct. 2010), p. 205012. DOI: 10.1088/0264-9381/27/20/205012. arXiv: 0912.1774 [astro-ph.SR].

[71] Michail Chabanov, Luciano Rezzolla, and Dirk H. Rischke. "General-relativistic hydrodynamics of non-perfect fluids: 3+1 conservative formulation and application to viscous black hole accretion". In: *Mon. Not. R. Astron. Soc.* 505.4 (Aug. 2021), pp. 5910–5940. DOI: 10.1093/mnras/stab1384. arXiv: 2102.10419 [gr-qc].

[74] Michail Chabanov, Samuel D. Tootle, Elias R. Most, and Luciano Rezzolla. "Crustal Magnetic Fields Do Not Lead to Large Magnetic-field Amplifications in Binary Neutron Star Mergers". In: *Astrophys. J. Lett.* 945.1, L14 (Mar. 2023), p. L14. DOI: 10.3847/2041-8213/acbbc5. arXiv: 2211.13661 [astro-ph.HE].

[75] Riccardo Ciolfi. "Collimated outflows from long-lived binary neutron star merger remnants". In: *Mon. Not. R. Astron. Soc.* 495.1 (June 2020), pp. L66–L70. DOI: 10.1093/mnrasl/slaa062. arXiv: 2001.10241 [astro-ph.HE].

[76] Riccardo Ciolfi. "The key role of magnetic fields in binary neutron star mergers". In: *General Relativity and Gravitation* 52.6, 59 (June 2020), p. 59. DOI: 10.1007/s10714-020-02714-x. arXiv: 2003.07572 [astro-ph.HE].

[77] Luciano Combi and Daniel M. Siegel. "GRMHD Simulations of Neutron-star Mergers with Weak Interactions: r-process Nucleosynthesis and Electromagnetic Signatures of Dynamical Ejecta". In: *Astrophys. J.* 944.1, 28 (Feb. 2023), p. 28. DOI: 10.3847/1538-4357/acac29. arXiv: 2206.03618 [astro-ph.HE].

[78] Luciano Combi and Daniel M. Siegel. "Jets from neutron-star merger remnants and massive blue kilonovae". In: *arXiv e-prints*, arXiv:2303.12284 (Mar. 2023), arXiv:2303.12284. DOI: 10.48550/arXiv.2303.12284. arXiv: 2303.12284 [astro-ph.HE].

[79] J. N. Cook, S. L. Shapiro, and B. C. Stephens. "Magnetic Braking and Viscous Damping of Differential Rotation in Cylindrical Stars". In: *Astrophys. J.* 599 (Dec. 2003), pp. 1272–1292.

[80] James M. Cordes and Shami Chatterjee. "Fast Radio Bursts: An Extragalactic Enigma". In: *An. Rev. Astron. & Astrophys.* 57 (Aug. 2019), pp. 417–465. DOI: 10.1146/annurev-astro-091918-104501. arXiv: 1906.05878 [astro-ph.HE].

[81] P. S. Cowperthwaite et al. "The Electromagnetic Counterpart of the Binary Neutron Star Merger LIGO/Virgo GW170817. II. UV, Optical, and Near-infrared Light Curves and Comparison to Kilonova Models". In: *Astrophys. J. Lett.* 848.2, L17 (Oct. 2017), p. L17. DOI: 10.3847/2041-8213/aa8fc7. arXiv: 1710.05840 [astro-ph.HE].

[82] Sanjana Curtis et al. “Outflows from Short-Lived Neutron-Star Merger Remnants Can Produce a Blue Kilonova”. In: *arXiv e-prints*, arXiv:2305.07738 (May 2023), arXiv:2305.07738. DOI: 10.48550/arXiv.2305.07738. arXiv: 2305.07738 [astro-ph.HE].

[83] Curt Cutler, Lee Lindblom, and Randall J. Splinter. “Damping Times for Neutron Star Oscillations”. In: *ApJ* 363 (Nov. 1990), p. 603. DOI: 10.1086/169370.

[84] Pushpita Das, Oliver Porth, and Anna L. Watts. “GRMHD simulations of accreting neutron stars with non-dipole fields”. In: *Monthly Notices of the Royal Astronomical Society* 515.3 (Sept. 2022), pp. 3144–3161. DOI: 10.1093/mnras/stac1817. arXiv: 2204.00249 [astro-ph.HE].

[85] Ashutosh Dash, Masoud Shokri, Luciano Rezzolla, and Dirk H. Rischke. “Charge diffusion in relativistic resistive second-order dissipative magnetohydrodynamics”. In: *Phys. Rev. D* 107.5, 056003 (Mar. 2023), p. 056003. DOI: 10.1103/PhysRevD.107.056003. arXiv: 2211.09459 [nucl-th].

[86] A. Dedner et al. “Hyperbolic Divergence Cleaning for the MHD Equations”. In: *Journal of Computational Physics* 175 (Jan. 2002), pp. 645–673. DOI: 10.1006/jcph.2001.6961.

[87] L. Del Zanna and N. Bucciantini. “An efficient shock-capturing central-type scheme for multidimensional relativistic flows. I. Hydrodynamics”. In: *Astron. Astrophys.* 390 (Aug. 2002), pp. 1177–1186. DOI: 10.1051/0004-6361:20020776. eprint: arXiv:astro-ph/0205290.

[88] L. Del Zanna, N. Bucciantini, and P. Londrillo. “An efficient shock-capturing central-type scheme for multidimensional relativistic flows. II. Magnetohydrodynamics”. In: *Astron. Astrophys.* 400 (Mar. 2003), pp. 397–413. DOI: 10.1051/0004-6361:20021641. eprint: arXiv:astro-ph/0210618.

[89] L. Del Zanna, O. Zanotti, N. Bucciantini, and P. Londrillo. “ECHO: a Eulerian conservative high-order scheme for general relativistic magnetohydrodynamics and magnetodynamics”. In: *Astron. Astrophys.* 473 (Oct. 2007), pp. 11–30. DOI: 10.1051/0004-6361:20077093. arXiv: 0704.3206.

[90] L. Del Zanna et al. “Relativistic viscous hydrodynamics for heavy-ion collisions with ECHO-QGP”. In: *European Physical Journal C* 73, 2524 (Aug. 2013), p. 2524. DOI: 10.1140/epjc/s10052-013-2524-5. arXiv: 1305.7052 [nucl-th].

[91] G S Denicol, T Kodama, T Koide, and Ph Mota. “Stability and causality in relativistic dissipative hydrodynamics”. In: *Journal of Physics G: Nuclear and Particle Physics* 35.11 (Sept. 2008), p. 115102. DOI: 10.1088/0954-3899/35/11/115102. URL: https://doi.org/10.1088%2F0954-3899%2F35%2F11%2F115102.

[92] G. S. Denicol, E. Molnár, H. Niemi, and D. H. Rischke. “Derivation of fluid dynamics from kinetic theory with the 14-moment approximation”. In: *The European Physical Journal A* 48.11 (Nov. 2012), p. 170. ISSN: 1434-601X. DOI: 10.1140/epja/i2012-12170-x. URL: https://doi.org/10.1140/epja/i2012-12170-x.

[93] G. S. Denicol, H. Niemi, E. Molnár, and D. H. Rischke. “Derivation of transient relativistic fluid dynamics from the Boltzmann equation”. In: *Phys. Rev. D* 85 (11 June 2012), p. 114047. DOI: 10.1103/PhysRevD.85.114047. URL: https://link.aps.org/doi/10.1103/PhysRevD.85.114047.

[94] G.S. Denicol et al. "Solving the heat-flow problem with transient relativistic fluid dynamics". In: *Phys. Rev. D* 89.7 (2014), p. 074005. DOI: 10.1103/PhysRevD.89.074005. arXiv: 1207.6811 [nucl-th].

[95] Tim Dietrich, Tanja Hinderer, and Anuradha Samajdar. "Interpreting binary neutron star mergers: describing the binary neutron star dynamics, modelling gravitational waveforms, and analyzing detections". In: *General Relativity and Gravitation* 53.3, 27 (Mar. 2021), p. 27. DOI: 10.1007/s10714-020-02751-6. arXiv: 2004.02527 [gr-qc].

[96] Tim Dietrich et al. "Multimessenger constraints on the neutron-star equation of state and the Hubble constant". In: *Science* 370.6523 (Dec. 2020), pp. 1450–1453. DOI: 10.1126/science.abb4317. arXiv: 2002.11355 [astro-ph.HE].

[97] K. Dionysopoulou et al. "General-relativistic resistive magnetohydrodynamics in three dimensions: Formulation and tests". In: *Phys. Rev. D* 88.4, 044020 (Aug. 2013), p. 044020. DOI: 10.1103/PhysRevD.88.044020. arXiv: 1208.3487 [gr-qc].

[98] Marcelo M. Disconzi, Vu Hoang, and Maria Radosz. "Breakdown of smooth solutions to the Müller-Israel-Stewart equations of relativistic viscous fluids". In: *Letters in Mathematical Physics* 113.3, 55 (June 2023), p. 55. DOI: 10.1007/s11005-023-01677-9.

[99] Marcelo M. Disconzi, Thomas W. Kephart, and Robert J. Scherrer. "On a viable first-order formulation of relativistic viscous fluids and its applications to cosmology". In: *International Journal of Modern Physics D* 26.13 (2017), p. 1750146. DOI: 10.1142/S0218271817501462. eprint: https://doi.org/10.1142/S0218271817501462. URL: https://doi.org/10.1142/S0218271817501462.

[100] Victor Doroshenko, Valery Suleimanov, Gerd Pühlhofer, and Andrea Santangelo. "A strangely light neutron star within a supernova remnant". In: *Nature Astronomy* (Oct. 2022), pp. 1–8. DOI: 10.1038/s41550-022-01800-1.

[101] M. R. Drout et al. "Light curves of the neutron star merger GW170817/SSS17a: Implications for r-process nucleosynthesis". In: *Science* 358 (Dec. 2017), pp. 1570–1574. DOI: 10.1126/science.aaq0049. arXiv: 1710.05443 [astro-ph.HE].

[102] Lipei Du and Ulrich Heinz. "(3+1)-dimensional dissipative relativistic fluid dynamics at non-zero net baryon density". In: *Computer Physics Communications* 251, 107090 (June 2020), p. 107090. DOI: 10.1016/j.cpc.2019.107090. arXiv: 1906.11181 [nucl-th].

[103] M. D. Duez, Y. T. Liu, S. L. Shapiro, and B. C. Stephens. "General relativistic hydrodynamics with viscosity: Contraction, catastrophic collapse, and disk formation in hypermassive neutron stars". In: *Phys. Rev. D* 69.10, 104030 (May 2004), p. 104030. DOI: 10.1103/PhysRevD.69.104030. eprint: astro-ph/0402502.

[104] Matthew D. Duez, Yuk Tung Liu, Stuart L. Shapiro, and Branson C. Stephens. "General relativistic hydrodynamics with viscosity: Contraction, catastrophic collapse, and disk formation in hypermassive neutron stars". In: *Phys. Rev. D* 69 (2004), p. 104030. eprint: gr-qc/0402502.

[105] Matthew D. Duez et al. "Comparison of momentum transport models for numerical relativity". In: *Phys. Rev. D* 102.10, 104050 (Nov. 2020), p. 104050. DOI: 10.1103/PhysRevD.102.104050. arXiv: 2008.05019 [gr-qc].

[106] Matthew D. Duez et al. “Evolution of magnetized, differentially rotating neutron stars: Simulations in full general relativity”. In: *Phys. Rev. D* 73 (2006), p. 104015. DOI: 10.1103/PhysRevD.73.104015. arXiv: astro-ph/0605331.

[107] M. Dumbser and E. F. Toro. “A Simple Extension of the Osher Riemann Solver to Non-Conservative Hyperbolic Systems”. In: *Journal of Scientific Computing* 48 (July 2011), pp. 70–88. DOI: 10.1007/s10915-010-9400-3.

[108] Carl Eckart. “The Thermodynamics of Irreversible Processes. III. Relativistic Theory of the Simple Fluid”. In: *Phys. Rev.* 58 (10 Nov. 1940), pp. 919–924. DOI: 10.1103/PhysRev.58.919. URL: https://link.aps.org/doi/10.1103/PhysRev.58.919.

[109] B. Einfeldt. “On Godunov-type methods for gas dynamics”. In: *SIAM J. Numer. Anal.* 25 (1988), pp. 294–318.

[110] Z. B. Etienne, V. Paschalidis, Y. T. Liu, and S. L. Shapiro. “Relativistic magnetohydrodynamics in dynamical spacetimes: Improved electromagnetic gauge condition for adaptive mesh refinement grids”. In: *Phys. Rev. D* 85.2, 024013 (Jan. 2012), p. 024013. DOI: 10.1103/PhysRevD.85.024013. arXiv: 1110.4633 [astro-ph.HE].

[111] Z. B. Etienne et al. “IllinoisGRMHD: an open-source, user-friendly GRMHD code for dynamical spacetimes”. In: *Class. Quantum Grav.* 32.17, 175009 (Sept. 2015), p. 175009. DOI: 10.1088/0264-9381/32/17/175009. arXiv: 1501.07276 [astro-ph.HE].

[112] Matthew Evans et al. “A Horizon Study for Cosmic Explorer: Science, Observatories, and Community”. In: *arXiv e-prints*, arXiv:2109.09882 (Sept. 2021), arXiv:2109.09882. DOI: 10.48550/arXiv.2109.09882. arXiv: 2109.09882 [astro-ph.IM].

[113] J. A. Faber and F. A. Rasio. “Binary Neutron Star Mergers”. In: *Living Reviews in Relativity* 15, 8 (July 2012), p. 8. DOI: 10.12942/lrr-2012-8. arXiv: 1204.3858 [gr-qc].

[114] B. D. Farris et al. “Binary Black-Hole Mergers in Magnetized Disks: Simulations in Full General Relativity”. In: *Phys. Rev. Lett.* 109.22, 221102 (Nov. 2012), p. 221102. DOI: 10.1103/PhysRevLett.109.221102. arXiv: 1207.3354 [astro-ph.HE].

[115] Rodrigo Fernández et al. “Long-term GRMHD simulations of neutron star merger accretion discs: implications for electromagnetic counterparts”. In: *Mon. Not. R. Astron. Soc.* 482.3 (Jan. 2019), pp. 3373–3393. DOI: 10.1093/mnras/sty2932. arXiv: 1808.00461 [astro-ph.HE].

[116] A. Figura et al. “Hybrid equation of state approach in binary neutron-star merger simulations”. In: *arXiv e-prints*, arXiv:2005.08691 (May 2020), arXiv:2005.08691. arXiv: 2005.08691 [gr-qc].

[117] J. A. Font et al. “Three-dimensional numerical general relativistic hydrodynamics. II. Long-term dynamics of single relativistic stars”. In: *Phys. Rev. D* 65.8, 084024 (Apr. 2002), p. 084024. DOI: 10.1103/PhysRevD.65.084024. eprint: gr-qc/0110047.

[118] H. Freistuhler and B. Temple. “Causal dissipation and shock profiles in the relativistic fluid dynamics of pure radiation”. In: *Proceedings of the Royal Society of London Series A* 470.2166 (Mar. 2014), pp. 20140055–20140055. DOI: 10.1098/rspa.2014.0055.

[119] Heinrich Freistühler. "Nonexistence and existence of shock profiles in the Bemfica-Disconzi-Noronha model". In: *Phys. Rev. D* 103.12, 124045 (June 2021), p. 124045. DOI: 10.1103/PhysRevD.103.124045. arXiv: 2103.16661 [math.AP].

[120] S. Fujibayashi et al. "Mass Ejection from the Remnant of a Binary Neutron Star Merger: Viscous-radiation Hydrodynamics Study". In: *Astrophys. J.* 860, 64 (June 2018), p. 64. DOI: 10.3847/1538-4357/aabafd. arXiv: 1711.02093 [astro-ph.HE].

[121] Sho Fujibayashi et al. "Comprehensive Study of Mass Ejection and Nucleosynthesis in Binary Neutron Star Mergers Leaving Short-lived Massive Neutron Stars". In: *Astrophys. J.* 942.1, 39 (Jan. 2023), p. 39. DOI: 10.3847/1538-4357/ac9ce0. arXiv: 2205.05557 [astro-ph.HE].

[122] Sho Fujibayashi et al. "Mass Ejection from the Remnant of a Binary Neutron Star Merger: Viscous-radiation Hydrodynamics Study". In: *The Astrophysical Journal* 860.1 (June 2018), p. 64. DOI: 10.3847/1538-4357/aabafd. URL: https://doi.org/10.3847%2F1538-4357%2Faabafd.

[123] Sho Fujibayashi et al. "Postmerger Mass Ejection of Low-mass Binary Neutron Stars". In: *Astrophys. J.* 901.2 (2020), p. 122. DOI: 10.3847/1538-4357/abafc2. arXiv: 2007.00474 [astro-ph.HE].

[124] F. Galeazzi, W. Kastaun, L. Rezzolla, and J. A. Font. "Implementation of a simplified approach to radiative transfer in general relativity". In: *Phys. Rev. D* 88.6, 064009 (Sept. 2013), p. 064009. DOI: 10.1103/PhysRevD.88.064009. arXiv: 1306.4953 [gr-qc].

[125] L. Gavassino, M. Antonelli, and B. Haskell. "Bulk viscosity in relativistic fluids: from thermodynamics to hydrodynamics". In: *Classical and Quantum Gravity* 38.7, 075001 (Apr. 2021), p. 075001. DOI: 10.1088/1361-6382/abe588. arXiv: 2003.04609 [gr-qc].

[126] L. Gavassino, M. Antonelli, and B. Haskell. "Thermodynamic Stability Implies Causality". In: *Phys. Rev. Lett.* 128.1, 010606 (Jan. 2022), p. 010606. DOI: 10.1103/PhysRevLett.128.010606. arXiv: 2105.14621 [gr-qc].

[127] Lorenzo Gavassino and Jorge Noronha. "Relativistic bulk-viscous dynamics far from equilibrium". In: *arXiv e-prints*, arXiv:2305.04119 (May 2023), arXiv:2305.04119. DOI: 10.48550/arXiv.2305.04119. arXiv: 2305.04119 [gr-qc].

[128] Robert Geroch and Lee Lindblom. "Causal theories of dissipative relativistic fluids". In: *Annals of Physics* 207.2 (May 1991), pp. 394–416. DOI: 10.1016/0003-4916(91)90063-E.

[129] B. Giacomazzo, L. Rezzolla, and L. Baiotti. "Can magnetic fields be detected during the inspiral of binary neutron stars?" In: *Mon. Not. R. Astron. Soc.* 399 (Oct. 2009), pp. L164–L168. DOI: 10.1111/j.1745-3933.2009.00745.x. arXiv: 0901.2722 [gr-qc].

[130] Bruno Giacomazzo, Luciano Rezzolla, and Luca Baiotti. "Accurate evolutions of inspiralling and magnetized neutron stars: Equal-mass binaries". In: *Phys. Rev. D* 83.4 (Feb. 2011), p. 044014. DOI: 10.1103/PhysRevD.83.044014.

[131] Bruno Giacomazzo et al. "Producing Magnetar Magnetic Fields in the Merger of Binary Neutron Stars". In: *Astrophys. J.* 809.1, 39 (Aug. 2015), p. 39. DOI: 10.1088/0004-637X/809/1/39. arXiv: 1410.0013 [astro-ph.HE].

[132] N.K. Glendenning. *Compact Stars: Nuclear Physics, Particle Physics, and General Relativity*. Astronomy and Astrophysics Library. Springer New York, 2000. ISBN: 9780387989778. URL: https://books.google.de/books?id=BBS0gxe2S1AC.

[133] S. K. Godunov. "A difference method for numerical calculations of discontinuous solutions of the equations of hydrpdynamics". In: *Mat. Sb.* 47 (1959). in Russian, p. 271.

[134] Ore Gottlieb et al. "On the Jet-Ejecta Interaction in 3D GRMHD Simulations of a Binary Neutron Star Merger Aftermath". In: *Astrophys. J. Lett.* 933.1, L2 (July 2022), p. L2. DOI: 10.3847/2041-8213/ac7728. arXiv: 2205.01691 [astro-ph.HE].

[135] Eric Gourgoulhon. *3+1 Formalism in General Relativity*. Vol. 846. Lecture Notes in Physics, Berlin Springer Verlag. Springer, 2012. DOI: 10.1007/978-3-642-24525-1.

[136] P. Grandclément and J. Novak. "Spectral Methods for Numerical Relativity". In: *Living Rev. Relativ.* 12.1 (2009). URL: http://www.livingreviews.org/lrr-2009-1.

[137] Carsten Gundlach, Jose M. Martin-Garcia, G. Calabrese, and I. Hinder. "Constraint Damping in the Z4 Formulation and Harmonic Gauge". In: *Class. Quantum Grav.* 22 (2005), pp. 3767–3774. DOI: 10.1088/0264-9381/22/17/025. eprint: gr-qc/0504114.

[138] M. E. Gusakov, E. M. Kantor, and D. D. Ofengeim. "Magnetic field evolution time-scales in superconducting neutron stars". In: *Mon. Not. R. Astron. Soc.* 499.3 (Dec. 2020), pp. 4561–4569. DOI: 10.1093/mnras/staa3160. arXiv: 2010.07673 [astro-ph.HE].

[139] E. Hairer and G. Wanner. *Solving Ordinary Differential Equations II - Stiff and Differential-Algebraic Problems*. 2nd. Springer, 1996.

[140] P. Hammond, I. Hawke, and N. Andersson. "Impact of nuclear reactions on gravitational waves from neutron star mergers". In: *Phys. Rev. D* 107.4, 043023 (Feb. 2023), p. 043023. DOI: 10.1103/PhysRevD.107.043023.

[141] P. Hammond, I. Hawke, and N. Andersson. "Thermal aspects of neutron star mergers". In: *Phys. Rev. D* 104.10, 103006 (Nov. 2021), p. 103006. DOI: 10.1103/PhysRevD.104.103006. arXiv: 2108.08649 [astro-ph.HE].

[142] M. Hanauske et al. "Rotational properties of hypermassive neutron stars from binary mergers". In: *Phys. Rev. D* 96.4, 043004 (Aug. 2017), p. 043004. DOI: 10.1103/PhysRevD.96.043004. arXiv: 1611.07152 [gr-qc].

[143] A. Harten, P. D. Lax, and B. van Leer. "On Upstream Differencing and Godunov-Type Schemes for Hyperbolic Conservation Laws". In: *SIAM Rev.* 25 (1983), p. 35. DOI: 10.1137/1025002.

[144] J. F. Hawley, L. L. Smarr, and J. R. Wilson. "A numerical study of nonspherical black hole accretion. I Equations and test problems". In: *Astrophys. J.* 277 (Feb. 1984), pp. 296–311. DOI: 10.1086/161696.

[145] Michal P. Heller and Michał Spali ński. "Hydrodynamics Beyond the Gradient Expansion: Resurgence and Resummation". In: *Phys. Rev. Lett.* 115 (7 Aug. 2015), p. 072501. DOI: 10.1103/PhysRevLett.115.072501. URL: https://link.aps.org/doi/10.1103/PhysRevLett.115.072501.

[146] S. Hild et al. "Sensitivity studies for third-generation gravitational wave observatories". In: *Class. Quantum Grav.* 28.9, 094013 (May 2011), p. 094013. DOI: 10.1088/0264-9381/28/9/094013. arXiv: 1012.0908 [gr-qc].

[147] D. Hilditch et al. "Compact binary evolutions with the Z4c formulation". In: *Phys. Rev. D* 88.8, 084057 (Oct. 2013), p. 084057. DOI: 10.1103/PhysRevD.88.084057. arXiv: 1212.2901 [gr-qc].

[148] W. A. Hiscock and L. Lindblom. "Generic instabilities in first-order dissipative relativistic fluid theories". In: *Phys. Rev. D* 31 (Feb. 1985), pp. 725–733. DOI: 10.1103/PhysRevD.31.725.

[149] W. A. Hiscock and L. Lindblom. "Stability and causality in dissipative relativistic fluids." In: *Annals of Physics* 151 (1983), pp. 466–496. DOI: 10.1016/0003-4916(83)90288-9.

[150] William A. Hiscock and Lee Lindblom. "Linear plane waves in dissipative relativistic fluids". In: *Phys. Rev. D* 35 (12 June 1987), pp. 3723–3732. DOI: 10.1103/PhysRevD.35.3723. URL: https://link.aps.org/doi/10.1103/PhysRevD.35.3723.

[151] T. Y. Hou and P. G. LeFloch. "Why Nonconservative Schemes Converge to Wrong Solutions: Error Analysis". In: *Math. Comp.* 62 (1994), pp. 497–530.

[152] Raphael E. Hoult and Pavel Kovtun. "Stable and causal relativistic Navier-Stokes equations". In: *Journal of High Energy Physics* 2020.6, 67 (June 2020), p. 67. DOI: 10.1007/JHEP06(2020)067. arXiv: 2004.04102 [hep-th].

[153] R.N. Hulse and J.H. Taylor. "Discovery of a pulsar in a binary system". In: *Astrophys. J.* 195 (1975), pp. L51–L53.

[154] Andrei P. Igoshev, Sergei B. Popov, and Rainer Hollerbach. "Evolution of Neutron Star Magnetic Fields". In: *Universe* 7.9 (Sept. 2021), p. 351. DOI: 10.3390/universe7090351. arXiv: 2109.05584 [astro-ph.HE].

[155] G. Inghirami et al. "Magneto-hydrodynamic simulations of Heavy Ion Collisions with ECHO-QGP". In: *Journal of Physics Conference Series*. Vol. 1024. Journal of Physics Conference Series. May 2018, p. 012043. DOI: 10.1088/1742-6596/1024/1/012043.

[156] Gabriele Inghirami et al. "Numerical magneto-hydrodynamics for relativistic nuclear collisions". In: *European Physical Journal C* 76.12, 659 (Dec. 2016), p. 659. DOI: 10.1140/epjc/s10052-016-4516-8. arXiv: 1609.03042 [hep-ph].

[157] W. Israel. "Nonstationary irreversible thermodynamics: A causal relativistic theory". In: *Annals of Physics* 100 (Sept. 1976), pp. 310–331. DOI: 10.1016/0003-4916(76)90064-6.

[158] W. Israel and J. M. Stewart. "Transient relativistic thermodynamics and kinetic theory". In: *Annals of Physics* 118.2 (Apr. 1979), pp. 341–372. DOI: 10.1016/0003-4916(79)90130-1.

[159] Amaresh Jaiswal. "Relativistic dissipative hydrodynamics from kinetic theory with relaxation-time approximation". In: *Phys. Rev. C* 87.5, 051901 (May 2013), p. 051901. DOI: 10.1103/PhysRevC.87.051901. arXiv: 1302.6311 [nucl-th].

[160] Amaresh Jaiswal, Rajeev S. Bhalerao, and Subrata Pal. "Complete relativistic second-order dissipative hydrodynamics from the entropy principle". In: *Phys. Rev. C* 87.2, 021901 (Feb. 2013), p. 021901. DOI: 10.1103/PhysRevC.87.021901. arXiv: 1302.0666 [nucl-th].

[161] Jin-Liang Jiang, Christian Ecker, and Luciano Rezzolla. "Bayesian analysis of neutron-star properties with parameterized equations of state: the role of the likelihood functions". In: *arXiv e-prints*, arXiv:2211.00018 (Oct. 2022), arXiv:2211.00018. arXiv: 2211.00018 [gr-qc].

[162] D. W. Jordan and P. Smith. *Nonlinear Ordinary Differential Equations : An Introduction for Scientists and Engineers*. Oxford, UK: Oxford University Press, 2007. ISBN: 9780199208258.

[163] Rahul Kashyap et al. “Numerical relativity simulations of prompt collapse mergers: Threshold mass and phenomenological constraints on neutron star properties after GW170817”. In: *Phys. Rev. D* 105.10, 103022 (May 2022), p. 103022. DOI: 10.1103/PhysRevD.105.103022. arXiv: 2111.05183 [astro-ph.HE].

[164] Wolfgang Kastaun, Jay Vijay Kalinani, and Riccardo Ciolfi. “Robust recovery of primitive variables in relativistic ideal magnetohydrodynamics”. In: *Physical Review D* 103.2 (2021), p. 023018.

[165] T. Kawamura et al. “Binary neutron star mergers and short gamma-ray bursts: Effects of magnetic field orientation, equation of state, and mass ratio”. In: *Phys. Rev. D* 94.6, 064012 (Sept. 2016), p. 064012. DOI: 10.1103/PhysRevD.94.064012. arXiv: 1607.01791 [astro-ph.HE].

[166] K. Kiuchi, K. Kyutoku, Y. Sekiguchi, and M. Shibata. “Global simulations of strongly magnetized remnant massive neutron stars formed in binary neutron star mergers”. In: *Phys. Rev. D* 97.12, 124039 (June 2018), p. 124039. DOI: 10.1103/PhysRevD.97.124039. arXiv: 1710.01311 [astro-ph.HE].

[167] K. Kiuchi, K. Kyutoku, and M. Shibata. “Three-dimensional evolution of differentially rotating magnetized neutron stars”. In: *Phys. Rev. D* 86.6, 064008 (Sept. 2012), p. 064008. DOI: 10.1103/PhysRevD.86.064008. arXiv: 1207.6444 [astro-ph.HE].

[168] K. Kiuchi et al. “Efficient magnetic-field amplification due to the Kelvin-Helmholtz instability in binary neutron star mergers”. In: *Phys. Rev. D* 92.12, 124034 (Dec. 2015), p. 124034. DOI: 10.1103/PhysRevD.92.124034. arXiv: 1509.09205 [astro-ph.HE].

[169] K. Kiuchi et al. “High resolution magnetohydrodynamic simulation of black hole-neutron star merger: Mass ejection and short gamma ray bursts”. In: *Phys. Rev. D* 92.6, 064034 (Sept. 2015), p. 064034. DOI: 10.1103/PhysRevD.92.064034. arXiv: 1506.06811 [astro-ph.HE].

[170] Kenta Kiuchi et al. “Self-consistent picture of the mass ejection from a one second-long binary neutron star merger leaving a short-lived remnant in general-relativistic neutrino-radiation magnetohydrodynamic simulation”. In: *arXiv e-prints*, arXiv:2211.07637 (Nov. 2022), arXiv:2211.07637. DOI: 10.48550/arXiv.2211.07637. arXiv: 2211.07637 [astro-ph.HE].

[171] Sven Koeppel, Luke Bovard, and Luciano Rezzolla. “A General-relativistic Determination of the Threshold Mass to Prompt Collapse in Binary Neutron Star Mergers”. In: *Astrophys. J. Lett.* 872.1, L16 (Feb. 2019), p. L16. DOI: 10.3847/2041-8213/ab0210. arXiv: 1901.09977 [gr-qc].

[172] K. D. Kokkotas and J. Ruoff. “Radial oscillations of relativistic stars”. In: *Astronomy and Astrophysics* 366 (Feb. 2001), pp. 565–572. DOI: 10.1051/0004-6361:20000216. arXiv: gr-qc/0011093 [gr-qc].

[173] Pavel Kovtun. “First-order relativistic hydrodynamics is stable”. In: *Journal of High Energy Physics* 2019.10 (Oct. 2019), p. 34. ISSN: 1029-8479. DOI: 10.1007/JHEP10(2019)034. URL: https://doi.org/10.1007/JHEP10(2019)034.

[174] L. D. Landau and E. M. Lifshitz. *Fluid Mechanics, Course of Theoretical Physics, Volume 6*. Oxford: Elsevier Butterworth-Heinemann, 2004.

[175] P. D. Lax and B. Wendroff. “Systems of conservation laws”. In: *Commun. Pure Appl. Math.* 13 (1960), pp. 217–237.

[176] Georgios Lioutas, Andreas Bauswein, and Nikolaos Stergioulas. "Frequency deviations in universal relations of isolated neutron stars and postmerger remnants". In: *Phys. Rev. D* 104.4, 043011 (Aug. 2021), p. 043011. DOI: 10.1103/PhysRevD.104.043011. arXiv: 2102.12455 [astro-ph.HE].

[177] Yuk Tung Liu, Stuart L. Shapiro, Zachariah B. Etienne, and Keisuke Taniguchi. "General relativistic simulations of magnetized binary neutron star mergers". In: *Phys. Rev. D* 78 (2008), p. 024012. DOI: 10.1103/PhysRevD.78.024012. arXiv: 0803.4193 [astro-ph].

[178] Frank Löffler et al. "The Einstein Toolkit: A Community Computational Infrastructure for Relativistic Astrophysics". In: *Class. Quantum Grav.* 29.11 (2012), p. 115001. DOI: doi:10.1088/0264-9381/29/11/115001. eprint: arXiv:1111.3344[gr-qc].

[179] Eleonora Loffredo, Albino Perego, Domenico Logoteta, and Marica Branchesi. "Muons in the aftermath of neutron star mergers and their impact on trapped neutrinos". In: *Astronomy and Astrophysics* 672, A124 (Apr. 2023), A124. DOI: 10.1051/0004-6361/202244927. arXiv: 2209.04458 [astro-ph.HE].

[180] P Londrillo and L Del Zanna. "On the divergence-free condition in Godunov-type schemes for ideal magnetohydrodynamics: the upwind constrained transport method". In: *Journal of Computational Physics* 195.1 (2004), pp. 17–48.

[181] F. Maione, R. De Pietri, A. Feo, and F. Löffler. "Binary neutron star merger simulations with different initial orbital frequency and equation of state". In: *Classical and Quantum Gravity* 33.17, 175009 (Sept. 2016), p. 175009. DOI: 10.1088/0264-9381/33/17/175009. arXiv: 1605.03424 [gr-qc].

[182] F. Maione, R. De Pietri, A. Feo, and F. Löffler. "Spectral analysis of gravitational waves from binary neutron star merger remnants". In: *Phys. Rev. D* 96.6, 063011 (Sept. 2017), p. 063011. DOI: 10.1103/PhysRevD.96.063011. arXiv: 1707.03368 [gr-qc].

[183] Ipsita Mandal, Arnab K. Ray, and Tapas K. Das. "Critical properties of spherically symmetric black hole accretion in Schwarzschild geometry". In: *Mon. Not. R. Astron. Soc.* 378.4 (July 2007), pp. 1400–1406. DOI: 10.1111/j.1365-2966.2007.11898.x. arXiv: astro-ph/0702733 [astro-ph].

[184] B. Margalit and B. D. Metzger. "Constraining the Maximum Mass of Neutron Stars from Multi-messenger Observations of GW170817". In: *Astrophys. J. Lett.* 850, L19 (Dec. 2017), p. L19. DOI: 10.3847/2041-8213/aa991c. arXiv: 1710.05938 [astro-ph.HE].

[185] Peter McCorquodale and Phillip Colella. "A high-order finite-volume method for conservation laws on locally refined grids". In: *Communications in Applied Mathematics and Computational Science* 6.1 (2011), pp. 1–25.

[186] M. McNelis, D. Bazow, and U. Heinz. "Anisotropic fluid dynamical simulations of heavy-ion collisions". In: *arXiv e-prints*, arXiv:2101.02827 (Jan. 2021), arXiv:2101.02827. arXiv: 2101.02827 [nucl-th].

[187] B. D. Metzger. "Kilonovae". In: *Living Reviews in Relativity* 20, 3 (May 2017), p. 3. DOI: 10.1007/s41114-017-0006-z. arXiv: 1610.09381 [astro-ph.HE].

[188] B. D. Metzger. "Welcome to the Multi-Messenger Era! Lessons from a Neutron Star Merger and the Landscape Ahead". In: *ArXiv e-prints* (Oct. 2017). arXiv: 1710.05931 [astro-ph.HE].

[189] Vassilios Mewes et al. "Numerical relativity in spherical coordinates: A new dynamical spacetime and general relativistic MHD evolution framework for the Einstein Toolkit". In: *Physical Review D* 101.10, 104007 (May 2020), p. 104007. DOI: 10.1103/PhysRevD.101.104007. arXiv: 2002.06225 [gr-qc].

[190] F. C. Michel. "Accretion of matter by condensed objects". In: *Astrophys. Spa. Sci.* 15 (1972), p. 153.

[191] M. C. Miller et al. "PSR J0030+0451 Mass and Radius from NICER Data and Implications for the Properties of Neutron Star Matter". In: *Astrophys. J. Lett.* 887.1, L24 (Dec. 2019), p. L24. DOI: 10.3847/2041-8213/ab50c5. arXiv: 1912.05705 [astro-ph.HE].

[192] M. C. Miller et al. "The Radius of PSR J0740+6620 from NICER and XMM-Newton Data". In: *Astrophys. J. Lett.* 918.2, L28 (Sept. 2021), p. L28. DOI: 10.3847/2041-8213/ac089b. arXiv: 2105.06979 [astro-ph.HE].

[193] E. Molnár, H. Niemi, and D. H. Rischke. "Numerical tests of causal relativistic dissipative fluid dynamics". In: *European Physical Journal C* 65.3-4 (Feb. 2010), pp. 615–635. DOI: 10.1140/epjc/s10052-009-1194-9. arXiv: 0907.2583 [nucl-th].

[194] Etele Molnár. "Comparing the first- and second-order theories of relativistic dissipative fluid dynamics using the 1+1 dimensional relativistic flux corrected transport algorithm". In: *European Physical Journal C* 60.3 (Apr. 2009), pp. 413–429. DOI: 10.1140/epjc/s10052-009-0927-0. arXiv: 0807.0544 [nucl-th].

[195] E. R. Most, L. Jens Papenfort, and L. Rezzolla. "Beyond second-order convergence in simulations of magnetized binary neutron stars with realistic microphysics". In: *Mon. Not. R. Astron. Soc.* 490.3 (Dec. 2019), pp. 3588–3600. DOI: 10.1093/mnras/stz2809. arXiv: 1907.10328 [astro-ph.HE].

[196] E. R. Most, L. R. Weih, L. Rezzolla, and J. Schaffner-Bielich. "New Constraints on Radii and Tidal Deformabilities of Neutron Stars from GW170817". In: *Phys. Rev. Lett.* 120.26, 261103 (June 2018), p. 261103. DOI: 10.1103/PhysRevLett.120.261103. arXiv: 1803.00549 [gr-qc].

[197] Elias R. Most and Jorge Noronha. "Dissipative magnetohydrodynamics for non-resistive relativistic plasmas: An implicit second-order flux-conservative formulation with stiff relaxation". In: *Phys. Rev. D* 104.10, 103028 (Nov. 2021), p. 103028. DOI: 10.1103/PhysRevD.104.103028. arXiv: 2109.02796 [astro-ph.HE].

[198] Elias R. Most, Jorge Noronha, and Alexander A. Philippov. "Modelling general-relativistic plasmas with collisionless moments and dissipative two-fluid magnetohydrodynamics". In: *Monthly Notices of the Royal Astronomical Society* 514.4 (Aug. 2022), pp. 4989–5003. DOI: 10.1093/mnras/stac1435. arXiv: 2111.05752 [astro-ph.HE].

[199] Elias R. Most and Eliot Quataert. "Flares, Jets, and Quasiperiodic Outbursts from Neutron Star Merger Remnants". In: *Astrophys. J. Lett.* 947.1, L15 (Apr. 2023), p. L15. DOI: 10.3847/2041-8213/acca84. arXiv: 2303.08062 [astro-ph.HE].

[200] Elias R. Most et al. "Emergence of microphysical viscosity in binary neutron star post-merger dynamics". In: *arXiv e-prints*, arXiv:2207.00442 (July 2022), arXiv:2207.00442. arXiv: 2207.00442 [astro-ph.HE].

[201] Elias R. Most et al. "On the deconfinement phase transition in neutron-star mergers". In: *European Physical Journal A* 56.2, 59 (Feb. 2020), p. 59. DOI: 10.1140/epja/s10050-020-00073-4. arXiv: 1910.13893 [astro-ph.HE].

[202] Elias R. Most et al. "Projecting the likely importance of weak-interaction-driven bulk viscosity in neutron star mergers". In: *Mon. Not. R. Astron. Soc.* 509.1 (Jan. 2022), pp. 1096–1108. DOI: 10.1093/mnras/stab2793. arXiv: 2107.05094 [astro-ph.HE].

[203] Philipp Mösta et al. "A magnetar engine for short GRBs and kilonovae". In: *Astrophys. J. Lett.* 901 (2020), p. L37. DOI: 10.3847/2041-8213/abb6ef. arXiv: 2003.06043 [astro-ph.HE].

[204] I. Mueller. "Zum Paradoxon der Wärmeleitungstheorie". In: *Zeitschrift fur Physik* 198 (Aug. 1967), pp. 329–344. DOI: 10.1007/BF01326412.

[205] A. Murguia-Berthier et al. "The Properties of Short Gamma-Ray Burst Jets Triggered by Neutron Star Mergers". In: *Astrophys. J. Lett.* 835, L34 (Feb. 2016), p. L34. DOI: 10.3847/2041-8213/aa5b9e. arXiv: 1609.04828 [astro-ph.HE].

[206] Azwinndini Muronga. "Causal theories of dissipative relativistic fluid dynamics for nuclear collisions". In: *Phys. Rev. C* 69 (3 Mar. 2004), p. 034903. DOI: 10.1103/PhysRevC.69.034903. URL: https://link.aps.org/doi/10.1103/PhysRevC.69.034903.

[207] T. Nakamura, K. Oohara, and Y. Kojima. "General Relativistic Collapse to Black Holes and Gravitational Waves from Black Holes". In: *Progress of Theoretical Physics Supplement* 90 (1987), pp. 1–218. DOI: 10.1143/PTPS.90.1.

[208] Antonios Nathanail et al. "3D magnetized jet break-out from neutron-star binary merger ejecta: afterglow emission from the jet and the ejecta". In: *Mon. Not. R. Astron. Soc.* 502.2 (Apr. 2021), pp. 1843–1855. DOI: 10.1093/mnras/stab115. arXiv: 2009.09714 [astro-ph.HE].

[209] Antonios Nathanail et al. "On the opening angle of magnetized jets from neutron-star mergers: the case of GRB170817A". In: *Mon. Not. R. Astron. Soc.* 495.4 (May 2020), pp. 3780–3787. DOI: 10.1093/mnras/staa1454. arXiv: 2003.03597 [astro-ph.HE].

[210] Vsevolod Nedora et al. "Spiral-wave Wind for the Blue Kilonova". In: *Astrophys. J. Lett.* 886.2, L30 (Dec. 2019), p. L30. DOI: 10.3847/2041-8213/ab5794. arXiv: 1907.04872 [astro-ph.HE].

[211] Ezra T. Newman and Roger Penrose. "An Approach to Gravitational Radiation by a Method of Spin Coefficients". In: *J. Math. Phys.* 3.3 (1962). erratum in J. Math. Phys. 4, 998 (1963), pp. 566–578. DOI: 10.1063/1.1724257.

[212] L. Nobili, R. Turolla, and L. Zampieri. "Spherical accretion onto black holes - A complete analysis of stationary solutions". In: *Astrophys. J.* 383 (Dec. 1991), pp. 250–262. DOI: 10.1086/170781.

[213] M. Obergaulinger, M. A. Aloy, and E. Müller. "Local simulations of the magnetized Kelvin-Helmholtz instability in neutron-star mergers". In: *Astron. Astrophys.* 515, A30 (June 2010), A30. DOI: 10.1051/0004-6361/200913386. arXiv: 1003.6031 [astro-ph.SR].

[214] HR Olivares Sánchez, O Porth, and Y Mizuno. "The Black Hole Accretion Code: adaptive mesh refinement and constrained transport". In: *J. Phys. Conf. Ser.* 1031.1 (May 2018), p. 012008. ISSN: 1742-6588. DOI: 10.1088/1742-6596/1031/1/012008. URL: http://stacks.iop.org/1742-6596/1031/i=1/a=012008?key=crossref.f3a1d22bc66dbcfa7943b00d4b6047f9.

[215] Timothy S. Olson and William A. Hiscock. "Plane steady shock waves in Isreal-Stewart fluids". In: *Annals of Physics* 204.2 (Dec. 1990), pp. 331–350. DOI: 10.1016/0003-4916(90)90393-3.

[216] J. R. Oppenheimer and G. M. Volkoff. "On Massive Neutron Cores". In: *Physical Review* 55.4 (Feb. 1939), pp. 374–381. DOI: 10.1103/PhysRev.55.374.

[217] F. Özel and P. Freire. "Masses, Radii, and the Equation of State of Neutron Stars". In: *Annual Review of Astronomy and Astrophysics* 54 (Sept. 2016), pp. 401–440. DOI: 10.1146/annurev-astro-081915-023322. arXiv: 1603.02698 [astro-ph.HE].

[218] C. Palenzuela, L. Lehner, O. Reula, and L. Rezzolla. "Beyond ideal MHD: towards a more realistic modelling of relativistic astrophysical plasmas". In: *Mon. Not. R. Astron. Soc.* 394 (Apr. 2009), pp. 1727–1740. DOI: 10.1111/j.1365-2966.2009.14454.x. arXiv: 0810.1838.

[219] C. Palenzuela et al. "Effects of the microphysical equation of state in the mergers of magnetized neutron stars with neutrino cooling". In: *Phys. Rev. D* 92.4, 044045 (Aug. 2015), p. 044045. DOI: 10.1103/PhysRevD.92.044045. arXiv: 1505.01607 [gr-qc].

[220] C. Palenzuela et al. "Electromagnetic and Gravitational Outputs from Binary-Neutron-Star Coalescence". In: *Phys. Rev. Lett.* 111.6, 061105 (Aug. 2013), p. 061105. DOI: 10.1103/PhysRevLett.111.061105. arXiv: 1301.7074 [gr-qc].

[221] Carlos Palenzuela et al. "Turbulent magnetic field amplification in binary neutron star mergers". In: *Phys. Rev. D* 106.2, 023013 (July 2022), p. 023013. DOI: 10.1103/PhysRevD.106.023013. arXiv: 2112.08413 [gr-qc].

[222] Alex Pandya, Elias R. Most, and Frans Pretorius. "Causal, stable first-order viscous relativistic hydrodynamics with ideal gas microphysics". In: *Phys. Rev. D* 106.12, 123036 (Dec. 2022), p. 123036. DOI: 10.1103/PhysRevD.106.123036. arXiv: 2209.09265 [gr-qc].

[223] Alex Pandya, Elias R. Most, and Frans Pretorius. "Conservative finite volume scheme for first-order viscous relativistic hydrodynamics". In: *Phys. Rev. D* 105.12, 123001 (June 2022), p. 123001. DOI: 10.1103/PhysRevD.105.123001. arXiv: 2201.12317 [gr-qc].

[224] Alex Pandya and Frans Pretorius. "Numerical exploration of first-order relativistic hydrodynamics". In: *Phys. Rev. D* 104.2, 023015 (July 2021), p. 023015. DOI: 10.1103/PhysRevD.104.023015. arXiv: 2104.00804 [gr-qc].

[225] L. J. Papenfort, R. Gold, and L. Rezzolla. "Dynamical ejecta and nucleosynthetic yields from eccentric binary neutron-star mergers". In: *Phys. Rev. D* 98, 104028 (Nov. 2018), p. 104028. DOI: 10.1103/PhysRevD.98.104028. arXiv: 1807.03795 [gr-qc].

[226] L. Jens Papenfort, Elias R. Most, Samuel Tootle, and Luciano Rezzolla. "Impact of extreme spins and mass ratios on the post-merger observables of high-mass binary neutron stars". In: *Mon. Not. Roy. Astron. Soc.* 513.3 (2022), pp. 3646–3662. DOI: 10.1093/mnras/stac964. arXiv: 2201.03632 [astro-ph.HE].

[227] L. Jens Papenfort et al. "New public code for initial data of unequal-mass, spinning compact-object binaries". In: *Phys. Rev. D* 104 (2 July 2021), p. 024057. DOI: 10.1103/PhysRevD.104.024057. URL: https://link.aps.org/doi/10.1103/PhysRevD.104.024057.

[228] Carlos Pares. "Numerical methods for nonconservative hyperbolic systems: a theoretical framework". In: *SIAM J. Numer. Anal.* 44.1 (2006), pp. 300–321.

[229] Lorenzo Pareschi and Giovanni Russo. "Implicit–Explicit Runge–Kutta Schemes and Applications to Hyperbolic Systems with Relaxation". In: *Journal of Scientific Computing* 25.1 (2005), p. 129. DOI: 10.1007/BF02728986.

[230] V. Paschalidis. "General relativistic simulations of compact binary mergers as engines for short gamma-ray bursts". In: *Classical and Quantum Gravity* 34.8, 084002 (Apr. 2017), p. 084002. DOI: 10.1088/1361-6382/aa61ce. arXiv: 1611.01519 [astro-ph.HE].

[231] V. Paschalidis, M. Ruiz, and S. L. Shapiro. "Relativistic Simulations of Black Hole-Neutron Star Coalescence: The Jet Emerges". In: *Astrophys. J. Lett.* 806, L14 (June 2015), p. L14. DOI: 10.1088/2041-8205/806/1/L14. arXiv: 1410.7392 [astro-ph.HE].

[232] Andrea Passamonti, Taner Akgün, José A. Pons, and Juan A. Miralles. "On the magnetic field evolution time-scale in superconducting neutron star cores". In: *Mon. Not. R. Astron. Soc.* 469.4 (Aug. 2017), pp. 4979–4984. DOI: 10.1093/mnras/stx1192. arXiv: 1704.02016 [astro-ph.HE].

[233] Andrea Passamonti, Taner Akgün, José A. Pons, and Juan A. Miralles. "The relevance of ambipolar diffusion for neutron star evolution". In: *Mon. Not. R. Astron. Soc.* 465.3 (Mar. 2017), pp. 3416–3428. DOI: 10.1093/mnras/stw2936. arXiv: 1608.00001 [astro-ph.HE].

[234] J. Peitz and S. Appl. "Dissipative fluid dynamics in the 3 + 1 formalism". In: *Class. Quantum Grav.* 16 (Mar. 1999), pp. 979–989. DOI: 10.1088/0264-9381/16/3/025.

[235] J. Peitz and S. Appl. "Viscous accretion discs around rotating black holes". In: *Mon. Not. R. Astron. Soc.* 286 (Apr. 1997), pp. 681–695. eprint: arXiv:astro-ph/9612205.

[236] Denis Pollney et al. "The Asymptotic Falloff of Local Waveform Measurements in Numerical Relativity". In: *Phys. Rev. D* 80 (2009), p. 121502. DOI: 10.1103/PhysRevD.80.121502. arXiv: 0910.3656 [Unknown].

[237] J. A. Pons and U. Geppert. "Magnetic field dissipation in neutron star crusts: from magnetars to isolated neutron stars". In: *Astronomy and Astrophysics* 470.1 (July 2007), pp. 303–315. DOI: 10.1051/0004-6361:20077456. arXiv: astro-ph/0703267 [astro-ph].

[238] J. A. Pons, J. A. Miralles, and U. Geppert. "Magneto-thermal evolution of neutron stars". In: *Astronomy and Astrophysics* 496.1 (Mar. 2009), pp. 207–216. DOI: 10.1051/0004-6361:200811229. arXiv: 0812.3018 [astro-ph].

[239] José A. Pons and Daniele Viganò. "Magnetic, thermal and rotational evolution of isolated neutron stars". In: *Living Reviews in Computational Astrophysics* 5.1, 3 (Dec. 2019), p. 3. DOI: 10.1007/s41115-019-0006-7. arXiv: 1911.03095 [astro-ph.HE].

[240] O. Porth et al. "The black hole accretion code". In: *Computational Astrophysics and Cosmology* 4, 1 (May 2017), p. 1. DOI: 10.1186/s40668-017-0020-2. arXiv: 1611.09720 [gr-qc].

[241] Alexander Y. Potekhin, José A. Pons, and Dany Page. "Neutron Stars—Cooling and Transport". In: *Space Science Reviews* 191.1-4 (Oct. 2015), pp. 239–291. DOI: 10.1007/s11214-015-0180-9. arXiv: 1507.06186 [astro-ph.HE].

[242] Frans Pretorius. "Evolution of binary black hole spacetimes". In: *Phys. Rev. Lett.* 95 (2005), p. 121101. eprint: gr-qc/0507014.

[243] D. J. Price and S. Rosswog. "Producing Ultrastrong Magnetic Fields in Neutron Star Mergers". In: *Science* 312 (May 2006), pp. 719–722. DOI: 10.1126/science.1125201. eprint: astro-ph/0603845.

[244] D. Radice. "General-relativistic Large-eddy Simulations of Binary Neutron Star Mergers". In: *Astrophys. J. Lett.* 838, L2 (Mar. 2017), p. L2. DOI: 10.3847/2041-8213/aa6483. arXiv: 1703.02046 [astro-ph.HE].

[245] D. Radice, S. Bernuzzi, and C. D. Ott. "One-armed spiral instability in neutron star mergers and its detectability in gravitational waves". In: *Phys. Rev. D* 94.6, 064011 (Sept. 2016), p. 064011. DOI: 10.1103/PhysRevD.94.064011. arXiv: 1603.05726 [gr-qc].

[246] D. Radice, A. Perego, S. Bernuzzi, and B. Zhang. "Long-lived remnants from binary neutron star mergers". In: *Mon. Not. R. Astron. Soc.* 481 (Dec. 2018), pp. 3670–3682. DOI: 10.1093/mnras/sty2531. arXiv: 1803.10865 [astro-ph.HE].

[247] D. Radice, A. Perego, F. Zappa, and S. Bernuzzi. "GW170817: Joint Constraint on the Neutron Star Equation of State from Multimessenger Observations". In: *Astrophys. J. Lett.* 852, L29 (Jan. 2018), p. L29. DOI: 10.3847/2041-8213/aaa402. arXiv: 1711.03647 [astro-ph.HE].

[248] D. Radice and L. Rezzolla. "THC: a new high-order finite-difference high-resolution shock-capturing code for special-relativistic hydrodynamics". In: *Astron. Astrophys.* 547 (June 2012), A26. DOI: 10.1051/0004-6361/201219735. arXiv: 1206.6502 [astro-ph.IM].

[249] D. Radice, L. Rezzolla, and F. Galeazzi. "High-order fully general-relativistic hydrodynamics: new approaches and tests". In: *Class. Quantum Grav.* 31.7, 075012 (Apr. 2014), p. 075012. DOI: 10.1088/0264-9381/31/7/075012. arXiv: 1312.5004 [gr-qc].

[250] D. Radice et al. "Dynamical Mass Ejection from Binary Neutron Star Mergers". In: *Mon. Not. R. Astron. Soc.* 460 (Aug. 2016), pp. 3255–3271. DOI: 10.1093/mnras/stw1227. arXiv: 1601.02426 [astro-ph.HE].

[251] David Radice. "Binary Neutron Star Merger Simulations with a Calibrated Turbulence Model". In: *Symmetry* 12.8 (July 2020), p. 1249. DOI: 10.3390/sym12081249. arXiv: 2005.09002 [astro-ph.HE].

[252] David Radice, Sebastiano Bernuzzi, and Albino Perego. In: ().

[253] David Radice, Sebastiano Bernuzzi, Albino Perego, and Roland Haas. "A new moment-based general-relativistic neutrino-radiation transport code: Methods and first applications to neutron star mergers". In: *Mon. Not. Roy. Astron. Soc.* 512.1 (2022), pp. 1499–1521. DOI: 10.1093/mnras/stac589. arXiv: 2111.14858 [astro-ph.HE].

[254] David Radice et al. "Binary Neutron Star Mergers: Mass Ejection, Electromagnetic Counterparts, and Nucleosynthesis". In: *Astrophys. J.* 869, 130 (Dec. 2018), p. 130. DOI: 10.3847/1538-4357/aaf054. arXiv: 1809.11161 [astro-ph.HE].

[255] Arnab K. Ray and J. K. Bhattacharjee. "Realizability of stationary spherically symmetric transonic accretion". In: *Phys. Rev. E* 66.6, 066303 (Dec. 2002), p. 066303. DOI: 10.1103/PhysRevE.66.066303. arXiv: astro-ph/0212558 [astro-ph].

[256] M. H. Lakshminarayana Reddy and Meheboob Alam. "Regularized extended-hydrodynamic equations for a rarefied granular gas and the plane shock waves". In: *Physical Review Fluids* 5.4, 044302 (Apr. 2020), p. 044302. DOI: 10.1103/PhysRevFluids.5.044302.

[257] C. Reisswig, N. T. Bishop, D. Pollney, and B. Szilágyi. "Unambiguous Determination of Gravitational Waveforms from Binary Black Hole Mergers". In: *Phys. Rev. Lett.* 103.22, 221101 (Nov. 2009), p. 221101. DOI: 10.1103/PhysRevLett.103.221101. arXiv: 0907.2637 [gr-qc].

[258] C. Reisswig and D. Pollney. "Notes on the integration of numerical relativity waveforms". In: *Class. Quantum Grav.* 28 (2011), p. 195015. arXiv: 1006.1632 [gr-qc].

[259] L. Rezzolla, E. R. Most, and L. R. Weih. "Using Gravitational-wave Observations and Quasi-universal Relations to Constrain the Maximum Mass of Neutron Stars". In: *Astrophys. J. Lett.* 852, L25 (Jan. 2018), p. L25. DOI: 10.3847/2041-8213/aaa401. arXiv: 1711.00314 [astro-ph.HE].

[260] L. Rezzolla and K. Takami. "Gravitational-wave signal from binary neutron stars: A systematic analysis of the spectral properties". In: *Phys. Rev. D* 93.12, 124051 (June 2016), p. 124051. DOI: 10.1103/PhysRevD.93.124051. arXiv: 1604.00246 [gr-qc].

[261] L. Rezzolla and O. Zanotti. *Relativistic Hydrodynamics*. Oxford, UK: Oxford University Press, 2013. ISBN: 9780198528906. DOI: 10.1093/acprof:oso/9780198528906.001.0001.

[262] L. Rezzolla et al. "The Missing Link: Merging Neutron Stars Naturally Produce Jet-like Structures and Can Power Short Gamma-ray Bursts". In: *Astrophys. J. Letters* 732, L6 (May 2011), p. L6. DOI: 10.1088/2041-8205/732/1/L6. arXiv: 1101.4298 [astro-ph.HE].

[263] Luciano Rezzolla et al. *The Physics and Astrophysics of Neutron Stars*. Vol. 457. 2018. DOI: 10.1007/978-3-319-97616-7.

[264] T. E. Riley et al. "A NICER View of PSR J0030+0451: Millisecond Pulsar Parameter Estimation". In: *Astrophys. J. Lett.* 887.1, L21 (Dec. 2019), p. L21. DOI: 10.3847/2041-8213/ab481c. arXiv: 1912.05702 [astro-ph.HE].

[265] B. Ripperda et al. "General-relativistic Resistive Magnetohydrodynamics with Robust Primitive-variable Recovery for Accretion Disk Simulations". In: *Astrophys. J., Supp.* 244.1, 10 (Sept. 2019), p. 10. DOI: 10.3847/1538-4365/ab3922. arXiv: 1907.07197 [physics.comp-ph].

[266] Roger W. Romani et al. "PSR J0952–0607: The Fastest and Heaviest Known Galactic Neutron Star". In: *Astrophys. J. Lett.* 934.2 (2022), p. L18. DOI: 10.3847/2041-8213/ac8007. arXiv: 2207.05124 [astro-ph.HE].

[267] Paul Romatschke and Ulrike Romatschke. *Relativistic Fluid Dynamics In and Out of Equilibrium: And Applications to Relativistic Nuclear Collisions*. Cambridge Monographs on Mathematical Physics. Cambridge University Press, 2019. DOI: 10.1017/9781108651998.

[268] M. Ruiz, R. N. Lang, V. Paschalidis, and S. L. Shapiro. "Binary Neutron Star Mergers: A Jet Engine for Short Gamma-Ray Bursts". In: *Astrophys. J. Lett.* 824, L6 (June 2016), p. L6. DOI: 10.3847/2041-8205/824/1/L6. arXiv: 1604.02455 [astro-ph.HE].

[269] M. Ruiz, S. L. Shapiro, and A. Tsokaros. "GW170817, general relativistic magnetohydrodynamic simulations, and the neutron star maximum mass". In: *Phys. Rev. D* 97.2, 021501 (Jan. 2018), p. 021501. DOI: 10.1103/PhysRevD.97.021501. arXiv: 1711.00473 [astro-ph.HE].

[270] Milton Ruiz, David Hilditch, and Sebastiano Bernuzzi. "Constraint preserving boundary conditions for the Z4c formulation of general relativity". In: *Phys. Rev. D* 83 (2011), p. 024025. DOI: 10.1103/PhysRevD.83.024025. arXiv: 1010.0523 [gr-qc].

[271] Milton Ruiz, Antonios Tsokaros, and Stuart L. Shapiro. "Magnetohydrodynamic simulations of binary neutron star mergers in general relativity: Effects of magnetic field orientation on jet launching". In: *Phys. Rev. D* 101.6, 064042 (Mar. 2020), p. 064042. DOI: 10.1103/PhysRevD.101.064042. arXiv: 2001.09153 [astro-ph.HE].

[272] Nikhil Sarin and Paul D. Lasky. "The evolution of binary neutron star post-merger remnants: a review". In: *General Relativity and Gravitation* 53.6, 59 (June 2021), p. 59. DOI: 10.1007/s10714-021-02831-1. arXiv: 2012.08172 [astro-ph.HE].

[273] R. F. Sawyer. "Bulk viscosity of a gas of neutrinos and coupled scalar particles, in the era of recombination". In: *Phys. Rev. D* 74 (4 Aug. 2006), p. 043527. DOI: 10.1103/PhysRevD.74.043527. URL: https://link.aps.org/doi/10.1103/PhysRevD.74.043527.

[274] Jürgen Schaffner-Bielich. *Compact Star Physics*. Cambridge University Press, Aug. 2020. ISBN: 978-1-316-84835-7, 978-1-107-18089-5. DOI: 10.1017/9781316848357.

[275] Björn Schenke, Sangyong Jeon, and Charles Gale. "Elliptic and Triangular Flow in Event-by-Event D=3+1 Viscous Hydrodynamics". In: *Phys. Rev. Lett.* 106.4, 042301 (Jan. 2011), p. 042301. DOI: 10.1103/PhysRevLett.106.042301. arXiv: 1009.3244 [hep-ph].

[276] Andreas Schmitt and Peter Shternin. "Reaction Rates and Transport in Neutron Stars". In: *Astrophysics and Space Science Library*. Ed. by Luciano Rezzolla et al. Vol. 457. Astrophysics and Space Science Library. Jan. 2018, p. 455. DOI: 10.1007/978-3-319-97616-7_9. arXiv: 1711.06520 [astro-ph.HE].

[277] Erik Schnetter, Scott H. Hawley, and Ian Hawke. "Evolutions in 3D numerical relativity using fixed mesh refinement". In: *Classical and Quantum Gravity* 21.6 (Mar. 2004), pp. 1465–1488. DOI: 10.1088/0264-9381/21/6/014. arXiv: gr-qc/0310042 [gr-qc].

[278] Stuart L. Shapiro. "Differential Rotation in Neutron Stars: Magnetic Braking and Viscous Damping". In: *Astrophys. J.* 544.1 (Nov. 2000), pp. 397–408. DOI: 10.1086/317209. arXiv: astro-ph/0010493 [astro-ph].

[279] M. Shibata. *Numerical Relativity*. Singapore: World Scientific, 2016. ISBN: 978-981-4699-71-6. DOI: 10.1142/9692.

[280] M. Shibata and K. Kiuchi. "Gravitational waves from remnant massive neutron stars of binary neutron star merger: Viscous hydrodynamics effects". In: *Phys. Rev. D* 95.12, 123003 (June 2017), p. 123003. DOI: 10.1103/PhysRevD.95.123003. arXiv: 1705.06142 [astro-ph.HE].

[281] M. Shibata and K. Kiuchi. "Gravitational waves from remnant massive neutron stars of binary neutron star merger: Viscous hydrodynamics effects". In: *Phys. Rev. D* 95.12, 123003 (June 2017), p. 123003. DOI: 10.1103/PhysRevD.95.123003. arXiv: 1705.06142 [astro-ph.HE].

[282] M. Shibata and T. Nakamura. "Evolution of three-dimensional gravitational waves: Harmonic slicing case". In: *Phys. Rev. D* 52 (Nov. 1995), pp. 5428–5444. DOI: 10.1103/PhysRevD.52.5428.

[283] Masaru Shibata, Sho Fujibayashi, and Yuichiro Sekiguchi. "Long-term evolution of a merger-remnant neutron star in general relativistic magnetohydrodynamics: Effect of magnetic winding". In: *Phys. Rev. D* 103.4, 043022 (Feb. 2021), p. 043022. DOI: 10.1103/PhysRevD.103.043022. arXiv: 2102.01346 [astro-ph.HE].

[284] Masaru Shibata, Sho Fujibayashi, and Yuichiro Sekiguchi. "Long-term evolution of neutron-star merger remnants in general relativistic resistive magnetohydrodynamics with a mean-field dynamo term". In: *Phys. Rev. D* 104.6, 063026 (Sept. 2021), p. 063026. DOI: 10.1103/PhysRevD.104.063026. arXiv: 2109.08732 [astro-ph.HE].

[285] Masaru Shibata and Kenta Hotokezaka. "Merger and Mass Ejection of Neutron Star Binaries". In: *Annual Review of Nuclear and Particle Science* 69.1 (2019), pp. 41–64. DOI: 10.1146/annurev-nucl-101918-023625. eprint: https://doi.org/10.1146/annurev-nucl-101918-023625. URL: https://doi.org/10.1146/annurev-nucl-101918-023625.

[286] Masaru Shibata, Kenta Kiuchi, and Yu-ichiro Sekiguchi. "General relativistic viscous hydrodynamics of differentially rotating neutron stars". In: *Phys. Rev. D* 95 (8 Apr. 2017), p. 083005. DOI: 10.1103/PhysRevD.95.083005. URL: https://link.aps.org/doi/10.1103/PhysRevD.95.083005.

[287] Masaru Shibata, Enping Zhou, Kenta Kiuchi, and Sho Fujibayashi. "Constraint on the maximum mass of neutron stars using GW170817 event". In: *Phys. Rev. D* 100.2, 023015 (July 2019), p. 023015. DOI: 10.1103/PhysRevD.100.023015. arXiv: 1905.03656 [astro-ph.HE].

[288] C. W. Shu. "High Order ENO and WENO Schemes for Computational Fluid Dynamics". In: *High-Order Methods for Computational Physics*. Ed. by T. J. Barth and H. Deconinck. Springer, 1999, pp. 439–582.

[289] D. M. Siegel, R. Ciolfi, A. I. Harte, and L. Rezzolla. "Magnetorotational instability in relativistic hypermassive neutron stars". In: *Phys. Rev. D R* 87.12, 121302 (June 2013), p. 121302. DOI: 10.1103/PhysRevD.87.121302. arXiv: 1302.4368 [gr-qc].

[290] Daniel M. Siegel, Philipp Mösta, Dhruv Desai, and Samantha Wu. "Recovery Schemes for Primitive Variables in General-relativistic Magnetohydrodynamics". In: *Astrophys. J.* 859.1, 71 (May 2018), p. 71. DOI: 10.3847/1538-4357/aabcc5. arXiv: 1712.07538 [astro-ph.HE].

[291] N. Stergioulas, A. Bauswein, K. Zagkouris, and H.-T. Janka. "Gravitational waves and non-axisymmetric oscillation modes in mergers of compact object binaries". In: *Mon. Not. R. Astron. Soc.* 418 (Nov. 2011), pp. 427–436. DOI: 10.1111/j.1365-2966.2011.19493.x. arXiv: 1105.0368 [gr-qc].

[292] Henning Struchtrup. "Stable transport equations for rarefied gases at high orders in the Knudsen number". In: *Physics of Fluids* 16.11 (Nov. 2004), pp. 3921–3934. DOI: 10.1063/1.1782751.

[293] Farid Taghinavaz. "Causality and Stability Conditions of a Conformal Charged Fluid". In: *JHEP* 08 (2020), p. 119. DOI: 10.1007/JHEP08(2020)119. arXiv: 2004.01897 [hep-th].

[294] K. Takami, L. Rezzolla, and L. Baiotti. "Constraining the Equation of State of Neutron Stars from Binary Mergers". In: *Phys. Rev. Lett.* 113.9, 091104 (Aug. 2014), p. 091104. DOI: 10.1103/PhysRevLett.113.091104. arXiv: 1403.5672 [gr-qc].

[295] K. Takami, L. Rezzolla, and L. Baiotti. "Constraining the Equation of State of Neutron Stars from Binary Mergers". In: *Phys. Rev. Lett.* 113.9, 091104 (Aug. 2014), p. 091104. DOI: 10.1103/PhysRevLett.113.091104. arXiv: 1403.5672 [gr-qc].

[296] K. Takami, L. Rezzolla, and L. Baiotti. "Spectral properties of the post-merger gravitational-wave signal from binary neutron stars". In: *Phys. Rev. D* 91.6, 064001 (Mar. 2015), p. 064001. DOI: 10.1103/PhysRevD.91.064001. arXiv: 1412.3240 [gr-qc].

[297] M. Takamoto and S.-I. Inutsuka. "A fast numerical scheme for causal relativistic hydrodynamics with dissipation". In: *Journal of Computational Physics* 230 (Aug. 2011), pp. 7002–7017. DOI: 10.1016/j.jcp.2011.05.030. arXiv: 1106.1732 [astro-ph.HE].

[298] T. M. Tauris and E. P. J. van den Heuvel. "Formation and evolution of compact stellar X-ray sources". In: *Compact stellar X-ray sources*. Vol. 39. 2006, pp. 623–665. DOI: 10.48550/arXiv.astro-ph/0303456.

[299] Saul A. Teukolsky. "Perturbations of a Rotating Black Hole. I. Fundamental Equations for Gravitational, Electromagnetic, and Neutrino-Field Perturbations". In: *Astrophys. J.* 185 (1973), pp. 635–647.

[300] Kip S. Thorne and Roger D. Blandford. *Modern Classical Physics. Optics, Fluids, Plasmas, Elasticity, Relativity, and Statistical Physics*. 2018.

[301] H. Togashi et al. "Nuclear equation of state for core-collapse supernova simulations with realistic nuclear forces". In: *Nucl. Phys.* A961 (2017), pp. 78–105. DOI: 10.1016/j.nuclphysa.2017.02.010. arXiv: 1702.05324 [nucl-th].

[302] Richard C. Tolman. "Static Solutions of Einstein's Field Equations for Spheres of Fluid". In: *Physical Review* 55.4 (Feb. 1939), pp. 364–373. DOI: 10.1103/PhysRev.55.364.

[303] Samuel D. Tootle, L. Jens Papenfort, Elias R. Most, and Luciano Rezzolla. "Quasi-universal Behavior of the Threshold Mass in Unequal-mass, Spinning Binary Neutron Star Mergers". In: *Astrophys. J. Lett.* 922.1, L19 (Nov. 2021), p. L19. DOI: 10.3847/2041-8213/ac350d. arXiv: 2109.00940 [gr-qc].

[304] E. F. Toro. *Riemann Solvers and Numerical Methods for Fluid Dynamics*. third. Springer-Verlag, 2009.

[305] Manuel Torrilhon. "Modeling Nonequilibrium Gas Flow Based on Moment Equations". In: *Annual Review of Fluid Mechanics* 48 (Jan. 2016), pp. 429–458. DOI: 10.1146/annurev-fluid-122414-034259.

[306] G. Toth. "The div B=0 Constraint in Shock-Capturing Magnetohydrodynamics Codes". In: *J. Comput. Phys.* 161 (2000), pp. 605–652. DOI: 10.1006/jcph.2000.6519.

[307] Roberto Turolla and Luciano Nobili. "On the Role of Viscosity in Spherically Symmetric Transonic Flows". In: *Astrophys. J.* 342 (July 1989), p. 982. DOI: 10.1086/167655.

[308] P. Van and T.S. Biro. "First order and stable relativistic dissipative hydrodynamics". In: *Phys. Lett. B* 709 (2012), pp. 106–110. DOI: 10.1016/j.physletb.2012.02.006. arXiv: 1109.0985 [nucl-th].

[309] Daniele Viganò, Ricard Aguilera-Miret, and Carlos Palenzuela. "Extension of the subgrid-scale gradient model for compressible magnetohydrodynamics turbulent instabilities". In: *Physics of Fluids* 31.10, 105102 (Oct. 2019), p. 105102. DOI: 10.1063/1.5121546. arXiv: 1904.04099 [physics.flu-dyn].

[310] Daniele Viganò et al. “General relativistic MHD large eddy simulations with gradient subgrid-scale model”. In: *Phys. Rev. D* 101.12, 123019 (June 2020), p. 123019. DOI: 10.1103/PhysRevD.101.123019. arXiv: 2004.00870 [gr-qc].

[311] Daniele Viganò et al. “Magneto-thermal evolution of neutron stars with coupled Ohmic, Hall and ambipolar effects via accurate finite-volume simulations”. In: *Computer Physics Communications* 265, 108001 (Aug. 2021), p. 108001. DOI: 10.1016/j.cpc.2021.108001. arXiv: 2104.08001 [astro-ph.HE].

[312] Darach Watson et al. “Identification of strontium in the merger of two neutron stars”. In: *Nature* 574.7779 (Oct. 2019), pp. 497–500. DOI: 10.1038/s41586-019-1676-3. arXiv: 1910.10510 [astro-ph.HE].

[313] L. R. Weih, E. R. Most, and L. Rezzolla. “On the stability and maximum mass of differentially rotating relativistic stars”. In: *Mon. Not. R. Astron. Soc.* 473 (Jan. 2018), pp. L126–L130. DOI: 10.1093/mnrasl/slx178. arXiv: 1709.06058 [gr-qc].

[314] Lukas R. Weih, Hector Olivares, and Luciano Rezzolla. “Two-moment scheme for general-relativistic radiation hydrodynamics: a systematic description and new applications”. In: *Mon. Not. R. Astron. Soc.* 495.2 (May 2020), pp. 2285–2304. DOI: 10.1093/mnras/staa1297. arXiv: 2003.13580 [gr-qc].

[315] Steven Weinberg. “Entropy Generation and the Survival of Protogalaxies in an Expanding Universe”. In: *Astrophys. J.* 168 (Sept. 1971), p. 175. DOI: 10.1086/151073.

[316] Inc. Wolfram Research. *Mathematica, Version 12.1*. Champaign, IL, 2020. 2020. URL: https://www.wolfram.com/mathematica.

[317] S. E. Woosley, A. Heger, and T. A. Weaver. “The evolution and explosion of massive stars”. In: *Rev. Mod. Phys.* 74 (Nov. 2002), p. 1015.

[318] James W. York. “Kinematics and Dynamics of General Relativity”. In: *Sources of gravitational radiation*. Ed. by Larry L. Smarr. Cambridge, UK: Cambridge University Press, 1979, pp. 83–126. ISBN: 0-521-22778-X.

[319] George Younes et al. “Pulse Peak Migration during the Outburst Decay of the Magnetar SGR 1830-0645: Crustal Motion and Magnetospheric Untwisting”. In: *Astrophys. J. Lett.* 924.2, L27 (Jan. 2022), p. L27. DOI: 10.3847/2041-8213/ac4700. arXiv: 2201.05517 [astro-ph.HE].

[320] J. Zrake and A. I. MacFadyen. “Magnetic Energy Production by Turbulence in Binary Neutron Star Mergers”. In: *Astrophys. J.* 769, L29 (June 2013), p. L29. DOI: 10.1088/2041-8205/769/2/L29. arXiv: 1303.1450 [astro-ph.HE].